SAPIENZA
UNIVERSITÀ DI ROMA

Dome-shaped two-dimensional crystals: A playground for the study of the crystal mechanical and optoelectronic properties

PhD in Physics, XXXV cycle

Candidate

Elena Blundo

Supervisor

Prof. Antonio Polimeni

PhD Coordinator

Prof. Fabio Sciarrino

Tutor from the PhD Board

Prof. Maria Grazia Betti

Contents

Introduction

The dawn of few-layer thick crystals can be traced back to several decades ago. Due to the fascinating phenomena potentially associated with (quasi) two-dimensional (2D) systems, great interest for these materials started arising since the first half of the 20^{th} century, much before the discovery of stable 2D crystals. In 1959, Richard Feynman gave an influential lecture entitled 'There's Plenty of Room at the Bottom' [1], wherein he envisioned a scientific breakthrough in the field of physics with his questions '*What could we do with layered structures with just the right layers? What would the properties of materials be if we could really arrange the atoms the way we want them?*'. However, the theories developed by Peierls and Landau in the '30s turned down the possible existence of truly 2D crystals in stable form due to a divergent contribution of thermal fluctuations [2, 3]. The latter should induce atom displacements comparable to the interatomic distances at any finite temperature and thus render atomically-thin systems unstable [4]. The argument was later supported by Mermin [5] and by experimental observations [6]. The possibility to explore a truly 2D world seemed, therefore, denied.

In a paper published in 1972 [7], however, thin layers of $NbSe_2$ were obtained in order to study the superconducting-resistive transition temperature as the crystal thickness was reduced. Interestingly, the author affirmed that '*because of the weak bonding between adjacent Se layers, the crystals are easily cleaved*' and '*thin crystals are obtained by sticking a crystal onto the substrate and peeling it away until a very thin crystal remains on the substrate*', obtaining flakes as thin as 6 layers. The same technique had already been used to obtain thin crystals of MoS_2 [8] —a material which, like $NbSe_2$, belongs to the class of transition metal dichalcogenides (TMDs). Still, notwithstanding these slow advancements, the research field aimed at the investigation of (quasi-)2D systems mostly laid dormant until the third millennium, when it received a tremendous boost with the ground-breaking discovery of graphene. Graphene —a single layer of carbon atoms tightly packed into a 2D honeycomb lattice— was first isolated in 2004 by A. K. Geim and K. S. Novoselov neither with specific devices nor via ultra-complicated techniques, but via the simple —though brilliant— use of scotch tape to 'peel away' single layers of graphite [9]. The isolation and stability of graphene, previously thought to be impossible, opened the doors of Flatland [10] to the condensed matter physics community. Since then, the family of 2D systems has grown rapidly, as many other crystals have

been found to be characterised by a layered structure akin to graphite, with different layers bound together by weak van der Waals (vdW) forces. Among them, graphene features a semi-metallic nature and is characterised by exceptionally high carrier mobilities; hexagonal boron nitride (hBN) is an extremely good insulator and dielectric with a large bandgap; black phosphorus (BP) possesses interesting properties that arise from its inherent in-plane anisotropy, and, as a consequence, from its anisotropic band structure; the family of transition metal dichalcogenides (TMDs, such as MoS_2, WS_2, $MoSe_2$, WSe_2, $MoTe_2$, WTe_2, NbS_2, $NbSe_2$, etc.) is richly varied, as it comprises some superconducting materials with charge density waves and Weyl semimetal properties, as well as many semiconducting materials, with bandgaps ranging from the visible to the near infrared spectral region. In the single layer limit, semiconducting TMDs are characterised by an extremely efficient light emission, which makes them ideal candidates for the realisation of innovative, flexible optoelectronic devices. Finally, post-transition-metal chalcogenides (MCs, such as InSe and GaSe) have recently attracted interest as 2D semiconductors, for their high carrier mobilities and their potentiality for hydrogen storage.

Aside from the possibility of exploring the effects of lower dimensionality on the properties of atomically thin crystals, the existence of these crystals in stable form opens new avenues to materials engineering. Indeed, the inherent all-surface nature of these systems entails a higher sensitivity to external perturbations [11, 12], which can in turn be exploited to modify the material properties. Among all possible external perturbations, the incredible mechanical flexibility and robustness [13–15] of 2D crystals have offered the possibility to subject them to high mechanical deformations, engendering strains larger than 10 %. Such strains are able to induce major modifications in the electronic, optical, magnetic, transport and chemical properties of 2D materials, leading to the observation of a plethora of intriguing phenomena —ripe with new physics and novel opportunities.

In the past decade, great attention has been devoted to the development of methods to mechanically deform 2D crystals, that enabled the attainment of strain fields much larger than those generally achievable in conventional bulk semiconductors and quantum wells [11, 16]. These studies have revealed how strain can induce major changes in the electronic structure of 2D crystals, originating intriguing novel phenomena and rendering these materials extremely promising and apt for flexible electronics [11, 12, 16]. Furthermore, single atomic layers with diverse chemical composition and optoelectronic characteristics can be stacked together to create heterostructures, which can be elastically deformed to create a wide number of novel layered materials with as yet unexplored physical properties [17, 18]. Research in this field is hot and is paving the way towards the creation of planar electronic devices with ultralow-power consumption, flexible electronics, sensors, and components for energy scavenging and storage [11].

Within such a flourishing research context, new discoveries have been seamlessly unveiled in the past few years, and still new targets are currently being reached.

This thesis will be focused on the development of an original strategy to induce

strain fields in 2D crystals, and on the study of the effect of strain on the peculiar properties of the material. The thesis will be articulated as follows:

- The Prologue will briefly introduce the reader to the 2D world, especially highlighting the peculiar properties of 2D TMDs and hBN, thanks to which a flourishing interest in these materials has arisen. The final part of the Prologue will instead provide the reader with an overview of the field of strain engineering of 2D crystals.

- Chapter 1 will present the innovative method to induce strain in TMDs and hBN pioneered by the candidate and her group. It will be discussed how, by irradiating bulk flakes of these materials with low-energy hydrogen ions, it is possible to induce —on the flake surface— the formation of domes with thickness of one-to-few layers and filled with pressurised hydrogen. The basic properties of these structures will be discussed. This Chapter will also discuss the effects of hydrogen-ion irradiation of other crystals, where the formation of domes was not achieved but other interesting phenomenologies were observed.

- Chapter 2 will present a characterisation of the vibrational properties of the domes, highlighting their link with the strain distribution. This chapter will focus in particular on Raman studies of TMD domes and on Raman and infrared (IR) characterisations of hBN domes. The observed huge shifts and splittings of the vibrational modes will be correlated with the strain magnitude and character, which will be estimated by numerical calculations.

- Chapter 3 will focus on the possibility to engineer the domes. Lithography-based approaches will be used to achieve control over their size and position, and eventually over the strain magnitude.

- Chapter 4 will investigate from a fundamental point of view the morphology and mechanics of the system. In particular, an analytical method to describe the system will be presented. The model, coupled to morphological and mechanical experimental measurements, allows one to obtain precious information on the elastic properties of the membrane and on the adhesion energy between the monolayer and the bulk crystal.

- Chapter 5 will discuss how strain affects the optoelectronic properties of TMDs. In particular, this chapter will present steady-state and time-resolved photoluminescence (PL) studies aimed at highlighting the effect of strain on the free excitons. Such measurements highlight intriguing behaviours, such as strain-induced direct-to-indirect exciton crossovers, that deeply affect the emitted light intensity and decay time.

- Chapter 6 will present a characterisation of direct and indirect excitons when subjected to high magnetic fields. Indeed, magnetic fields induce a Zeeman effect in TMD MLs, which is promising for their utilisation for valleytronics.

The effect of strain on the Zeeman effect has however not been investigated so far. The results presented in this chapter shed light on this, and highlight an unexpected behaviour, that unveils hybridisation phenomena between nearly resonant direct and indirect excitons.

- Chapter 7 will demonstrate the possibility to exploit strained 2D materials for quantum applications. In particular, this chapter will discuss the observation of single photon emitters at cryogenic temperatures in hBN-capped TMD domes.

- Finally, Chapter 8 will investigate a novel perspective: that of exploiting selective strain engineering in van der Waals heterostructures. Specifically, we will here focus on heterostructures made of a TMD dome and of an InSe unstrained layer, showing how strain is able to modify the electronic properties of the heterostructure.

Prologue: transition metal dichalcogenides, hexagonal boron nitride, and strain engineering

Within the wide family of 2D crystals beyond graphene, TMDs and hBN have attracted particular interest. TMDs have chemical formula MX_2, being constituted by one layer of a transition metal M sandwiched in between two layers of a chalcogen atom X, as illustrated in Fig. 0.1. From a top view, the atoms are arranged in a honeycomb configuration, similar to that of graphene. The height of the single layer of TMD (namely, the X-M-X sandwich) is about 0.6-0.7 nm [19–21], and the M atom is bound to the X atoms by strong covalent bonds. The orbitals involved in the creation of these bonds are the d orbitals of the M atom and the p orbitals of the X atoms [22]. hBN is a single layer of B and N atoms arranged in a honeycomb configuration analogous to that of graphene. The height of the single layer is about 0.33 nm [20, 21].

hBN is an insulating material, while the family of TMDs comprises superconducting materials with charge density waves and Weyl semimetal properties, as well as several semiconducting materials, with bandgaps ranging from the visible to the near infrared spectral region. All TMDs are generally characterised by a strong spin-orbit coupling (SOC): The high orbital velocities in the partially filled d subshells of the relatively heavy metal atoms M make it arise a strong SOC that splits the valence band into two spin-polarised bands [23]. Time-reversal symmetry requires the spin and momentum degrees of freedom to be coupled, so that the **K** and **K'** valleys carry opposite spin polarisations, as shown in Fig. 0.2. This unique spin and valley texture makes it possible to control the spin and valley degrees of freedom in 2D TMDs and provides a route towards the utilisation of 2D materials with strong spin-orbit coupling and inversion symmetry breaking for valleytronics and spintronics [24]. This property is peculiar of TMDs since the most common 2D materials, such as graphene and hBN, are instead characterised by a weak SOC [25] (see Fig. 0.2).

hBN and TMDs in the 2H phase are also characterised by inversion symmetry

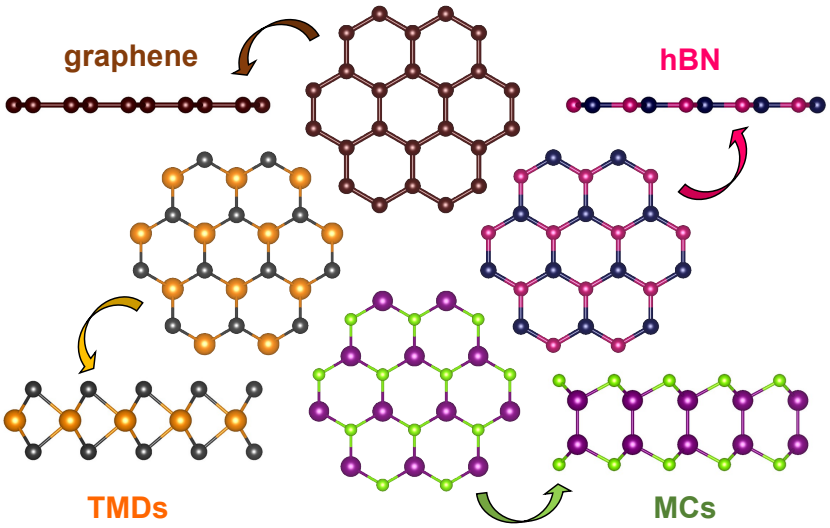

Figure 0.1: From a top view, the most common 2D materials such as graphene, hBN, TMDs and MCs display a honeycomb structure. The single layer of graphene is constituted by carbon atoms; that of hBN by an alternation of boron and nitrogen atoms; that of TMDs by a central layer of transition metal atoms sandwiched in between two layers of a chalcogen atom; and that of MCs by two central layer of post transition metal atoms sandwiched in between two layers of a chalcogen atom.

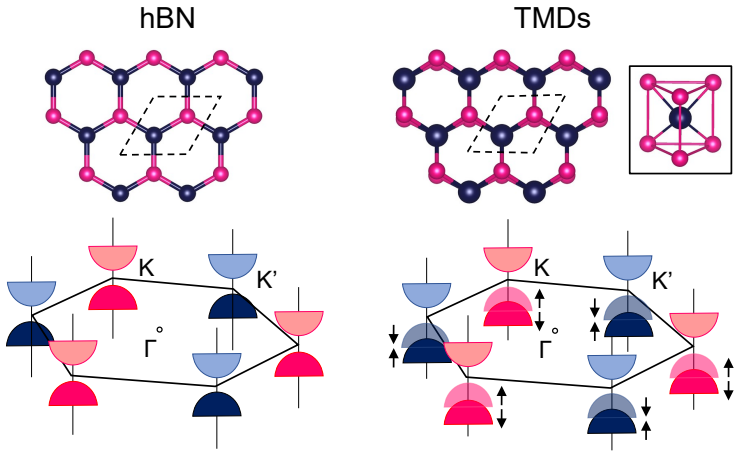

Figure 0.2: Lattice structures and band structures at the corners of the first Brillouin zone for hBN and TMDs in the 2H form. The dashed lines in the lattice diagrams indicate the unit cells. Due to spin-orbit coupling, the valence band of TMDs is split into two spin-polarised bands (as indicated by the arrows).

breaking [24]. For TMDs, the unit cell of the bulk contains two unit cells of the monolayer (ML) and has the inversion centre located in the middle plane. It follows that the single layer lacks an inversion centre and it is therefore said to be non-

centrosymmetric. This property can give rise to interesting phenomena such as the valley Hall effect, where carriers in different valleys (**K** or **K'**) flow to opposite transverse edges when an in-plane electric field is applied, thus implying potential applications in the field of valleytronics [24]. The lack of inversion symmetry is also at the origin of non-linear optical processes such as second harmonic generation (SHG) [26, 27], a typical property of all non-centrosymmetric media which, in the light of their broken symmetry, are characterised by a non-linear susceptibility [28, 29]. Peculiarly, in the case of ML TMDs, the non-linear susceptibility is found to be nearly three orders of magnitude larger than for other common non-linear crystals, resulting in an extraordinary SHG [27]. In general, all thin TMDs with an odd number of layers (*i.e.* the non-centrosymmetric ones) exhibit SHG, but this process is much more efficient when the monolayer limit is reached [30]. hBN is also non-centrosymmetric for flakes with an odd number of layers but, contrary to TMDs, it generally features a strong SHG both for mono- and multi-layered flakes [30].

In this thesis, the focus will be mainly on a subgroup of the TMD class, consisting of those TMDs whose metal atom is either tungsten (W) or molybdenum (Mo), and the chalcogen atom is sulphur (S) or selenium (Se) or tellurium (Te). The resulting compounds MoS_2, WS_2, $MoSe_2$, WSe_2, and $MoTe_2$ are semiconducting materials, with the only exception of WTe_2, which is instead a semimetal.

Semiconducting TMDs

Quantum confinement and the lack of the bulk dielectric screening have profound effects on the electronic and optical properties of 2D semiconducting TMDs. Semiconducting TMDs in the bulk form have indirect bandgaps. The valence-band maximum (VBM) and conduction band minimum (CBM) are in fact characterised by different wavevectors, the VBM being at the Γ point of the Brillouin zone, and the CBM at an intermediate point between the Γ point and the K point (called either Λ or T), as shown in the leftmost panel of Fig. 0.3 (where the calculation is done for MoS_2, but the same qualitative behaviour is found for all the other semiconducting TMDs). A direct transition is also present, involving the K points in both conduction band (CB) and valence band (VB), but this is at sizeable larger energy. Indeed, this indirect nature of bulk TMDs makes them poor in terms of light emission. If, starting from a bulk TMD, the number of layers N is reduced to up to two layers, the gap becomes larger since the CBM shifts upward (towards higher energies) and the VBM downwards (see the central panels of Fig. 0.3). However, if the monolayer limit is reached, the material undergoes a transition to a direct bandgap (see the rightmost panel in the same figure) [31], which results in a much stronger optical absorption and more efficient radiative recombination. The poor emitter bulk TMD suddenly becomes an efficient emitter and a jump is observed in the photoluminescence efficiency when the single layer limit is achieved.

The physical mechanism governing the evolution of band-edge states with N is intimately related to the nature of the electronic wave functions in this system, hav-

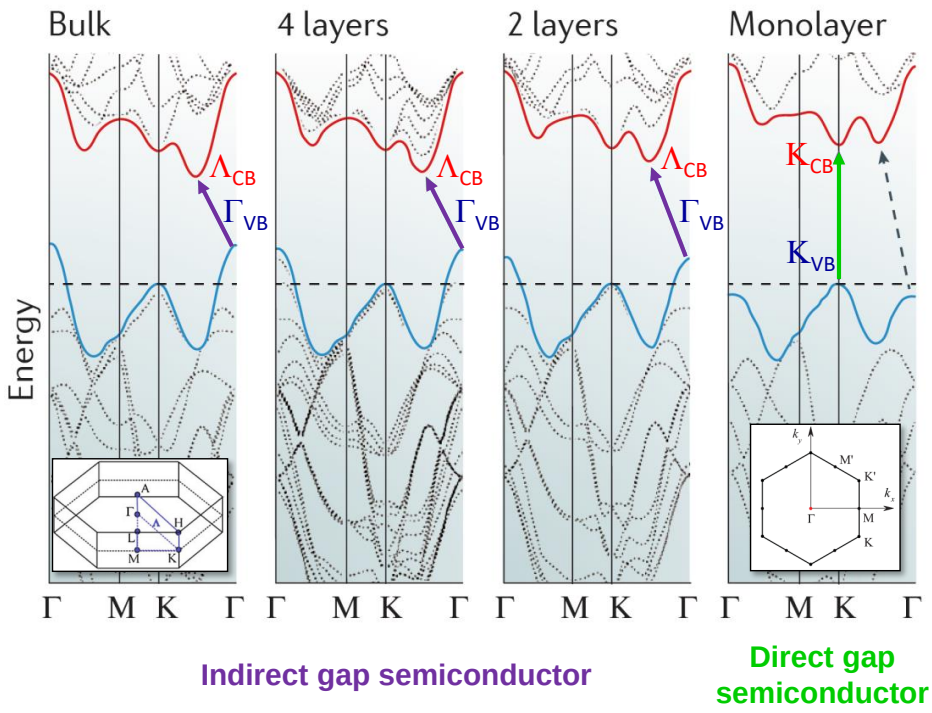

Figure 0.3: (a) From left to right, calculated band structures of: bulk MoS_2, quadrilayer MoS_2, bilayer MoS_2, and ML MoS_2. The solid arrows indicate the lowest energy transitions. The critical points involved in the transition are also reported. Bulk MoS_2 is characterised by an indirect bandgap. A direct transition occurs at high energies at the K point. With reducing the layer thickness, the indirect bandgap becomes larger, while the direct transition barely changes. A dramatic change occurs when achieving the ML MoS_2 limit, since in this form MoS_2 becomes a direct bandgap semiconductor. Insets: First Brillouin zones in the bulk and ML cases. Figure adapted with permission from A. Splendiani *et al.*, Nano Lett. **10**, 1271 (2010) [31]. Copyright 2010 American Chemical Society.

ing van der Waals (vdW) bonding between layers and covalent bonding within each layer. In TMDs, the K_{VB} and K_{CB} states, made of mainly the d orbitals of M and the p_x and p_y orbitals of X, are atomically localised within each X-M-X sandwich and do not leak into the interlayer space. Yet, the Γ_{VB} and Λ_{CB} states made of mainly the M d orbitals and the X p_z orbitals leak notably outside the X-M-X layers showing substantial delocalisation in the interlayer region. Being these states delocalised outside the sandwich, they are indeed sensitive to the presence of neighbouring layers. Consequently, the behaviour of the band energies of these interlayer extended states with N shows significant energy variation, in sharp contrast to the pinned 'zero confinement states' of K_{VB} and K_{CB} [22].

The calculations are confirmed by experimental results [32], obtained through angle resolved photoemission spectroscopy with submicron spatial resolution (micro-ARPES). The measurements reported for the bulk confirm the indirect nature of

its fundamental transition. Analogous measurements —repeated on few-layer-thick (FL), bilayer (BL) and monolayer (ML) samples— show that a remarkable change occurs when reaching the monolayer limit, clearly pointing to a direct bandgap in the single layer limit [32].

The direct bandgap of TMD MLs is indeed confirmed also by PL experiments, showing a much higher PL efficiency than in the case of multilayers. Optical transitions in these materials are mediated by excitons, with remarkably high binding energies, up to room temperature and above. This differs from what typically happens in conventional semiconductors and nanostructures, where the contribution of uncorrelated single particle transitions may be evidenced by temperature- [33], polarisation- [34], and magnetic field-dependent [35] absorption and PL studies [36]. Fig. 0.4 compares the exciton binding energy *vs* the bandgap of two classes of materials: bulk (or 3D) semiconductors and 2D materials. In the latter case, the exciton binding energy exceeds the same quantity in 3D crystals between one and more than two orders of magnitude. Such a strong electron-hole interaction is due to the strongly diminished dielectric screening caused by the absence of a bulk medium and by the large confinement that obliges the charge carriers to stay at a smaller distance [37, 38]. In the specific case of TMDs, the main exciton transitions are those

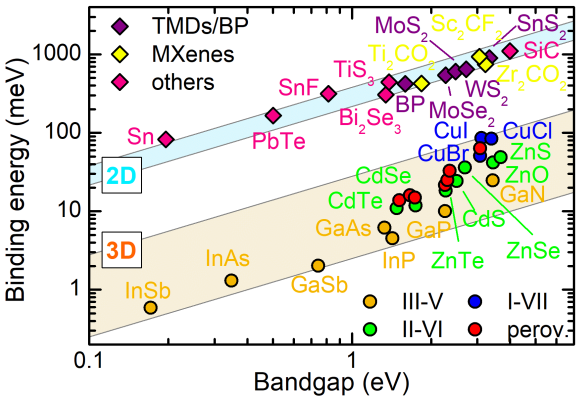

Figure 0.4: Exciton binding energy *vs* bandgap of the most common conventional 3D semiconductors (from `https://www.tf.uni-kiel.de/matwis/amat/semi_en/kap_5/advanced/t5_1_3.html` and Ref. [39] for GaP) and perovskites (measured experimentally in Ref. [40]), and those calculated theoretically for several 2D materials in Ref. [37]. The cyan and sand yellow shaded regions highlight the ranges of exciton binding energies of 2D and 3D semiconductors, respectively. Reproduced with permission from E. Blundo *et al.*, Appl. Phys. Rev. 8, 021318 (2021) [41]. Copyright 2021, The Authors.

related to electrons and holes sitting at the K point of the Brillouin zone. Indeed, as previously discussed and shown in Fig. 0.2, TMDs are characterised by strong spin-orbit coupling, that manifests itself in a noticeable splitting of the VB edge at the K point. Such a splitting is mainly governed by the atomic spin–orbit coupling of the metal atom, and it will therefore result to be stronger for heavier atoms (W with respect to Mo; Se with respect to S). Typical splittings are of $\sim 0.38 - 0.43$ eV

for WS_2, $\sim 0.14 - 0.16$ eV for MoS_2, $\sim 0.40 - 0.51$ eV for WSe_2, and $\sim 0.18 - 0.20$ eV for $MoSe_2$ [42]. A moderate splitting of ~ 32 meV for WS_2, ~ 3 meV for MoS_2, ~ 37 eV for WSe_2, and ~ 21 eV for $MoSe_2$ [42] is induced also at the CB K point. This results in the formation of two exciton transitions at the K point, named A and B exciton, involving different spin-split subbands; see sketches in Fig. 0.5, where the spin-split subbands are referred to as CB_+ and CB_- for the CB, and VB_+ and VB_- for the VB. Indeed, optical fields couple only to the orbital part of the wave function and spin is conserved in the optical transitions, implying that only excitons involving conduction and valence subbands with same spin are optically active. In TMDs,

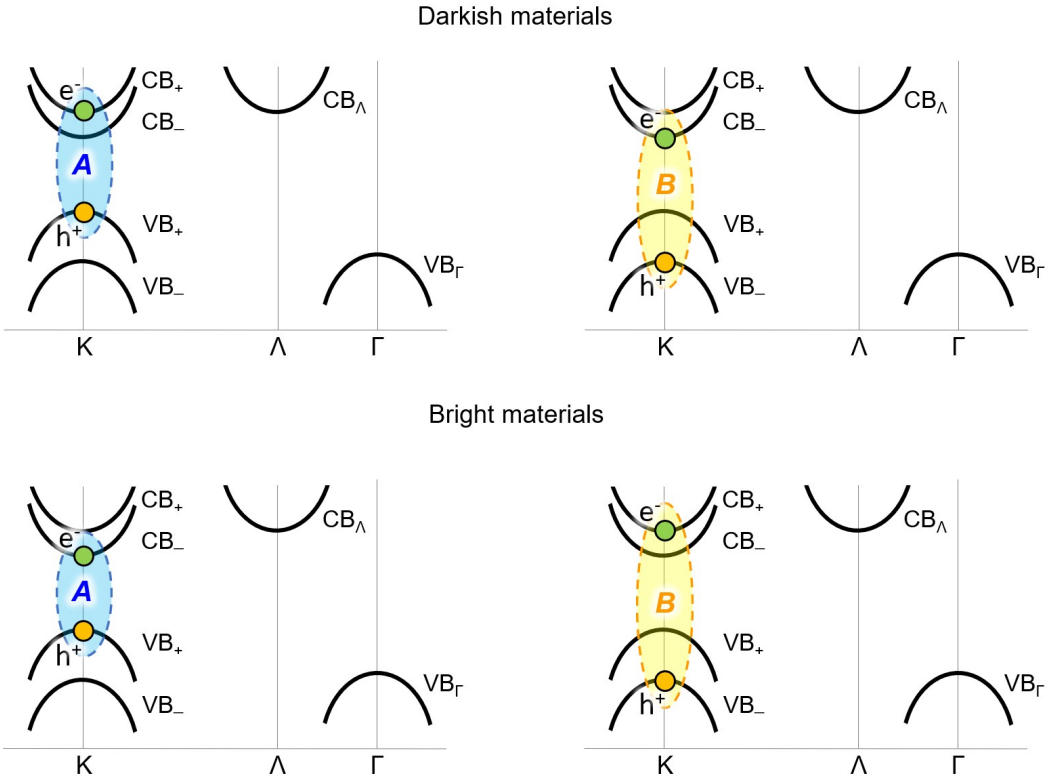

Figure 0.5: Sketch of the A (left) and B excitons (right) in darkish and bright TMDs.

two possible scenarios can be found: that in which the A exciton —*i.e.*, the lowest energy exciton transitions— involves VB_+ and the upper spin-spit conduction band CB_+ (Fig. 0.5, top), or that in which the A exciton involves VB_+ and the lower spin-spit conduction band CB_- (Fig. 0.5, bottom). The first case is found in most TMDs, including WS_2, WSe_2 and MoS_2 [43, 44], which are referred to as *darkish materials*, since the lowest energy state (CB_-,VB_+) involves states with opposite spin and is therefore optically dark. The second case is found in some TMDs, such as in $MoSe_2$, which are referred to as *bright materials* since (CB_-,VB_+) is optically active. Fig. 0.5 shows also the second band edges in both CB (at the Λ point) and

VB (at the Γ point). These states do not play a sizeable role in planar TMD MLs, but can play a relevant role in strained TMDs or in TMD-based HSs, as we will discuss in the following chapters. *A* and *B* excitons are typically clearly observable in reflectance/absorption/transmission measurements [43, 45–52]. In PL experiments, on the other side, the *A* exciton dominates the spectrum and the *B* exciton is typically seen only in the case of Mo-based compounds and not in W-based compounds; some exemplifying PL spectra that we acquired on WS_2, WSe_2, MoS_2 and $MoSe_2$ MLs at room temperature are shown in Fig. 0.6.

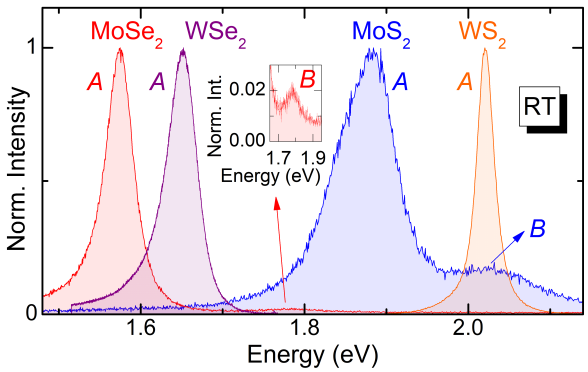

Figure 0.6: Room-temperature (RT) PL spectra of MLs of the most common semiconducting TMDs ($MoSe_2$, WSe_2, MoS_2 and WS_2), where the *A* and *B* excitons are highlighted. Inset: zoom over the *B* exciton of $MoSe_2$.

The direct bandgap nature of TMDs and the consequent ability to emit light efficiently, along with the strong SOC, are responsible for the huge interest of the scientific community for these materials. It's also worth mentioning that TMDs such as MoS_2 are naturally found, so that MLs of this material can be produced at a relatively low cost, thus enhancing their appeal towards their utilisation for applications and devices.

hBN

Hexagonal boron nitride (hBN) is a wide-gap layered material [53] that features a marked chemical inertness [54, 55] and mechanical robustness [56]. Thanks to these properties, hBN is an ideal substrate or capping material for other two-dimensional crystals [57–62] protecting them from oxidation [63] and bringing about a substantial improvement of the charge carrier mobility and of the light emission characteristics [59, 60, 64]. Indeed, hBN capping is routinely employed to fabricate high-quality heterostructures (HSs), wherein intriguing carrier potential landscapes can be realised [65, 66]. hBN is attracting an increasing interest also for its intrinsic properties, sustaining the propagation of hyperbolic phonon-polaritons (HPPs) [67, 68] and hosting single-photon emitters operating at room temperature [69–73].

Strain Engineering

The incredible mechanical flexibility and robustness of 2D crystals have triggered the interest in the field of strain engineering. Interestingly, despite their atomic thickness, 2D membranes possess remarkable mechanical robustness, with, *e.g.*, breaking strengths of about $\sim$ 25 N/m (15 N/m) and Young's modulus of $\sim$ 280 N/m (160 N/m) for hBN (MoS_2) [15, 41, 56, 74–76]. Indeed, 2D crystals can be subjected to remarkably high mechanical deformations, engendering strains larger than 10 % [41, 76]. Such strains have been shown to induce major modifications in the peculiar properties of the materials, leading to the observation of intriguing phenomena and paving the way towards the utilisation of 2D membranes for flexible electronics. For instance, strain was exploited in TMDs to enable the observation of single photon emitters and tune their energy [77], and to enhance carrier harvesting [78]. In hBN, it was exploited for high-quality mechanical resonators [79] and to reversibly tune the emission wavelength of single-photon emitters via stretching [80]; strained wrinkles were also found to be ideal candidates for launching HPPs [81].

Indeed, the ability to control the properties of deformed 2D materials relies on the development of controllable techniques to stretch or compress the crystal matrix, either at the macro-, micro-, or nano- scale. A variety of strategies were thus developed over the past decades to strain atomically-thin materials. A survey of the most commonly employed methods is shown in Fig. 0.7. Indeed, 2D materials allow for the use of many different methods to induce mechanical deformations, at variance with bulk crystals. The rigidity of bulk crystals, in fact, limits the number of techniques that can be employed to deform reversibly samples and devices. Likewise, nanostructures, such as quantum wells and quantum dots, are typically embedded in a bulk lattice and cannot be easily stressed. Apart from the strain inherent to lattice mismatch growth [90], the main methods to induce strain in bulk crystals are hydrostatic pressure [91] and bending devices [92]. Hydrostatic pressure can be applied to three-dimensional semiconductors [93] and bulk-embedded nanostructures [94] using anvil [91] or clamp cells [95] via a suitable transfer medium. Bending is instead particularly suited for micro- and nano-wires [96]. On the contrary, the nearly all-surface nature of two-dimensional (2D) crystals, along with their exceptional flexibility and robustness [15], boosts the number of methods —as well as their effectiveness— that can be exploited to modify and control the physical properties of these materials. Differently from 3D semiconductors, in 2D materials it is possible to create strain gradients on a mesoscopic scale.

Since the earliest investigations of 2D materials, it was immediately clear that this class of materials is unavoidably affected by intrinsic uncontrollable deformations, showing up as local nanometre-size strained areas, with random spatial distribution. For instance, early electron-diffraction studies of free-standing graphene monolayers indicated the presence of an intrinsic rippling, with $\sim$ 1 nm-high out-of-plane corrugations over a characteristic lateral scale of 10–25 nm [97]. These corrugations, observed many times in graphene monolayers deposited on top of insulating sub-

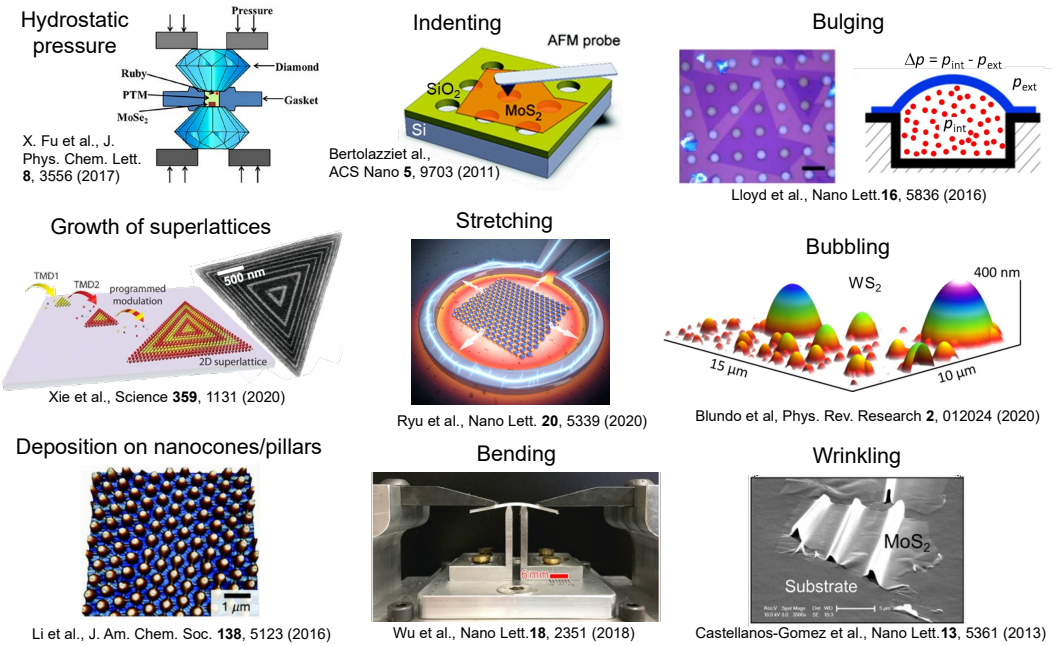

Figure 0.7: Survey of the most common straining methods employed nowadays to mechanically deform 2D crystals, such as: hydrostatic pressure [82], growth of superlattices [83], deposition on nanocones/pillars [84], indenting [15], stretching [85], bending [86], bulging [87], bubbling [88], and wrinkling [89] .

strates [98–103], were theoretically argued as necessary to stabilise the suspended sheets against the thermal instabilities present in ideal 2D systems [104]. However, Lui *et al.* [105] demonstrated that the rippling can be eventually suppressed by depositing the graphene onto an appropriate substrate (specifically, on mica). The finding of the so-called *ultraflat graphene* first demonstrated the importance of the appropriate substrate selection, as atomically thin membrane may simply reflect the roughness of their underlying support.

However, uncontrolled substrate-driven deformations may also arise because of the fabrication strategy. As the quest for large coverage of high-quality 2D materials increased, chemical vapor deposition (CVD) growth has been widely adopted to this aim, disclosing new experimental challenges and opportunities. The CVD growth of 2D materials, indeed, is profoundly affected by the presence of wrinkles, originating during the post-growth cooling, because of the different thermal expansion coefficient between the 2D sheet and the metallic substrate [106–111]. The epitaxial growth of vertical stacks of thin films, or *planar heterostructures*, also generally gives rise to strain at the interface.

Additionally, uncontrollable deformations take place when transferring and manipulating 2D materials. During this process, gases or liquids (*e.g.* air, water and/or hydrocarbons) get trapped between the 2D layer and its substrate, or in between

stacks of 2D heterostructrures, giving rise to spontaneously formed nano/micro-blisters [112–116]. These protrusions have been used as the signature of adhesion quality between the 2D material and its substrate, thus ensuring the presence of contaminant-free large inter-blisters areas [117].

However, while all the examples above enable the observation of interesting effects and can be exploited to investigate several material properties, their formation is almost uncontrollable, and their spatial distribution is random. For this reason, a huge effort has been devoted to developing experimental approaches to obtain controllable deformations of 2D materials. Such deformations were created, for instance, by (i) exploiting the mismatch between the thermal coefficient expansion of the 2D crystal and that of the substrate on which growth occurs [118]; (ii) transferring the 2D crystal on top of pre-stretched elastomeric substrates, to be relaxed afterwards [119]; (iii) using pre-patterned, 3D micro- and nano-structured interfaces. Several geometries, such as nanorods, nanotents [77, 120–122], nanogaps [123], nanowires [124], and nanocones [125] were used as substrate architectures, and, due to the exceptional flexibility of single- and multiple-layered 2D materials, these latter exhibited the capability of conforming to the underneath substrate shape.

Other techniques to induce strain at the micro-scale were developed, based on indentation or bulging of a 2D material. These classes of straining methods hold particular relevance since on one side, they give rise to intriguing phenomena such as carrier funnelling, pseudo-magnetic fields, and much more, on the other side they represent unique platforms where to explore the mechano-elastic and adhesive properties of the layered materials.

Chapter 1

Hydrogen-ion irradiation of TMDs and hBN: Formation of micro/nano-domes

The effects of hydrogen irradiation on conventional bulk crystals have been extensively studied, and a plethora of fascinating effects were observed. Hydrogen is one of the most pervasive elements and is chemically very reactive. H plays a very important role in solids, especially in semiconductors, where the interest in H-related effects arises from two diametrically opposed motivations. First, H can be introduced unintentionally into the lattice during most phases of growth and processing of semiconducting materials and of the related mass-production of electronic and optoelectronic devices [126]. On the other hand, H can be incorporated deliberately for the purpose of passivating dopants or lattice imperfections. Indeed, H tends to bind to dangling bonds generated by point and extended defects. Consequently, it cleans up the band gap from related energy levels [127–129] leading to a large modification of conductivity and it often removes the detrimental consequences associated to crystal imperfections [126, 130–132]. To this respect, an interesting and technologically groundbreaking example is the double-faced role played by H in GaN. Therein, H increases the Mg solubility (Mg is the most efficacious p-type dopant in this material) [133] and at the same time binds to Mg impurities forming a complex [134] that voids the related doping effects [135]. The subsequent thermal annealing and removal of H from GaN:Mg restores the p-type conductivity of the host crystal [136], as discovered in 1992 by S. Nakamura (2014 Nobel laureate in Physics). Eventually this enabled the first realisation of a p-n junction in GaN, and later in InGaN, thus paving the way to the realisation of blue and white LEDs. With respect to the Kaufman source that was employed in this Thesis work, a few examples can be quoted. H irradiation by this source was found to improve greatly the emission intensity of InAs and InGaAs self-assembled quantum dots, likely due to the passivation of threading dislocation-related states [132, 137]. The same source was exploited for engineering the electronic and structural properties of a class of

semiconductors, named dilute nitrides, such as GaAsN and GaPN (materials that attracted attention for photovoltaic applications and light emitting/detecting devices for telecoms). In these alloys, the formation of stable N-H complexes modifies in a controllable manner the band gap energy, the carrier effective mass and gyromagnetic factor, the refractive index, as well as the crystal lattice constant of the material [138]. Eventually, this led to the creation site-controlled quantum dots featuring single-photon emission [139]. A variation of the band gap energy was also induced in InN by proton irradiation. In this instance, the formation of a complex involving 4 H atoms around an In atom led to a dramatic band gap opening of 400 meV [140].

In the past decade, the interaction of hydrogen with 2D crystals has started receiving attention, especially aiming at the investigation of the gas sieving properties of 2D crystals. A series of theoretical studies of graphene showed how it poses a very high energy barrier of several eV for the penetration of atoms and molecules [141], which should prohibit any gas permeation under ambient conditions. Indeed, one can estimate that at room temperature, it would take longer than the lifetime of the Universe to find an atom energetic enough to pierce a defect-free graphene membrane of any realistic size [142]. Experimentally, the gas permeation through graphene and other 2D membranes was probed through the creation of micrometric blisters. Pioneering studies by Scott Bunch and co-workers [87, 143, 144] investigated bulging devices like that in Fig. 0.7. The system exploits the pressure difference Δp that can be created between the sides of a 2D layer sealing a cavity in order to make it bulge upwards (or downwards). The cavity is usually formed by etching cylindrical micro-holes on a SiO_2/Si substrate. The 2D sample is then deposited over the hole and the system (cavity+membrane) is pressurised by N_2, Ar, He or H_2 up to about $p_{\text{int}} = 1000$ atm [87, 143–145]. When the system is removed from the pressurisation chamber and is brought to ambient pressure (1 atm) a sizable $\Delta p = p_{\text{int}} - p_{\text{ext}} > 0$ establishes and the membrane bulges upwards. The devices were then investigated through atomic force microscopy (AFM) measurements, in order to probe the height profile of the bulge. A series of studies revealed a change in the height profile with time due to a gas leakage, which was however shown to occur at the 2D material / SiO_2 substrate interface [144]. Further studies were performed by Andre Geim and co-workers using analogous bulging devices but sealing the devices [142]. In particular, the micro-holes were in that case dug into a crystal of graphite or hBN instead of into a SiO_2/Si substrate to have a flatter top surface (and thus improve the adhesion at the 2D material / substrate interface), and the holes were then sealed with ring-shaped polymer masks created by electron beam lithography, to avoid gas leakages. Their experiments led to the following conclusions [142]: (i) MoS_2 and hBN MLs are impermeable to all gases; (ii) graphene MLs are impermeable to all gases but hydrogen; interestingly, they are also impermeable to deuterium. The permeability of graphene to H_2 was explained in terms of the intrinsic non-flatness of graphene. In fact, locally curved and strained graphene surfaces are known experimentally to be chemically reactive [146, 147] and are expected to lower the energy required for

dissociation of molecular hydrogen [148, 149]. Since the graphene ML is naturally rippled, the above facts allow for the permeation of H_2.

The same group investigated also the permeability of 2D crystals to ions [150, 151]. In that case, suspended monolayers were used to separate two compartments filled with hydrochloric acid (HCl) at chosen concentrations. In such a geometry, protons account for all the electrical current and chloride ions are blocked. Thus, electrical conductance measurements provide information on the proton permeation. Their studies [150, 152] demonstrated that: (i) hBN MLs, hBN BLs and graphene MLs are proton-conductive (hBN ML being the most conductive one, followed by hBN BL and graphene ML) while graphene BL shows instead negligible conductivity; (ii) MoS_2 does not show proton-conductivity; (iii) graphene and hBN are also permeable to deuterons, but the deuteron-conductivity is about a factor of 10 lower than in the case of protons. It should be noticed that in these studies, the conductivity to thermal (*i.e.*, not accelerated) ions was probed.

A few other works focused instead on the interaction of accelerated ions with 2D crystals. Although, only high-energy beams were employed, with kinetic energies ranging from some hundreds of eV to a few MeV [153]. Such studies were performed on van der Waals crystals with thicknesses ranging from just 1 layer to hundreds of layers, and typically resulted in sizeable damaging effects [153].

The range in between exposure to thermal ions and irradiation with high-energy beams has remained unexplored for long.

This Thesis originates from the study of the effects of low-energy hydrogen-ion irradiation of van der Waals crystals. Specifically, our group possess a Kaufman source like that schematised in Fig. 1.1. The Kaufman source is capable of generating low-energy ion beams and steering them onto the desired samples. The samples are mounted in a vacuum chamber, reaching basal pressures of about 1×10^{-6} mbar, and heated up by a heating lamp to the desired temperature (in the room temperature - 500 °C range). Molecular hydrogen is then introduced in the *discharge chamber*, where it is ionised by a heated tungsten filament; a magnet controls the motion of electrons such that they have several ionising collisions with the source gas, thus increasing the ionisation process cross section. We typically ionise the ions with the electrons emitted from the filament being accelerated at about 100 eV. According to previous studies in a different system [155], for such an electron energy we expect the hydrogen ions to be about 97 % H_2^+ and 3 % H^+ ions. The hydrogen ions are then steered towards the sample thanks to a system of biased grids that separate the discharge chamber from the main chamber. The bias controls the ion beam energy. The latter can be varied in the $5 - 1500$ eV range, thus allowing us to irradiate the samples with noticeably low energies. Importantly, Kaufman sources are configured to have the region of gas ionisation physically separated from the intended target, thus avoiding exposure of the samples to intense and potentially damaging electric fields, such as in plasma sources (see, *e.g.*, Ch. 2 of Ref. [126]). This turns out to be especially critical in ultra-thin samples, such as 2D crystals. The system could in principle be used with other gases; in the present thesis, we focused on

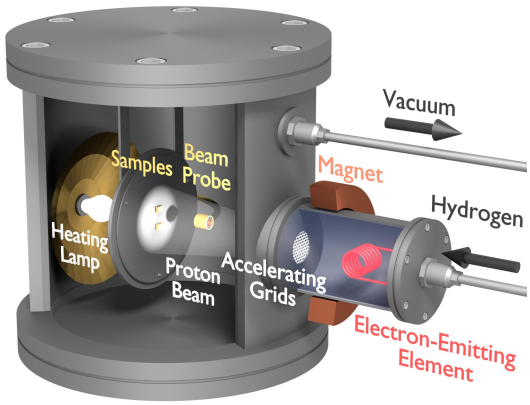

Figure 1.1: Schematic of the Kaufman ion source for incorporation of hydrogen, whose working principle is as follows: (i) Molecular hydrogen is ionised through a heated filament; a magnet controls the motion of electrons such that they have several ionising collisions with the source gas, thus increasing the ionisation process cross section; (ii) a system of biased grids accelerates the ions towards the sample. A Faraday cup is used to measure the beam current, and a heating lamp is used to adjust the sample temperature to the desired one (in the room temperature -500 °C range). Reproduced with permission from J. Felton *et al.*, Molecules **25**, 2526 (2020) [154]. Copyright 2020, The Authors.

the use of hydrogen (or its isotope deuterium). Only a few check experiments were performed with helium. Hydrogen irradiation treatments were performed on several van der Waals crystals. We will discuss in detail the peculiar effects obtained for semiconducting TMDs and hBN, while we will briefly mention the effects obtained in other systems at the end of this chapter.

1.1 Semiconducting TMDs

Hydrogen-ion irradiations were performed on semiconducting TMDs: MoS_2, WS_2, $MoSe_2$, WSe_2, and $MoTe_2$. The metallic TMD WTe_2 was also irradiated. The samples, consisting of thick (tens to hundreds of MLs) TMD flakes, were obtained by mechanical exfoliation, deposited on Si substrates (either on SiO_2/Si substrates on or bare Si ones), and afterwards irradiated using the Kaufman source. The samples were typically kept at 150 °C during the irradiation process and were electrically grounded. More details can be found in Ref. [156]. Differently from the other works in the literature concerning hydrogen-ion irradiation of TMDs ——where beams with energies $\gtrsim 10^5$ eV were used to create defects [153]—— here we irradiate the flakes with low energy beams of $6 - 30$ eV, with the specific goal of suppressing the defect formation process. Fig. 1.2 shows the optical image of a typical WS_2 flake prior

to irradiation (panel a) and of the same flake following H-ion irradiation with dose $d_H = 8 \times 10^{16}$ ions/cm^2 (panel b). Indeed, after irradiation, the flake surface shows the appearance of circular features. Atomic force microscopy (AFM) studies reveal that the features bulge out from the flake surface, in the shape of domes, as shown in Figs. 1.2(c-d). By varying the ion dose, the size and density of the domes change. This is clearly highlighted in Figs. 1.2(c-e), showing how domes with height < 30 nm are obtained by irradiating a WS_2 flake with dose $d_H = 1 \times 10^{16}$ ions/cm^2, while bigger domes with height up to 140 nm are obtained in a WS_2 flake irradiated with a 4-time-larger dose. To characterise the domes, we performed a series of

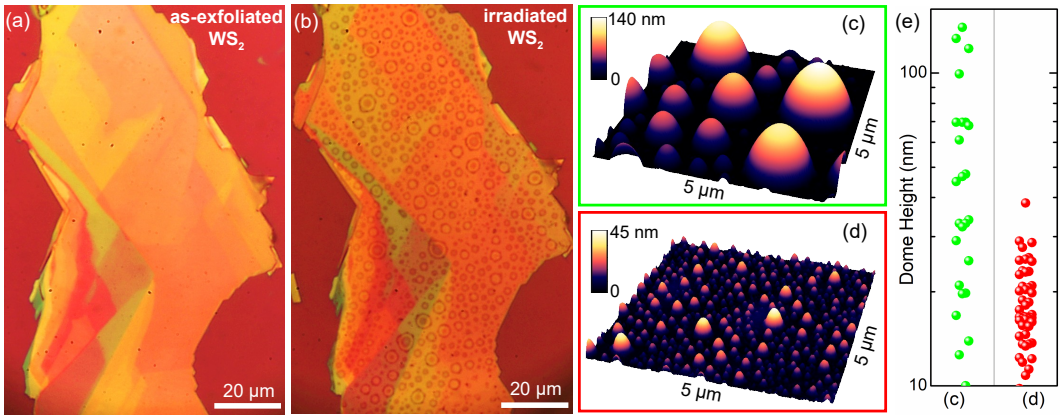

Figure 1.2: Optical image of a WS_2 flake before (a) and after (b) irradiation with H ions. The H dose was $d_H = 8 \times 10^{16}$ ions/cm^2. (c) AFM image of a TMD flake treated with dose $d_H = 4 \times 10^{16}$ ions/cm^2, showing the presence of relatively large domes (diameter of a few μm); (d) AFM image of a TMD flake treated with lower dose, $d_H = 1 \times 10^{16}$ ions/cm^2, showing the presence of smaller domes (diameter of tens to hundreds of nm). (e) Statistical analysis of the height of the domes measured in the whole area displayed in panel (c), and in a portion of the area (one fourth of the area) displayed in panel (d). Only domes with height > 10 nm were considered, since for smaller domes the resolution employed for these measurements was not high enough to have a precise estimate of the height. Panels (a)-(b) are reproduced with permission from D. Tedeschi, E. Blundo *et al.*, Adv. Mater. **31**, 1903795 (2019) [156]. Copyright 2019 WILEY-VCH Verlag GmbH & Co. KGaA, Weinheim.

optical studies including photoluminescence (PL) and SHG measurements [156]. Fig. 1.3 shows the optical image of a WS_2 flake showing the presence of domes after irradiation (panel a) and the image of the light emitted by the flake (panel b). Indeed, a strong PL signal in the red wavelength region ($\lambda \approx 690$ nm) coming from the domes is observed at room temperature. The RT μ-PL spectrum of one dome (singled out from the ensemble of panel b) is provided in the inset. The luminescence of an untreated WS_2 ML measured under the same excitation/collection conditions is shown for comparison. The energy of the PL peak (corresponding to the A exciton recombination) of a typical WS_2 dome is about 200 meV lower than that of the ML, mainly because of the strain exerting on the dome surface, as we will discuss in more detail in the following. The width of the PL bands of the domes is typically broader

than that of the ML (with full width at half maximum, FWHM, in the range $20-100$ meV). This is attributable to the presence of a non-uniform strain (the resulting PL emission is the convolution of the light emitted from regions subjected to different strain values) and to the effect that strain has on the bandstructure of the material, as we will discuss in detail in Chapter 5. Notably, no significant linewidth broadening is observed when many such domes are measured together, as demonstrated by the PL spectrum of a dome ensemble, displayed in the same inset as a red line. The presence of a low-energy shoulder can be noticed in the ensemble, whose origin will be clarified in Chapter 5. The spectral homogeneity of the light emitted by the domes suggests that the same average strain is present in each dome, irrespective of the dome size.

A statistical analysis of the energy and FWHM of the PL spectra measured in several WS_2 and $MoSe_2$ domes can be found in Additional Material, sec. A1.

The evidence shown in Fig. 1.3(a-b) demonstrates that, through the formation of domes, indirect-gap bulk WS_2 can be turned into an efficient light emitter with no size restrictions, like those typically affecting exfoliated flakes or samples grown by chemical vapour deposition.

Panel (c) shows instead the optical image of a different WS_2 flake and the image of the second harmonic signal generated by the flake. Indeed, the domes act as efficient SHG hotspots. The huge PL intensity of the domes and their strong second harmonic signal suggest a ML thickness for the domes. In fact, as discussed in the Prologue, both the ability to emit light efficiently and to generate second harmonic signals efficiently are characteristic of MLs.

Further studies confirm that most of the domes are characterised by a thickness of just 1 layer [156]:

- We caused the explosion of some domes by focusing a high-power laser onto them. After the explosion, the PL peak from the patches of the exploded dome is centred at the same energy to that of an unstrained ML, as shown, *e.g.*, for a $MoSe_2$ dome in Fig. 1.4(a). The spectrum of the dome before the explosion is instead redshifted by about 200 meV due to the strain exerting on the dome surface.

- By performing AFM measurements on the exploded domes, we measured the thickness of the patches. The measured values suggest a single ML thickness for most of the domes, as for the dome in Fig. 1.4(a). Indeed, while this procedure allows the direct measurement of the thickness, most often the patches do not perfectly adhere to the substrate and are not flat, so that these measurements are typically complicated. This is why we performed many other optical, non-invasive measurements.

- Another characteristic typical just of single layers of TMDs is that they feature a relatively high degree of circular polarisation (DCP). Hence, we performed circular-polarisation measurements in condition of quasi-resonant excitation on a WS_2 dome. As shown in Fig. Fig. 1.4(b), we found a DCP of about 50

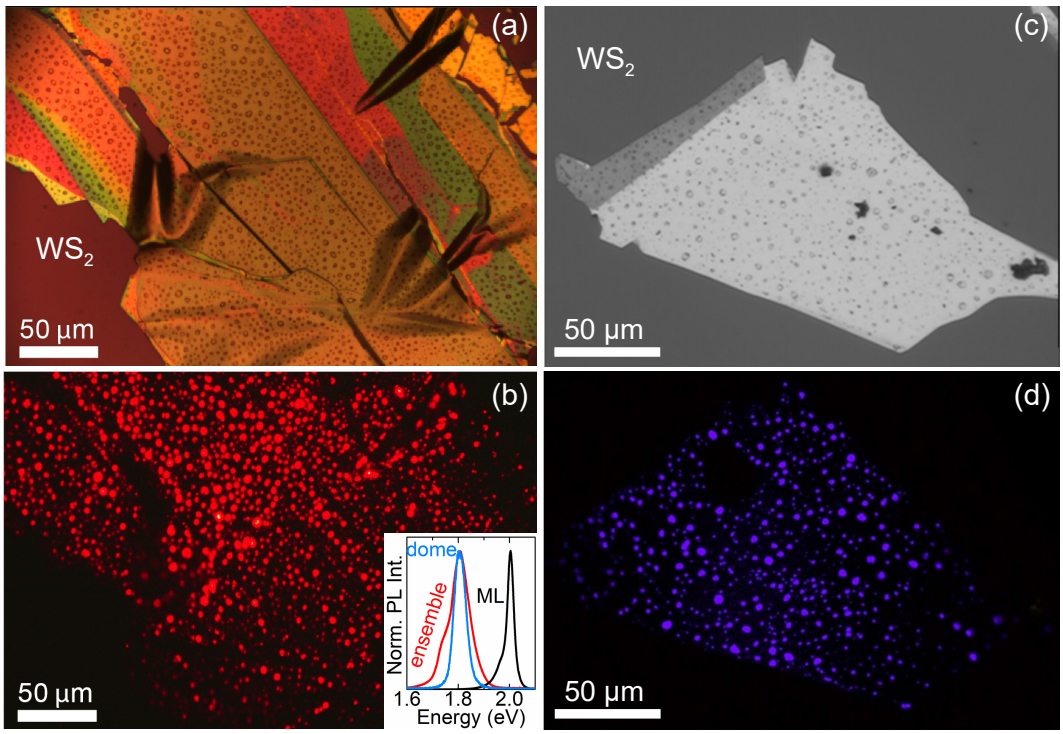

Figure 1.3: (a) Optical image of a WS_2 flake after H-irradiation, showing the presence of domes on its surface. (b) Optical image of the light emitted by the same flake obtained by exciting the flake with a green laser and detecting the PL signal with a CCD camera (the laser light was filtered out by a filter when acquiring the image). Inset: Normalised μ-PL spectrum of a dome (cyan line) singled out from the ensemble displayed in the main panel; the black line is the μ-PL spectrum of a WS_2 ML, whereas the red dashed line is the macro-PL spectrum of an ensemble formed by $\approx$ 2500 domes. (c) Optical image of another irradiated WS_2 flake. (d) Optical image of the second harmonic signal emitted by the same flake. Panels (a)-(b) are readapted with permission from D. Tedeschi, E. Blundo *et al.*, Adv. Mater. **31**, 1903795 (2019) [156]. Copyright 2019 WILEY-VCH Verlag GmbH & Co. KGaA, Weinheim. Panels (c)-(d) are courtesy of Prof. Yuerui Lu and of Boqing Liu (School of Engineering, College of Engineering and Computer Science, The Australian National University, Canberra, Australia).

%, which is compatible with the DCP of about 60 % measured on flat MLs. To the contrary, thicker TMDs feature a DCP of about 10 %.

Based on the percentage of visible domes that double as strong light emitters, 85–90 % of the domes can be estimated to be one-ML thick. A more accurate estimate can be obtained by SHG studies, performed in collaboration with Prof. Yuerui Lu, and Boqing Liu (The Australian National University, Canberra, Australia), and Dr. Tanju Yildirim (National Institute for Materials Science, NIMS, Ibaraki, Japan). Their studies show that with increasing ion dose, the number of conglomerates of domes increases, and more structures like that in Fig. 1.5(a) are found. A SHG

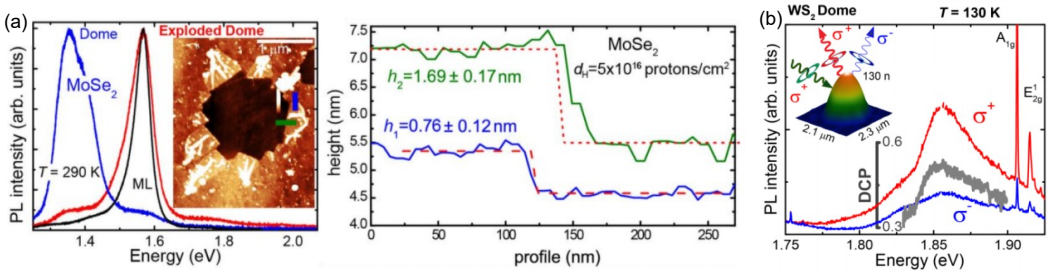

Figure 1.4: Left: PL signal of a $MoSe_2$ dome (blue curve) and of the same $MoSe_2$ dome after causing its explosion with a high power focused laser (red curve). The signal from a flat monolayer is also shown for comparison (black curve) showing an overlap with the signal from the exploded dome. The AFM image of the exploded dome is shown as inset. Right: AFM profiles measured along the blue and green lines shown in the 2D AFM image. The red dashed lines are fits to the data via an edge function. The blue line refers to the step between the patch located around the pristine dome footprint and the area outside the dome. The profile step value h_1 points to a thickness of a monolayer. The green line refers to the step h_2 between a patch located around the pristine dome footprint and the area inside the exploded dome. In this case, the profile step value points to a thickness of two layers, which confirms a single layer thickness for the dome's peel. (b) Circular-polarisation-resolved μ-PL spectra of a WS_2 dome (whose AFM image is shown in the inset): the dome was excited by a σ^+ circularly polarised, 632.8 nm laser at 130 K (in a quasi-resonant condition), and the emission spectra were filtered by $\sigma^{\pm}$ polarisation resulting in the degree of circular polarisation (DCP) shown as a grey line. This value is comparable to that of a flat ML, which varies between 0.4 and 0.8. All panels are reproduced with permission from D. Tedeschi, E. Blundo *et al.*, Adv. Mater. **31**, 1903795 (2019). [156]. Copyright 2019 WILEY-VCH Verlag GmbH & Co. KGaA, Weinheim.

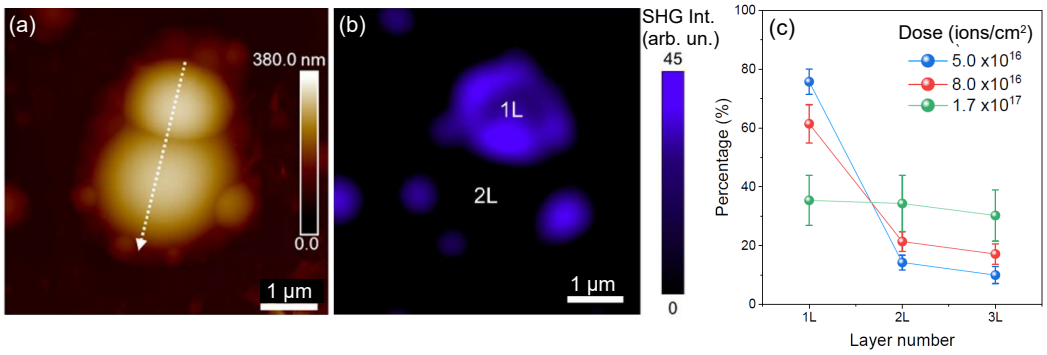

Figure 1.5: (a) AFM image of adjoining WS_2 domes. (b) Second harmonic signal emitted by the adjoining domes, revealing that the largest one is has a bilayer thickness, while the smallest have a monolayer thickness. (c) Formation yield percentage of 1-3L WS_2 domes as a function of H ion irradiation dose. The data were collected from WS_2 flakes on SiO_2 substrates. For each dosage level, more than 150 domes were sampled. B. Liu *et al.*, Nat. Commun. (2023), in press [157].

study reveals that in most cases, adjoining domes in the conglomerate configuration are characterised by different thicknesses, in between 1 and 3 layers. A quantitative analysis of the SHG intensity allows for the estimate of the relative percentage of 1L-, 2L- and 3L-thick domes, as shown in Fig. 1.5(b) for different WS_2 samples, irradiated with three different ion doses.

The evidence reported so far demonstrates that indirect-gap bulk WS_2 can be turned into an efficient light emitter with no size restrictions, like those typically affecting exfoliated flakes or samples grown by chemical vapor deposition. The domes can in fact be created over large size crystals of several centimetres. We point out that the reported phenomenon is substantially independent of the specific MX_2 composition (besides WS_2, domes are obtained as well in $MoSe_2$, MoS_2, $MoTe_2$, WSe_2, and WTe_2) and is exclusively induced by the interaction of the material with H ions. No effect was found in samples exposed to molecular hydrogen or ionised helium atoms under the same temperature and gas flow conditions. We recall that our H ion beam is composed of both H_2^+ ions and protons (H^+ ions). Given the impermeability of 2D crystals to molecules and the permeability of graphene and hBN to protons [142, 150], we hypothesise that the formation of domes is attributable to the interaction of TMDs with the accelerated protons solely, while the H_2^+ ions do not contribute.

Clues on the internal make-up of the domes can be derived by following their low-temperature evolution [156]. Fig. 1.6(a) shows the 300 K and 4 K optical microscopy images of a bulk WS_2 sample irradiated with $d_H = 8 \times 10^{16}$ ions/cm^{-2}. At 300 K, many domes featuring iridescence (Newton's rings) are visible. For $T \lesssim 30$ K the domes disappear, and the sample surface looks conspicuously flat. As T is increased, at ≈30 K, the domes bulge suddenly (within our system resolution equal to 10 mK). This sudden transition suggests the occurrence of a liquid-to-vapour phase transition of the substance inside the domes. As a reference, the $(p-T)$ phase diagrams of several common substances, including hydrogen and deuterium [158], are shown in Fig. 1.6(b). As illustrated in Fig. 1.6(c), the transition temperature distribution was sampled over more than 500 domes obtained on several H-ion irradiated flakes. The resulting average transition temperature is $T_{LV}^H = (32.2 \pm 2.4)$ K, a number close to the critical temperature of H_2 (33.18 K) and thus compatible exclusively with the presence of molecular hydrogen inside the domes: when T is sufficiently low/high, H_2 liquefies/boils, and the domes deflate/inflate always in the same position. The fluctuations observed in the liquid-vapor transition temperature T_{LV}^H are chiefly due to the spread in the size (and hence in the internal pressure) of the domes. To reinforce our hypothesis, we considered the study of isotopic effects in our system and we repeated our analysis on 500 more WS_2 domes, obtained by deuterium-ion irradiation (panel d). Indeed, the $(p-T)$ phase diagrams of hydrogen and deuterium [158] in panel (b) show an isotopic shift in the liquid-vapour phase transition temperature of about 2.9 K (the exact value depending on the pressure of the gas). The histogram and cumulative function of deuterium-ion irradiated samples is displayed in Fig. 1.6(d): differently from hydrogen-ion irradiated samples, the behaviour is in

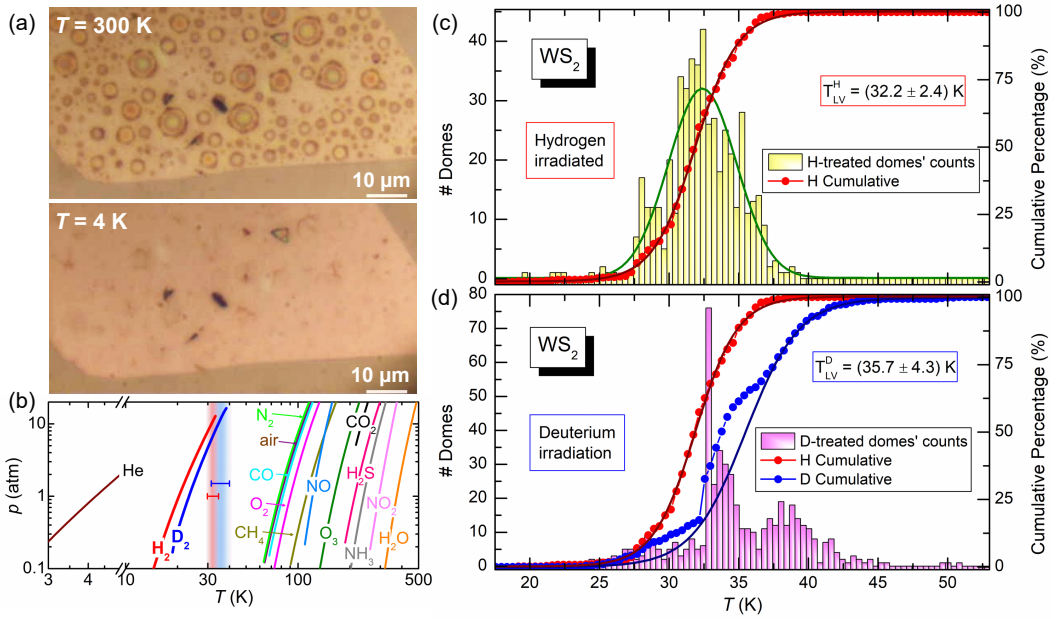

Figure 1.6: (a) Optical microscopy image of an H-ion irradiated ($d_{\mathrm{H}} = 8\times10^{16}$ ions/cm^{-2}) WS_2 sample at $T = 300$ K and $T = 4$ K. (b) $(p-T)$ phase diagram of various substances. Lines mark off the liquid (left) and vapour (right) phases. The vertical coloured bars are the $T_{\mathrm{LV}}^{\mathrm{H,D}}$ values derived in by the analysis performed on the domes and shown in panels (c) and (d). The thickness of the bars represents the experimental uncertainty (error bars are also shown). (c-d) Histogram (bars; left axis) and cumulative function (point-line; right axis) of the liquid-vapour transition temperature of domes formed on hydrogen irradiated (c) and deuterium irradiated (bottom) WS_2 flakes. The dark-green line in panel (c) is a gaussian fit to the histogram, while the wine solid line is a sigmoidal fit to the cumulative function. The fits give an average transition temperature $T_{\mathrm{LV}}^{\mathrm{H,D}} = (32.2 \pm 2.4)$ K. In panel (d), the average liquid-vapour transition temperature is deduced from fitting (navy solid line) the cumulative function only on the high-temperature data ($T > 36$ K), where no effect from hydrogen is expected, resulting in $T_{\mathrm{LV}}^{\mathrm{H,D}} = (35.7 \pm 4.3)$ K. The red point-line and wine line are the cumulative function and fit, respectively, of hydrogen irradiated samples and are displayed for ease of comparison. All panels are adapted with permission from D. Tedeschi, E. Blundo *et al.*, Adv. Mater. **31**, 1903795 (2019). [156]. Copyright 2019 WILEY-VCH Verlag GmbH & Co. KGaA, Weinheim.

this case characterised by a composite shape, corresponding to the three different steps that are apparent in the cumulative function. We ascribe empirically these three steps to the presence of H_2, HD, and D_2 molecules [159] within the domes. There are several possible explanations why H may be present also in deuterium-ion treated samples: (1) even the highest purity deuterium bottles contain a 0.25 % of H_2 and HD molecules; (2) deuterons permeate through graphene and hBN monolayers much slower (about a factor of 10) than protons [150]. This effect could be even much stronger in the case of TMDs, whose single layer is constituted by three atomic planes; (3) the hydrogen evolution reaction is expected to be remarkably faster with

respect to the deuterium evolution reaction because of the high mass difference between the two isotopes [160, 161]. For deuterium irradiated samples, a sigmoidal fit was thus performed only to the high-temperature data of the cumulative function, where no effect from hydrogen is expected. The fit estimates a transition temperature of $T_{\mathrm{LV}}^{\mathrm{D}} = (35.7 \pm 4.3)$ K, resulting in a difference between the centres of the distributions equal to (3.5 ± 0.4) K, consistent with the $(p-T)$ diagram of the two isotopes. Indeed, the measured transition temperatures are consistent only with the presence of H_2 (or its isotopes) within the domes. We can therefore hypothesise that, during irradiation, accelerated protons penetrate through the top MX_2 basal plane, becoming confined in between two X–M–X layers, see sketch in Fig. 1.7. The penetration process is indeed ruled by the potential barrier met by protons at the interface with the bulk flake, which should be determined by both the binding energy profile of protons [141] and the electric fields/charges establishing at the sample surface [162, 163]. Therein, the hydrogen evolution reaction takes place

$$2\mathrm{H}^+ + 2\mathrm{e}^- \rightarrow \mathrm{H}_2$$

with electrons e^- being supplied from the ground contact or possibly also from the bulk flakes themselves. This hypothesis is supported by the fact that the formation

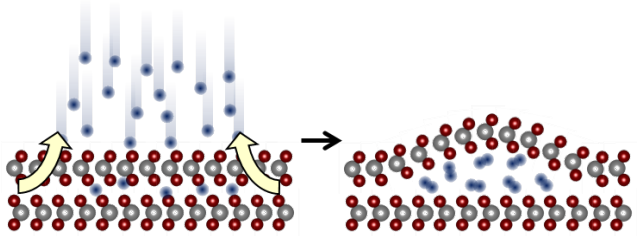

Figure 1.7: (a) Sketch of the formation process of domes by H-irradiation: A bulk crystal is irradiated with H ions that penetrate through its first layer(s); molecular hydrogen forms and coalesces, leading to the blistering of the upper layer(s) and thus to the formation of domes. Reproduced with permission from E. Blundo *et al.*, Phys. Rev. Lett. **127**, 046101 (2021) [116]. Copyright 2021 American Physical Society.

of domes is strongly quenched in flakes deposited on an insulating substrate (Kapton tape). The subsequent build-up of H_2 molecules, stored just beneath the top surface, leads to the local blistering of one (or a few) X–M–X plane(s), and eventually to the formation of the domes (see sketch in Fig. 1.7). The above scenario is supported by theoretical studies, which showed that thermal protons remain trapped in the metal plane of X–M–X layers and do not diffuse, thus favouring the accumulation of H_2 molecules in the interlayer regions [141]. An estimate of the number of molecules accumulated after irradiation (via AFM measurements and the mechanical model described in the following) indicates that <3 % of the impinging ions penetrate and lead to the formation of molecular hydrogen. This is consistent with the hypothesis that only protons penetrate, and with estimate that about 97 % of the ions are H_2^+

ions and 3 % are H^+ ions. The H_2^+ ions are likely repelled by the potential barrier met at the sample surface.

The so-formed domes are characterised by a remarkable robustness and durability [156]. Indeed, the domes remain intact ——and keep exhibiting strong light emission—— for temperatures up to 510 K. In addition, the shape and size of these nano / microstructures remain unchanged with time ——in the best cases over more than two years—— as illustrated by Fig. 1.8. This confirms the notable absence of gas-permeable, nanometre-scale pores in TMD materials, as already reported in the literature [87]; moreover, the exceptional durability of our domes is likely also aided by the strong adhesion forces existing between the ML forming the dome and its parent substrate, as well as by the low permeability to H_2 of TMDs. Our system is therefore advantageous if compared to the bulging devices commonly employed to induce strain in TMD membranes [87, 143], that deflate within weeks, mostly due to leakages at the membrane / substrate interface. It's also worth mentioning that other methods to form TMD domes have been developed in the literature. The latter are based on top-down deposition processes, in which a 2D membrane is deposited atop of a substrate or atop of of another vdW crystal; during this process, unavoidably present contaminants (air, water, hydrocarbons) remain trapped, leading to the appearance of domes [112]. These structures, however, form randomly, without possibility to control their shape, their density, and their formation. Our method overcomes these issues and, as we will discuss in the following in Chapter 3, allows also for a high degree of control over the position and dimension of the domes.

To conclude this section, it's worth spending a few words on the strain of the domes, while a more in-depth analysis will be faced in Chapters 2 and 4. First, we notice that the energy of the PL peak of a typical (single-layer) dome is about 200 meV lower than that of the ML (see, *e.g*, Fig. 1.4(a)), because of the strain exerting on the dome surface [156], as we will discuss in more detail in the following. The spectral homogeneity of the light emitted by the domes suggests that the same average strain is present in all domes, irrespective of their size. This agrees with previous mechanical models [112, 115, 164, 165] and experiments on domes created by trapping of contaminants [112, 166, 167], showing how a constant height-to-radius ratio (or aspect ratio) is expected for domes of a given material, irrespective of their size. AFM measurements on our system confirm that a constant aspect ratio is found, with values ranging in between 0.13 (in the case of WTe_2) and 0.19 (in the case of $MoSe_2$) [116, 156]. A more detailed statistical analysis will be presented in Chapter 4. It's important to highlight that the strain is directly linked to the dome profile. In general, the strain can be described in terms of two in-plane components, the radial component ε_r and the circumferential component ε_θ, and by an out-of-plane or perpendicular component ε_z. A sketch of the strain components is provided in Fig. 1.9(a). The evolution of the strain distribution across the dome surface can be computed numerically. First, we highlight that at the dome summit the strain is isotropic biaxial (*i.e.*, $\varepsilon_r = \varepsilon_\theta$), and it can be related via a simple analytical

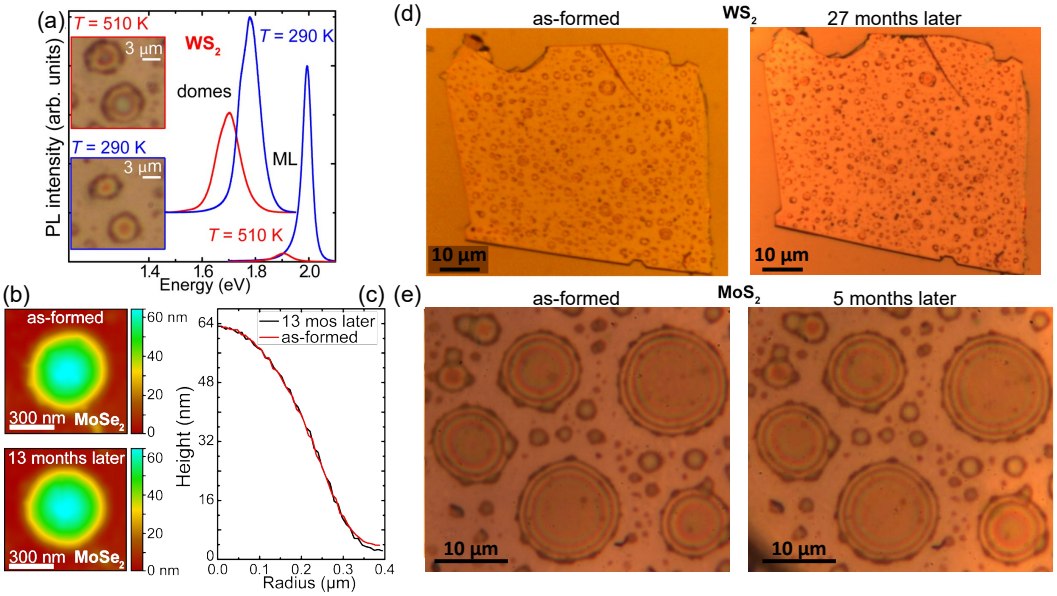

Figure 1.8: (a) μ-PL spectra recorded on an ensemble of about 100 WS_2 domes and on a WS_2 ML at RT (blue lines) and $T = 510$ K (red lines). Insets: optical microscope images of domes recorded at the same temperatures as the PL. The different colouration exhibited by the domes at different Ts is a result of the H_2 expansion leading to different conditions for light interference (Newton's rings). Such an expansion in the dimensions of the domes can result in the coalescence of some domes, leading to the formation of larger domes. However, this is a pretty rare process: In a WS_2 flake with ~ 350 visible domes, brought to 510 K, only two coalescence phenomena were observed. (b)-(c) AFM images of the same $MoSe_2$ dome, recorded a few hours after the hydrogenation process that resulted in the dome formation (panel b) and 13 months later (panel c). (d) Height profile of the two AFM images of panels b and c. (e) Optical images of a WS_2 flake (20×, NA = 0.4), recorded a few hours after the hydrogenation process that resulted in the dome formation (left) and 27 months later (right). During this period the sample was thermally cycled tens of times. The two pictures appear seemingly identical, with a large majority of the domes displaying the same size and position. However, few domes coalesced, and another (small) subset shrunk. These events were likely induced by the large number of thermal cycles. (F) Optical images of the same MoS_2 flake (100×, NA = 0.75) where remarkably large domes formed (the footprint diameter of the largest one is equal to 14.6 μm). The images were recorded a few hours after the hydrogenation process that resulted in the dome formation (left) and 5 months later (right). This sample was not thermally cycled, and none of the largest domes shows any difference in size. All panels are reproduced with permission from D. Tedeschi, E. Blundo *et al.*, Adv. Mater. **31**, 1903795 (2019). [156]. Copyright 2019 WILEY-VCH Verlag GmbH & Co. KGaA, Weinheim.

relationship to the dome aspect ratio, as:

$$\varepsilon_r(0) = \varepsilon_\theta(0) = f(\nu)\left(\frac{h_0}{R}\right)^2, \tag{1.1}$$

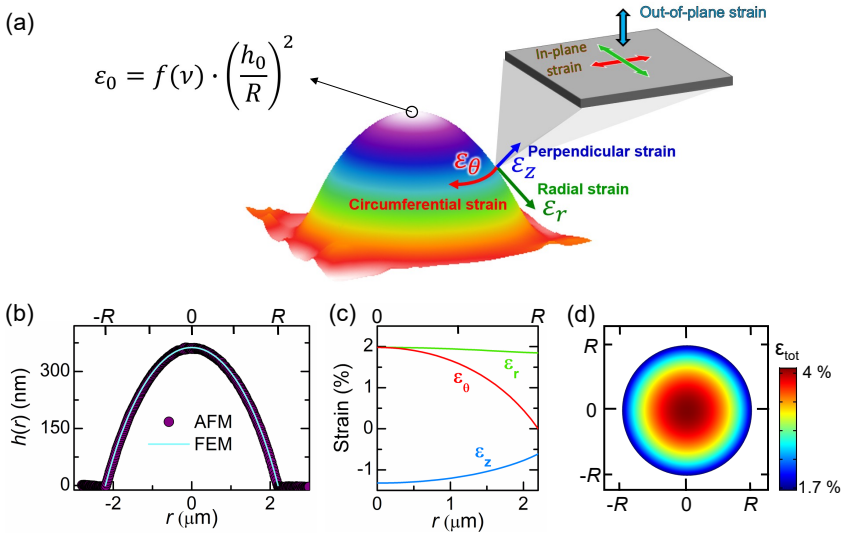

Figure 1.9: Sketch of the strain components along the surface of a dome: the strain can be described in terms of two in-plane components, the radial component ε_r and the circumferential component ε_θ, and by an out-of-plane or perpendicular component ε_z.

where h_0 and R are the maximum height and the footprint radius of the dome, respectively, and where $f(\nu)$ is a function of the Poisson's ratio ν (*i.e.*, the elastic parameter that keeps into account how much the material compresses in one of the in-plane directions if it is stretched in the perpendicular in-plane direction), that can be computed numerically [164]. A summary of the Poisson's ratio of the most common 2D crystals is provided in the Additional Material, sec. A2. This relationship is known as Hencky's relationship [116, 164]. Aside from the centre, $\varepsilon_r \neq \varepsilon_\theta$ and the strain is thus anisotropic. The strain components can be estimated numerically via finite element method (FEM) calculations (see Additional Material, sec. A3). FEM calculations also allow us to simulate the height profile of the dome starting from the knowledge of R and h_0. Fig. 1.9(b-c) show the simulated height profile and strain components for a MoS_2 dome. From being isotropic biaxial at the dome summit, strain gradually becomes uniaxial as the circumferential component goes to zero near the dome edge, as shown in panel (c). In the middle between these two limits, strain is anisotropic, being the two in-plane components different. The perpendicular component is negative, accounting for a compression of the membrane in the out-of-plane direction (induced by the tensile strain in the in-plane direction), and it is related to the other components via the relation

$$\varepsilon_z = -\frac{C_{13}}{C_{33}}\varepsilon_p, \tag{1.2}$$

where we define the in-plane strain ε_p as

$$\varepsilon_p = \varepsilon_r + \varepsilon_\theta. \tag{1.3}$$

Since ε_z is proportional to ε_p, the latter embeds all the crucial information. The colour plot in panel (d) shows the spatial distribution of ε_p across the dome surface.

1.2 hBN

Analogously to TMDs, we exfoliated thick hBN flakes either from commercial hBN crystals (hq graphene) or high quality hBN crystals grown by T. Taniguchi and K. Watanabe [168]. The flakes were deposited on Si/SiO_2 substrates and initially characterised by AFM. The samples were the subjected to H (or D)-ion irradiation by the Kaufman ion gun [154, 156] in high vacuum conditions at 150 °C, with the samples electrically grounded to avoid charging. To avoid the formation of defects, low ion-beam energies < 35 eV were employed. After the treatment, optical microscope images of the flakes may reveal a slightly non-homogeneous colouration related to the presence of barely visible circular or elongated features. AFM measurements demonstrate the presence of domes, wrinkles, or both on the flakes, as shown in Fig. 1.10(a-c). A statistical AFM study [169] allows us to establish a correspondence between the different morphologies and the flake thickness t: for $t \gtrsim 10$ nm, only domes form (Fig. 1.10(a)); for $t \simeq 10$ nm, both domes and wrinkles can be observed (Fig. 1.10(b)); in thin flakes with $t \lesssim 10$ nm, wrinkles and irregular structures predominate (Fig. 1.10(c)). In the latter case, molecular hydrogen likely forms, accumulates, and percolates at the flake/substrate interface, giving rise to irregular structures and wrinkles (Fig. 1.10(c)). On the other hand, the formation of spherically shaped domes in thick flakes ($t \gtrsim 10$ nm) can be attributed to the formation and trapping of molecular hydrogen in the hBN interlayers, as we also observe in TMDs [156] and as also observed in H-plasma-treated hBN [170]. We thus hypothesise that protons with kinetic energies of $\sim 10 - 30$ eV penetrate through hBN for ∼10 nm and that the formation of wrinkles or domes depends on where H_2 remains caged. To support this hypothesis, we intentionally induced the explosion of some domes via a high-power (some mWs), highly focused laser beam, and measured the height difference between the crater of the exploded dome and the flake surface outside the crater by AFM. In samples irradiated with H ions (beam energies < 34 eV) we measured thicknesses ranging from 1.8 to 12 nm (corresponding to about 5 to 36 monolayers). The formation of thicker structures if compared to those obtained in TMDs is indeed consistent with the ion conduction studies reported in the literature, showing that hBN is the most permeable crystal to protons among 2D crystals [150]. To form thinner domes, we irradiated some samples with deuterium ions (beam energies < 25 eV) —which are known to penetrate less through hBN with respect to protons [150]— and we measured dome thicknesses as thin as ∼0.5 nm (*i.e.*, a couple of layers). This demonstrates the remarkable flexibility of our method, which – unlike H-plasma-based methods [170] – enables us to obtain domes thinner than ten monolayers.

We performed AFM measurements to study the morphological properties of domes and wrinkles and measured their aspect ratio h_m/R, where h_m is the maxi-

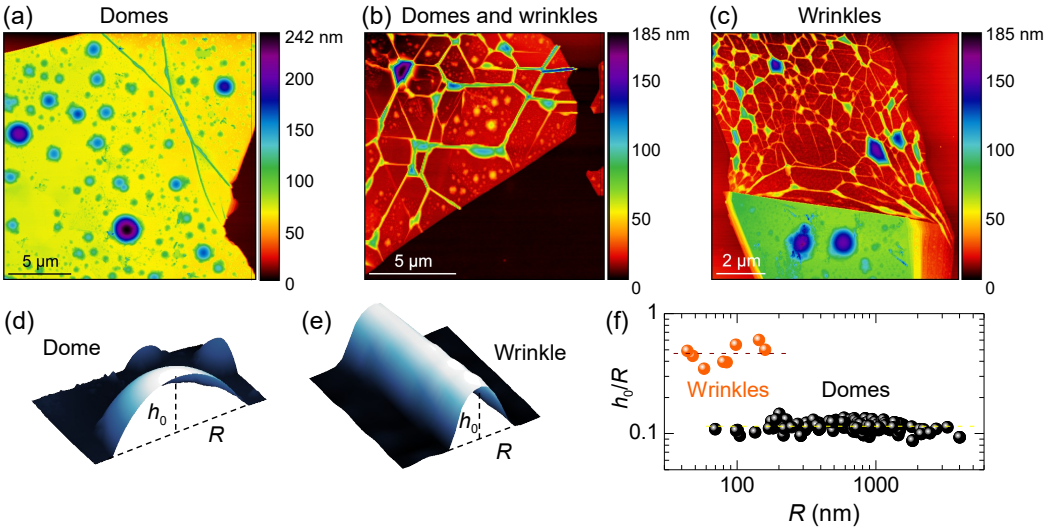

Figure 1.10: Formation of hydrogen-filled domes and of wrinkles in hBN. (a-b-c) AFM images of multi-layer hBN flakes after H irradiation. The flakes have thicknesses of 55 nm (a), 10 nm (b), and 5 nm (c, thin part corresponding to the top side of the figure) and the images show the presence of only domes, both domes and wrinkles, and only wrinkles, respectively. (d-e) 3D AFM images of half a dome (panel d, where $R = 2.06$ μm and $h_0 = 225$ nm) and part of a wrinkle (panel e, where $R = 144$ nm and $h_0 = 88$ nm). The definitions of maximum height (h_0) and footprint radius (R) are depicted. (f) Statistical analysis of the aspect ratios (h_0/R) measured in wrinkles and domes. The dashed lines represent the average aspect ratios estimated for each set of data. All panels are reproduced with permission from E. Blundo *et al.*, Nano Lett. **22**, 1525 (2022) [169]. Copyright 2022, The Authors.

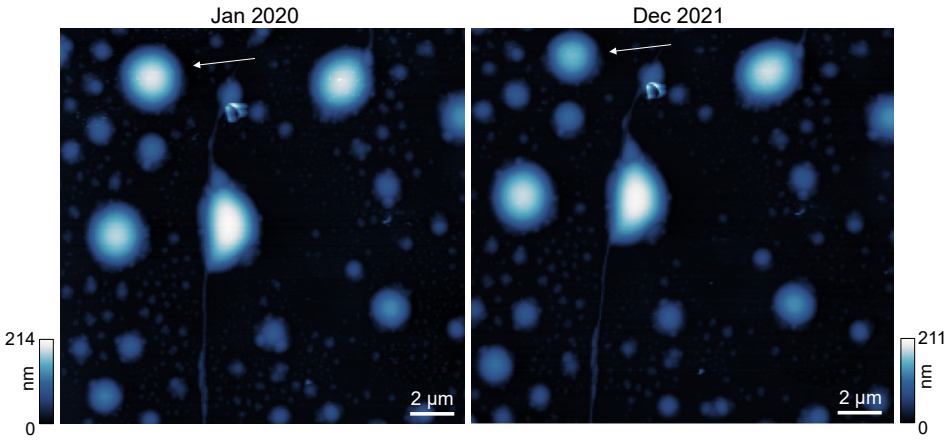

Figure 1.11: AFM images of an hBN flake irradiated with a 6-eV deuterium beam. The image on the right was recorded 23 months after that on the left, in about the same area. The white arrows indicate a dome, which deflated over time. The other domes remained instead almost unchanged. Reproduced with permission from E. Blundo *et al.*, Nano Lett. **22**, 1525 (2022) [169]. Copyright 2022, The Authors.

mum height of the object and R is its half width (see Fig. 1.10(d-e)). The results are summarised in Fig. 1.10(f). The wrinkles feature a narrow width distribution and aspect ratios in the $0.3-0.6$ range. The domes show a much wider size distribution and a size-independent aspect ratio, as expected based on previous theoretical [112, 116, 165] and experimental [112, 116, 156, 167, 170, 171] studies. For our domes, we find $h_{\mathrm{m}}/R = 0.115 \pm 0.011$, in agreement with that reported for hydrocarbon-filled monolayer domes [112] and multilayer domes created by H-plasma treatments [170]. The constant aspect ratio, independent of size and thickness, found for hBN domes will be motivated and discussed in more detail in Chapter 4.

Notably, the domes feature a long durability of several years, as shown in Fig. 1.11. This fact, along with Raman studies, suggests that the low-energy beams employed here do not induce a sizeable amount of defects in the crystal, unlike higher-energy heavier-atom beams [172–178].

1.3 Other van der Waals materials

To conclude this Chapter, we will briefly mention the effect of hydrogen-ion irradiation in other vdW systems. Indeed, we performed analogous treatments to that of TMDs and hBN also for other crystals. Fig. 1.12 shows an overview of four different systems (MoO_3, nanoporous graphene, SnS_2, and InSe) that we exposed to hydrogen ions with our Kaufman source, and where peculiar and different effects were obtained.

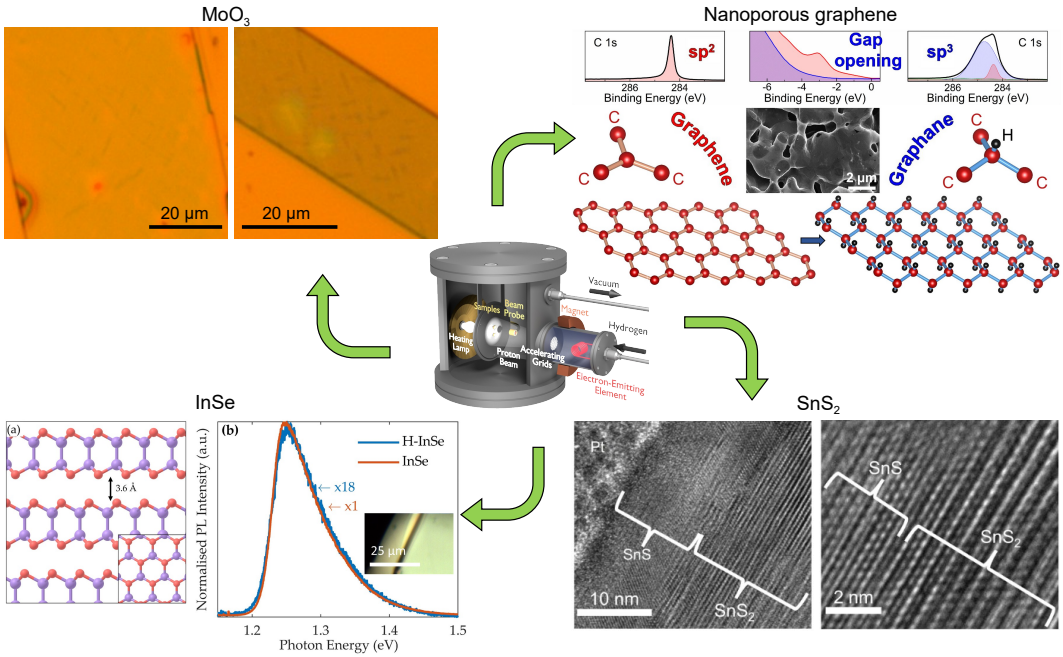

Figure 1.12: Examples of 4 different vdW materials exposed to H ions by the Kaufman source: (1) MoO_3: optical images of two flakes, showing the presence of some needle-like structures following H-ion irradiation. (2) Nanoporous graphene: SEM image of the sample (centre), sketch of the crystal lattice of graphene and graphane and corresponding C 1s spectra aimed at studying the presence of sp^2 and sp^3 bonds; valence band spectrum (top-centre) aimed at highlighting the opening of a gap. Reproduced with permission from M. G. Betti *et al.*, Nano Lett. **22**, 2971 (2022) [179]. Copyright 2022, The Authors. (3) SnS_2: TEM images of a SnS_2 flake following exposure to hydrogen, revealing the presence of a uniform film of SnS in the top part of the flake, due to the hydrogen-induced chemical conversion of Sn_2 into SnS. Reproduced with permission from J. Felton *et al.*, Small **18**, 2202661 (2022) [180]. Copyright 2022, The Authors. [180]. (4) InSe: Crystal structure of InSe (left) and PL spectra of a virgin InSe flake and of the same flake after H-ion irradiation, showing a decrease of the PL intensity due to the incorporation of atomic hydrogen. Reproduced with permission from J. Felton *et al.*, Molecules **25**, 2526 (2020) [154]. Copyright 2020, The Authors.

MoO_3

MoO_3 (in its α phase) is a vdW crystals that has attracted interest for its capability to host phonon polaritons (PhPs). Polaritons are hybrid quasiparticles originating from the coupling of light and dipole-like excitations in matter. PhPs with strong field confinement, low loss, and a long lifetime can enable a wide range of applications in light transmission, electro-optical modulation, sub-diffraction focusing and imaging, and molecular detection. Control of their properties is however needed for their utilisation into applications, which is a difficult task owing to the wide bandgap (∼2–10 eV) in polar crystals, making the common electrical-gating method impractical [181].

Recent studies demonstrated in-plane anisotropic and ultra-low-loss PhPs in MoO_3 [182, 183].

Triggered by this, Wu et al. [181] developed a strategy to successfully induce chemical switching of PhPs in nanometre-thick MoO_3 by precisely modifying its crystal structure via hydrogen intercalation. In particular, the samples were exposed to hydrogen plasma, leading to the formation of a mixture of type I H_xMoO_3 and α-MoO_3. Most interestingly, this chemical modification resulted in the appearance of needle-like hydrogenated nanostructures on the flake surface, functioning as in-plane antennas effectively reflecting and launching PhPs and forming well-aligned cavities.

Inspired by this result, we performed hydrogen-ion irradiations with beam energies of about 10 eV on MoO_3 crystals. After irradiation, the flake surface shows also in our case needle-like structures, like those shown in Fig. 1.12. The samples are currently being studied by the group of Prof. Javier M. Sanchez and Prof. Pablo Alonso-González, showing an efficient PhP launching.

Our hydrogenation method leads therefore to analogous results to those obtained by hydrogen plasma [181], with the advantage that in our case the hydrogenation time is of a few hours and it is thus controllable with high accuracy, while in the case of hydrogen plasma very short exposure times of a few seconds are needed, with lower degree of accuracy.

Nanoporous graphene

If graphene is characterised by an exceptional carrier mobility, on the other side, its semimetallic nature hinders its utilisation into optoelectronic devices. Numerous efforts have thus been done to make graphene semiconducting. One of the most successful strategies proposed theoretically to make graphene semiconducting is the incorporation of hydrogen, to form the so-called graphane. In graphane, each carbon atom in the honeycomb lattice is ideally bound to hydrogen with alternately up and down sp^3 distorted bonds. The conjugation of graphene π electrons is thus disrupted, leading to an insulating behaviour with band gap predicted to depend on the H chemisorption configuration. [184, 185].

Experimentally, however, only a low H storage capacity has been reached so far

with non-negligible contamination and defects. The maximum H uptake depends on both the morphology of graphene specimens (substrate-supported, transferred flakes, etc.) and the hydrogenation methods. Several attempts to incorporate a high percentage of hydrogen have been carried out in the last decades, exploiting a variety of strategies on different samples, reaching at most a partial hydrogenation of graphene, with an upper limit of H uptake $\Theta \sim$36 at.% [186]. This limit can be due to several concurrent drawbacks, such as oxygen contamination, the influence of the substrate, and the presence of defects/edges in graphene flakes (either pre-existing or induced by the hydrogenation).

A crucial challenge to fully exploit graphene for hydrogen storage is to employ defect-free graphene specimens with very high specific surface area, where hydrogen adsorbs strongly enough on the surface as to form a thermodynamically stable arrangement, achieving an ideal graphane pattern. Nano-porous graphene (NPG) –constituted by a compact, bi-continuous interconnected 3D arrangement of high-quality graphene veils, composed by one to a few weakly interacting layers [187, 188]– can present great advantages to achieve a high uptake of hydrogen in graphene [179, 189, 190]. The free-standing structure curved at the sub-micron scale, with intrinsically smooth rippling, can foster hydrogen chemisorption, favoured by the increased electron affinity of hydrogen and the energy barrier decrease in the convex regions [191].

We thus exploited high-quality NPG samples, with high specific area (1000 m^2/g) [192–194] and very low density of defects to incorporate hydrogen in the graphene matrix. Hydrogen incorporation was then verified by a series of experimental characterisations, including spectromicroscopy photoemission studies (performed in collaboration with Prof. Maria Grazia Betti and Prof. Carlo Mariani) and Raman measurements (performed by the candidate), combined with state-of-the-art theoretical predictions. Our results reveal that unprecedentedly high H uptakes can be obtained in NPG, leading to a gap opening. By H-ion and D-ion irradiations with the Kaufman source, hydrogen/deuterium uptakes of about 40 % were obtained [189, 190].

SnS_2

Amongst 2D materials, vdW crystals based on Sn and S offer an interesting platform for hydrogen studies. They can exist in a variety of stoichiometries, lattice structures, and with Sn-atoms in the different oxidation states Sn^{4+}, Sn^{2+} and Sn^0 [195]. Of particular interest are SnS_2 and SnS as they are not only found as stable vdW crystals down to single layers, but their electronic and optical properties can be tuned by the layer thickness [196, 197]. These materials have been incorporated as active components in water-splitting devices for the generation of hydrogen [198–200]. Furthermore, the ability of hydrogen to form bonds with sulphur, such as those found in H_2S, makes hydrogen a perfect candidate to modify these materials. We thus investigated the interaction of low-energy hydrogen-ion beams with SnS_2, as well as the interaction of molecular hydrogen with SnS_2 [180]. The latter

was done by keeping the samples into a molecular hydrogen atmosphere without triggering the ionisation process. The exposed samples were studied by PL and Raman spectroscopy, and by transmission electron microscopy (TEM) and XRD in collaboration with the group of Prof. Amalia Patanè (University of Nottingham, UK). Quite surprisingly, our studies led to the discovery that molecular hydrogen can induce a controlled chemical conversion of SnS_2 into semiconducting SnS. In particular, the upper layers of the exposed SnS_2 flake are found to be transformed into SnS, with a noticeably sharp interface between SnS and the underlying SnS_2 flake. An analogous effect is obtained also by exposure to low-energy hydrogen-ion beams, but in that case the chemical conversion progresses further, with the creation of clusters of Sn [180].

InSe

The vdW crystal InSe, despite attracting interest for its high carrier mobility and electronic properties, is also widely investigated as a promising material for hydrogen storage. As such, its interaction with hydrogen has been investigated. The incorporation of hydrogen has however been pursued mainly electrochemically, reaching compositions of up to H_5InSe [201]. In our group, we exposed InSe crystals to hydrogen ions by the Kaufman source and investigated the samples with a variety of techniques, including PL and Raman experiments, X-ray photoemission spectroscopy (XPS), DFT calculations and Monte Carlo simulations. This combined experimental/theorical characterisations indicate that atomic hydrogen is incorporated in the crystal by binding with Se atoms [154].

Chapter 2

Vibrational properties of highly strained TMD and hBN domes

The ability to control strain paves the way to the fine-tuning of the band structure of 2D crystals, and, thus, of their electronic and optical properties. In order to fully unleash the potential of strain engineering for tailoring new functionalities in 2D materials, however, the development of methods to effectively induce controlled lattice deformations must be complemented by the availability of efficient tools for measuring strain independently. Indeed, the effective amount of strain induced in a 2D compound can be quite different from the nominal one and/or from theoretical expectations, due to different extrinsic effects, such as slippage, substrate adhesion, etc.

Besides being coupled with the electronic degrees of freedom, strain also affects significantly the lattice dynamics. In conventional solids, as a general rule, lattice stretching (tensile strain) induces a softening of the phonon modes, whereas lattice shrinking (compressive strain) leads to a corresponding phonon hardening. Few exceptions to such trend can be found, as in ZrW_2O_8 [202–204], and, most noticeably, for some acoustic modes in graphene [205]. Monitoring the phonon spectral properties in the presence of induced strain thus provides a powerful tool for characterising the amount of strain effectively present in the system, as well as its degree of anisotropy. With respect to these goals, Raman spectroscopy has been established as the technique of choice for investigating phonons in 2D crystals, while also providing a powerful and non-invasive means for determining accurately the number of layers, the amount of disorder and the charge doping present in a given material [206–210]. Moreover, micro-Raman (μ-Raman) measurements allow us to collect this information at a sub-μm scale. Raman spectroscopy is a two-photon process related to the derivatives of the polarisability. At the first-order (single-phonon) it essentally probes lattice modes with zero momentum ($\mathbf{q} = 0$), in the centre of the Brilllouin zone (Γ point), so that only few phonon modes with selected symmetry are Raman active. At a higher order level, it can probe as well coupled phonon excitations with opposite momenta ($\mathbf{q}$, $-\mathbf{q}$), or edge-zone modes triggered by defect scattering. Such

processes have resulted to be particularly relevant in graphene, where, for instance, the spectral properties of the $2D$ peak have been used to characterize the number of layers and the amount of doping.

The most common means for evaluating the amount of strain in 2D materials is provided by a quantitative analysis of the energy peak position of the Raman phonon modes.

In general, the different long-wavelength phonon branches in a given crystal correspond to different symmetries of vibration of the atoms in the unit cell and are characterised by irreducible representations of the space group of the crystal lattice. Hence, in the infinite-wavelength approximation for the Raman phonons, the crystal point group can be used in classifying the phonon symmetries [211]. The correspondence between irreducible representations and Raman modes permits to determine the Raman tensor of each mode and, in turn, to define its peculiar properties. For instance, this allows us to say if a mode is a single mode or doubly-degenerate. This is particularly relevant because anisotropic strains in 2D materials break the degeneracies thus inducing mode splittings. These splittings can be exploited for a full characterisation of the applied strain, and, in particular, to determine the strain direction, together with its magnitude.

Let us consider, for completeness, the most general case of anisotropic in-plane strain. Such a strain can be described by a longitudinal ε_l component along the main strain direction, and a ε_t component along the transverse one. In this circumstance, a (two-degenerate) in-plane Raman mode with frequency ω_E will split by symmetry in two modes, with frequencies ω_E^+ and ω_E^-. It is convenient to define an average frequency

$$\omega_E^{\mathrm{av}} = \frac{\omega_E^+ + \omega_E^-}{2}, \tag{2.1}$$

and the mode splitting

$$\sigma_E = \omega_E^+ - \omega_E^-. \tag{2.2}$$

It is understood that both quantities depend on the magnitude and structure of the strain tensor $\overleftrightarrow{\varepsilon}$, so that $\omega_E^{\mathrm{av}} = \omega_E^{\mathrm{av}}(\overleftrightarrow{\varepsilon})$, and $\sigma_E = \sigma_E(\overleftrightarrow{\varepsilon})$.

The frequency shift (softening or hardening) upon strain of the two phonon modes ω_E^+ and ω_E^- can be captured by the frequency shift rate:

$$\Delta_E = -\frac{\partial \omega_E^{\mathrm{av}}}{\partial \varepsilon_{\mathrm{tot}}}, \tag{2.3}$$

and by the splitting rate:

$$\Sigma_E = \frac{\partial \sigma_E}{\partial \varepsilon_{\mathrm{diff}}}, \tag{2.4}$$

where $\varepsilon_{\mathrm{tot}}$ and $\varepsilon_{\mathrm{diff}}$ represent the sum and difference, respectively, of the in-plane components of the principal strain tensor, namely $\varepsilon_{\mathrm{tot}} = \varepsilon_l + \varepsilon_t$, $\varepsilon_{\mathrm{diff}} = \varepsilon_l - \varepsilon_t$.

It is furthermore convenient to introduce dimensionless quantities, as the phonon mode Grüneisen parameter:

$$\gamma_E = \frac{\Delta_E}{\omega_E^0}, \tag{2.5}$$

and the shear deformation potential:

$$\beta_E = \frac{\Sigma_E}{\omega_E^0}, \tag{2.6}$$

where ω_E^0 is the mode frequency in the absence of strain.

For biaxial strains, in the absence of in-plane symmetry breaking, there is no mode splitting and the only relevant parameter is the shift rate (alternatively, the Grüneisen parameter) [209, 212–214]. The same occurs of course for Raman modes involving out-of-plane displacements, as for instance for the A_{1g} modes in TMDs.

The above analysis has a more direct application in specific strain setups, as, for instance, in the following particular cases:

- *bending or uniaxially-stretching devices*: in bending setups the main strain ε_l is achieved along the bending direction and its magnitude can be described by $\varepsilon = \frac{\tau}{2R}$, where τ and R are the thickness and curvature radius of the flexible polymeric film on which the samples are deposited, respectively. When referring to the strain applied to the membrane in bending setups, it's common use to refer to this longitudinal strain component $\varepsilon_l = \varepsilon$ rather than to the total strain. In fact, the longitudinal strain results as well in a deformation in the transverse direction given by $\varepsilon_t = -\nu\varepsilon$, where ν is the Poisson's ratio of the material or of the substrate, depending on the setup. In general, it's under debate which choice is the most correct one. Following the analysis of Ref. [215], when comparing our results to those obtained in bending setups, we will here employ the Poisson's ratio of the material. Hence, the total strain would be given by $\varepsilon_{\text{tot}} = (1-\nu)\varepsilon$, and the shift rate and the splitting rate take the form:

$$\Delta_E = -\frac{1}{1-\nu} \cdot \frac{\partial \omega_E^{\text{av}}(\varepsilon)}{\partial \varepsilon}, \tag{2.7}$$

$$\Sigma_E = \frac{1}{1+\nu} \cdot \frac{\partial \sigma_E(\varepsilon)}{\partial \varepsilon}, \tag{2.8}$$

  with ν being given in the Additional Material, sec. A2. The same holds also for uniaxially-stretching devices.

- *spherical bulges and domes*: the principal strain tensor is given in polar coordinates, as shown in Fig. 1.9. In this case, the shift and splitting rates can be expressed as functions of the radial coordinate r as:

$$\Delta_E = -\frac{\partial \omega_E^{\text{av}}(r)}{\partial \varepsilon_{\text{tot}}(r)}, \tag{2.9}$$

$$\Sigma_E = \frac{\partial \sigma_E(r)}{\partial \varepsilon_{\text{diff}}(r)}, \tag{2.10}$$

  where $\varepsilon_{\text{tot}}(r) = \varepsilon_r(r) + \varepsilon_\theta(r)$ and $\varepsilon_{\text{diff}}(r) = \varepsilon_r(r) - \varepsilon_\theta(r)$.

2.1 TMD domes

μ-Raman measurements were performed by scanning the laser along the diameter of the domes. Low powers were used in the experiment, not to heat the system. Technical details can be found in the Additional Materials, sec. A4. We performed the measurements on 1-layer-thick MoS_2 domes created by hydrogen-ion irradiation, which are good candidates to probe strain since relatively large domes could be created, which is necessary when dealing with diffraction-limited measurements. The choice of MoS_2 is also grounded on the fact that this material is characterised by a relatively high Raman signal. The MoS_2 spectrum presents two Raman-active modes: The in-plane E^1_{2g} and the out-of-plane A_{1g} mode, see sketches in Fig. 2.1(a). The A_{1g} mode features a modest linear redshift with strain, while the in-plane E^1_{2g} is particularly interesting because it features a larger linear redshift with strain and it is also double-degenerate. In the presence of anisotropic strains, the degeneracy breaks and the mode splits into two peaks.

First, in Fig. 2.1(b), we show the colour plot of the Raman measurements acquired along the diameter of a MoS_2 dome (left), with radius $R = 1.6$ μm. The intensity of the Raman signal is modulated by interferential phenomena and possibly also by strain itself, as we will discuss in more detail in the following. In order to follow more clearly the shift of the Raman peaks, in Fig. 2.1(c), we considered separately the two phonon regions of the A_{1g} and E^1_{2g} modes and normalised the data from the dome in each region (after subtracting the signal from the bulk). We thus display the colour plots obtained from the normalised data. In such a manner, the splitting of the peaks can be followed much better. Indeed, our measurements show a clear redshift while going from the edge towards the centre and a clear splitting at the edges, suggesting the maximum strain to be reached at the center, and anisotropic strains being present at the edges. This agrees with the behaviour found via FEM calculations for the in-plane strain components —*i.e.* the circumferential (ε_θ) and radial (ε_r) components— showing how the strain is equibiaxial at the centre ($\varepsilon_\theta = \varepsilon_r$) and uniaxial at the edges ($\varepsilon_\theta = 0$, $\varepsilon_r \neq 0$), see Fig. 1.9.

Some spectra —while going from the left edge towards the centre— from the map of Fig. 2.1 are shown in Fig. 2.2(a). The relationship between the spectra and the position was established by careful calibration of the piezoelectric stages used during the maps, as discussed in the Experimental Section. For this dome, the scanning step was ∼55 nm. The intensity modulation of the spectra is chiefly attributable to interference phenomena, since the dome itself act as a Fabry-Perót interferometer [156, 216]. In the spectra, one can see both the peaks related to the strained dome and the peaks originating from the parent bulk substrate. Indeed, while the bulk signal does not feature any shift, the dome peaks show a clear redshift while going from the edge (bottom) to the centre (top). As already observable in the colour map, the E^1_{2g} mode is clearly split into two components close to the edges, while the two components are degenerate at the centre. By fitting the A_{1g} mode with

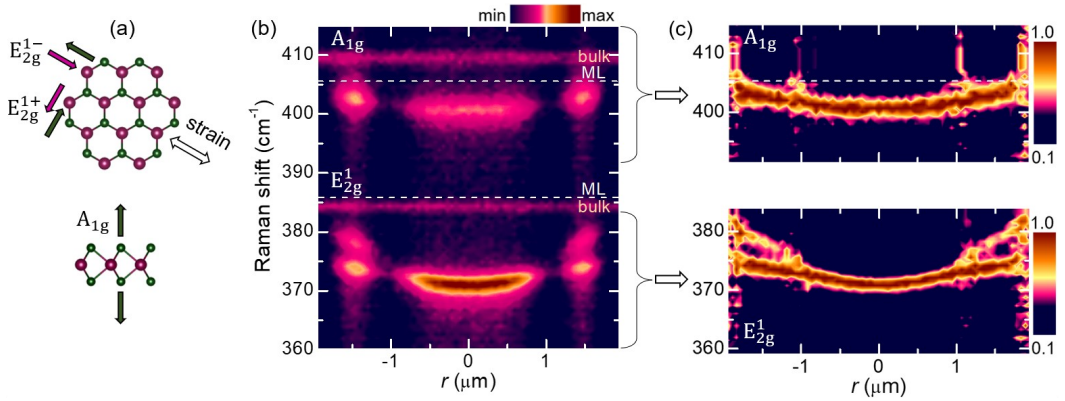

Figure 2.1: (a) Sketch of the E^1_{2g} and A_{1g} phonon modes. (b) RT μ-Raman colour-map (see colour-bar) along the diameter of a MoS_2 dome —having radius $R = 1.6$ μm— in the spectral region of the E^1_{2g} and A_{1g} phonon modes. The minus (plus) sign of r stands for the left (right) side of the dome. The E^1_{2g} and A_{1g} modes of bulk MoS_2 can be noticed, due to the presence of the bulk flake beneath the dome. The white dashed lines indicate the frequencies of the unstrained monolayer (ML) modes. (c) colour maps in the two phonon regions of the E^1_{2g} and A_{1g} modes, obtained after subtracting the bulk signal and normalising the spectra. These maps allow us to follow in more detail the frequency behavior of the Raman modes. Figure reproduced with permission from E. Blundo *et al.*, Phys. Rev. Lett. **127**, 046101 (2021) [116]. Copyright 2021 American Physical Society.

one lorentzian, and the E^1_{2g} mode with two lorentzians, we find the shifts shown in panels (b) and (c) of Fig. 2.2. The shift of the E^1_{2g} and A_{1g} modes and the splitting of the E^1_{2g} mode across the dome are quantified by the Grüneisen parameters (γ_{2g} and γ_{1g}) and the shear deformation potential (β_{2g}), where, for ease of notation, we indicate with the subscripts 2g and 1g the parameters related to the E^1_{2g} and A_{1g} mode, respectively. Such parameters can be expressed as [116]:

$$\gamma_{2g} = \frac{1}{\omega^0_{2g}} \cdot \frac{\omega^0_{2g} - \omega^{av}_{2g}(r)}{\varepsilon_r(r) + \varepsilon_\theta(r)}, \qquad \gamma_{1g} = \frac{1}{\omega^0_{1g}} \cdot \frac{\omega^0_{1g} - \omega_{1g}(r)}{\varepsilon_r(r) + \varepsilon_\theta(r)},$$
$$\beta_{2g} = \frac{1}{\omega^0_{2g}} \cdot \frac{\sigma_{2g}(r)}{\varepsilon_r(r) - \varepsilon_\theta(r)} \tag{2.11}$$

where ω is the mode frequency, ω^0 indicates its value at 0 strain, ω^{av} is the average frequency $[\omega^{av}_{2g}(r) = 1/2 \cdot (\omega^+_{2g}(r) + \omega^-_{2g}(r))]$ and σ is the mode splitting $[\sigma_{2g}(r) = \omega^+_{2g}(r) - \omega^-_{2g}(r)]$.

By acquiring Raman measurements on non-strained monolayers, we found $\omega^0_{2g} = 385.5$ cm^{-1} and $\omega^0_{1g} = 405.6$ cm^{-1}.

In the presence of strain, the A_{1g} mode redshift is ruled by the total in-plane

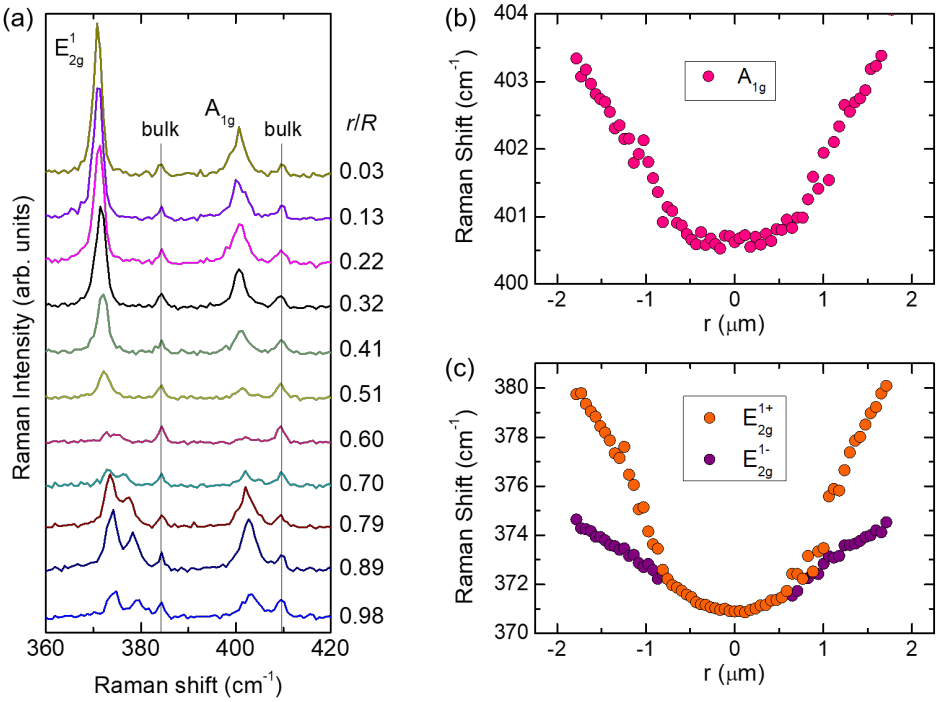

Figure 2.2: (a) Some spectra from the left side of the Raman map of Fig. 2.1. The spectra are stacked by y-offset for ease of comparison. The bulk peaks are highlighted to distinguish them from the dome modes. The normalised spatial coordinate is displayed on the right. (b) Extracted peak position for the A_{1g} mode as a function of the distance from the centre. (c) Same for the E^{1+}_{2g} and the E^{1-}_{2g} modes. Figure reproduced with permission from E. Blundo *et al.*, Phys. Rev. Lett. **127**, 046101 (2021) [116]. Copyright 2021 American Physical Society.

strain, so that this latter can be found from the shifts according to [116]:

$$\varepsilon_{\mathrm{sum}}(r) = \varepsilon_r(r) + \varepsilon_\theta(r) = \frac{\omega^0_{1\mathrm{g}} - \omega_{1\mathrm{g}}(r)}{\gamma_{1\mathrm{g}}\omega^0_{1\mathrm{g}}}, \tag{2.12}$$

An analogous relationship holds also for the average shift of the E^1_{2g} modes:

$$\varepsilon_{\mathrm{sum}}(r) = \varepsilon_r(r) + \varepsilon_\theta(r) = \frac{\omega^0_{2\mathrm{g}} - \omega^{\mathrm{av}}_{2\mathrm{g}}(r)}{\gamma_{2\mathrm{g}} \cdot \omega^0_{2\mathrm{g}}}, \tag{2.13}$$

The splitting of this mode is instead related to the shear deformation potential $\beta_{2\mathrm{g}}$, according to:

$$\varepsilon_{\mathrm{diff}}(r) = \varepsilon_r(r) - \varepsilon_\theta(r) = \frac{\sigma_{2\mathrm{g}}(r)}{\beta_{2\mathrm{g}} \cdot \omega^0_{2\mathrm{g}}}. \tag{2.14}$$

Hence, one can express the two strain components in terms of the frequencies as

[116]:

$$\varepsilon_r(r) = \frac{1}{2\gamma_{2g}\omega^0_{2g}}\left[\omega^0_{2g} + \left(\frac{2\gamma_{2g} - \beta_{2g}}{2\beta_{2g}}\right)\omega^+_{2g}(r) - \left(\frac{2\gamma_{2g} + \beta_{2g}}{2\beta_{2g}}\right)\omega^-_{2g}(r)\right], \quad (2.15)$$

and

$$\varepsilon_\theta(r) = \frac{1}{2\gamma_{2g}\omega^0_{2g}}\left[\omega^0_{2g} - \left(\frac{2\gamma_{2g} + \beta_{2g}}{2\beta_{2g}}\right)\omega^+_{2g}(r) + \left(\frac{2\gamma_{2g} - \beta_{2g}}{2\beta_{2g}}\right)\omega^-_{2g}(r)\right]. \quad (2.16)$$

To verify the agreement between our data and the numerical strain distribution, we performed a fit to estimate the γ_{2g} and β_{2g} coefficients that give the best agreement between data and numerical results. To do that, we kept into account the finite resolution of our optical system by convolving the numerical strain distributions within the laser spot size (modelled as a gaussian with $\sigma = 230$ nm, see Additional Material, sec. A4). The fit was performed on the convolved strain distribution. For the dome in Fig. 2.1, we estimated $\gamma_{2g} = 0.82 \pm 0.16$ and $\beta_{2g}/\gamma_{2g} = 0.97 \pm 0.04$ via Eqs. (2.15) and (2.16), and $\gamma_{1g} = 0.22 \pm 0.04$ via Eq. (2.12) [116]. These estimates agree well with those of previous works [41, 87, 215]. A comparison between the deconvolved strains obtained by the Raman data (from both sides of the map, see circles in Fig. 2.3) and the numerical distribution (see lines in Fig. 2.3) is shown in Fig. 2.3, and a good agreement between experiment and theory is indeed found.

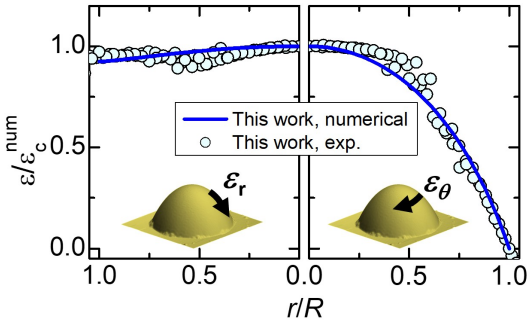

Figure 2.3: Circumferential (ε_θ) and radial (ε_r) in-plane strain components as a function of the normalised radial coordinate, calculated by FEM calculations (lines), and obtained by the Raman data (circles), for the dome in Figs. 2.1 and 2.2. The strain values are normalised to the numerical strain at the centre. The strain values obtained by the Raman data were deconvolved to keep into account the finite resolution of our optical system. Insets: Sketches of the strain components. Adapted with permission from E. Blundo *et al.*, Phys. Rev. Lett. **127**, 046101 (2021) [116]. Copyright 2021 American Physical Society.

Analogous results were obtained also for other domes. For instance, in Fig. 2.4(a) we show the colour map acquired on a larger structure [116]. Some spectra acquired

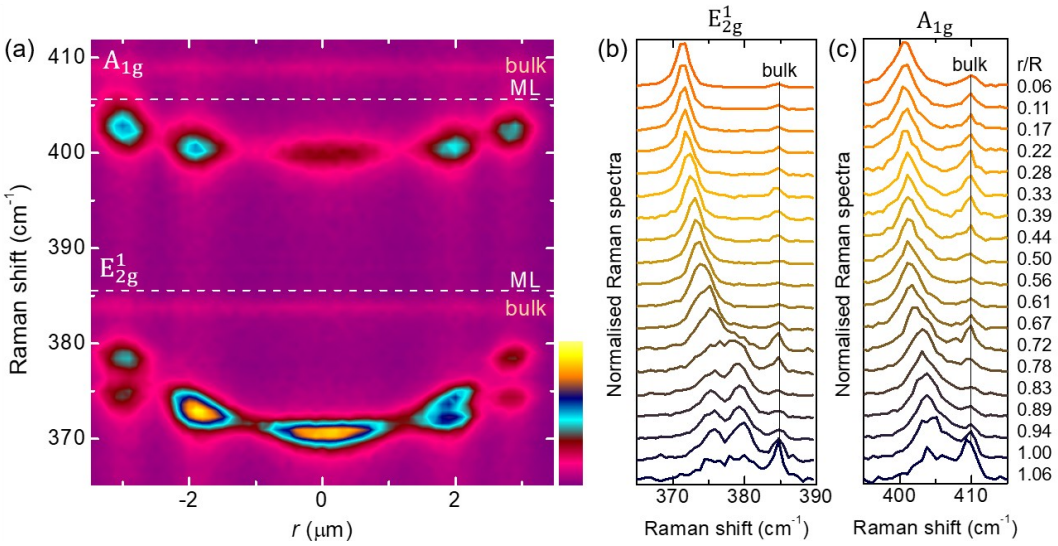

Figure 2.4: (a) One-dimensional, RT μ-Raman scan across a MoS_2 dome —having radius $R = 3.2$ μm— in the spectral region of the E^1_{2g} and A_{1g} phonon modes. The horizontal axis indicates the laser spot position with respect to the dome centre (r), where the minus sign indicates the left side and the plus sign the right side of the dome. The vertical axis indicates the Raman shift with respect to the laser line. The μ-Raman intensity is shown in a false colour scale (see colourbar). The E^1_{2g} and A_{1g} modes of bulk MoS_2 can be noticed, due to the presence of the bulk flake underneath. The white dashed lines indicate the frequencies of the unstrained monolayer (ML) modes. (b) Some spectra from the left side of the Raman map of Fig. 2.4. The two panels refer to the E^1_{2g} (left) and A_{1g} phonon modes (right). In each panel, the spectra are normalised to 1 and stacked by y-offset for ease of comparison. The bulk peaks are highlighted to distinguish them from the dome modes. The normalised spatial coordinate is displayed on the right. Figure reproduced with permission from E. Blundo *et al.*, Phys. Rev. Lett. **127**, 046101 (2021) [116]. Copyright 2021 American Physical Society.

on the left side of the map are also shown in Fig. 2.4(b). Also in this case, both the out-of-plane and the in-plane mode clearly redshift while going towards the centre, and the E^1_{2g} is clearly split towards the edges. The intensity modulation differs from that of the previous dome. This is due, on the one side, to the larger size of this structure, implying a different interference pattern; on the other side, strain itself induces intensity modulations, which might be attributable to on/off resonant Raman scattering resulting from the strain tuning of a higher level energy transition to be in resonance with the laser [87]. To show this effect, in Fig. 2.5, we compare the reflectance data acquired on the same dome with the integrated area of the dome E^1_{2g} and A_{1g} modes. Indeed, while there is a correspondence between the minima at $r \sim 2.5$ μm, which suggests it to be an interference-induced-minimum, the Raman minimum at $r \sim 1$ μm and the maximum at the centre do not show a correlation with the reflectance data. This suggests the influence of strain on the electronic structure of the material to be the main reason for this modulation.

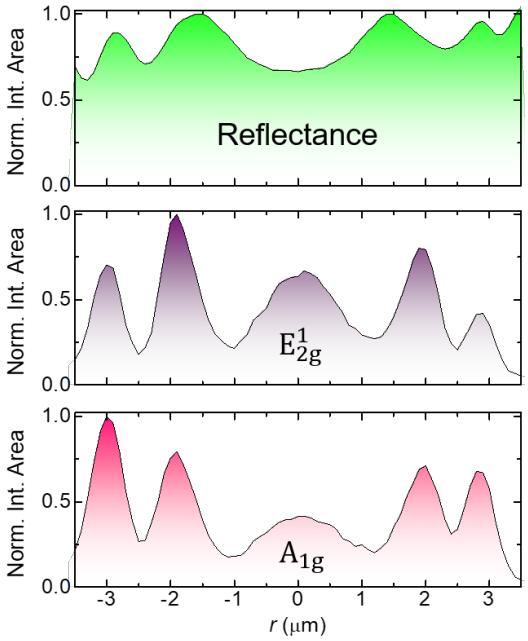

Figure 2.5: Top: normalised laser reflectivity at 532.2 nm as a function of the position of the laser spot. The displayed profile was obtained by collecting the light reflected by the sample as the laser was scanned across the dome, under the same experimental conditions used for μ-Raman measurements (RT, confocal configuration). Middle: Evolution of the integrated intensity of the E^1_{2g} Raman mode as the laser is scanned across the dome. Bottom: Same for the A_{1g} mode. Figure reproduced with permission from E. Blundo *et al.*, Phys. Rev. Lett. **127**, 046101 (2021) [116]. Copyright 2021 American Physical Society.

To account for the strain distribution, we performed for this dome an analogous analysis to that discussed above, and we estimated $\gamma_{2g} = 0.86 \pm 0.14$, $\beta_{2g}/\gamma_{2g} = 0.77 \pm 0.07$, and $\gamma_{1g} = 0.26 \pm 0.05$ [116]. Also in this case, these estimates agree well with those of previous works [41, 87, 215]. A comparison between the deconvolved strains obtained by the Raman data (from both sides of the map, see circles in Fig. 2.6) and the numerical distribution (see lines in Fig. 2.6) is shown in Fig. 2.6. A good agreement is indeed found also in this case.

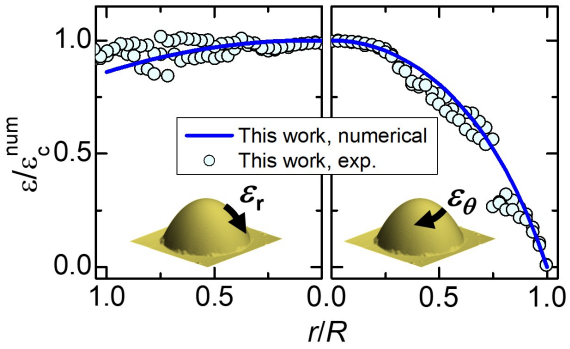

Figure 2.6: Circumferential (ε_θ) and radial (ε_r) in-plane strain components as a function of the normalised radial coordinate, calculated by FEM calculations (lines), and obtained by the Raman data (circles), for the dome in Figs. 2.4 and 2.5. The strain values are normalised to the numerical strain at the centre. The strain values obtained by the Raman data were deconvolved to keep into account the finite resolution of our optical system. Insets: Sketches of the strain components. Figure reproduced with permission from E. Blundo *et al.*, Phys. Rev. Lett. **127**, 046101 (2021) [116]. Copyright 2021 American Physical Society.

2.2 hBN domes

In the case of hBN, we focus on two specific in-plane transverse modes, which are IR-active (E_{1u}) and Raman-active (E_{2g}). Their lattice displacements are sketched in Fig. 2.7.

Fig. 2.8(a) displays the AFM image of a circular hBN dome with diameter $D = 2R = 4.54$ μm and height $h_\mathrm{m} = 267$ nm ($h_\mathrm{m}/R = 0.117$) obtained by deuterium-ion irradiation [169]. The AFM profile recorded along the cyan dashed line is shown in Fig. 2.8(b) (circles). The yellow line is the profile evaluated by FEM numerical calculations; see Additional Material, sec. A3. The latter also provide the strain distribution [116, 156], as shown on the left side of Fig. 2.8(c), where ε_r and ε_θ are the radial and circumferential in-plane strain components in polar coordinates, respectively [116, 217]. The calculated spatial distribution of the total strain $\varepsilon_\mathrm{tot} = \varepsilon_r + \varepsilon_\theta$ is displayed as a false-colour image on the right side of panel (c). Analogously to the case of TMDs, strain features an anisotropic character, changing from tensile uniaxial at its edge ($r/R = 1$, $\varepsilon_r \neq 0$ and $\varepsilon_\theta = 0$) to tensile equi-biaxial at the summit of the dome ($r/R = 0$, $\varepsilon_r = \varepsilon_\theta$). On these premises, we expect the in-plane transverse phonon frequency ω_t to undergo a decrease with respect to unstrained hBN due to stretching, as well as a splitting in ω_t^+ and ω_t^-, whose extent depends on the position on the dome.

The E_{1u} mode (see lattice displacements in Fig. 2.7) was studied by nano Fourier transform infrared spectroscopy (nano-FTIR) and scanning near-field optical microscopy (SNOM) measurements [218, 219] performed by our collaborators Prof. Leonetta Baldassarre (Sapienza, University of Rome) and Dr. Davide Spirito (IHP-Leibniz Institut fur Innovative Mikroelektronik, Frankfurt, Germany), see Addi-

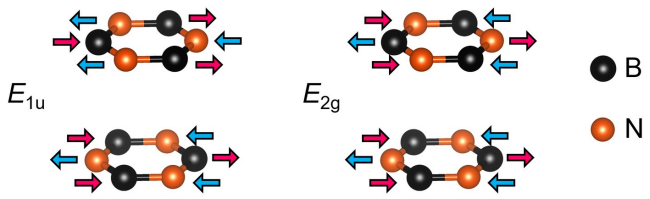

Figure 2.7: Sketch of the atom displacements corresponding to the IR-active E_{1u} mode and to the Raman-active E_{2g} mode. Differently coloured arrows indicate opposite atom motions. Figure reproduced with permission from E. Blundo *et al.*, Nano Lett. **22**, 1525 (2022) [169]. Copyright 2022, The Authors.

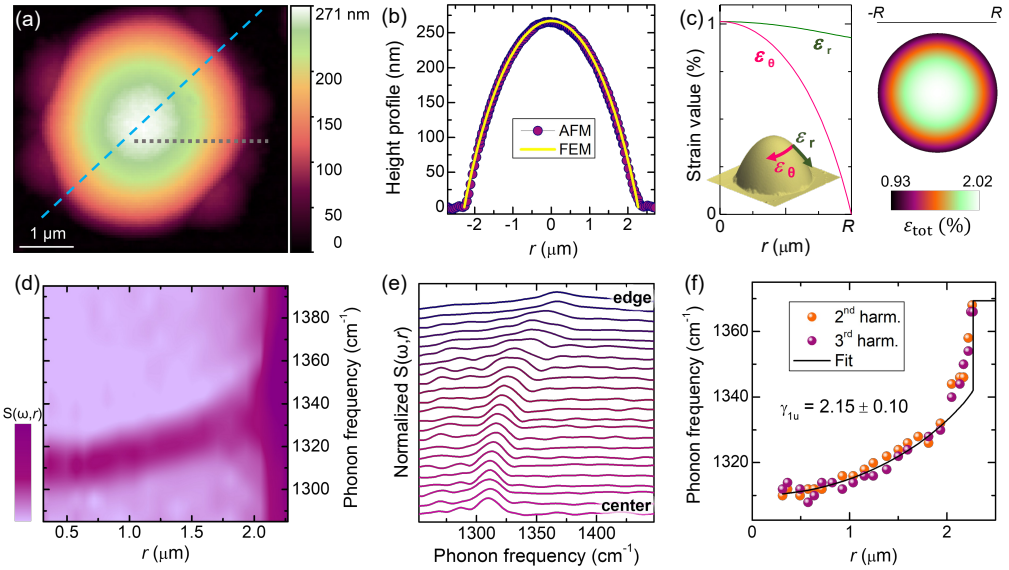

Figure 2.8: IR-active mode *vs* strain. (a) 2D AFM image of a hBN dome exhibiting a circular symmetric shape, but on its edge, where smaller satellite domes nucleated. The dome has $R = 2.27$ μm and $h_0 = 267$ nm ($h_m/R = 0.117$) and was created in a deuterated sample (beam energy equal to 6 eV) to minimise the dome thickness. (b) Comparison between the AFM profile acquired along a diameter of the dome (highlighted in panel (a) by a cyan dashed line) and the profile obtained by FEM calculations. (c) Left: Radial dependence —obtained by FEM calculations— of the in-plane circumferential (ε_θ) and radial (ε_r) strain components, a sketch of which is depicted as inset. Right: Spatial distribution of the total in-plane strain $\varepsilon_{tot} = \varepsilon_r + \varepsilon_\theta$. (d-e) Colour map of the near-field amplitude $S(\omega, r)$ (d) and corresponding spectra (e), where the IR active mode (E_{1u}) is visible. The measurements were taken along the gray short-dashed line shown in panel (a). The 2$^{\text{nd}}$ harmonic is considered here. (f) IR phonon frequency dependence on the radial distance r, as deduced from the spectra shown in panel (e) and the AFM profile. The 3$^{\text{rd}}$ harmonic data were also included here. The black solid line is a fit to the data assuming a linear dependence of the phonon frequency on ε_{tot}, provided by Eqs. (2.3) and (2.5). Figure reproduced with permission from E. Blundo *et al.*, Nano Lett. **22**, 1525 (2022) [169]. Copyright 2022, The Authors.

tional Material, sec. A5, for details. This technique has been widely employed in two-dimensional systems, *e.g.*, to probe phonon-polaritons in hBN [220–222], phonons in hBN superlattices [223], electron-phonon interactions in graphene [224], and intersubband transitions in two-dimensional quantum wells [225], but the E_{1u} hBN mode sensitivity to strain has not been investigated, to our knowledge. Fig. 2.8(d) shows the normalised near-field amplitude $S(\omega, r)$, as obtained with a spectral line scan along the gray short-dashed line in Fig. 2.8(a). The near-field signal originates from the tip-sample interaction and provides a lateral resolution of about 20 nm; see Additional Material, sec. A5. The corresponding spectra are shown in Fig. 2.8(e). The phonon peak frequency from the bulk region outside the dome is $\omega_{1\mathrm{u}} = 1367$ cm^{-1}, in agreement with previous reports [226]. An abrupt decrease of $\omega_{1\mathrm{u}}$ is noticed when the tip approaches the dome edge, where a 0.9 % tensile strain is already present (see Fig. 2.8(c)). On moving further toward the dome center, $\omega_{1\mathrm{u}}$ seamlessly decreases, in agreement with the expected tensile strain increase. To quantify the mode shift variation *vs* total strain $\varepsilon_{\mathrm{tot}}(r)$, we established a one-to-one correspondence between the AFM-derived dome profile (h *vs* r) and the calculated strain components shown in Fig. 2.8(c). In turn, this allowed us to establish a correspondence between each measured $\omega_{1\mathrm{u}}$ and $\varepsilon_{\mathrm{tot}}(r)$, given that the $h(r)$ values were measured by the SNOM tip in the very same points where $\omega_{1\mathrm{u}}$ was probed. To reduce the background signal we collected the near-field data at several harmonics. In Fig. 2.8(f) we show the spatial dependence of the second and third harmonic of the signal associated to the E_{1u} phonon (see Additional Material, sec. A5 and Additional Material, sec. A6). We reproduce quite successfully the dependence of $\omega_{1\mathrm{u}}$ on r using as fitting parameters the mode frequency at zero strain $\omega^0_{1\mathrm{u}} = (1369.7 \pm 2.4)$ cm^{-1} and the shift rate $\Delta_{1\mathrm{u}} = (29.5 \pm 1.4)$ cm^{-1}/%, resulting in a Grüneisen parameter (see Equation (2.5)) $\gamma_{1\mathrm{u}} = 2.15 \pm 0.10$ [169]. Analogous measurements were performed on other domes, see Table 2.1 and Additional Material, sec. A6. [169].

Table 2.1: Effect of strain on the vibrational modes of hBN. Parameters obtained for the $E_{1\mathrm{u}}$ and $E_{2\mathrm{g}}$ from the nano-FTIR and Raman measurements, respectively, The frequency at zero strain (ω_t), shift rate (Δ), Grüneisen parameter (γ_t), splitting rate (Σ_t), shear deformation potential (β_t), and the ratio γ_t/β_t were estimated for several domes.

Mode	ω_t^0 (cm^{-1})	Δ (cm^{-1}/%)	γ_t	Σ_t (cm^{-1}/%)	β_t	β_t/γ_t
$E_{1\mathrm{u}}$ (IR)	1369.9 ± 2.3	29.4 ± 1.8	2.15 ± 0.12	/	/	/
	1369.7 ± 2.4	29.5 ± 1.4	2.15 ± 0.10	/	/	/
	1369.0 ± 5.2	36.2 ± 3.6	2.64 ± 0.27	/	/	/
$E_{2\mathrm{g}}$ (Raman)	1370	24.6 ± 0.60	1.79 ± 0.04	11.2 ± 1.9	0.82 ± 0.14	0.46 ± 0.08
	1370 [1]	25.1 ± 4.5	1.83 ± 0.33	/	/	/
	1370 [1]	28.5 ± 8.4	2.08 ± 0.61	15.6 ± 3.8	1.14 ± 0.28	0.56 ± 0.14
	1370 [1]	33.2 ± 5.2	2.43 ± 0.40	/	/	/

[1] This value was kept fixed since it was otherwise affected by too large uncertainties.

It should be noticed that the zero-strain limit $\omega^0_{1\mathrm{u}}$ ($\sim$1370 cm^{-1}) of the dome E_{1u} mode is larger than that of bulk hBN ($\sim$1367 cm^{-1}). This is consistent with the frequency increase reported for the Raman-active $E_{2\mathrm{g}}$ mode in the few-layer limit

[227–229].

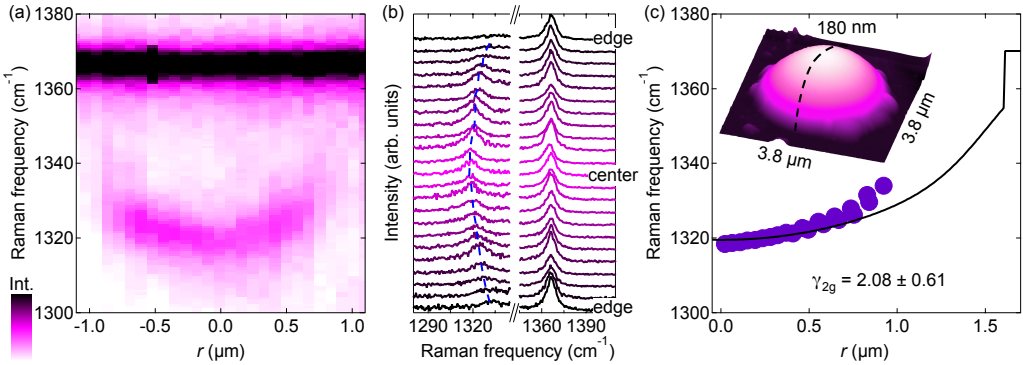

Figure 2.9: Raman-active mode *vs* strain. (a) False colour image of the intensity of the E_{2g} Raman mode as a function of position along a diameter of a dome. The dome has $R = 1.61$ μm and $h_0 = 179$ nm ($h_m/R = 0.111$) and was created in a deuterated sample (beam energy equal to 25 eV). (b) Raman spectra corresponding to the map of panel (a). (c) E_{2g} Raman mode frequencies as a function of the distance from the centre of the dome. The solid line is a linear fit to the frequency *vs* r behavior, γ_{2g} being the fitting parameter. Inset: AFM image of the investigated structure. The dashed line indicates the diameter along which the spectra were measured. Figure reproduced with permission from E. Blundo *et al.*, Nano Lett. **22**, 1525 (2022) [169]. Copyright 2022, The Authors.

Let us now discuss our studies of the E_{2g} mode (see lattice displacements in Fig. 2.7). We performed μ-Raman measurements of the hBN dome ($R = 1.61$ μm, $h_m = 179$ nm, $h_m/R = 0.111$, created by D irradiation) whose AFM image is shown as inset of Fig. 2.9(c) [169]. Fig. 2.9(a) is the spectrally and spatially resolved intensity map of the light scattered by the dome in the spectral region of the E_{2g} mode. The map was recorded along a diameter (see inset of panel (c)) and the corresponding spectra are shown in Fig. 2.9(b). The spot size and spectral resolution are ~ 0.5 μm and 0.7 cm^{-1}, respectively; see Additional Material, sec. A4. The intense peak at 1366.2 cm^{-1} comes from the bulk hBN flake from which the dome swelled. The E_{2g} signal from the dome is much less intense —due to the reduced thickness— and exhibits a spatially dependent and lower frequency due to strain. We notice that, unlike the IR signal, the Raman signal becomes negligibly small as the laser approaches the edge of the dome due to optical interference effects [88, 156]. The correspondence between the measured ω_{2g} values and $\varepsilon_{tot}(r) = \varepsilon_r(r) + \varepsilon_\theta(r)$ is established by evaluating the strain via FEM calculations based on the AFM profile; see Additional Material, sec. A4. The spatial dependence of ω_{2g} is shown in Fig. 2.9(c) and it is best reproduced with a shift rate $\Delta_{2g} = (28.5 \pm 8.4)$ cm^{-1}/% and a Grüneisen parameter (see Equation (2.5)) $\gamma_{2g} = 2.08 \pm 0.61$ [169]. The extrapolation frequency at zero strain was set at 1370 cm^{-1}, which is greater than the corresponding bulk mode (1366.2 cm^{-1}) like in the case of the E_{1u} IR-active mode and consistently with published results [227–229]. Similar measurements were

performed on different domes, see Additional Material, sec. A7, and the estimated parameters are displayed in Table 2.1 [169]. We also performed a statistical analysis of the shift at the dome summit including many other domes, showing how average Grüneisen parameters $\gamma_{2g} = 2.04 \pm 0.48$ ($\Delta_{2g} = (27.9 \pm 6.6)$ cm^{-1}/%) are obtained (see Additional Material, sec. A8). Our statistical analysis also shows how the E_{1u} and E_{2g} are characterised by similar Grüneisen parameters [169].

Previous μ-Raman studies on hBN domes created by H-plasma treatments [170] reported only a modest shift of about 3 cm^{-1} between the centre and bulk hBN. Similar small shifts (~ 3 cm^{-1}) were observed in hBN monolayers subject to thermal compression (biaxial strain of -0.17 %) [228], resulting in $\gamma_{2g} = 0.62$. Finally, uniaxial strains up to 0.4 % were applied to thin hBN flakes (2-4 layers) using a bending apparatus, achieving frequency softenings < 6 cm^{-1}. Grüneisen parameters γ_{2g} between 1.77 and 2.07 were estimated in this case [230], on average slightly lower than our estimates (see Table 2.1). By comparison with the current literature, our approach permits to achieve a much larger total strain —on average equal to $\sim$1.9 %— with unprecedented shifts in excess of 50 cm^{-1} [169].

In addition to the E_{2g} mode shift, a splitting is expected in the spectra due to the imbalance between ε_θ and ε_r. Fig. 2.10(a) displays an intensity map formed by polarisation-dependent μ-Raman spectra recorded on a given point of the same dome of Fig. 2.9 [169]. The point is 790-nm-away from the centre (*i.e.*, $r/R = 0.49$) and is marked by the black dot superimposed to the strain anisotropy degree plot in Fig. 2.10(c), the anisotropy being defined as $\alpha = (\varepsilon_r - \varepsilon_\theta)/(\varepsilon_r + \varepsilon_\theta)$. Therein, the arrows indicate the strain direction. The radial distance r was determined by the relationship between ω_{2g} and r given in Fig. 2.9(c). Each spectrum of Fig. 2.10(a) was recorded by keeping the polarisation direction of the laser fixed at an arbitrary, unknown angle ϕ_0 with respect to a reference crystal direction (*e.g.*, the armchair/zigzag direction). Likewise, strain is oriented along the radius, and its direction was thus also fixed at an unknown angle θ with respect to the same lattice reference. The angle ϕ between the polarisation of the Raman-scattered and Raman-exciting photons was then varied from 0° to 360°. While the E_{2g} bulk mode at 1366.2 cm^{-1} remains constant in intensity and frequency, the strain-softened E_{2g} mode in the 1320-1340 cm^{-1} range exhibits a marked angular dependence of its center-of-mass frequency, pointing to a mode splitting. This is exemplified in Fig. 2.10(b), showing two μ-Raman spectra recorded with opposite polarisations ($\phi = 0°$ and 90°). Indeed, it can be demonstrated that the intensities $I^{\pm}_{2g}$ of the $E^{\pm}_{2g}$ modes split by uniaxial strain are given by [41]:

$$\begin{aligned} I^{+}_{2g} &= c^2 \cos^2(\phi + 2\phi_0 + \theta) \\ I^{-}_{2g} &= c^2 \sin^2(\phi + 2\phi_0 + \theta) \\ I_{2g} &= I^{+}_{2g} + I^{-}_{2g} = c^2, \end{aligned} \tag{2.17}$$

where c is a constant. By performing a lineshape fitting of the Raman spectra, we extracted $I^{\pm}_{2g}$ as a function of ϕ, where E^{+}_{2g} and E^{-}_{2g} refer to the high- and low-frequency components, respectively. Fig. 2.10(d) shows the resulting polar plot,

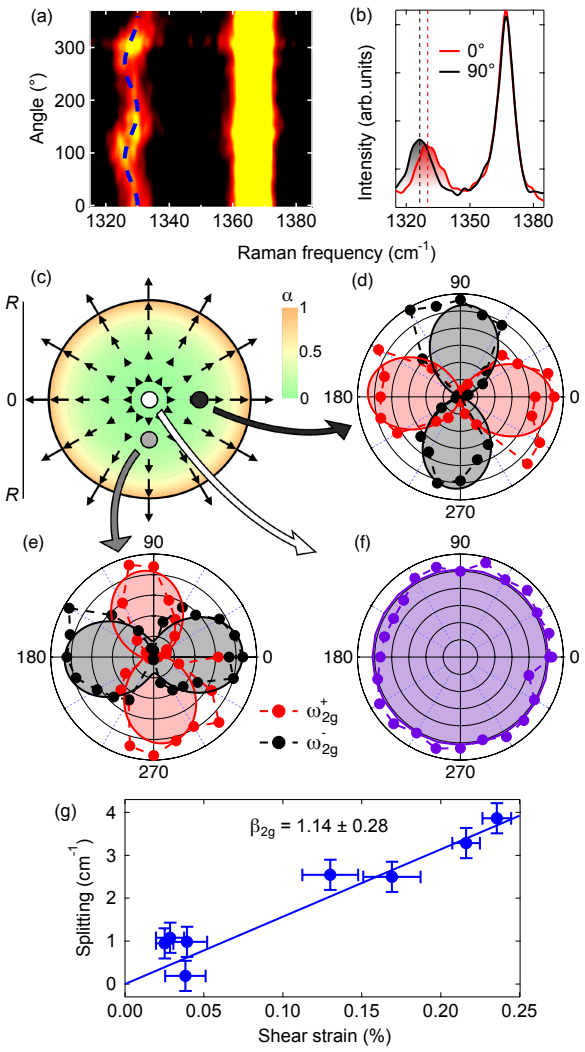

Figure 2.10: (a) False colour map of the intensity of the E_{2g} Raman mode as a function of the angle of the polarisation analyser. The dashed line is a sinusoidal guide to the eye. (b) μ-Raman spectra measured at polarisations parallel and perpendicular to the uniaxial strain direction. (c) Radial dependence of the strain anisotropy $\alpha = (\varepsilon_r - \varepsilon_\theta)/(\varepsilon_r + \varepsilon_\theta)$, determined based on FEM calculations. The arrows point to the direction of the strain field. Their length is calculated as $\log_{10}(100\alpha)$. The dots depict the position of the excitation spots of the polarisation-resolved Raman measurements. (d-f) Intensity of the low frequency (ω_{1u}^-) and high frequency (ω_{1u}^+) Raman modes as a function of the analyser angle for excitation performed (d) on the right (black dot), (e) at the bottom (gray dot), and (f) at the centre of a (white dot). (g) Mode splitting as a function of the shear strain. The solid line is a linear fit. Figure reproduced with permission from E. Blundo *et al.*, Nano Lett. **22**, 1525 (2022) [169]. Copyright 2022, The Authors.

obtained from the data of panel (a). The reference angle $(2\phi_0 + \theta)$ is set to zero for simplicity reasons. The two components are clearly in counter phase, as expected. Fig. 2.10(e) shows a similar set of measurements acquired on a point of the dome positioned symmetrically at 90° with respect to the previous one (at $r = 680$ nm), see grey dot in panel (c). In this case, the strain direction is given by $\theta' = \theta + 90°$ and, as a consequence of Eq. (2.17), the $E^{\pm}_{2g}$ components follow an angular dependence which is $\pi/2$ out-of-phase with respect to that of the previous point (panel (d)). These results are fully consistent with the strain field calculated numerically, whereby the ε_r component dictates the strain direction. Finally, the μ-Raman spectra recorded at the centre (white dot in panel (c)), where the strain is equi-biaxial, show no mode splitting, see Fig. 2.10(f). Other polarisation maps were acquired in different points of the dome. For each point, the average frequency ω^{av}_{2g} corresponds to a given r value (see Fig. 2.9(c)). In turn, via numerical simulations, we obtain $\varepsilon_{shear}(r) = \varepsilon_{diff}(r) = \varepsilon_r(r) - \varepsilon_\theta(r)$. Fig. 2.10(g) shows the dependence of the mode splitting σ_{2g} *vs* $\varepsilon_{shear}(r)$. Considering Eq. (2.6), we estimate a splitting rate $\Sigma_{2g} = 15.6 \pm 3.8$ $cm^{-1}/\%$ and a shear deformation potential $\beta_{2g} = 1.14 \pm 0.28$ [169]. Thus, for this dome, we get $\beta_{2g}/\gamma_{2g} = 0.56 \pm 0.14$. We performed similar measurements on another dome with lower Grüneisen parameter, see Additional Material, sec. A9, and found $\beta_{2g} = 0.82 \pm 0.14$ and $\beta_{2g}/\gamma_{2g} = 0.46 \pm 0.08$, see Table 2.1, showing how the ratio β_{2g}/γ_{2g} is less affected by fluctuations than β_{2g} and γ_{2g} [169]. We are aware of only one previous report of the hBN shear potential in the few-layer limit, where the ratio β_{2g}/γ_{2g} was found to vary between 0.45 and 0.52 [230].

Chapter 3

Engineered domes: achieving control over size, position and strain

Size and position engineering

Besides durability, the application prospects of our TMD domes are greatly enhanced by the possibility to precisely control their size and position. The dome formation process via low-energy hydrogen-ion irradiation is indeed characterised by a high yield, the domes usually forming over the entire irradiated flakes, as shown in Figs. 1.2 and 1.3. This allows the dome formation process to be engineered, by exploiting a lithography-based approach. This can be achieved by depositing an H-opaque masking layer prior to H-ion irradiation. The pattern is realised by depositing a film with uniform thickness of hydrogen silesquioxane (HSQ) on the sample. HSQ is a negative tone electron-beam (e-beam) resist, which was employed because of its property to be H-opaque under the irradiation conditions used in this work. Therefore, the fabrication of H-opaque masks was performed by means of e-beam lithography employing a Vistec EPBG 5HR system working at 100 kV. The fabrication was performed by our collaborator Dr. Giorgio Pettinari (Institute of Photonics and Nanotechnologies, National Research Council, Rome). The sketch of a typical mask design is shown in Fig. 3.1. The desired pattern (wine areas in the figure) is obtained by electron-irradiating the whole sample surface apart for the white areas visible in the figure (octagonal openings and corridors) where the domes will form upon H-ion irradiation. An electron dose of 300 μC/cm^2 was used for the patterning. The choice of realising octagonal openings rather than circular ones is aimed at reducing the e-beam lithography exposure time while still creating openings with a circular-like shape. After the electron exposure, the resist is developed in an aqueous solution of tetramethyl ammonium hydroxide at 2.4 % to remove the unexposed resist and leave the desired openings. The samples are then irradiated with H (or D) ions, and ordered arrays of isolated domes with different sizes can be created during

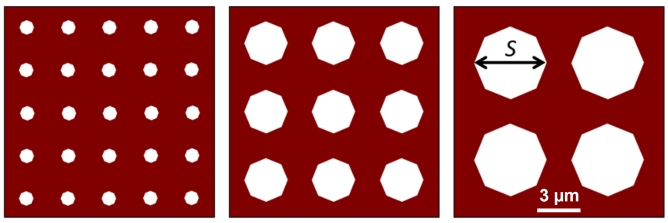

Figure 3.1: Sketch of a typical mask designed for patterning the samples: arrays of openings (in white) with different characteristics are arranged in different squares (in wine) with same dimensions. S indicates the diameter of the openings. The sketch here shown might represent a basic module to be repeated periodically all over the sample. Reproduced with permission from Ref. [171]

the same irradiation process. Fig. 3.2 shows the comparison between the AFM image of a flake with random MoS_2 domes, and the AFM images of MoS_2 domes formed in arrays of different size, with openings of size $S = 5$ μm, 3 μm, and 1 μm. This

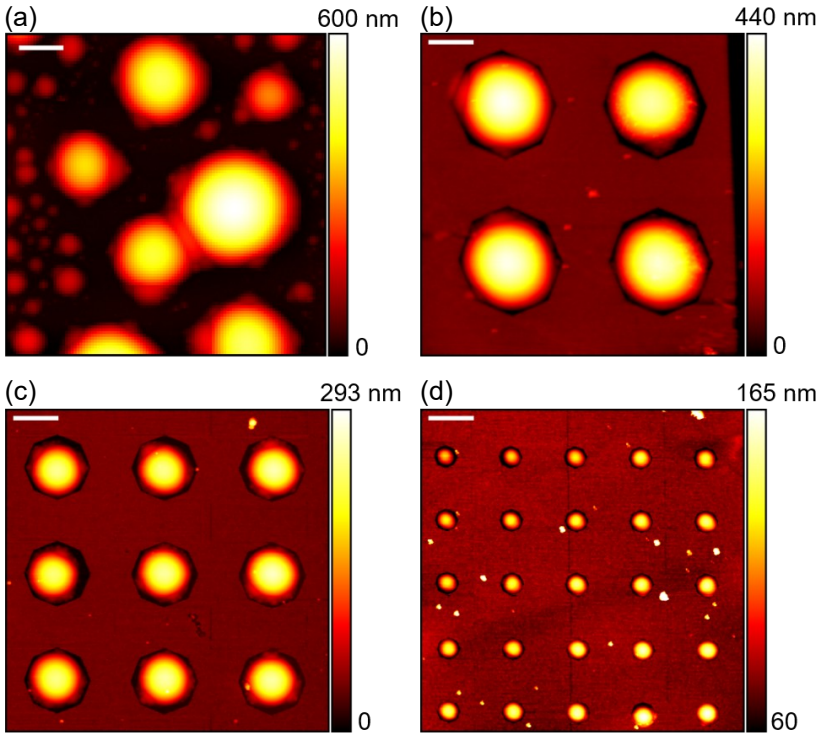

Figure 3.2: Formation of random and patterned MoS2 domes. (a) AFM image of a 15 × 15 μm^2 area of a proton-irradiated MoS_2 flake. (b-d) Same for MoS_2 flakes patterned with an 80-nm-thick mask with openings of size $S = 5$ μm (b), 3 μm (c), and 1 μm (d). The scalebars correspond to 2 μm, while the origin of the z axis is set at the flake surface. All panels are reproduced with permission from Ref. [171].

strategy allows us to create ordered arrays of domes with the desired size and in the desired position. Furthermore, the mask can also be removed by chemical etching in an aqueous solution of potassium borates at 5-15 % and potassium hydroxide at 2 %, which dissolves HSQ but does not attack the TMD sample. The AFM images of ordered arrays of WS_2 domes after HSQ removal are show in Fig. 3.3(a). Such an engineering process allows us to achieve ordered arrays of light emitters or of SHG hotspots. An example of a SHG map from an array of WS_2 domes is shown in Fig. 3.3(b).

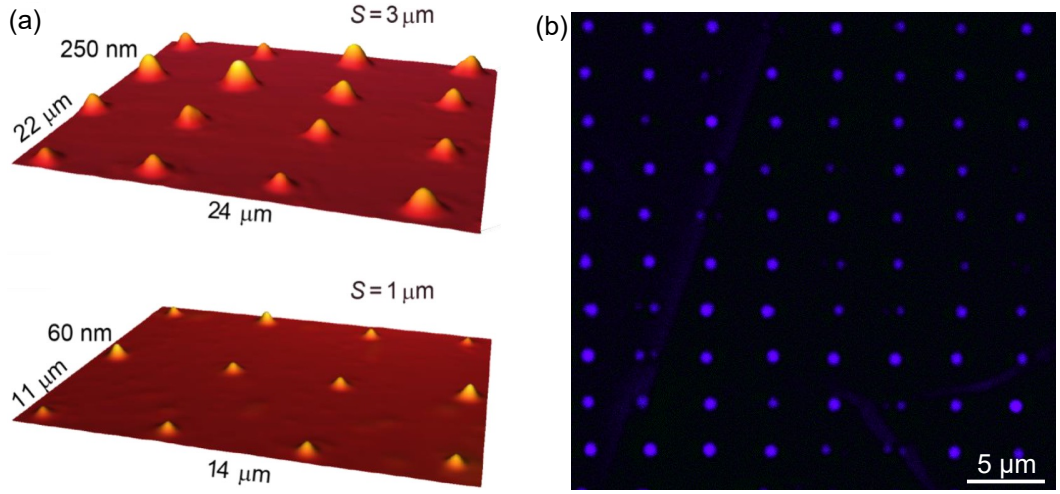

Figure 3.3: AFM images of two arrays of WS_2 domes with openings $S = 3$ μm (top) and $S = 1$ μm (bottom) obtained during the same H-ion irradiation process and acquired after the mask removal. The same aspect ratio (10:1) between horizontal and vertical scale is applied to both the upper and lower panel. (b) SHG map collected on an array of ordered WS_2 domes. All panels are reproduced with permission from D. Tedeschi, E. Blundo *et al.*, Adv. Mater. **31**, 1903795 (2019). [156]. Copyright 2019 WILEY-VCH Verlag GmbH & Co. KGaA, Weinheim.

Strain engineering

Indeed, the application of strain-engineering protocols to TMDs holds a great potentiality for optoelectronics, spin- and valley-tronics. Several methods for straining atomically thin materials have been developed, as previously shown in Fig. 0.7, including bending apparatuses, deposition on pillars, epitaxial growth of superlattices, and creation of bulges by means of specific devices, or spontaneous formation of domes [41]. Bulges or domes exploit the pressure exerted on the crystal by trapped gases and nowadays represent the most efficient method for achieving highly strained 2D membranes, also allowing a certain degree of control over the spatial distribution of the deformation [87, 112]. This is particularly relevant for ML-TMDs, where the creation of strain gradients leads to a seamless reduction of the band gap and can re-

sult in pseudo-gauge fields able to rule the quasiparticle motion [41]. In turn, stable and periodic strain modulations are promising for broadband light absorption and carriers' harvesting [78], and for the generation of persistent currents [231], which make them on the one side apt to photovoltaics, photocatalysis and photodetection devices, on the other side a fruitful platform for the observation of novel physical phenomena. However, the great promise of these systems is hindered by the fact that the durability of the bulges is limited to a few weeks [87], whilst the deformation of the domes is governed by energy minimisation [112, 116, 217], that establishes an upper bound for the achievable strains. Given the higher flexibility of our approach for the formation of domes, we moved a step further by developing a method to affect the strain distribution in order to achieve unprecedented periodic, durable and extremely high strain gradients. To do so, we tried to optimise the masking process and H-ion dose. We thus realised several HSQ resists different thicknesses in between 20 and 100 nm on MoS_2 bulk flakes. All the resists were having openings of size $S = 5$ μm, 3 μm, and 1 μm. We thus played with the H-ion dose during the irradiation process. In fact, domes with size smaller than the opening form if the H-ion dose is relatively low, while a high H-ion dose leads to the explosion of some domes. As an example, in Fig. 3.4(a), we show the AFM image of a dome formed in a sample patterned with a 30-nm-thick resist. First, the sample was irradiated with dose $d_0 = 5.5 \cdot 10^{16}$ ions/cm^2, resulting in the formation of domes still not filling the openings. A sketch of the irradiation process is also shown. The sample was then re-irradiated with dose $d_1 = 2.0 \cdot 10^{16}$ ions/cm^2, and the footprint of the domes was brought to nearly totally occupy the openings (see Fig. 3.4(b)). A comparison between the filling percentages after the first and second irradiation is shown in Fig. Fig. 3.4(c). Following this result, all the samples were irradiated with doses equal to $6 - 7 \cdot 10^{16}$ ions/cm^2, representing the best trade-off between high filling and high formation yield. The morphological properties of the domes were probed by AFM.

As theoretically predicted [112, 116, 165] and experimentally demonstrated [112, 116, 156, 167, 170, 171] atomically thin domes feature a universal aspect ratio (h_0/R, with h_0 maximum height and R footprint radius) which remains constant independently of the radius value. For MoS_2 random domes on MoS_2 flakes, the universal h_0/R value is $\sim 0.16 - 0.17$ [112, 116, 156]. We find the same average value for random domes (as exemplified by the dome whose profile is shown in Fig. 3.5(a), with $h_0/R = 0.165$) and for the patterned domes of Fig. 3.4, even when filling the openings, implying that a 30-nm-thick resist does not alter the mechanics of the formation process. Samples with thicker resists were then prepared: The three patterned domes in Figs. 3.5(b-d) were created in masks thicker than 50 nm, and have $h_0/R = 0.186$ ($S = 5$ μm, Fig. 3.5(b)), 0.219 ($S = 3$ μm, Fig. 3.5(c)), and 0.264 ($S = 1$ μm, Fig. 3.5(d)). Interestingly, in this case the mask acts as a strong constraint over the spontaneous formation of the domes and allows to overcome the natural, universal limit. This is particularly relevant because the higher the deformation, the higher the strain values and strain gradients. According to Hencky's model (see Eq. (1.1)), MoS_2 domes are characterised at the summit by a total in-

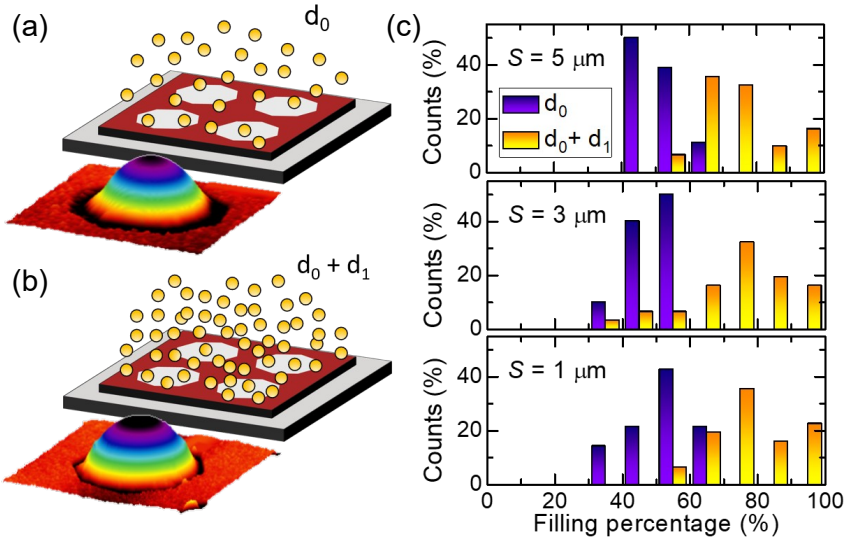

Figure 3.4: Optimisation of the proton-irradiation process. (a) Sketch of a patterned (wine area) sample (gray part) irradiated with protons (orange particles) with dose d_0. The inset is an AFM 3D image of a typical dome (in an opening with diameter $S = 5$ μm) formed in a sample patterned with a 30-nm-thick mask and irradiated with H-ion dose $d_0 = 5.5 \cdot 10^{16}$ ions/cm^2. The dome is not totally filling the opening, as demonstrated by the presence of the black region around the dome footprint. (b) Same as panel (a), but for the use of a higher proton dose $d_0 + d_1$, with $d_1 = 2.0 \cdot 10^{16}$ ions/cm^2. In this case, a typical dome (in an opening with diameter $S = 5$ μm) almost entirely occupies the opening. (c) Histograms of the filling percentages (footprint of the dome divided by the area of the opening) for the sample described in panel (a) after irradiation with ion dose d_0 (blue columns) and $d_0 + d_1$ (orange columns), for different opening sizes. Figure reproduced with permission from Ref. [171].

plane strain $\varepsilon_p = \varepsilon_r + \varepsilon_\theta = 2 \cdot f(\nu) \cdot (h_m/R)^2$, with $f(\nu) = 0.721$, while numerical methods have to be employed to calculate the strain field distribution across the dome surface. For this reason, FEM calculations were used to simulate the profiles of the domes. Details on such calculations are provided in Additional Material, sec. A3.

The simulated profiles are in good agreement with the AFM profiles, see Fig. 3.5(a-d). From the simulations, we can also derive the strain components [116, 156]. In the right panels of Figs. 3.5(a-d), we show the spatial distribution of the total in-plane strain ε_p associated to the domes in the left panels. Our calculations show how extremely high strains –larger than 10 %– are achieved for domes created in small openings ($S = 1$ μm). To our knowledge, such high strains, close to the rupture limit, could only be achieved so far by indentation of suspended monolayers [15] or with bulging devices [87], but in this latter case the structures are not durable [87, 143]. With our method, instead, the domes typically last for years [156]. The general validity of the results of Fig. 3.5(a-d) is confirmed by the AFM statistical analysis

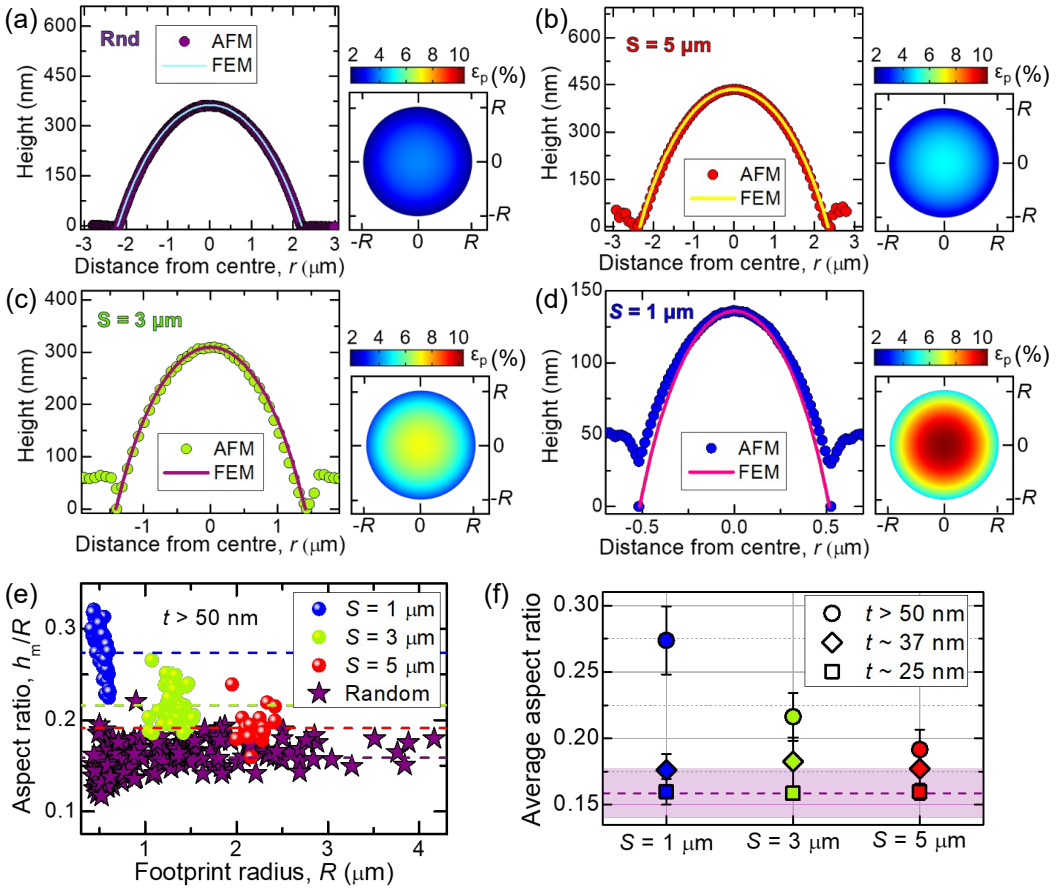

Figure 3.5: (a-d) Height profile and total in-plane strain in MoS_2 domes. Left panels: AFM profiles (coloured dots) along a diameter of a random (a), and three patterned domes created in openings with size $S = 5$ μm (b), $S = 3$ μm (c), and $S = 1$ μm (d). For the dome in panel (d) the AFM tip was not able to measure its base and the two points at 0 were set by measuring the thickness of the resist in a nearby corridor. The ratio between the vertical and horizontal axis is the same for the 4 plots, to emphasize the differences in the aspect ratios of the domes. The solid lines represent the profiles calculated via FEM simulations. Right panels: spatial distribution of the total percentage in-plane strain for the domes on the left, according to the colour bar displayed on top. The same scale has been used for the 4 plots. (e) Aspect ratios measured by AFM in patterned MoS_2 domes (openings with size $S = 1$ μm, blue dots; $S = 3$ μm, green dots; and $S = 5$ μm, red dots; resists with thickness 50 nm $< t <$ 100 nm), and on random MoS_2 domes (purple stars) as a function of the footprint radius. The coloured dashed lines highlight the average aspect ratios calculated for each set of data. (f) Average aspect ratio calculated by the data in panel (a) (circles) and in samples with thinner resists ($t = 37 \pm 6$, rhombi; $t = 25 \pm 5$, squares) for different sizes of the openings. The purple dashed line highlights the average aspect ratio measured for random domes, and the shaded area provides the associated uncertainty. All panels are reproduced with permission from Ref. [171].

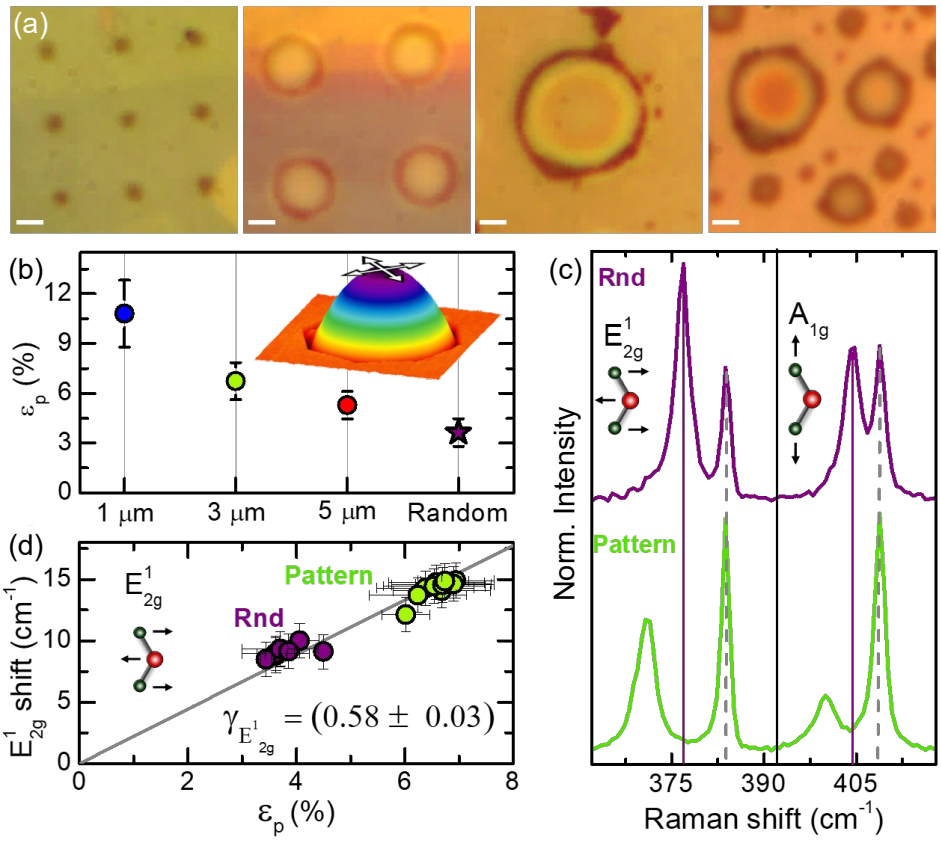

Figure 3.6: Micro-Raman measurements at the summit of random and patterned domes. (a) Optical images acquired with a 10× objective with NA=0.9 of (from left to right) patterned domes for $S = 1$ μm, for $S = 3$ μm, for $S = 5$ μm, and of random domes. The white scalebar is equal to 1.15 μm, that approximately corresponds to the size of our laser spot. (b) Average in-plane strain, ε_p, at the summit of patterned ($t > 50$ nm) and random domes, where strain is isotropic biaxial and reaches its maximum value. Inset: AFM 3D image of a patterned dome depicting the two in-plane strain components (white arrows) at the dome summit. (c) Raman spectra acquired at the summit of a patterned ($S = 3$ μm) dome (bottom, green) and of a random dome with similar radius (top, purple) in the region of the in-plane E^1_{2g} and out-of-plane A_{1g} modes. A sketch of the two vibrational modes is displayed as inset. The grey dashed lines highlight the position of the peaks originating from the bulk flake, while the peaks at lower energy with respect to the bulk modes originate from the domes. The purple lines are set in correspondence of the modes of the random dome, to highlight the redshift of the modes of the patterned dome. (d) Redshifts for the in-plane mode (see sketch as inset) with respect to an unstrained ML measured on top of several random (purple) and patterned (green, $S = 3$ μm) domes with analogous dimensions, plotted as a function of the estimated in-plane strain. The grey line is a linear fit to the data, leading to the Grüneisen parameter $\gamma_{E^1_{2g}}$ reported as inset. Figure reproduced with permission from Ref. [171].

of the aspect ratios shown in Fig. 3.5(e), performed on several flakes patterned with masks of thickness t between 50 and 100 nm, and on different samples. As a matter of fact, we obtain aspect ratios that range, on average, from 0.191 ± 0.015 for domes in openings with $S = 5$ μm, to 0.216 ± 0.018 for domes where $S = 3$ μm, to 0.274 ± 0.026 for domes where $S = 1$ μm, while in random domes we get 0.159 ± 0.018. Histograms from the data in Fig. 3.5(e) and their statistical analysis can be found in Additional Material, sec. A10. The average aspect ratio in patterned domes decreases to $\sim$0.18 (almost independently of S) for $t \sim$37 nm, to approach the universal value for $t \sim$25 nm (see Fig. 3.5(f)). Indeed, this effect is attributable to the mechanical constraint applied by the mask on the domes: If the mask is too thin, its contribution to the total energy of the system is negligible, so that the highly pressurised gas within the domes is able to raise the resist; if the mask it thick enough, its contribution is instead significant and the aspect ratio of the domes is increased. As a further proof of this statement, we used the AFM tip to apply an extra mechanical stress to a patterned dome ($S = 3$ μm) with $h_0/R = 0.206$, as discussed in more detail in Additional Material, sec. A10. By pushing down the tip, we induced a deflating process and separated the original dome in four smaller domes, all with an aspect ratio of about 0.16. Finally, by scanning the tip over the domes we were able to induce a coalescence phenomenon, resulting in the formation of a single dome. This dome has smaller dimensions than the original one due to the initial deflation, and $h_0/R = 0.169$, close the universal ratio (see Additional Material, sec. A10).

Indeed, the high aspect ratios obtained in thick masks lead to high strains, which should result in significant shifts of the Raman modes and exciton energies [41]. Therefore, μ-Raman measurements were here used to confirm the presence of high isotropic biaxial strains acting at the summit of domes patterned in thick resists, like those in Fig. 3.6(a). In Fig. 3.6(b), we show the average total in-plane strain at the summit of such domes ($\varepsilon_{\mathrm{p}}^{\mathrm{summit}}$, calculated via Hencky's model or, equivalently, by FEM calculations). While the structures created in openings with $S = 1$ μm have the largest aspect ratio —with $\varepsilon_{\mathrm{p}}^{\mathrm{summit}}$ on average equal to (10.8 ± 2.0) %—, the spatial resolution of our optical setup (our laser spot can be modelled as a gaussian with $\sigma = 0.23$ μm) is not enough to perform spatially-resolved optical measurements, as clear from Fig. 3.6(a), where the white scalebar corresponds to the size of the laser-spot. For this reason, domes in openings with $S = 3$ μm were chosen, as the best trade-off between high ratios and acceptable spatial resolution. In order to have a one-to-one comparison between the optical measurements in random and patterned domes, Raman spectra were acquired at the maximum symmetry point for the domes —*i.e.*, their summit— as in Ref. [87] for blisters. Fig. 3.6(c) shows a comparison between the μ-Raman spectrum acquired on top of a random dome (purple) and of a patterned dome (green), in the region of the in-plane $E_{2\mathrm{g}}^1$ and out-of-plane $A_{1\mathrm{g}}$ modes (see inset). The chosen random dome has diameter similar to the patterned dome. For each mode, the peaks at higher frequency —highlighted by dashed grey lines— originate from the bulk flake beneath the domes, while the lower-frequency peaks originate from the domes. Notably, Fig. 3.6(c) points to a

significant redshift of both the Raman modes in the patterned dome. To verify the consistency of our results with the measured aspect ratios, in Fig. 3.6(d) we plot the Raman redshifts for the E^1_{2g} mode (with respect to a strain-free ML) as a function of ε_p^{summit}, measured for several patterned domes ($S = 3$ μm) and random domes with similar dimensions. As expected, the tensile biaxial strain induces a softening of the modes that varies linearly with strain, with a redshift rate of (2.2 ± 0.1) cm^{-1}/% and a Grüneisen parameter $\gamma_{E^1_{2g}} = 0.58 \pm 0.03$. This result agrees well with previous estimations of $\gamma_{E^1_{2g}} = 0.57 \pm 0.11$ in Ref. [232], 0.68 in Ref. [87], and 0.73 in Ref. [233], thus providing further confirmation of the enormous strains achieved with our method.

Our approach indeed represents a versatile method to achieve high, stable strains, which are otherwise difficult to achieve. In Tables 3.1 and 3.2, we summarise the maximum strain values obtained for uniaxial and biaxial strains, respectively, in the literature, for different kinds of straining devices. Our results are highlighted in bold in Table 3.2. Indeed, remarkably high strain values are achieved in our case.

Table 3.1: Typical uniaxial strain values achieved by different devices and in different materials (BP stands for black phosphorus). For each work, the maximum strain achieved is displayed.

Ref.	material	strain	max. value (%)
	growth		
[234]	MoS_2	uniaxial	3.0
	bending devices[1]		
[235]	graphene	uniaxial	0.5
[236]	graphene	uniaxial	0.6
[233]	graphene	uniaxial	0.7
[237]	graphene	uniaxial	1.3
[230]	hBN	uniaxial	0.45
[235]	MoS_2	uniaxial	0.5
[238]	MoS_2/WS_2	uniaxial	0.7
[86]	WSe_2	uniaxial	3.6
[239]	WS_2, MoS_2, MoS_2/WS_2	uniaxial	0.6
[240]	$MoSe_2$, WSe_2, WS_2, MoS_2	uniaxial	1.5
[241]	MoS_2	uniaxial	0.8
[242]	WSe_2	uniaxial	2.0
[243]	MoS_2	uniaxial	2.4
[244]	MoS_2	uniaxial	0.4
[245]	MoS_2	uniaxial	1.9
[246]	MoS_2	uniaxial	1.5
[246]	WSe_2	uniaxial	1.7
[246]	WS_2	uniaxial	5.7
[247]	$ReSe_2$	uniaxial	-1.1
[248]	InSe	uniaxial	-0.62; +1.06
[249]	InSe	uniaxial	1.15
[250]	InSe	uniaxial	1.2
[251]	GaSe	uniaxial	0.7
[252]	BP	uniaxial	-0.3; +0.8
[253]	BP	uniaxial	0.85
[254]	BP	uniaxial	0.9
[255]	BP	uniaxial	$< \pm 5\%$
	stretching devices[1]		
[256]	MoS_2	uniaxial	0.5
[257]	WS_2	uniaxial	0.2
[258]	graphene	uniaxial	1.6
[259]	graphene	uniaxial	-0.15; +0.8

Table 3.2: Typical biaxial strain values achieved by different devices and in different materials (BP stands for black phosphorus). For each work, the maximum strain achieved is displayed. Our results obtained in patterned domes are displayed in bold.

Ref.	material	strain	max. value (%)
		growth	
[83]	WS_2/WSe_2	biaxial	1.4
[118]	WS_2	biaxial	-0.14; +0.94
		patterned substrates	
[260]	MoS_2	biaxial	0.6
[84]	MoS_2	biaxial	1.0
[125]	MoS_2	biaxial	0.5
[77]	WSe_2	biaxial	0.6
[261]	MoS_2	biaxial	1.35
[262]	MoS_2	biaxial	2.4
		stretching devices	
[85]	MoS_2	biaxial	0.64
[263]	MoS_2	biaxial	-0.2
[228]	hBN	biaxial	-0.13
[264]	InSe	biaxial	0.13
[265]	InSe	biaxial	-0.22; +0.23
		indenting devices	
[266]	graphene	biaxial	12-13
[56]	hBN	biaxial	6-7
[15]	MoS_2	biaxial	5-6
[267]	WSe_2	biaxial	3.7
[268]	$MoTe_2$	biaxial	5
[269]	BP	biaxial	4.6
[270]	Bi_2Se_3	biaxial	4
[271]	Bi_2Te_3	biaxial	1-2
		bulging devices	
[87]	MoS_2	biaxial	5.6
		blistering	
[166]	MoS_2	biaxial	~ 2
[272]	MoS_2	biaxial	2.1
[156]	MoS_2	biaxial	1.8
[156]	$MoSe_2$	biaxial	2.3
[156]	$MoTe_2$	biaxial	2.0
[156]	WS_2	biaxial	2.0
[156]	WSe_2	biaxial	1.6
[156]	WTe_2	biaxial	1.2
[171]	**MoS_2**	**biaxial**	**7.4**
		blistering+indenting	
[75]	**MoS_2**	**biaxial**	**$\sim$7-8**

Chapter 4

Strained domes as platforms to probe the mechanical and adhesive properties of van der Waals crystals

The outstanding mechanical performances of 2D materials make them appealing for the emerging fields of flextronics and straintronics. However, their manufacturing and integration in 2D crystal-based devices rely on a thorough knowledge of their mechanical properties. Generally, 2D materials can be deformed by in-plane stretching or by out-of-plane bending, thus requiring the introduction of both in-plane and bending moduli for an exhaustive description of their elasticity. On the other side, if 2D vdW materials have already revealed extraordinary potentialities per se, new rich scenarios are envisaged by creating 2D HSs. Peculiarly, 2D crystals bind together via weak vdW forces, and 2D HSs can be assembled layer-by-layer with unprecedented tunability [18]. The exploration of this wide field has just commenced, but has already led to intriguing results, among which the observation of unconventional superconductivity [273]; fascinating interaction effects between charge carriers [274–279]; and the realisation of high-quality devices [11, 18, 280–285]. The success or failure in exfoliating and assembling 2D materials depends on their elastic properties and on the strength of the reciprocal interaction between layers. The latter is quantified equivalently by the *exfoliation* or *adhesion* or *binding energy* γ, representing the energy cost to detach/stick a single layer from/onto a bulk crystal, or to bring all the layers of a crystal apart [286]. Despite its prominent relevance, the determination of γ still represents an issue.

In this Chapter, we will show how domes made of 2D materials are unique platforms to probe both the elastic properties of the materials and their vdW interaction with the underlying substrate.

4.1 Elasto-mechanical properties of 2D systems

The most used approach to probe the elasto-mechanical properties of crystals is through nano-indentation experiments performed with an AFM.

In the case of thin sheets, the latter are typically suspended over lateral supports like beams or over circular apertures, and an AFM tip is usually employed to elastically deform the sheet. From a practical point of view, the realisation of a circular-plate membrane typically entails the transfer [15, 287–291] or the mechanical exfoliation [144, 266, 292–294] of the 2D material on top of a substrate, previously patterned with cylindrical holes. Similarly, the fabrication of doubly-clamped beams can be obtained by mechanically exfoliating the 2D material on top of patterned trenches [295], or in more elaborated ways, requiring the 2D material to be first sandwiched in between PMMA layers [296] or SiO_2 and metal electrodes [297], and subsequently exposed to e-beam lithography or local etching. The suspended membranes are then subjected to local nano-indentations.

In the framework of very thin plates under large deformations [298, 299], Föppl and von-Kármán wrote a system of coupled, non-linear, partial differential equations, establishing the relationship between the following quantities: deflection of the plate, stress σ, stretching or Young's modulus of the material Y, geometrical dimensions of the plate (size and thickness t), applied load, and bending modulus or flexural rigidity $D = \frac{Yt^3}{12(1-\nu^2)}$ (where ν is the Poisson's ratio of the material). Generally, the thinner the plates, the weaker the bending/flexural contribution to the deformation. The effect of the bending modulus may thus become substantial only in the case of a multilayer structure: increasing the number of layers would indeed cause a transition from the membrane-like to the linear plate-like behavior [217, 300, 301]. The elasticity of single layers of 2D materials is thus often characterised by neglecting the bending contribution and thus by limiting the discussion exclusively to the stretching modulus E_{2D} (or equivalently to Y, being $E_{2D} = Yt$).

Relatively recent theoretical and experimental studies on the mechanical properties of 2D materials have largely pointed out a clear dependence of their elasticity on the extent of the applied load. For instance, first principle calculations have predicted graphene to exhibit a linear (nonlinear), anisotropic behavior of its stress-strain (σ - ε) diagram when subjected to very small (large) deformation, with the threshold being predicted at a $\varepsilon \sim 5\%$ [302–304]. On the other hand, most 2D materials exhibit a linear, isotropic elastic response to small deformations, with the tendency to exert a reduced stiffness for large tensile strains [305, 306]. Under moderate to large deformations (but lower than the fracture point occurring at the intrinsic stress σ_{int}), the continuum thin shell theory establishes the following constitutive relation:

$$\sigma = E_{2D}\varepsilon + d\varepsilon^2, \tag{4.1}$$

where the coefficient d of the second-order term is expected to be negative, thus reproducing the tendency to exhibit a reduced stiffness with increasing the tensile

strain ε. The intrinsic strength and associated strain are thus defined as:

$$\sigma_{\text{int}} = -\frac{E_{\text{2D}}^2}{4d}, \tag{4.2}$$

$$\varepsilon_{\text{int}} = -\frac{E_{\text{2D}}}{2d}. \tag{4.3}$$

The elastic response of 2D material is typically probed by AFM nano-indentation studies. In such tests, the nanometre-sized indenter, the AFM probe, is moved with the typical AFM lateral resolution (∼nm) on selected areas of interest. A local nano-indentation is thus performed by loading the 2D membrane with a controlled force (with sub-nN resolution). The membrane displacement, due to the applied load, is measured simultaneously. The so-called loading force *vs* distance curves (FDCs) are then recorded, exploiting the elastic response of the membrane in a $\sigma - \varepsilon$ -like diagram, with the strain being proportional to the membrane displacement caused by the applied load (stress). Finally, the material mechanical properties are extracted by fitting the measured FDCs to a suitable analytical model. All the nano-indentation experiments discussed in this Chapter were performed by Dr. Cinzia Di Giorgio and Prof. Fabrizio Bobba (Physics Department, University of Salerno, Fisciano, Italy). The analytical modelling of the nano-indentation experiments and related data interpretation were performed by Dr. Cinzia Di Giorgio and the candidate.

Nano-indentation of suspended membranes

This section will introduce the reader to nano-indentation experiments on suspended membranes. Starting from the theoretical and experimental background herein discussed, in the next section we will focus on nano-indentation experiments on the domes.

Upon mechanical modelling —typically taking as a starting point the Landau's theory of elasticity and the Föppl–von-Kármán equations [298, 307]— the relation between loading force F and membrane displacement δ (*i.e.*, the distance between the final position and the initial position of the indented membrane in correspondence of the indentation point) in nano-indentation experiments features linear ($F_{\text{linear}} = A\delta$) and cubic ($F_{\text{cubic}} = B\delta^3$) terms. This holds true both in the case of doubly-clamped beams and clamped circular thin plates, subjected to a point force at their centre, resulting in a FDC described by:

$$F = A \cdot \delta + B \cdot \delta^3. \tag{4.4}$$

The coefficients A and B can be expressed in terms of the relevant geometrical and physical quantities of the system, and they provide information on (i) the Young's modulus Y of the material; (ii) the pre-tension (T) of the membrane.

The explicit force-displacement relations for circular suspended and doubly-clamped membranes are thus given by Eqs. (4.5) [300] and (4.6) [269], respectively:

$$\text{Circular drum}: \quad F(\delta) = \left[\frac{4\pi Yt}{3(1-\nu^2)}\left(\frac{t}{R}\right)^2 + \pi T\right]\delta + \frac{q^3 Yt}{R^2}\delta^3, \tag{4.5}$$

$$\text{Beam}: \quad F(\delta) = \left[\frac{\pi^4 wYt^3}{6L^3} + \frac{T}{L}\right]\delta + \frac{\pi^4 wYt}{8L^3}\delta^3, \tag{4.6}$$

where R is the radius of the hole, q is a constant depending on the Poisson's ratio as $q = 1/(1.04912 - 0.14622\nu - 0.15827\nu^2)$ [308], w and L are the width and length of the suspended part of the stripe, and t is the membrane thickness. It is worth noticing that Eq. (4.6) has also been used for suspended nanoribbons [309].

In the case of both Eq. (4.5) and Eq. (4.6), the three terms on the right-hand side of the equation correspond to the bending, pre-tension and stretching contribution to the elastic response of the 2D membrane, respectively. In the limit of small indentations, $\delta < t$, the bending contribution dominates the elastic behaviour. However, as soon as the indentation depth increases, the stretching term becomes more and more significant, so that, when $\delta \gg t$, the bending term can be neglected and Eqs. (4.5) and (4.6) can be re-written as:

$$\text{Circular drum}: \quad F(\delta) = \pi T\delta + \frac{q^3 Yt}{R^2}\delta^3, \tag{4.7}$$

$$\text{Beam}: \quad F(\delta) = \frac{T}{L}\delta + \frac{\pi^4 wYt}{8L^3}\delta^3. \tag{4.8}$$

It is worth mentioning that Eqs. from (4.5) to (4.8) are modelled in the ideal case of a point load, or zero-size indenter. Vella *et al.* [307] derived the corresponding behavior of F *vs* δ in the case of a finite size indenter, R_{tip}, indenting on a circular clamped plate of footprint radius R, in the limit $R_{\text{tip}} \ll R$. The authors calculated the explicit expression of $F(\delta)$ in the limit of small and large indentations, as well as in the intermediate regime, demonstrating that the simple algebraic sum of linear and cubic terms can often lead to inaccuracies in the estimated values of $E_{2\text{D}}$ and T. They found the following F *vs* δ relations:

$$\text{Small indentation}: \quad F(\delta) = \frac{2\pi T^{\frac{1}{2}}}{log\left(\frac{R}{R_{\text{tip}}}\right)}\delta \tag{4.9}$$

$$\text{Intermediate indentation}: \quad F(\delta) = \frac{2\pi T^{\frac{1}{2}}}{log\left(\frac{4RT^{\frac{1}{2}}}{\delta E_{2\text{D}}^{\frac{1}{2}}}\right)}\delta \tag{4.10}$$

$$\text{Large indentation}: \quad F(\delta) = \frac{E_{2\text{D}}^{\frac{1}{2}}}{R^2}\delta^3 + O\left(\frac{R_{\text{tip}}}{R}\delta^3\right) \tag{4.11}$$

for small, intermediate and large indentation regime, respectively.

The relation between the indentation load F and displacement δ can be thus recorded by performing local AFM nano-indentations on the free-standing areas, and the elastic parameters of interests of the 2D material can be extracted by fitting the measured FDC with the appropriate analytical model.

The AFM indentation experiments on free-standing 2D membranes were first pioneered by Lee *et al.* [266], who investigated the elastic properties and intrinsic strength of mechanically exfoliated graphene, highlighting an impressive Young's modulus of $Y \sim 1$ TPa ($E_{2D} \sim 330$ N/m) [310]. Since that pioneering work, the AFM nano-indentation of free-standing membranes has become a standard tool to investigate the elasticity of 2D materials, their fracture strength and the correlation between mechanics and nanoscale defects.

Figure 4.1(b) and Table 4.1 summarise the elastic moduli of many different 2D materials, found by using nano-indentation methods, both in the single-layer and few layer limits. Results from the analysis of the wrinkle profiles [311] and of a few other more complicated methods, including bimodal AFM-based techniques [312] or mechanical resonance measurements [313], have been also included. Indeed, the values measured by different groups and using different techniques for a same material are generally in good agreement with each other.

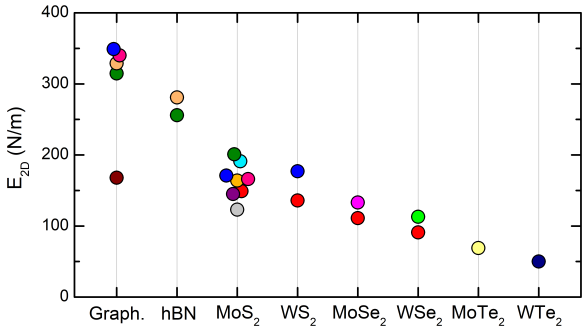

Figure 4.1: Elastic moduli measured experimentally (see Table 4.1) for the most common 2D materials, including graphene, hBN, and TMDs. All TMDs are in the 2H phase, but for WTe_2 which is in the $1T_d$ phase. These data were measured in Refs. [314] (blue), [266] (pink), [315] (olive), [295] (wine), [56] (light-pink), [300] (cyan), [312] (yellow), [15] (purple), [311] (red), [75] (orange), [305] (grey), [316] (magenta), [317] (green), [268] (light-yellow) and [313] (navy). Whenever E_{2D} was measured for different layer thicknesses, a weighted average of the measured values was here considered. Reprinted with permission from C. Di Giorgio, E. Blundo *et al.*, Adv. Mater. Interfaces **9**, 2102220 (2022) [76]. Copyright 2022 The Authors.

Additionally, AFM-based nano-indentation can be a valuable tool to evaluate the fracture strength of 2D materials [266]. The fracture stress and strain values obtained for different 2D materials are also summarised in Table 4.1.

Table 4.1: 2D Young's moduli (E_{2D}) and fracture (or intrinsic) stress (σ_{int}) and strain (ε_{int}) of graphene, hBN and TMDs measured by exploiting mechanical deformations (the specific system used in each work is given). E_{2D} and σ_{int} are calculated for a 1L-thick membrane as $E_{2D}^{1L} = E_{2D}/N$ and $\sigma_{int}^{1L} = \sigma_{int}/N$, where N is the number of layers, in order to have a direct comparison between the displayed values. It should be noticed that different values of the Poisson's ratio ν were used in different works. To have a direct comparison, here we re-scaled some of the values in order to use always the same ν value (displayed in the table) for a given material. As a consequence, the values displayed here might differ slightly from those reported in the original works. The following single-layer thicknesses were considered: $t = 0.625$ nm for TMDs, $t = 0.335$ nm for graphene, $t = 0.333$ nm for hBN. "Ind." stands for "indentation".

Material	Ref.	System	Thickness	E_{2D}^{1L} (N/m)	σ_{int}^{1L} (N/m)	ε_{int} (%)
Graphene ($\nu = 0.165$)	Frank *et al.* [295]	Beam - Indentation	6L-24L	168	/	/
	Wang *et al.* [74]	Blister - Mechanics	10L-70L	314.7 ± 7.3	/	/
	Lee *et al.* [266]	Circ. Drum - Ind.	1L	340 ± 50	43.6 ± 3.4	25
	Falin *et al.* [56]	Circ. Drum - Ind.	1L	342 ± 8	41.9	/
			2L	323 ± 8	36.1 ± 1.5	/
			3L	328 ± 3	35.4 ± 2.0	/
			8L	/	28.6 ± 1.8	/
	Liu *et al.* [314]	Circ. Drum - Ind.	1L	349 ± 12	/	/
hBN ($\nu = 0.223$)	Wang *et al.* [74]	Blister - Mechanics	10L-70L	255.9 ± 4.3	/	/
	Falin *et al.* [56]	Circular Drum	1L	287 ± 24	23.5 ± 1.8	∼ 17
			2L	293 ± 19	22.6 ± 2.3	/
			3L	272 ± 15	25.6 ± 0.8	/
MoS_2 ($\nu = 0.250$)	Cooper *et al.* [305]	Circ. Drum - Ind.	1L	123 ± 31	16.5	/
	Iguiñiz *et al.* [311]	Wrinkles	3L-11L	149 ± 21	/	/
	Di Giorgio *et al.* [75]	Dome - Ind.	1L	164 ± 39	> 15	> 12
	Li *et al.* [312]	Bimodal AFM	1L	166 ± 8	/	/
	Liu *et al.* [314]	Circ. Drum - Ind.	1L	171 ± 11	/	/
	Bertolazzi *et al.* [15]	Circ. Drum - Ind.	1L	183 ± 61	15 ± 3	6-11
		Circ. Drum - Ind.	2L	132 ± 35	14 ± 4	6-11
	Castellanos-Gomez *et al.* [300]	Circ. Drum - Ind.	5L-25L	191 ± 40	/	/
	Wang *et al.* [74]	Blister - Mechanics	10L-70L	200.9 ± 5.4	/	/
WS_2 ($\nu = 0.217$)	Iguiñiz *et al.* [311]	Wrinkles	3L-8L	136 ± 37	/	/
	Liu *et al.* [314]	Circ. Drum - Ind.	1L	177 ± 12	/	/
$MoSe_2$ ($\nu = 0.239$)	Iguiñiz *et al.* [311]	Wrinkles	5L-10L	133 ± 24	/	/
	Yang *et al.* [316]	Beam - Stretching	1L	111.9 ± 4.6	1.9 ± 0.4	(1.7 ± 0.4)
			2L	110.2 ± 5.5	3.5 ± 1.8	(3.2 ± 1.8)
WSe_2 ($\nu = 0.196$)	Iguiñiz *et al.* [311]	Wrinkles	4L-9L	91 ± 22	/	/
	Zhang *et al.* [317]	Circ. Drum - Ind.	5L	115.5 ± 4.5	> 43	> 7.3
			6L	111.4 ± 4.0	/	/
			12L	113.9 ± 4.9	/	/
			14L	111.7 ± 3.9	/	/
2H-$MoTe_2$ ($\nu = 0.235$)	Sun *et al.* [268]	Circ. Drum - Ind.	5-6L (3.6 nm)	56	4.5	8.3
			9-10L (6.0 nm)	72	4.4	6.2
			10-11L (6.7 nm)	63	2.8	4.6
1T-$MoTe_2$ ($\nu = 0.235$)	Sun *et al.* [268]	Circ. Drum - Ind.	14-15L (9.0 nm)	66	1.7	2.7
			17-18L (11.0 nm)	62	1.6	2.6
T_d-$MoTe_2$ ($\nu = 0.235$)	Sun *et al.* [268]	Circ. Drum - Ind.	16-17L (10.5 nm)	66	2.0	3.1
			20-11L (13.0 nm)	65	2.0	3.2
			22-23L (14.0 nm)	55	1.4	2.5
T_d-WTe_2 ($\nu = 0.16$)	Lee *et al.* [313]	Nanoresonator	12L-43L	∼ 50	/	/

Nano-indentation of micro-domes

The previous section introduced the AFM nano-indentation of free-standing membranes of 2D materials. However, in many cases the membrane is also subjected to a constant pressure difference, Δp, as in domes/blisters of micrometric and submicrometric size. When indenting on a bulged, pressurised membrane, the role of the inner pressurised gas cannot be neglected in the evaluation of the elastic response of the 2D material. By modeling the AFM tip as a finite indenter of radius $R_{\text{tip}} \ll R$, where R is the membrane footprint radius, exerting a normal load on the top of the pressurised domes, the problem of indentation on the clamped, pressurised and pre-tensed membrane can be written by incorporating the differential pressure $\Delta p = p - p_0$ —where p and p_0 are the internal and external pressure, respectively— in the normal force balance equation [307]:

$$\psi(r)\frac{\mathrm{d}\zeta}{\mathrm{d}r} = \frac{F}{2\pi} - \frac{\Delta p}{2}r^2, \tag{4.12}$$

where $\psi(r)$ is the Airy stress function, related to the radial and circumferential stress components as $\sigma_r = \psi/r$ and $\sigma_\theta = \mathrm{d}\psi/\mathrm{d}r$, and $\zeta(r)$ is the out-of-plane membrane displacement due to the simultaneous action of indentation force F and internal pressure. Eq. (4.12) can be solved numerically, together with the strain compatibility equation:

$$r\frac{\mathrm{d}}{\mathrm{d}r}\left[r\frac{\mathrm{d}(r\psi)}{\mathrm{d}r}\right] = -\frac{1}{2}E_{2\mathrm{D}}\left(\frac{\mathrm{d}\zeta}{\mathrm{d}r}\right)^2, \tag{4.13}$$

with boundary conditions $\zeta(r \leq R_{\text{tip}}) = h_0 - \delta$, and $\zeta(R) = 0$. This equation sets the unique relation between the stress and the out-of-plane displacement, through the stretching modulus, or 2D Young's modulus, $E_{2\mathrm{D}}$. Here, the indentation depth δ is the contribution to the normal membrane displacement due to the action of the external load, and a spatially uniform deformation depth $h_0 - \delta$ is assumed at any distance $r \leq R_{\text{tip}}$ during the AFM indentation.

Solutions to Eqs. (4.12) and (4.13) can be sought numerically in the limits of small and large indentations, leading again to $F = k\delta$ (linear regime) and $F = \alpha\delta^3$ (cubic regime). Here:

$$k = \frac{2\pi A_\tau (\Delta p R)^{\frac{2}{3}} E_{2\mathrm{D}}^{\frac{1}{3}}}{log(\frac{R}{R_{\text{tip}}})}, \qquad \alpha = \mathfrak{f}\left(\nu, \frac{R_{\text{tip}}}{R}\right)\frac{E_{2\mathrm{D}}}{R^2} \tag{4.14}$$

where A_τ is a function of the Poisson's ratio ν and $\mathfrak{f}$ indicates a function of ν and R_{tip}/R. It is worth noticing that, differently from indentation on free-standing membranes, the linear stiffness k depends on $E_{2\mathrm{D}}$, as well as on the pressure Δp. Upon analytical modelling (as we will demonstrate later on in this chapter), it can be shown that the inner pressure of pressurised domes/blisters is related to their

height and radius through this relation:

$$h_0 = A_h \left(\frac{\Delta p R^4}{E_{2D}} \right)^{\frac{1}{3}}, \tag{4.15}$$

where A_h is a function of Poisson's ratio. By putting Eqs. (4.14) and (4.15) together, one can demonstrate that the knowledge of both the height of the dome (before AFM indentation) and its stiffness (*i.e.*, the slope of the FDC in the small indentation range) is sufficient for both p and E_{2D} to be inferred [75, 307]. Indeed, one can find:

$$E_{2D} = log \left(\frac{R}{R_{tip}} \right) \frac{A_h^2 R^2 k}{2\pi A_\tau h_0^2}, \tag{4.16}$$

$$\Delta p = log \left(\frac{R}{R_{tip}} \right) \cdot \frac{h_0 k}{(2\pi A_h A_\tau R^2)}. \tag{4.17}$$

The signature of being in the small indentation regime is given by an approximately constant behaviour of the linear stiffness k (*i.e.*, linear behaviour of the loading force curve). Fig. 4.2 shows the results of nano-indentation experiments on both random and engineered domes (refer to Fig. 3.2), and validates the condition of being in the small indentation regime. As sketched in the inset, during a nano-indentation experiment, a loading force is applied along the normal direction after positioning the AFM tip on the top of the dome, and force-distance curves are recorded on each selected membrane. The main panel of Fig. 4.2(a) shows three typical loading force curves measured on big (red, corresponding to a mask opening size $S = 5$ μm), medium (orange, $S = 3$ μm) and small (blue, $S = 1$ μm) engineered domes, where the indentation depth δ is normalised to the maximum dome height (h_0). A loading force as high as 500 nN is applied, and an indentation depth of about 8 %, 12 %, and 17 %, is reached for big, medium, and small domes, respectively. The black dashed lines represent their linear fits, having relative errors of 0.05 %, 0.06 % and 0.19 %, respectively. These very small values confirm the accuracy of the linear fitting model with respect to the experimental behaviour. A slight increase of the relative error is found as the dome size shrinks, indicating that the nonlinearity arises at lower forces in smaller domes. On the other hand, Fig. 4.2(b-d) compares indentation experiments performed on big (b), medium (c), and small (d) engineered and spontaneous domes (the latter having footprint radii close to the three engineered cases, and differing by 1 %, 9 % and 16 %, respectively), by employing a maximum loading force of 100 nN. In the case of spontaneous domes, we avoided applying higher loads to prevent potentially irreversible situations from occurring, such as the splitting and slipping of the domes. Indeed, spontaneous domes can move under the AFM solicitation by profiting of a local delamination of the top-most layer at the unconstrained edge. In this scenario, the presence of the HSQ coating, surrounding the engineered domes, guarantees higher stability under the external load. Experimental loading force curves measured on engineered and spontaneous domes are plotted in Fig. 4.2(b-d) as black and red dots, respectively. One

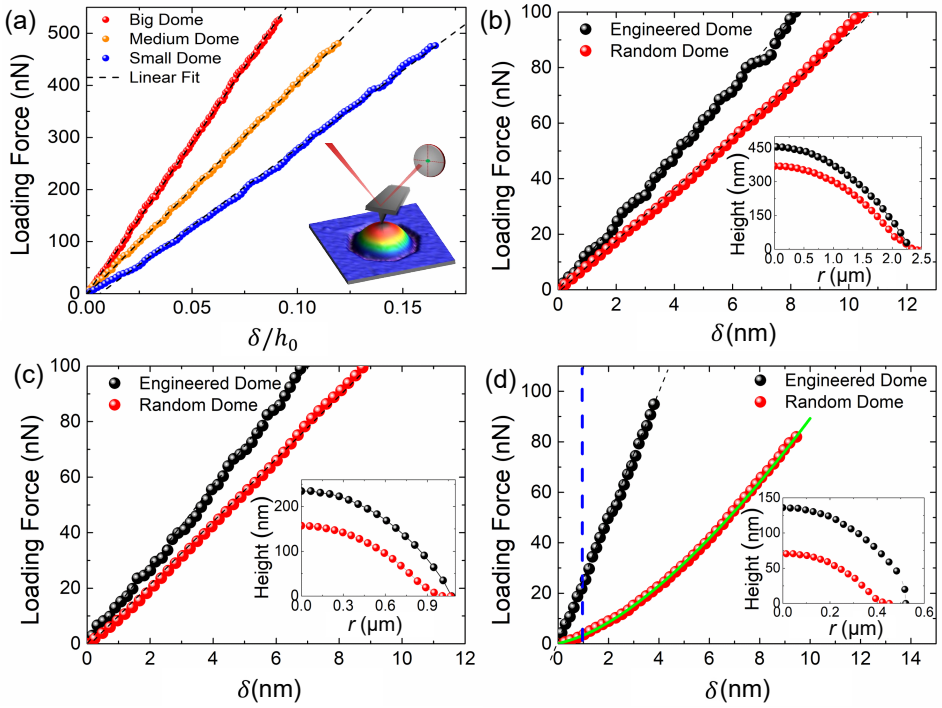

Figure 4.2: (a) Main: Three typical loading force curves measured on big (red), medium (orange), and small (blue) engineered domes. Black dashed lines are their linear fits. Inset: sketch of the AFM nano-indentation experiment; a loading force is applied through the AFM probe at the dome summit. (b–d) Main: loading force curves acquired on big, medium, and small engineered (black dots) and spontaneous (red dots) domes. Insets: Corresponding height profiles of the engineered (black) and spontaneous (red) domes. (d) Blue dashed line: threshold depth between linear and nonlinear regime. Green solid line: fit of the loading force curve by Eq. (4.18). Figure adapted with permission from C. Di Giorgio *et al.*, Adv. Mater. Interfaces **7**, 2001024 (2020) [75]. Copyright 2020 Wiley-VCH Verlag GmbH & Co. KGaA, Weinheim.

can notice that (i) engineered domes are, in general, stiffer than spontaneous ones (the same loading force leads to a higher indentation depth in spontaneous domes), pointing toward a lower pressurisation in the latter; (ii) in the linear regime, the loading force required to achieve a certain indentation increases as the dome size decreases (which, given the same elastic properties of the MoS_2 membrane, would be qualitatively consistent with an increase of the H_2 pressure); (iii) a nonlinearity is easily reached in small-size spontaneous domes. The arise of such a nonlinear behavior indicates that, in the investigated case (spontaneous dome with $h_0 = 69$ nm, $R = 437$ nm, $h_0/R = 0.157$), the range of indentation depth, achieved by using a loading force of 80 nN ($\delta/h_0 = 14\%$), covers the intermediate regime (between large and small indentation).

Figures 4.3(a) and (b) show the distribution of both p and E_{2D}, obtained by performing small range indentations on MoS_2 domes, and by fitting the results with

$F = k\delta$. By combining the knowledge of k, and that of the system geometrical parameters h_0 and R, we used Eq. (4.16) and (4.17) to quantify E_{2D} and p in two different species of domes [75]. Red stars correspond to the nano-indentations performed on domes produced randomly by H-ion irradiation of a MoS_2 bulk crystal. Black scatters result from the indentation of engineered domes produced on demand, with a full control of their lateral size and distribution on top of the sample surface [75, 156]. The measured values of E_{2D} fully lie in the expected range of MoS_2 Young's modulus, highlighted by the yellow region in Fig. 4.3(b) (see also Table 4.1), while the estimated p (Fig. 4.3(a)) discloses an increasing trend as the size of the domes is reduced. A similar approach was used by Tan *et al.* [318] to measure the contents, thickness, and internal pressure of MoS_2 nanoblisters, fabricated by electrochemical water splitting, and by Khestanova *et al.* [112] in domes formed spontaneously in mechanically exfoliated graphene and MoS_2 by trapping of contaminants. To achieve

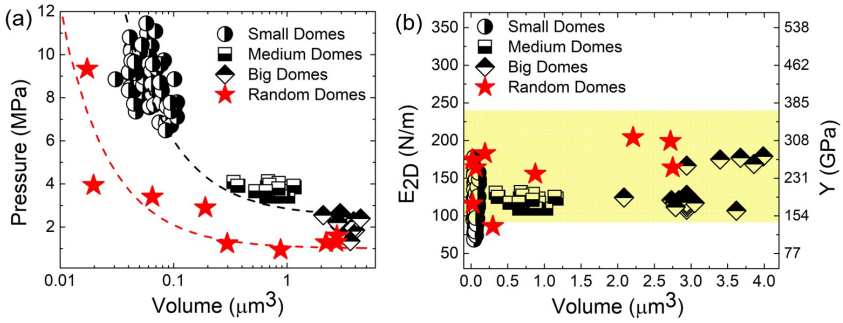

Figure 4.3: (a) H_2 pressure *vs* volume for engineered (half-black scatters) and spontaneous (red stars) domes. Black and red dashed lines work as a guide for the eye to follow the behavior of p versus V. (b) Stretching modulus E_{2D} *vs* V for engineered (half-black scatters) and spontaneous (red stars) domes. The yellow area highlights the range of E_{2D} values reported in literature for the MoS_2 monolayer. Panels (a-b) reprinted with permission from C. Di Giorgio *et al.*, Adv. Mater. Interfaces **7**, 2001024 (2020) [75]. Copyright 2020 Wiley-VCH Verlag GmbH & Co. KGaA, Weinheim.

more information on the nonlinear regime and on the robustness of the domes, we performed further studies by fully indenting our structures, *i.e.*, by pushing the tip down until the tip/membrane system reached the bulk flake underneath [319]. Fig. 4.4(a) shows the AFM image of an array of engineered domes created in openings with size $S = 1$ μm. All the domes in the array (54 in total) were subjected to a full indentation process, after which almost all the domes remained intact and unvaried. Panel (b) shows the AFM image of the same array after the indentation, showing how only three domes were irreversibly damaged due to the indentation. This attests the incredible robustness of the domes and the remarkable elasticity of the system. It should be noticed that to perform such a full indentation experiment, domes created in ordered arrays needed to be exploited. This was essential, since random ones (*i.e.*, not contained within openings) slide during indentations, thus not enabling to perform a full indentation procedure [319]. Fig. 4.4(c) shows typical loading

(black) and unloading (red) FDCs acquired in a full indentation process. Indeed, the data deviate from the linear behaviour, though the cubic regime predicted for large indentations is actually never reached. The transition between linear and non-linear behavior is indeed clearly observed, as a consequence of moving from the small to the intermediate indentation range. Since the transition region between small and large indentation depths is hard to model analytically, it is a common use to fit such an intermediate regime, with a sum of the asymptotic models obtained in the small and large indentation limits. However, Vella *et al.* have shown that this approach can lead to large errors, especially as the indenter size shrinks [307]. To avoid fitting inaccuracies in the estimate of the system properties, we thus developed a different fitting approach, based on the combination of linear ($F_L = k\delta$) and nonlinear ($F_{NL} = \alpha\delta^{\omega}$) components, both weighted by the Heaviside function $\Theta(\delta - \delta_{\mathrm{T}})$, with δ_{T} being the depth threshold between the linear and nonlinear regime, at small and intermediate indentation depths, respectively:

$$F(\delta) = k\delta \cdot [1 - \Theta(\delta - \delta_{\mathrm{T}})] + [k\delta_{\mathrm{T}} + \alpha(\delta^{\omega} - \delta_{\mathrm{T}}^{\omega})] \cdot \Theta(\delta - \delta_{\mathrm{T}}). \tag{4.18}$$

The stiffness k, the parameter α, the exponent ω, and the threshold δ_T are used as fitting parameters of the measured FDCs. The green solid line in Fig. 4.4(c) is the fitting the approach FDC through Eq. (4.18). The fit, performed from the tip-membrane snap-to-contact (indicated as feature (1)) to feature (2), agrees with the measured behavior by introducing a non-linearity of $\omega = 1.3$, arising at $\delta = (17.1 \pm 0.3)$ nm. Feature (2) consists in a sharp variation in the FDC, with a decrease in the loading force as δ increases. We ascribe this behaviour to the emergence of vdW interactions between the dome membrane and the bulk MoS_2 substrate underneath. The vertical behavior of the FDC at feature (3) corresponds instead to the indentation of the bulky substrate, reached after the AFM tip has travelled through the dome by a distance equivalent to its height. Importantly, no irreversible changes are induced in the dome by the indentation operation, as the unloading curve aligns back to the loading one. The origin of the hysteresis observed between the two curves is attributed to the adhesion between the dome membrane and the bulky substrate and will be further discussed in section 4.2.

4.2 Adhesive properties of van der Waals materials

Blisters and domes represent excellent candidates to probe not only the elastic properties of the 2D membrane, but also vdW adhesion forces.

This is particularly relevant because such forces rule the fundamental physics of layered materials: if graphene and other 2D materials could be isolated, it is thanks to the fact that the different layers are kept together by weak vdW forces. Despite the importance of vdW adhesion, its experimental quantification remained prohibitive for a long time. Previous studies of the morphology of carbon nanotubes enabled its quantification for graphite [320]. That method, however, is not readily applicable to other materials. Theoretically, γ was also quantified for graphite by

molecular dynamics [321], but the difficulty in finding proper potentials to model more complex structures prevented their use for other crystals. Indeed, density functional theory (DFT) calculations allowed for its estimation [286, 322], but the coexistence of weak vdW and strong covalent bonds did not allow for an accurate material-dependent characterisation. Experimental methods to probe the vdW adhesion based on blisters and domes started to be developed [114, 116, 319, 323–325]. Here, we discuss different approaches that we developed, based on the morphological study of the domes, to obtain precious information on the vdW adhesion.

4.2.1 Nano-indented domes

An interesting method based on blisters to probe the adhesion between a 2D membrane and a metallic or Si-based surface was developed by Liu *et al.* [325]. Their studies relied on the design of blisters with a particular geometry. In particular, graphene flakes were in this case suspended over an annular ring etched into a silicon oxide wafer (bare SiO_x or gold-coated SiO_x). Differently from the usual blisters, in this case the circular cavity contains a cylindrical post at its centre, so that, if the device is only weakly pressurised, the graphene sheet remains adhered to the inner post and deforms in a donut shape. Interestingly, at sufficiently high Δp, the force is large enough to overcome the adhesion energy of the graphene flake to the inner post, and the graphene membrane delaminates from it, becoming a spherical cap. Indeed, the membrane sticks to the inner post only if the distance between them is low enough, so that the membrane can feel the vdW attraction. A statistical analysis of the distance at which the membrane sticks to the post —referred to as *pull-in distance*— could then be carried out (the height was varied by changing the pressure), for graphene flakes of thickness ranging between 1 and 5 layers. The authors showed how the vdW attraction can be modelled in terms of an attractive pressure of the form:

$$P_{\mathrm{vdW}} = \frac{\beta}{h_0^4}, \tag{4.19}$$

where β is a constant which accounts for the vdW attraction. Their studies show that β scales linearly with the number of layers, confirming the additive nature of vdW forces [325].

Their experiment is somehow similar to our full indentation experiment discussed in the previous section [319]. In our case, the membrane is brought closer and closer to the underlying bulk MoS_2 flake by the AFM tip, allowing us to probe the vdW interaction between ML and bulk. As discussed in the previous section and shown in Fig. 4.4(c), the FDC acquired in a full indentation process presents several features. Feature (1) represents the tip-sample snap-to-contact point; the loading force then increases with δ, at first linearly and then following a non-linear behaviour (see Eq. (4.18)); however, by further pushing down the tip, an abrupt decrease in the force is observed, marked as feature (2): Such a decrease continues

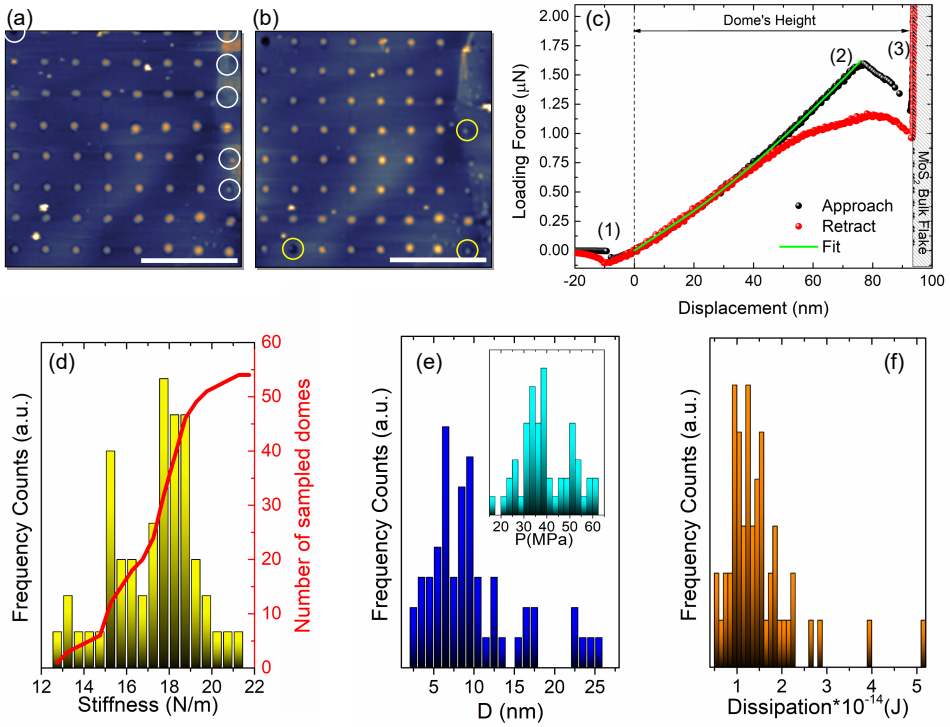

Figure 4.4: (a-b) Tapping-mode AFM topography, 24.5 μm $\times$ 24.5 μm, of an array made of 8 $\times$ 8 openings before (a) and after (b) performing the nano-indentations; scale bar: 10 μm. White circles in (a) indicate a few missing domes in the matrix. Yellow circles in (c) highlight the domes damaged because of indentation. (c) Typical approach (black scatters) and retract (red scatters) FDCs, with the former fitted by Eq. (4.18) (green line). (e) Typical approach (black scatters) and retract (red scatters) FDCs. Feature (1) represents the snap-to-contact at the tip-dome contact point; feature (2) represents second snap-to-contact-like feature, that we attribute to the vdW attraction by the substrate; feature (3) represents the tip-to-substrate contact point. (d) Stiffness distribution (histogram) and cumulative function (red line) obtained by fitting 54 approach FDCs with Eq. (4.18). (e) Distribution of the distance D between the feature (2) and the bulk MoS_2 flake (feature (3)); Inset: inner pressure distribution at D. Right: Dissipation distribution evaluated by measuring the hysteresis between the approach and retract FDCs. Figure reproduced with permission.[319] Copyright 2021, American Chemical Society.

until the tip/membrane systems touches the substrate (feature (3)). Initially, when the tip is retracted, see red curve in Fig. 4.4(c), the curve does not overlap with the approach curve; at large membrane-to-bulk distances, however, the two curves show a near-perfect overlap. This result proves that the dome can withstand very large deformations without damaging, and suggests an analogy between the dome system and superelastic materials. This analogy is suggested by the presence of: (i) two subsequent elastic branches, representative of indentation on the bulged MoS_2 monolayers, and on the bulk (feature (3)), respectively; (ii) a large hysteresis when

performing a loading-unloading cycle because of the system transition from ML to bulk (when the ML sticks to the substrate); and (iii) full reversibility of the whole process. The observed behaviour can be explained in terms of vdW forces between the ML and the bulk, which start playing a role when the membrane is pushed close enough to the substrate, in analogy with the donut blister experiment. Indeed, the attractive vdW interaction decreases the force needed to push the membrane down, leading to feature (2) in the FDC. Such a peculiar diagram allows one to extract various information on the system. First, by fitting the FDC from feature (1) to feature (2) by Eq. (4.18), it is possible to estimate the membrane stiffness. The stiffness values estimated by performing a full indentation procedure on 54 MoS_2 domes are displayed in Fig. 4.4(d). Second, by making a statistical analysis of the distance D between features (2) and (3), it is possible to observe how the vdW attraction starts to play a significant role at a distance of ~ 7 nm, see Fig. 4.4(e). This result is in excellent agreement with the pull-in distance estimated in donut blisters.

The experiment here discussed can provide further information if a more quantitative analysis is carried out. In particular, one can model the problem of an indenter pushing against the pressurised dome as a quasistatic process where, point by point [319]:

$$F_{\text{probe}} - F_{\text{gas}} + F_{\text{vdW}} = 0, \tag{4.20}$$

F_{probe} being the force exerted by the AFM tip, F_{gas} that exerted by the gas and F_{vdW} being the vdW interaction force between the dome and the bulk flake beneath. The latter is non-negligible only when the membrane-to-bulk distance D is small enough, see Fig. 4.4(e). If we assume that the only portion of the membrane subjected to the vdW attraction is that close to the indenter tip, and that the membrane acquires the same curvature of the AFM tip (with curvature radius R_{tip}), the vdW interaction can be modeled in the geometry of the sphere-plane interaction as [319]:

$$U_{\text{vdW}} = -\frac{HR_{\text{tip}}}{6\pi D}, \tag{4.21}$$

where H is the so-called Hamaker constant ($H = 6.51 \cdot 10^{-19}$ J for a MoS_2 ML on a MoS_2 bulk flake [319]). In turn, the vdW force can be calculated as:

$$F_{\text{vdW}} = -\frac{dU}{dD} = -\frac{HR_{\text{tip}}}{6\pi D^2}. \tag{4.22}$$

Once F_{vdW} is derived, and being F_{probe} a known quantity, it is possible to derive F_{gas} from Eq. (4.20), and thus the gas pressure P_{gas} by dividing F_{gas} by the indented area. The pressure estimated with this approach in the same full indentation procedures made to estimate the stiffness and D is shown as inset in Fig. 4.4(e). Finally, it should be noticed that the hysteresis between the approach and retract FDCs provides information on the energy dissipated during the indentation process. In particular, it can be demonstrated that the total work W done by the tip equals the

work done by the vdW force [319]:

$$W_{\text{probe}}^{\text{approach}} - W_{\text{probe}}^{\text{retract}} = -(W_{\text{vdW}}^{\text{approach}} - W_{\text{vdW}}^{\text{retract}}). \tag{4.23}$$

Fig. 4.4(f) displays a statistical analysis of the energy dissipated when performing full indentation procedures, with values mostly ranging between 0.5 and $2.3 \cdot 10^{-14}$ J. By roughly normalising these values to the tip area ($A_{\text{tip}} = \pi R_{\text{tip}}^2$), one finds $(4.7 \pm 2.5) \cdot 10^{-21}$ J/Å^2 $= 30 \pm 16$ meV/Å^2, remarkably close to the adhesion energy expected from DFT calculations [286, 322] and to that estimated experimentally with the approach we will discuss in the following section [116].

4.2.2 Energy minimisation in microscopic domes

A somewhat simpler approach to estimate the adhesion energy between different vdW materials relies on the study of the equilibrium shape of 2D material domes. Indeed, the total energy of the system is given by:

$$U_{\text{tot}} = U_{\text{int}} + U_{\text{stretch}} + U_{\text{bend}} + U_{\text{adh}}, \tag{4.24}$$

where U_{int} represents the internal energy of the fluid within the dome, U_{stretch} and U_{bend} are the elastic energy contributions associated to stretching and bending, and U_{adh} is related to the detachment of the membrane from the substrate. The bending term is generally negligible, and would contribute only for very small and rather thick domes. For sake of completeness, we include it in our equations and we will neglect it *a posteriori*. These energy contributions depend on several physical quantities, such as the height profile of the domes $h(r)$, the differential pressure of the fluid trapped inside Δp, the in-plane strain components ε_r and ε_θ, the Young's modulus $E_{2\text{D}}$, Poisson's ratio ν and bending modulus D, and the adhesion energy between the membrane and the substrate γ.

Indeed, the knowledge of the height profile and strain components is essential to determine the energy contributions. Thus, for an analytical theory to be formulated, the knowledge of the dome profile is the first essential step.

Theoretical framework

The mechanical behavior of a thin dome can be described starting from the idea that we want to map a two-dimensional (2D) plane (flat membrane before bulging) to a three-dimensional (3D) space (bulged membrane) [217, 326]. In the framework of the theory of elasticity discussed by Landau and Lifshitz [298], the mechanical effect of a deformation can be described in terms of a displacement vector consisting of an in-plane component $\boldsymbol{u} = (u_x(x, y), u_y(x, y))$ related to pure stretching and an out-of-plane component $h(x, y)$ related to the transverse displacement. The kinematics of deformation is then described by an in-plane Green–Lagrange strain tensor and a curvature tensor, both defined with respect to a reference state in 2D (*i.e.*, the

ground state of the flat membrane before bulging). Under the assumption of relatively small deformation but with moderately large deflection, the Green–Lagrange strain tensor components and the curvature are given by:

$$\varepsilon_{ij} = \frac{1}{2}\left(\frac{\partial u_i}{\partial x_i} + \frac{\partial u_j}{\partial x_j}\right) + \frac{1}{2}\frac{\partial h}{\partial x_i}\frac{\partial h}{\partial x_j}, \tag{4.25}$$

and

$$\kappa_{ij} = \frac{\partial^2 h}{\partial x_i \partial x_j}, \tag{4.26}$$

respectively, where $i, j = x, y, z$.
The associated strain density function is given by

$$\Phi = \Phi_\varepsilon + \Phi_\kappa, \tag{4.27}$$

where Φ_ε is the strain energy due to the in-plane strain:

$$\Phi_\varepsilon = \frac{E_{2D}}{2(1+\nu)} \sum_{ij} \left(\varepsilon_{ij}\varepsilon_{ij} + \frac{\nu}{1-\nu}\varepsilon_{ii}\varepsilon_{jj}\right), \tag{4.28}$$

and Φ_κ is the strain energy due to the curvature:

$$\Phi_\kappa = \sum_{ij} \left(\frac{D - D_G}{2}\kappa_{ij}\kappa_{ij} + \frac{D_G}{2}\kappa_{ii}\kappa_{jj}\right), \tag{4.29}$$

D and D_G being the bending moduli corresponding to the mean curvature and to the gaussian curvature, respectively. In the classical plate theory $D_G = (1-\nu)D$ [217]. From the energy density functions, one can obtain the 2D stress tensor:

$$N_{ij} = \frac{\partial \Phi_\varepsilon}{\partial \varepsilon_{ij}} = \frac{E_{2D}}{1+\nu}\left(\varepsilon_{ij} + \frac{\nu}{1-\nu}\sum_k \varepsilon_{kk}\delta_{ij}\right), \tag{4.30}$$

and the bending moments:

$$M_{ij} = \frac{\partial \Phi_\kappa}{\partial \kappa_{ij}} = (1-\nu)D\kappa_{ij} + \nu D \sum_k \kappa_{kk}\delta_{ij}. \tag{4.31}$$

To describe the mechanics of thin domes, in-plane force equilibrium and momentum equilibrium conditions have to be considered. These conditions can be expressed as:

$$\frac{\partial N_{ij}}{\partial x_j} = 0, \tag{4.32}$$

and

$$\frac{\partial^2 M_{ij}}{\partial x_i \partial x_j} - N_{ij}\frac{\partial^2 h}{\partial x_i \partial x_j} = Q, \tag{4.33}$$

where Q is the lateral loading intensity, keeping into account all possible internal and external forces per unit area acting on the deformed membrane (*e.g.*, the internal gas pressure). By substituting the explicit expression for the moments M_{ij} —given by Eq. (4.31)— into the latter equation, we obtain a set of nonlinear equations to describe the mechanics of the dome:

$$D\nabla^4 h - N_{ij}\frac{\partial^2 h}{\partial x_i \partial x_j} = Q. \tag{4.34}$$

For circular domes, the problem can be expressed in polar coordinates, by taking the origin of our reference frame at the centre of the dome, so that the radial coordinate r represents the distance from the centre. We can express the radial and height displacements as:

$$u_r = u(r), \tag{4.35}$$

$$u_\theta = 0, \tag{4.36}$$

$$h = h(r). \tag{4.37}$$

The strain tensor components defined in (4.25) become:

$$\varepsilon_{rr} = \varepsilon_r(r) = u'(r) + \frac{1}{2}h'(r)^2, \tag{4.38}$$

$$\varepsilon_{\theta\theta} = \varepsilon_\theta(r) = \frac{u}{r}. \tag{4.39}$$

$$\varepsilon_{r\theta} = 0. \tag{4.40}$$

ε_r and ε_θ are referred to as radial and circumferential component, respectively.
The curvature components defined in (4.26) become instead:

$$\kappa_{rr} = \kappa_r(r) = h''(r), \tag{4.41}$$

$$\kappa_{\theta\theta} = \kappa_\theta(r) = \frac{1}{r}h'(r). \tag{4.42}$$

$$\kappa_{r\theta} = 0. \tag{4.43}$$

Notice that the above quantities have to satisfy some boundary conditions at the clamped edge of the bulged membrane (*i.e.*, for $r = R$) and at the centre:

- The out-of-plane displacement is null at the boundary:

$$h(R) = 0; \tag{4.44}$$

- The radial displacement is null both at the edges and at the centre:

$$u(0) = 0; \quad u(R) = 0; \tag{4.45}$$

- Under the hypothesis that the membrane is fully attached outside the dome, without deformation or sliding, the circumferential strain is null at the edge:

$$\varepsilon_\theta(R) = 0; \tag{4.46}$$

- Due to the circular symmetry of the problem, the strain is equibiaxial at the center:

$$\varepsilon_r(0) = \varepsilon_\theta(0). \tag{4.47}$$

Finally, we can then express the stress components given by Eq. (4.30) in polar coordinates as:

$$N_r = \frac{E_{2D}}{(1-\nu^2)}\left(\varepsilon_r + \nu\varepsilon_\theta\right), \tag{4.48}$$

$$N_\theta = \frac{E_{2D}}{(1-\nu^2)}\left(\varepsilon_\theta + \nu\varepsilon_r\right), \tag{4.49}$$

or, equivalently, we can express the strain components in term of the stress components:

$$\varepsilon_r = \frac{N_r - \nu N_\theta}{E_{2D}}, \tag{4.50}$$

$$\varepsilon_\theta = \frac{N_\theta - \nu N_r}{E_{2D}}. \tag{4.51}$$

In a polar coordinate formalism, the force equilibrium equation (Eq. (4.32)) becomes

$$N_r'(r) + \frac{N_r - N_\theta}{r} = 0, \tag{4.52}$$

which can be written explicitly by substituting Eqs. (4.48) and (4.49) as:

$$u''(r) + \frac{1}{r}u'(r) - \frac{u}{r^2} = \frac{\nu-1}{2r}h'(r)^2 - h'(r)h''(r). \tag{4.53}$$

On the other side, the nonlinear moment equilibrium equation (Eq. (4.34)) can be integrated with respect to r, and gives:

$$D\left(h'''(r) + \frac{1}{r}h''(r) - \frac{1}{r^2}h'(r)\right) - h'(r)N_r = \frac{1}{r}\int_0^r Q(r^*)r^*dr^*. \tag{4.54}$$

In the absence of external forces, the only contribution to the lateral loading intensity is given by the pressure due to the presence of a compressed fluid within the dome, so that $Q(r^*) = \Delta p$ (where Δp is the pressure difference between the pressure of the fluid inside and the external one).

It should be noticed that the same set of nonlinear equations (Eqs. (4.53) and (4.54)) can be analogously obtained by a variational procedure. In particular, by

integrating the strain density function (Eq. (4.28)), one obtains the stretching energy. In radial coordinates, since:

$$\Phi_\varepsilon = \frac{E_{2D}}{(1-\nu^2)}\left[\varepsilon_r^2 + 2\nu\varepsilon_r\varepsilon_\theta + \varepsilon_\theta^2\right] =$$
$$= \frac{E_{2D}}{(1-\nu^2)}\left[u'(r)^2 + u'(r)h'(r)^2 + \frac{h'(r)^4}{4} + 2\nu\frac{u(r)u'(r)}{r} + \nu h'(r)^2\frac{u(r)}{r} + \frac{u(r)^2}{r^2}\right], \tag{4.55}$$

the stretching energy is given by:

$$U_{\text{stretch}}[u] =$$
$$= \frac{E_{2D}}{(1-\nu^2)}\int_0^R\int_0^{2\pi} dr\cdot r d\theta\cdot\left[u'(r)^2 + u'(r)h'(r)^2 + \frac{h'(r)^4}{4} + \frac{u(r)^2}{r^2}\right] + \tag{4.56}$$
$$+\nu\frac{E_{2D}}{(1-\nu^2)}\int_0^R\int_0^{2\pi} dr\cdot r d\theta\cdot\left[2\frac{u(r)u'(r)}{r} + h'(r)^2\frac{u(r)}{r}\right].$$

By minimising U_{stretch} with respect to the in-plane displacement u, one obtains exactly the same result expressed by Eq. (4.53). This equation establishes a relationship between the height profile of the dome, $h(r)$, and the in-plane displacement profile, $u(r)$. On the other side, the momentum equilibrium condition establishes a relationship between lateral loading (*i.e.*, the pressure), height profile and in-plane displacement profile.

This general formulation represents the basis both for the numerical approaches and to find approximate analytical solutions.

In the typical circumstance in which the height profile, in-plane displacement profile, strain distribution, and pressure are unknown, the two sets of coupled equations obtained above do not allow us to obtain a purely analytical solution, as pointed out in Ref. [217]. For this reason, it is necessary to rely on some assumptions to develop an analytical method, and an analytical solution is then typically found by minimising the total energy of the dome rather than via Eq. (4.54). Indeed, the most reasonable choice is that of making an assumption of the height profile, since in this case the appropriateness of the assumption can be directly verified by a comparison with the experimental morphological data. Further assumptions on the in-plane displacement (or on the strain) are also necessary, as we will discuss in the following.

Different analytical methods —based on different assumptions concerning the height profile— were developed. In Additional Material, sec. A11, we summarise the main concepts and results (*i.e.*, the equations for the pressure) of the previous analytical models in order to provide a comparison between the model developed in this work and the previous models.

Analysis of the height profile of the domes

For micron-sized domes with circular base, previous models assumed the height profile to be described by the membrane expression: $h_{membrane}(r) = h_0\left(1 - r^2/R^2\right)$,

where r represents the distance from the dome centre and h_0 and R are its maximum height and footprint radius, respectively (see Additional Material, sec. A11). This is expected to be true for negligible bending rigidity and for $h_0/R \ll 1$. The bending stiffness is negligible for thin micro-domes (say, $R \gtrapprox 100$ nm, as discussed below). On the other side, the condition $h_0/R \ll 1$ has been generally assumed, without checking its validity. To shed light on this, we assumed a more general shape:

$$h(r) = h_0 \left[1 - \left(\frac{r}{R}\right)^q\right]. \tag{4.57}$$

To achieve a complete understanding of the system, we studied both domes created by us with our H-ion irradiation approach, and we also created domes with the top-down approach typically used in the literature, consisting in the exfoliation and deposition of 2D materials on other vdW materials and on the formation of domes due to the trapping of contaminants. In particular, we exploited our H-ion irradiation approach to create homo-structured domes, *i.e.* domes made of the same material of the underlying flake. The homo-structured nature of the domes is intrinsically related to the fact that our approach is a bottom-up one, in which the dome directly blisters from the irradiated flake. With the top-down approach, on the other side, we could create hetero-structured domes, *i.e.* domes made of a different material than that of the flake beneath. The hetero-structured domes were fabricated with a 2D transfer system from hq-graphene. To do that, thin crystal of vdW materials were first exfoliated onto PDMS and the crystal/PMDS sandwich was then placed face down and pressed onto thick flakes exfoliated over a Si substrate; the polymer was then peeled off. Annealing treatments were performed in high vacuum (10^{-6} mbar) at 150 °C for several hours, and the spontaneous formation of domes was observed (analogously to Ref. [112]). We then probed the thickness of the deposited 2D material by PL measurements. We mostly deposited monolayers, but in some cases we deposited also slightly thicker layers. We summarised the relevant information concerning the samples we studied (including the fabrication methods, number of flakes and domes that we studied and dome thickness) in Table 4.2.

With the top-down method, the formation process of the domes is random, and most of the domes have no round shape, as shown in Fig. 4.5, left. Sometimes, some round domes can be found, as shown in the middle panel, even though their density is rather small. Therefore, it is often necessary to prepare many samples in order to be able to measure a few domes. To the contrary, with the H-ion irradiation approach we form a lot of domes all over the flakes, as shown in the right panel. Indeed, for the top-down approach, since the fabrication method itself —consisting on the exfoliation of the thin material, its deposition, and the annealing— is time-consuming, this method is much less efficacious than the bottom-up process to characterise the domes. Furthermore, in the top-down method, the initial cleanness of the bulk flakes serving as a substrate plays an essential role and the prepared samples are not always good ones, further reducing the dome formation yield.

We then characterised the shape of the domes by fitting them with the following

Material	Fabrication	No. of studied flakes	Dome thickness
MoS_2	bottom-up	>5 flakes (66 bubbles)	mostly 1L
$MoSe_2$	bottom-up	3 flakes (54 bubbles)	mostly 1L
$MoTe_2$	bottom-up	2 flakes (25 bubbles)	1L and few-L
WS_2	bottom-up	>5 flakes (167 bubbles)	mostly 1L
WSe_2	bottom-up	3 flakes (55 bubbles)	mostly 1L
WTe_2	bottom-up	1 flake (20 bubbles)	1L and few-L
hBN	bottom-up	3 flakes (37 bubbles)	few-L
MoS_2/WS_2	top-down	1 flake (8 bubbles)	all 1L
MoS_2/hBN	top-down	2 flakes (8 bubbles)	1L and 3L
WSe_2/WS_2	top-down	1 flake (7 bubbles)	all 1L
WSe_2/hBN	top-down	3 flakes (8 bubbles)	1L and 3L
hBN/$MoTe_2$	top-down	1 flake (3 bubbles)	few-L

Table 4.2: Details about the homo- and hetero-structured domes realised and studied in this work. For each material, we highlight the fabrication method we employed, the number of flakes we characterised via AFM measurements (and the total number of AFM profiles of the domes we analysed), and the thickness of the domes.

function:

$$z(x) = z_0 + h_0 \left[1 - \left(\frac{|x - x_0|}{R}\right)^q\right] \Theta(R - |x - x_0|), \tag{4.58}$$

where Θ is the Heaviside function.

One exemplifying experimental profile and fit for each material combination is shown in Fig. 4.6 for homostructured domes and in Fig. 4.7 for heterostructured domes. For the homostructured domes, we fabricated and studied the profiles of tens of domes for each material (see Table 4.2). A large statistical analysis of the q values could thus be performed. The cumulative functions obtained via this analysis are shown in Fig. 4.8 as coloured points, while the black lines represent the corresponding fits. From the fits, we could estimate the average q value for each material. For the heterostructures, the fabrication process is more complex and requires many steps, and only few domes can be created each time (see Table 4.2). For this reason, we could not perform an analogously large statistical analysis on the heterostructures, and we studied 7-8 domes for each combination of materials. Only in the case of hBN/$MoTe_2$ we studied less domes because $MoTe_2$ quickly oxidizes, which makes the fabrication process more demanding since the samples have to be kept in a protected environment. The results obtained for the heterostructures are shown in Fig. 4.9. In this case, we performed an average of the measured q values, represented by the lines shown in each plot.

To gain a more complete picture of the mechanical properties of the domes, we also studied several AFM profiles extracted from the literature [87, 112, 156, 166, 170, 216, 327–329], finding $q \simeq 2.2$, see Additional Material, sec. A12.

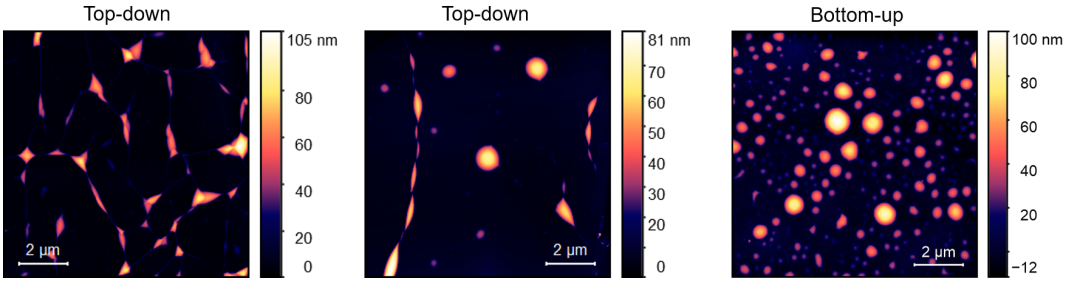

Figure 4.5: AFM images of two samples fabricated by the top-down approach (a WS_2/MoS_2 sample on the left, and a MoS_2/hBN sample at the center) and of one sample fabricated by the bottom-up approach ($MoTe_2/MoTe_2$). Reproduced with permission from E. Blundo *et al.*, Phys. Rev. Lett. **127**, 046101 (2021) [116]. Copyright 2021 American Physical Society.

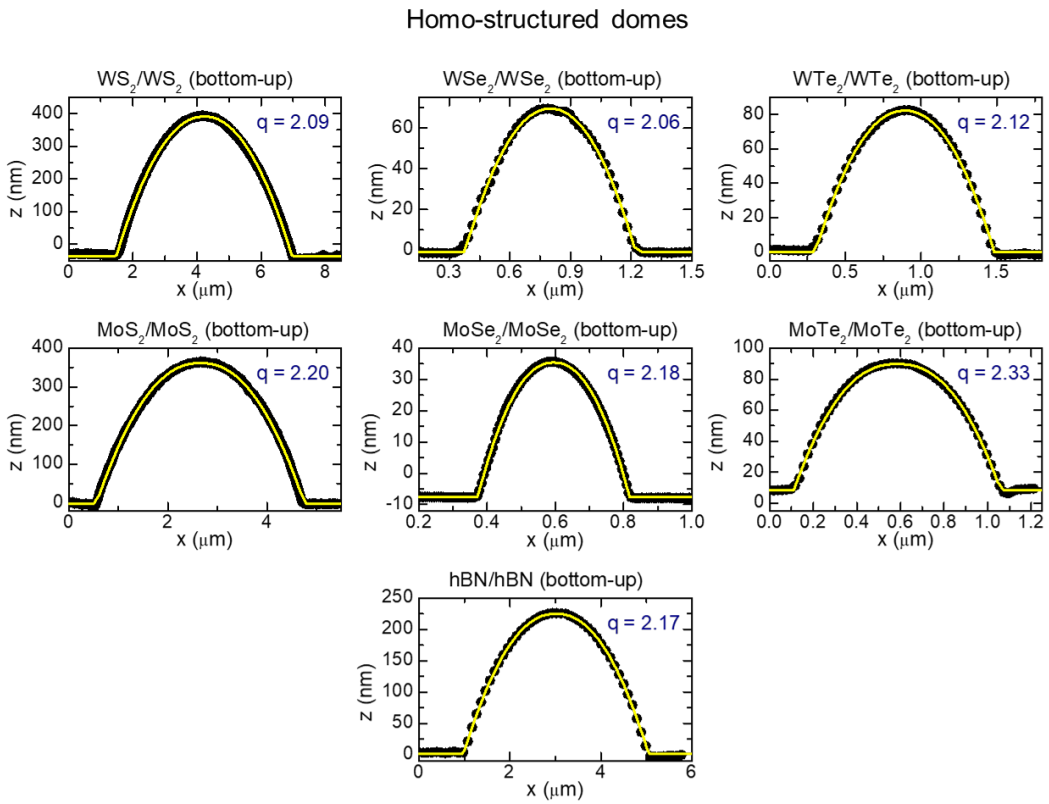

Figure 4.6: AFM profiles (black dots) of exemplifying homostructured domes (one for each material) obtained in this work, and fits (yellow lines) via (4.58). The q value resulting from the fit is given in each panel. Reproduced with permission from E. Blundo *et al.*, Phys. Rev. Lett. **127**, 046101 (2021) [116]. Copyright 2021 American Physical Society.

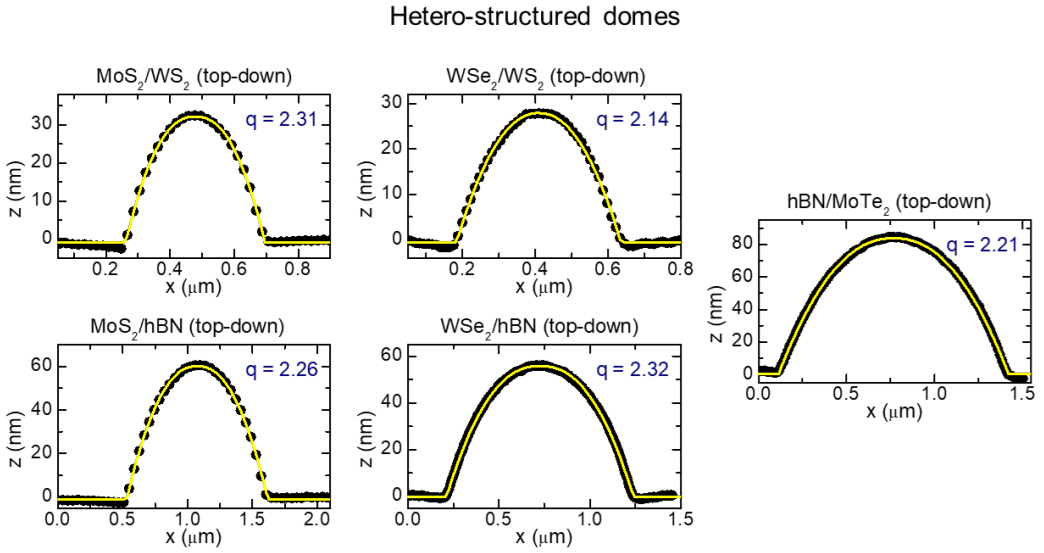

Figure 4.7: AFM profiles (black dots) of exemplifying heterostructured domes (one for each material) obtained in this work, and fits (yellow lines) via (4.58). The q value resulting from the fit is given in each panel. Reproduced with permission from E. Blundo *et al.*, Phys. Rev. Lett. **127**, 046101 (2021) [116]. Copyright 2021 American Physical Society.

To pinpoint the observation that $q \approx 2.2$ rather than being $q \approx 2.0$ as predicted by the membrane model, we performed FEM calculations in the framework of the nonlinear membrane theory (see Additional Material, sec. A3) to simulate the dome shape and determine the q values. To that purpose, we calculated the height profile of domes with fixed R and by changing h_0. We thus estimated q for h_0/R varying in the largest range that can be explored via numerical calculations, see details in Additional Material, sec. A13. The calculated trend is displayed in Fig. 4.10. Therein, $q \approx 2.0$ only for non-physically flat domes ($h_0/R \lessapprox 0.01$). Instead, in the range where the experimental h_0/R values lie (see orange-shaded area) larger q values are found, centred around $q \approx 2.2$, in excellent agreement with our analysis of the experimental profiles. The same behavior is found independently of R, and q shows only a weak dependence on the membrane thickness, see Additional Material, sec. A13. This finding highlights a weakness in all previous models.

The second step for an analytical model is the characterisation of the strain field, whose knowledge is essential to evaluate the elastic energy contribution to the total energy and thus to develop a complete description of the system.

Strain of the domes

Differently from previous works, rather than making assumptions on the radial displacement, we make an ansatz on the strain components. More specifically, we take

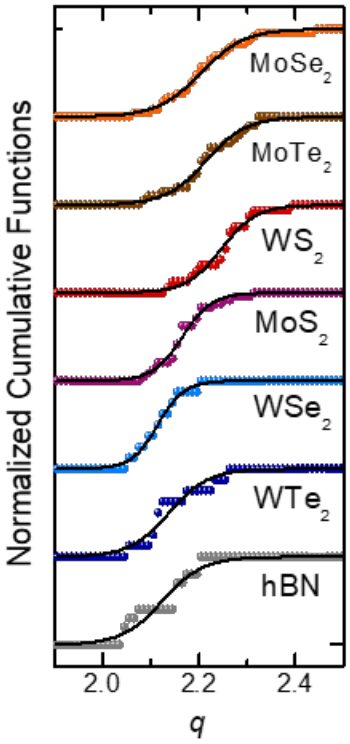

Figure 4.8: Normalised cumulative functions of the q values obtained by analysing the AFM profiles of the homostructured domes. The data concerning the different materials are stacked by y-offset. The black lines are fits to the data. Reproduced with permission from E. Blundo *et al.*, Phys. Rev. Lett. **127**, 046101 (2021) [116]. Copyright 2021 American Physical Society.

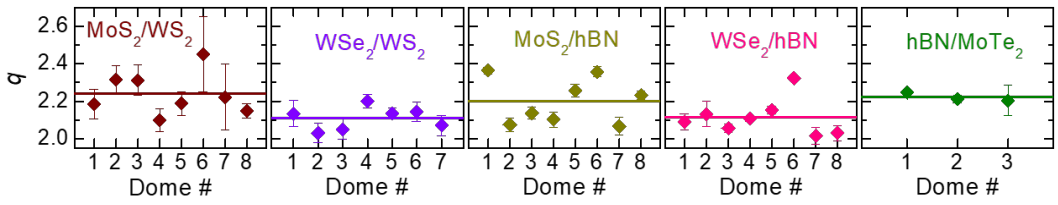

Figure 4.9: q values obtained by analysing the AFM profiles of the heterostructured domes. The lines represent the average values. Reproduced with permission from E. Blundo *et al.*, Phys. Rev. Lett. **127**, 046101 (2021) [116]. Copyright 2021 American Physical Society.

the boundary conditions for the strain components given by Eqs. (4.46) and (4.47) as our starting points. The analysis of the Raman data suggested the circumferential component to decrease with r with a quasi-parabolic behavior, in agreement with

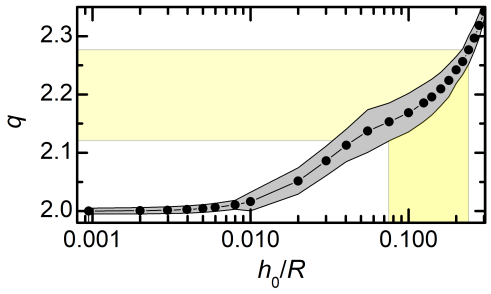

Figure 4.10: Numerical calculations of the constant q in Eq. (4.57) *vs* h_0/R. The black dots concern MoS_2, while the grey-shaded area embeds other 2D materials ($MoSe_2$, $MoTe_2$, WS_2, WSe_2, WTe_2, hBN, graphite). The orange-shaded areas highlight the range of aspect ratios measured experimentally in 2D-material domes. Reproduced with permission from E. Blundo *et al.*, Phys. Rev. Lett. **127**, 046101 (2021) [116]. Copyright 2021 American Physical Society.

the numerical estimate. We thus assume this component to be given by:

$$\varepsilon_\theta(r) = f(\nu, q)\frac{h_0^2}{R^2}\left[1 - \left(\frac{r}{R}\right)^c\right], \tag{4.59}$$

so that the boundary conditions are satisfied and the strain at the centre is proportional to the square of the aspect ratio, in agreement with Eq. (4.66). c is a constant to be determined, and which we expect to be close to 2.

From the Green-Lagrange equations in polar coordinates (Eqs. (4.38) and (4.39)), we can obtain the in-plane displacement and radial strain component:

$$u(r) = f(\nu, q)\frac{h_0^2}{R^2}\cdot r\left[1 - \left(\frac{r}{R}\right)^c\right], \tag{4.60}$$

and

$$\varepsilon_r(r) = f(\nu, q)\frac{h_0^2}{R^2}\left[1 - (c+1)\left(\frac{r}{R}\right)^c + \frac{1}{2}\frac{q^2}{f(\nu,q)}\left(\frac{r}{R}\right)^{2q-2}\right]. \tag{4.61}$$

By imposing the force equilibrium condition (Eq. (4.53)), we obtain that:

$$q^2\left(\frac{2q-1-\nu}{2}\right)\frac{r^{2q-3}}{R^{2q-2}} = f(\nu,q)\cdot(c+2)c\cdot\frac{r^{c-1}}{R^c}. \tag{4.62}$$

In order for this relation to be valid $\forall\ r \in [0, R]$, it must be $c = 2q-2$, and we find that:

$$f(\nu, q) = q^2\left[\frac{2q-1-\nu}{2c(c+2)}\right] = \frac{q}{8}\left[\frac{2q-1-\nu}{q-1}\right]. \tag{4.63}$$

Hence, we have that the strain components are given by:

$$\varepsilon_r(r) = f(\nu,q)\frac{h_0^2}{R^2}\left[1 - g(\nu,q)\left(\frac{r}{R}\right)^{2q-2}\right], \quad \varepsilon_\theta(r) = f(\nu,q)\frac{h_0^2}{R^2}\left[1 - \left(\frac{r}{R}\right)^{2q-2}\right], \tag{4.64}$$

with

$$g(\nu, q) = c + 1 - \frac{4q(q-1)}{2q-1-\nu} = 2q - 1 - \frac{4q(q-1)}{2q-1-\nu}. \tag{4.65}$$

To verify the accuracy of our analytical results, in Fig. 4.11 we compare the strain calculated analytically for the dome studied by Raman in Figs. 2.1, 2.2 and 2.3 with the strain calculated numerically for the same dome and with the strain derived by the Raman data. Indeed, the analytical model matches very well with the theoretical one and, in turn, agrees well with the experimental data. Indeed, our model also

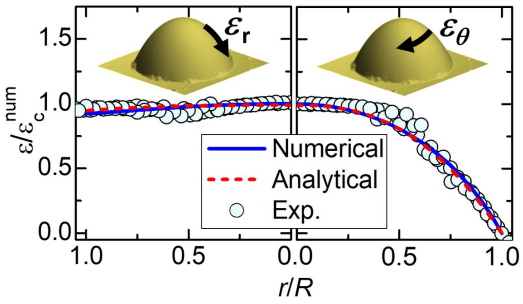

Figure 4.11: Radial dependence of the circumferential (ε_θ) and radial (ε_r) in-plane strain components (sketched as insets), derived by the Raman data, and calculated by FEM-numerical calculations and Eqs. (4.64). The strain values were normalised to the numerical strain at the centre (ε_c^{num}). Reproduced with permission from E. Blundo *et al.*, Phys. Rev. Lett. **127**, 046101 (2021) [116]. Copyright 2021 American Physical Society.

provides a much better description than all previous analytical models. Previous models assumed that large enough domes are described by the membrane profile ($q = 2.0$ in Eq. (4.57)) or considered polynomial expansions, as discussed in the Additional Material, sec. A11. Further assumptions on the in-plane displacement were done (differing depending on the model). While the membrane height profile shows a relatively good agreement with the experimental data (though not excellent, see Additional Material, sec. A12), the assumption on the radial displacement $u(r)$ cannot be directly verified. However, starting from these two assumptions one can calculate the expression for the radial and circumferential strain components. All the analytical models predict that the strain at the dome centre (ε_c) is related to the square of the aspect ratio by the formula:

$$\varepsilon_c = f(\nu) \left(\frac{h_0}{R}\right)^2, \tag{4.66}$$

(see also Eq. (1.1)) though the function $f(\nu)$ differs depending on the model. In the case of the membrane theory [217, 326], the strain components —as shown in Fig. 4.12— which suggests the assumption on the radial displacement to be incorrect. In particular, the strain at the dome centre —given by Eq. (4.66)— is overestimated by a factor ∼1.5-2 (see Fig. 4.12(a)). Furthermore, both the radial and circumferential strain components feature different behaviours, as shown in Fig. 4.12(b-d), where we

plot the radial dependence of the strain components for homostructured domes made of MoS_2, graphene, and hBN. The choice of these three compounds is grounded on the different Poisson's ratio they exhibit (graphene is characterised by the smallest Poisson's ratio [equal to 0.176], MoS_2 by the largest [equal to 0.250], and hBN by a Poisson's ratio in between [equal to 0.223]).

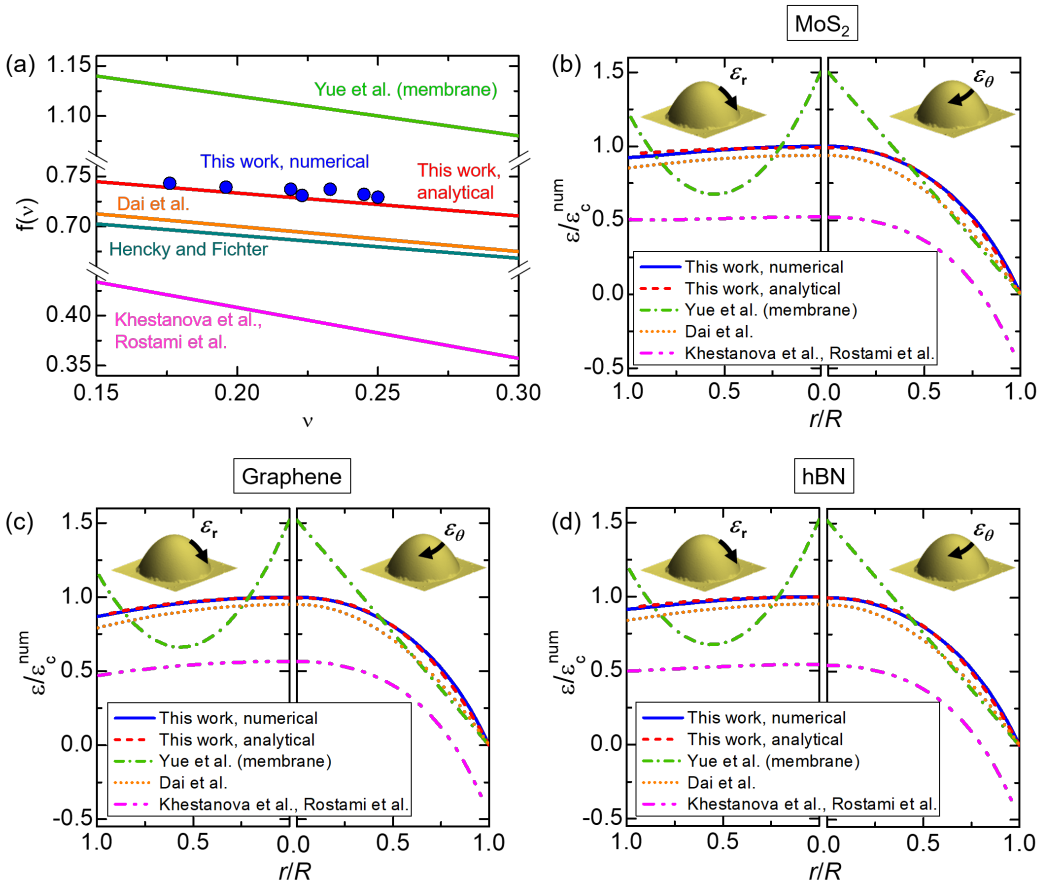

Figure 4.12: (a) Calculated trends for the function $f(\nu)$ relating the strain at the summit of the domes to the aspect ratio according to (4.66). $f(\nu)$ was estimated both numerically (blue points, for values of ν corresponding to several vdW materials), and analytically (lines), with the models discussed in this note. Our analytical estimate, that will be discussed in the following, is also shown for comparison. (b) Spatial distribution of the radial (left) and circumferential (right) strain components for a micron-sized MoS_2 dome (with Poisson's ratio $\nu = 0.250$), estimated numerically and with the analytical methods of panel (a). The strain values were normalised to the numerical strain at the centre. (c-d) Same as the previous panel in the case of a graphene ($\nu = 0.176$) and a hBN ($\nu = 0.223$) dome, respectively. Reproduced with permission from E. Blundo *et al.*, Phys. Rev. Lett. **127**, 046101 (2021) [116]. Copyright 2021 American Physical Society.

A much more accurate description was achieved by Hencky, who suggested a polynomial expansion for the height profile and stress components [87, 164]. This

model would generally require the support of numerical calculations to estimate all the coefficients of the polynomial expansion and find a solution [164], but it leads to a relatively simple analytical formula for the strain at the dome centre, given by Eq. (1.1).

Hencky estimated $f(\nu)$ for some values of ν, but an error was found in Hencky's estimate, which was corrected by Fichter [164]. By considering Fichter's estimates, we obtain the behavior shown in Fig. 4.12(a) for $f(\nu)$. Indeed, the results obtained by Hencky and Fichter underestimate $f(\nu)$ by about 7 %. This is probably due to the fact that they considered only a finite number of terms (up to $n = 10$) in the polynomial expansions.

A good compromise between the membrane analysis and Hencky and Fichter's model was found by Dai *et al.* [115], who assumed the height profile given by the membrane theory but a different in-plane displacement, as discussed in the Additional Material, sec. A11. Under the assumption of the absence of slippage, their model leads to a relatively good qualitative agreement with the numerical strain behaviour, but to a general underestimate of both the strain components. Thus, also in this case the calculated $f(\nu)$ underestimates the numerical result (by about 5 %, see Fig. 4.12).

As for the model by Khestanova *et al.*, an analytical expression for the strain components based on that model was calculated by Rostami *et al.* [330] and the result is shown in Fig. 4.12. In this case, the strain distribution differs in that the circumferential component becomes negative close to the edges and the strain at the centre is about 1/2 than the numerical value. An analogous result can be obtained also with the model by Dai *et al.*, when including slippage contributions.

The analytical strain distribution obtained with our analytical method is also shown for comparison, and a good agreement with the numerical results is indeed obtained independently of the Poisson's ratio.

This discussion highlights how different results can be obtained by using different analytical models and makes it essential to look for an experimental counterpart to join this debate. Our comparison with the Raman data, shown in Fig. 4.11 provides therefore an important feedback that confirms the validity of our model.

Energy minimisation

To solve our problem analytically, we need to calculate the total energy of the system. Given the above analytical formula for the height and strain profile, we can express the strain density functions defined in Eqs. (4.28) and (4.29) as:

$$\begin{aligned}\Phi_\varepsilon = \frac{E_{2D}}{(1-\nu^2)}\left[\varepsilon_{rr}^2(1-\nu)+\varepsilon_{rr}^2\nu+2\varepsilon_{rr}\varepsilon_{\theta\theta}\nu+\varepsilon_{\theta\theta}^2(1-\nu)+\varepsilon_{\theta\theta}^2\nu\right] = \\ = \frac{E_{2D}}{(1-\nu^2)}\left[\varepsilon_r^2+2\nu\varepsilon_r\varepsilon_\theta+\varepsilon_\theta^2\right],\end{aligned} \tag{4.67}$$

$$\begin{aligned}\Phi_\kappa &= \nu\frac{D}{2}(\kappa_{rr}^2 + 2\kappa_{rr}\kappa_{\theta\theta} + \kappa_{\theta\theta}^2) + (1-\nu)\frac{D}{2}(\kappa_{rr}^2 + \kappa_{\theta\theta}^2) = \\ &= \frac{D}{2}\left[\kappa_r^2 + \kappa_{\theta\theta}^2) + 2(1-\nu)\kappa_r\kappa_\theta\right] = \\ &= \frac{D}{2}\left[h''(r)^2 + \frac{1}{r^2}h'(r)^2 + \frac{2\nu}{r}h'(r)h''(r)\right]\end{aligned} \tag{4.68}$$

The strain energy can then be obtained by integrating the strain density functions given in Eqs. (4.67) and (4.68):

$$U_{\text{stretch}} = \int_0^R \int_0^{2\pi} dr \cdot r d\theta \cdot \Phi_\varepsilon(r), \tag{4.69}$$

$$U_{\text{bend}} = \int_0^R \int_0^{2\pi} dr \cdot r d\theta \cdot \Phi_\kappa(r). \tag{4.70}$$

In addition to these contributions, the total energy will comprise a term related to the adhesion and a term related to the internal energy of the fluid within the bubble. These contributions can be expressed as [112, 165, 321, 326]:

$$U_{\text{adh}} = \gamma\pi R^2, \tag{4.71}$$

$$U_{\text{int}} = -\Delta p \int_0^R \int_0^{2\pi} dr \cdot r d\theta \cdot h(r), \tag{4.72}$$

where Δp is the difference between the trapped fluid pressure and the external pressure. The total energy is then given by the sum of these four terms (see Eq. (4.24)). By substituting the explicit expressions for the height profile and strain components and calculating the integrals, we get that:

$$U_{\text{stretch}} = \zeta(\nu, q)\frac{E_{2D}}{1-\nu^2}f^2(\nu, q)\frac{h_0^4}{R^2}, \tag{4.73}$$

with

$$\zeta(\nu, q) = \left[(1+\nu)\cdot\frac{c - 2g(\nu, q)}{c+2} + \frac{g^2(\nu, q) + 1 + 2\nu\cdot g(\nu, q)}{2c+2}\right]; \tag{4.74}$$

and

$$U_{\text{bend}} = \xi(\nu, q)\pi D\frac{h_0^2}{R^2}, \tag{4.75}$$

with

$$\xi(\nu, q) = q^2\cdot\frac{q + 2(q-1)\nu}{2q-2}; \tag{4.76}$$

and finally

$$U_{\text{int}} = -\frac{q}{q+2}\pi\Delta p h_0 R^2. \tag{4.77}$$

The bending term is actually expected to be negligible in atomically thin domes. However, we include it in order to verify *a posteriori* that the bending stiffness does

not play a significant role in the investigated system.

By minimising U_{tot} with respect to h_0 we obtain an explicit expression for the pressure:

$$\Delta p = \frac{q+2}{q}\left[4\zeta(\nu,q)\frac{E_{2D}}{1-\nu^2}f^2(\nu,q)\cdot\frac{h_0^3}{R^4}+2\xi(\nu,q)D\cdot\frac{h_0}{R^4}\right]. \tag{4.78}$$

To verify the accuracy of our analytical model, we compared the pressure calculated analytically via Eq. (4.78) and numerically, for MoS_2, graphene, and hBN domes (Fig. 4.13). Indeed, there is excellent agreement between our analytical estimate and the numerical one, while previous analytical models underestimated the numerical value by 7-50 %. In the case of MoS_2, we also compared our estimates

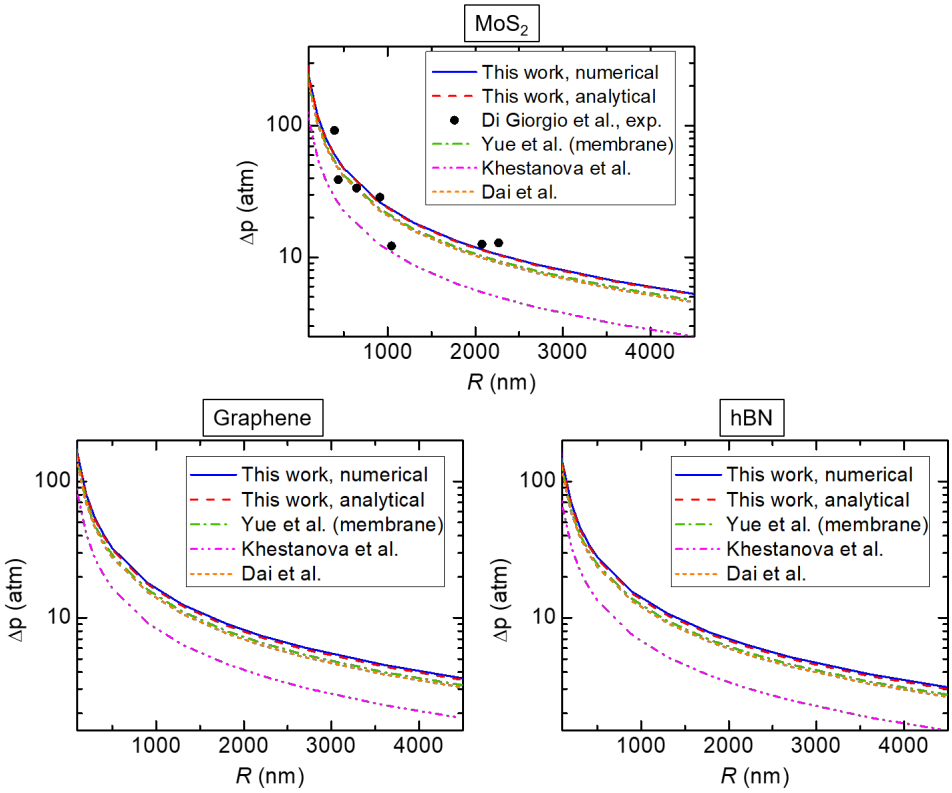

Figure 4.13: Pressure calculated analytically via (4.78) and compared to the numerical estimate. The calculations are performed for MoS_2 domes with aspect ratio equal to 0.16 and for graphene and hBN domes with universal aspect ratio equal to 0.115. The results obtained with previous analytical models are also shown for comparison. In the case of MoS_2, the pressure values measured experimentally in Ref. [75] on domes with aspect ratio equal to 0.16±0.02 are also displayed for comparison. Reproduced with permission from E. Blundo *et al.*, Phys. Rev. Lett. **127**, 046101 (2021) [116]. Copyright 2021 American Physical Society.

with the pressure values measured in universally shaped domes (with h_0/R between 0.14 and 0.18) via nano-indentation experiments interpreted in the membrane limit of the Föppl–von Karman equation in our previous work on nano-indentation experiments [75] (refer to Fig. 4.3). Indeed, there is a very good agreement between the theoretical trends and the experimental data.

An equivalent expression for the pressure can also be achieved by minimising U_{tot} with respect to R. In fact, by setting $\partial_R U_{\mathrm{tot}} = 0$, we get:

$$\Delta p = \frac{q+2}{q}\left[\frac{\gamma}{h_0} - \zeta(\nu,q)\frac{E_{2D}}{1-\nu^2}f^2(\nu,q)\cdot\frac{h_0^3}{R^4} - \xi(\nu,q)D\cdot\frac{h_0}{R^4}\right], \tag{4.79}$$

which brings to light the dependence of Δp on γ. Finally, by putting together Eqs. (4.78) and (4.79), we obtain an explicit expression for γ as a function of the Young's modulus:

$$\gamma = 5\zeta(\nu,q)\frac{E_{2D}}{1-\nu^2}f^2(\nu,q)\cdot\frac{h_0^4}{R^4} + 3\xi(\nu,q)D\cdot\frac{h_0^2}{R^4}. \tag{4.80}$$

If we define:

$$S(\nu,q) = 5\zeta(\nu,q)\frac{E_{2D}}{1-\nu^2}f^2(\nu,q), \tag{4.81}$$

Eq. (4.80) yields:

$$\left(\frac{h_0}{R}\right)^2 = \sqrt{\frac{\gamma}{S(\nu,q)} + \left(\frac{3\xi(\nu,q)D}{2S(\nu,q)}\right)^2\frac{1}{R^4}} - \frac{3\xi(\nu,q)D}{2S(\nu,q)}\frac{1}{R^2}. \tag{4.82}$$

This equation shows how, for negligible bending stiffness D, the aspect ratio is constant:

$$\frac{h_0}{R} \approx \left(\frac{\gamma}{S(\nu,q)}\right)^{\frac{1}{4}} = \left[\frac{\gamma}{E_{2\mathrm{D}}}\cdot\frac{1-\nu^2}{5\zeta(\nu,q)f^2(\nu,q)})\right]^{\frac{1}{4}}. \tag{4.83}$$

According to the idealised nonlinear plate model, the bending stiffness would take the form:

$$D = \frac{E_{2D}t^2}{12(1-\nu^2)}, \tag{4.84}$$

where t is the thickness of the membrane, while previous work argued that the bending rigidity of 2D materials should be actually lower due to the weak interlayer shear interactions typical for these materials [74]. This expression can be therefore intended as an upper limit for the real bending stiffness. By plugging Eq. (4.84) into Eq. (4.82), we obtain the behaviors shown in Fig. 4.14 for homostructured MoS_2 and hBN domes.

To make this plot, we fixed the adhesion energy γ so that the universal aspect ratio coincides with the experimentally measured one. We performed the calculations for different dome thicknesses (1 layer, 10 layers, 20 layers, 30 layers) and in the range of radii typically obtained via top-down and bottom-up approaches. The bending stiffness induces slight deviations from the universal value only for domes with thickness $>$ 20 layers and small size ($R < 200$ nm). Since the calculation was

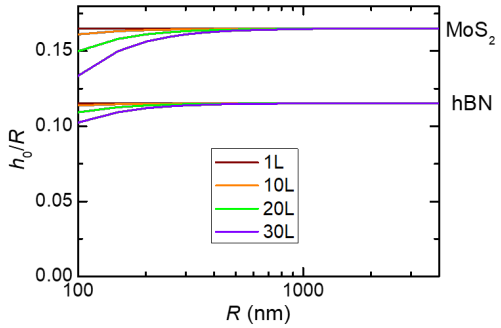

Figure 4.14: Aspect ratio calculated via Eq. (4.82) for MoS_2 and hBN homostructured domes as a function of the footprint radius, for several dome thicknesses. The bending term was estimated by taking the upper limit for the bending stiffness D, given by Eq. (4.84). Reproduced with permission from E. Blundo *et al.*, Phys. Rev. Lett. **127**, 046101 (2021) [116]. Copyright 2021 American Physical Society.

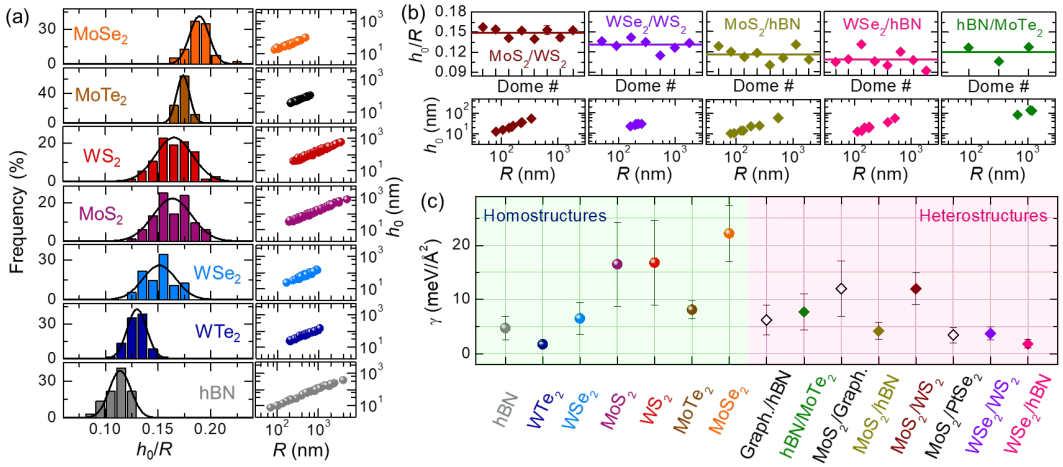

Figure 4.15: (a) Histograms of the aspect ratios (left) and corresponding h_0 *vs* R values (right) measured in homostructured domes. (b) h_0/R values (top; the lines are average values) and corresponding h_0 *vs* R (bottom) obtained for heterostructured domes. (c) Adhesion energies γ obtained via Eq. (4.80). Panels (a-b-c) reproduced with permission from Reproduced with permission from E. Blundo *et al.*, Phys. Rev. Lett. **127**, 046101 (2021) [116]. Copyright 2021 American Physical Society.

done by taking the upper limit for D given in (4.84), the real effect would be actually observable only in even smaller and thicker domes.

By neglecting the bending term, we see that the morphology of the dome — described by its aspect ratio h_0/R— is directly linked to the ratio between the adhesion energy γ and the elastic modulus E_{2D}, being $h_0/R \propto (\gamma/E_{2D})^{1/4}$ (see Eq. (4.83)). Therefore, our model for the adhesion energy leads to two important consequences. First, it predicts that, whenever D is negligible, the aspect ratio is universal, *i.e.*, constant independently of R. Second, it creates a direct link

between h_0/R and the adhesion energy and elastic parameters. Physically, the fluid expansion within a 2D-membrane-dome is counter-balanced by the elastic and adhesive properties of the membrane: The stiffness limits the vertical expansion of the dome, and thus the higher E_{2D}, the lower h_0/R; the adhesive energy, instead, tends to keep the membrane attached to the substrate thus limiting the lateral expansions, so that the higher γ, the higher h_0/R. The universality of the aspect ratio has already been predicted numerically [165] —but in that case the relationship between the different parameters is not apparent— and analytically [112, 326] — leading however to significant discrepancies for γ with respect to the numerical estimation, as discussed later. Notice that Eq. (4.82) holds independently of the dome thickness, in agreement with the fact that thick hBN domes in Ref. [170], few-layer-thick hBN domes in this work, and single-layer hBN domes in Ref. [112] are characterised by the same h_0/R value (~ 0.11), despite being characterised by different thicknesses. This is related to the fact that both γ —as proven in Ref. [325]— and E_{2D} (being defined as $E_{2D} = Yt$, where Y is the 3D Young's modulus) scale linearly with the number of layers N, implying that the aspect ratio doesn't show any dependence on N. This is particularly relevant because γ can be directly estimated from the measurement of h_0/R and q and the knowledge of the elastic parameters, whilst the exact knowledge of N (which is often hard to determine experimentally) is not needed.

By measuring hundreds of AFM profiles, we experimentally determined the universal h_0/R values for a variety of homo- and hetero-structured domes, as shown in Fig. 4.15(a-b). In the former case, we could perform large statistical analyses. For the HSs, large statistical analyses could not be performed due to the lower fabrication yield. We thus estimated the universal value as an average of the measured h_0/R values. Indeed, a constant aspect ratio is found for each material/substrate combination, in agreement with theory and with previous experimental observations [112, 156, 166, 170, 171, 216].

Indeed, once the universal aspect ratio is determined, it is possible to estimate the adhesion energy γ via Eq. (4.80), given that $E_{2\mathrm{D}}$ is known by experiments such as those discussed previously, the Poisson's ratio ν is known from theory, and the constant q in Eq. (4.57) has been determined experimentally [116]. In Table 4.3, we list the elastic parameters employed in this work, and more specifically the Poisson's ratio ν and the Young's modulus Y.

The Poisson's ratio cannot be easily determined experimentally, and we have to rely on theoretical calculations. It should be noticed, however, that the Poisson's ratio does not vary much depending on the material. By looking at the values calculated via several approaches and in different works, the variations we find are such that the adhesion energy we estimate changes by less than 3 %. Thus, the uncertainty in this parameter will not affect our estimates remarkably.

On the other side, the Young's modulus can be estimated experimentally, as discussed previously. The results obtained in different works in the literature with different methods and on a same materials are generally consistent among them-

selves, which ensures that it is reasonable to rely on the values measured in the literature. In this work, we thus relied on the Poisson's ratio ν of each material taken from The Materials Project [21, 331] or Ref. [332], and on the Young's modulus Y measured experimentally in Refs. [74, 333, 334] for graphene, [56, 74] for hBN, [15, 74, 75, 305, 311, 334, 335] for MoS_2, [311, 316] for $MoSe_2$, [336] for $MoTe_2$, [311, 334] for WS_2, [311, 317] for WSe_2, and [313] for WTe_2. For most of the materials, Y was measured in several works and we considered an average value. The 2D Young's moduli E_{2D} are related to the 3D values Y by: $E_{2D} = Y \cdot t$, where t is the membrane thickness. Therefore, $E_{2D} = N \cdot E_{2D}^{1L}$, where N is the number of layers and by considering the following single-layer thicknesses: $t_{TMDs} = 0.625$ nm for TMDs, $t_{Graph.} = 0.335$ for graphene, and $t_{hBN} = 0.333$ for hBN.

Material	ν	Y (GPa)	E_{2D}^{1L} (N/m)
Graph.	0.176	997	334
hBN	0.223	817	272
MoS_2	0.250	269	168
$MoSe_2$	0.233	201	125
$MoTe_2$	0.245	102	64
WS_2	0.219	260	162
WSe_2	0.196	165	103
WTe_2	0.176	80	50

Table 4.3: Values of the Poisson's ratio ν (from Refs. [21, 331] or Ref. [332]), and of the 3D Young's modulus Y (calculated as an average of the values measured in Refs. [15, 74, 313, 316, 317, 333–337]) used in this work. From Y, we derived the 2D Young's modulus for a 1L-thick membrane as: $E_{2D}^{1L} = Y \cdot t^{1L}$, where the following single-layer thicknesses were considered: $t_{TMDs} = 0.625$ nm for TMDs, $t_{Graph.} = 0.335$ for graphene, and $t_{hBN} = 0.333$ for hBN.

The parameters of Table 4.3 were used to describe the elastic properties of the domes. As for the uncertainty, by estimating the standard deviation in the case of MoS_2, for which many different estimates of the Young's modulus are available, a relative error of 15 % is obtained. For the other materials, less estimates are available so that the standard deviation may be underestimated. We thus associated a relative uncertainty equal to 15 % to all the values displayed in Table 4.3.

The adhesion energy values determined with this approach for several vdW material combinations are shown in Fig. 4.15(c) and collected in Table 4.4, along with the average experimental aspect ratios and the q values that we obtained for each material combination (according to the notation: 2D-material/substrate). The aspect ratios measured in some previous works in the literature [112, 166, 170] are also displayed for comparison. For the material combinations not studied in this work (*i.e.*, for graphene/hBN, MoS_2/graphite, and MoS_2/$PtSe_2$), we relied on the q values estimated via FEM calculations. From the knowledge of q, we could calculate

2D-Mat./Substr.	h_0/R this work	h_0/R literature	q	$f(\nu,q)$	$g(\nu,q)$	$\zeta(\nu,q)$	$\xi(\nu,q)$	γ (meV/Å^2)
hBN/hBN	0.108 ± 0.012	0.10 [170], 0.11 [112]	2.124 ± 0.042	0.715	0.091	0.756	5.269	4.7 ± 2.2
MoS_2/MoS_2	0.164 ± 0.018	0.15 [166], 0.17 [112]	2.166 ± 0.030	0.716	0.055	0.795	5.526	16.5 ± 7.7
$MoSe_2/MoSe_2$	0.189 ± 0.009	/	2.204 ± 0.045	0.725	0.059	0.795	5.607	22.2 ± 5.2
$MoTe_2/MoTe_2$	0.174 ± 0.006	/	2.215 ± 0.042	0.728	0.061	0.794	5.625	8.1 ± 1.7
WS_2/WS_2	0.165 ± 0.018	/	2.247 ± 0.037	0.738	0.074	0.784	5.645	16.8 ± 7.8
WSe_2/WSe_2	0.151 ± 0.016	/	2.115 ± 0.027	0.719	0.121	0.727	5.119	6.5 ± 2.9
WTe_2/WTe_2	0.130 ± 0.009	/	2.138 ± 0.041	0.728	0.137	0.714	5.098	1.7 ± 0.5
Graph./hBN	/	0.11 [112]	2.19 (FEM)	0.737	0.126	0.728	5.257	6.2 ± 2.7
$hBN/MoTe_2$	0.120 ± 0.012	/	2.210 ± 0.037	0.730	0.074	0.780	5.549	7.7 ± 3.3
MoS_2/Graph.	/	0.15 [166]	2.21 (FEM)	0.724	0.047	0.807	5.676	12.0 ± 5.1
MoS_2/hBN	0.116 ± 0.010	0.14 [112] 0.15 [166]	2.20 ± 0.12	0.722	0.049	0.804	5.635	4.2 ± 1.6
MoS_2/WS_2	0.149 ± 0.007	0.14 [166]	2.24 ± 0.11	0.730	0.041	0.815	5.781	12.0 ± 2.9
$MoS_2/PtSe_2$	/	0.11 [166]	2.18 (FEM)	0.718	0.053	0.799	5.573	3.4 ± 1.4
WSe_2/WS_2	0.131 ± 0.009	/	2.109 ± 0.061	0.718	0.122	0.725	5.101	3.7 ± 1.2
WSe_2/hBN	0.109 ± 0.012	/	2.114 ± 0.097	0.719	0.121	0.726	5.116	1.8 ± 0.8

Table 4.4: Universal aspect ratio and q value we obtained for each material combination via the statistical analysis shown in Fig. 4.15, and in Figs. 4.8 and 4.9. For the aspect ratio, the values measured in domes created via the top-down method in Refs. [112, 166] and via the bottom-up method in ref [170] are also displayed for comparison. From the q values, we estimated analytically $f(\nu,q)$ via (4.63), $g(\nu,q)$ via (4.65), $\zeta(\nu,q)$ via (4.74), and $\xi(\nu,q)$ via (4.76). Finally, we could estimate the adhesion energy via (4.80) for negligible bending stiffness and for 1L-thick membranes. In the case of graphene/hBN, MoS_2/graphite, and $MoS_2/PtSe_2$, the h_0/R values were taken from the literature and not measured in this work; in the absence of information on the experimental q values, for these materials we determined q via FEM calculations.

analytically the parameters $f(\nu,q)$ via Eq. (4.63), $g(\nu,q)$ via Eq. (4.65), $\zeta(\nu,q)$ via Eq. (4.74), and $\xi(\nu,q)$ via Eq. (4.76). All the calculated values are displayed in the Table. Finally, we could estimate the adhesion energy via Eq. (4.80) (for negligible bending stiffness). To do that, we used the h_0/R values and q values estimated by our analysis, and we employed the values from the literature only in the absence of our estimates (*i.e.*, for graphene/hBN, MoS_2/graphite, and $MoS_2/PtSe_2$). It should be noticed that the adhesion energy is estimated for a 1L-thick membrane, since the E_{2D} values plugged into Eq. (4.80) are those displayed in Table 4.3. The uncertainty was estimated by error propagation, *i.e.* as:

$$\sigma(\gamma) = \sqrt{\left(\frac{\partial\gamma}{\partial E_{2D}}\sigma(E_{2D})\right)^2 + \left(\frac{\partial\gamma}{\partial(h_0/R)}\sigma(h_0/R)\right)^2}. \tag{4.85}$$

All the relevant values and parameters are summarised in Table 4.4.

To check that our model gives correct results, we performed a numerical estimate of γ for MoS_2 domes, assuming a universal ratio of 0.164. To do that, we ran our simulations for a fixed height value and different radii, in order to vary the aspect

ratio between 0.12 and 0.22. For each (R, h_0) pair, we determined the pressure, height profile, and strain distribution by FEM calculations. Since the total energy of the system is given by Eq. (4.24), the adhesion energy can be estimated by calculating each contribution to the total energy (from (4.69) to (4.72)) numerically, and minimising U_{tot} numerically with respect to R for fixed h_0.

In Table 4.5, we compare the adhesion energy calculated numerically with the analytical value obtained with our model, showing that there is a very good agreement between the two. We also notice that all the previous analytical models would lead to an underestimation of the adhesion energy. For instance, by energy minimisation in Yue *et al.* model and Dai *et al.* model, we find adhesion energy values underestimated by about 15 %, while by using Khestanova *et al.* model we find an adhesion energy value underestimated by about 50 %.

Model	γ (meV/Å^2)	Discrepancy
Numerical	17.12	/
This work, analytical ($q = 2.216$)	17.27	0.9 %
Yue *et al.* [326]	14.80	13.6 %
Dai *et al.* [115]	14.29	16.5 %
Khestanova *et al.* [112]	8.49	50.4 %

Table 4.5: Adhesion energy calculated numerically and analytically in the case of MoS_2 (from domes with $h_0/R = 0.164$) with the model developed in this work and with previous models (see Additional Material, sec. A11. In the case of our analytical model, we performed the calculation by setting $q = 2.216$, in order to perform the calculations on the same profile given by the numerical simulations. The discrepancy with respect to the numerical result is also displayed.

From the analysis of Fig. 4.15 and Table 4.4, we notice that, remarkably, γ varies by about one order of magnitude depending on the material combination, in contrast with the material-independent adhesion energy estimated for layered materials by DFT [286, 322]. Indeed, on the one side DFT calculations encounter difficulties in finding appropriate functionals to describe the system whenever strong local atom bonds and weak nonlocal vdW forces coexist. On the other side, DFT simulates an ideal system, which might differ from the real crystal, being characterised by the intrinsic presence of defects or subjected to oxidation. The development of methods to probe the adhesion energy experimentally —like those presented in this section— is therefore of prominent relevance.

The different γ values found experimentally for different crystals can be attributed to the different interplay between covalent and vdW bonds for the different crystals, to the different chemical environment for different atomic species, and to other effects. For instance, a slightly ionic bonding character was reported for hBN [338]; additionally, WTe_2, $MoTe_2$, and WSe_2 are known to quickly oxidise and degrade [339], and oxidation might lead to an adhesion energy decrease [340], as we observed

for these materials with respect to the other TMDs. The γ values measured for the HSs are generally comparable to or lower than those of the constituent layers. In this case, the use of top-down processes might render the system more susceptible to the surface state. In this respect, our model can thus be exploited to test the quality of HSs, since it provides valuable feedback on the actual adhesion between layers.

Chapter 5

Strain effect on the optoelectronic properties of TMDs

In the previous chapter, we have learned that 2D domes host sizeable and non-uniform strains, which can be estimated with relatively high accuracy by means of numerical or even analytical methods. This provides us with the opportunity to study how such strains affect the peculiar properties of the material and establish a correlation between strain and the observed effects.

Given the high interest in TMDs as materials for optoelectronics, we focused our attention on TMD domes and performed micro-PL (μ-PL) experiments along the diameter of the domes.

The high sensitivity of the band structure of TMDs to strain was clearly outlined in a series of early theoretical studies, wherein the effects of a uniform (uniaxial and biaxial) in-plane strain in TMD MLs were first investigated [212–214, 341–349]. In all cases, it was shown that the bandgap character, generally direct in unstrained TMD MLs, becomes indirect above a relatively low threshold of $\sim 1-3$ %, for both tensile and compressive strain. For tensile strain, this is due to a reordering of the critical points in the VB, while for compressive strain to a reordering in the CB [41]. Such evolution of the bandgap character descends directly from the different effects of strain on the different band edges. Fig. 5.1(a) shows the results of DFT calculations highlighting the effect of strain on the bandstructure; the calculations were performed by our collaborators Dr. Paulo E. Faria Jr and Prof. Jaroslav Fabian (Institute for Theoretical Physics, University of Regensburg, Germany) [350]. As a general rule, tensile/compressive strain leads to a reduction/increase of the direct bandgap energy at the K point, with a shift rate in the range $\sim 50-100$ meV/% (where the rate is referred to the total in-plane strain ε_{tot}) [41]. The precise value depends on the number of layers and on the specific MX_2 material. Such bandgap tuning can be efficiently characterised —*e.g.* via PL or reflectance measurements— by tracing the peak energy of the A exciton, a quantity which is known to move

together with the direct bandgap (given an almost strain-independent binding energy for the A exciton), as discussed later. The evolution of the B exciton has also been shown to follow closely that of the A exciton, in agreement with the idea of a pure, weakly strain-dependent, spin orbit-induced splitting. Strain has however a much stronger effect on the CB_Λ point (equivalently referred to also as the CB_Q or CB_T point) in the CB and on the VB_Γ point of the VB. More in detail, *tensile* strain affects the band structure by shifting upwards the valence band edge at the VB_Γ point at an higher rate with respect to the VB_K point, resulting in the establishment of an *indirect* VB_Γ-CB_K gap above a strain threshold of ~ 2 %, see Fig. 5.1(a).

On the other hand, one of the crucial effects of a *compressive* strain is the lowering of the conduction band edge at Λ_{CB}, while the K point shifts upward, resulting in a indirect Λ_{CB}-K_{VB} gap. In both the tensile and compressive strain cases, a further increase of the strain up to $\varepsilon_{tot} > 10 - 15$ % is predicted to result in an insulator-to-metal transition.[214, 345, 351, 352]

This general qualitative behaviour holds for all TMDs, with quantitative differences depending on the compound, as shown in Ref. [353], where the calculated trends with strain for the most relevant optical transitions are shown. The crossover strain varies depending on the compound, that accounts for a remarkable possibility to tune the electronic properties of single layer TMDs, holding relevance for the realisation of devices, where strain could be exploited on demand according to the specific needs.

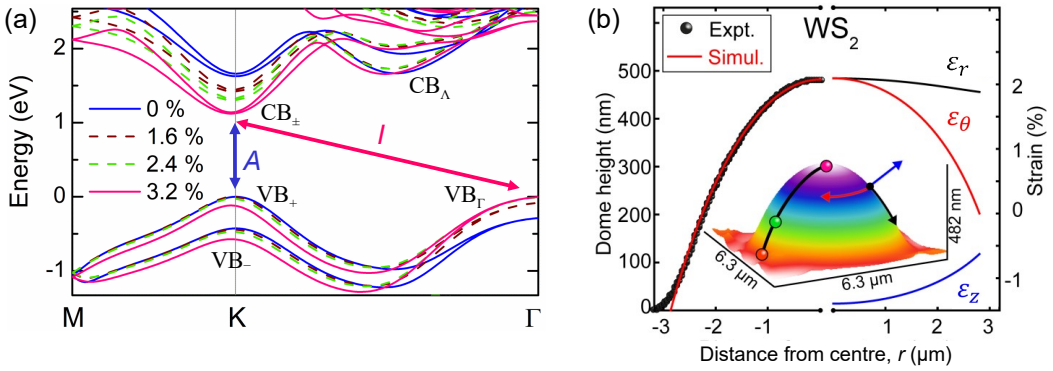

Figure 5.1: (a) First-principles calculations of the band structure of WS_2 ML for different biaxial tensile strain values. Adapted with permission from E. Blundo *et al.*, Phys. Rev. Lett. **129**, 067402 (2022) [350]. Copyright 2022 American Physical Society. (b) Left: Height profile of a WS_2 dome, measured by AFM (black dots; the AFM image is shown as inset), and computed by FEM calculations (solid red line). Right: FEM calculated strain tensor components, represented as colour-coded arrows in the inset. Adapted with permission from E. Blundo *et al.*, Phys. Rev. Res. **2**, 012024(R) (2020) [88]. Published under a Creative Commons Attribution 4.0 International License, Copyright 2020 The Author(s).

Several experiments confirmed the predicted bandgap reduction (increase) upon the application of in-plane tensile (compressive) strains, mostly via optical measure-

ments –as discussed in the following– and more rarely via direct inspection, *e.g.* via scanning tunnelling spectroscopy (STS). STS measurements offer the unique opportunity to measure at the same time the local strain and the electronic bandgap but they are indeed less easily accessible [354–357].

Although the possibility of using strain to switch the bandgap character of TMD MLs from direct to indirect is of significant fundamental interest, the reverse task, namely the possibility of changing in a controlled way the bandgap character of TMD multilayers from *indirect* to *direct*, would arguably represent an even bigger achievement, due to its potential importance for optoelectronic applications. The opportunity of using strain to achieve this goal is seemingly provided by WSe_2 multilayers, wherein a strain-induced indirect-to-direct bandgap transition was observed experimentally in PL experiments.[118, 242]

Probing strain effects in TMD domes by μ-PL

To probe the effect of strain on the optoelectronic properties of TMD MLs, we performed μ-PL experiments by scanning our laser spot along the diameter of TMD domes, such as that in Fig. 5.1(b). We now focus our discussion on WS_2, *i.e.* the material we investigated in more detail due to its high optical efficiency and to the fact that relatively large WS_2 domes (diameters of several μm) can be formed. Indeed, the formation of large domes allows us to probe strain effects with higher precision (due to the limited resolution of any optical setup). Fig. 5.2(a) shows the optical microscope image of a WS_2 flake acquired with a 50× (NA = 0.5) objective. The outer circular borders locate the footprint while the internal patterns of the domes are due to interference effects, the domes behaving as Fabry-Perót interferometers [156]. Fig. 5.2(b) shows an optical image of the same flake, excited by a defocused 532-nm laser, see Additional Material, sec. A4. The image was acquired at room temperature by filtering out the laser, thus letting the red luminescence (at ∼690 nm) generated by the domes be revealed. Peculiarly, the brightly emitting region is restricted to an outer ring-like area independently of the dome footprint [88]. It should be noticed that the non perfect uniformity of the collected light (in all domes, the luminescence pattern appears to be dimmer towards the bottom left edge) is related to the geometry of the setup, since the laser excites the sample laterally and therefore reaches the dome edges at different angles depending on the side, as discussed in detail in Additional Material, sec. A4 (specifically, see Fig. A4.3).

The fact that an analogous patter is found independently of the dome size excludes interference (which would be largely dependent on the dome size) to be the main origin of the observed luminescence pattern, differently from what recently reported in WS_2 domes obtained after annealing of chemical-vapour-deposition-grown MLs [216]. In that work, interference effects are likely enhanced by the SiO_2 substrate located right beneath the ML domes and strongly modulate the emission. On the contrary, in the present case, the peculiar ring-like emitting area stems from the strain field acting over the domes, as detailed in the following.

To perform our spatially resolved mapping experiments, the sample was placed

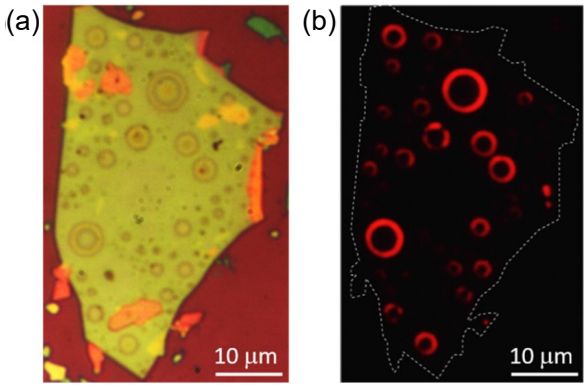

Figure 5.2: (a) Optical image of a WS_2 flake, where many relatively large domes formed after H-ion irradiation. (b) Laser-excited red luminescence coming from the same flake shown in (a). Reproduced with permission from E. Blundo *et al.*, Phys. Rev. Res. **2**, 012024(R) (2020) [88]. Published under a Creative Commons Attribution 4.0 International License, Copyright 2020 The Author(s).

on piezoelectric motors. The mapping was performed along a dome diameter (rather than over the whole dome) to reduce the data acquisition time and thus increase the accuracy of the measurements. The scanning step was 80 nm. Whenever we measured a certain dome, we checked that similar results were obtained also along different diameters. We will now discuss in particular the evolution of the μ-PL spectra of the same WS_2 dome whose AFM profile and calculated strain tensor are shown in Fig. 5.1(b) [88]. This dome was chosen since its size ($R = 2.85\mu$m) is much larger than the probing laser spot ($\sigma = 0.23$ μm), thus minimising diffraction effects. It's however important to note that the dome aspect ratio and, consequently, the strain distribution remains unchanged with the dome size [116], see Fig. 4.15, thus ensuring the general significance of the following results.

The normalised PL spectra acquired while moving from one edge to the apex of the dome are shown in Fig. 5.3 (where the bottommost spectrum is taken at the edge, and the uppermost at the apex of the dome) [88]. In particular, the three shadowed spectra (in red at the bottom, in purple on top, and in green in between) were acquired in the positions highlighted by the three dots displayed in the 3D AFM image of the dome shown in Fig. 5.1(b). Our PL mapping experiment reveals that the strain modulation across the dome indeed leads to dramatic variations in the PL lineshape on moving from the edge toward the centre of the dome and, concomitantly, the emission efficiency drops by about one order of magnitude, as we show in the colourmap of Fig. 5.4 [88]. Indeed, as shown in Fig. 5.3, the μ-PL spectra recorded close to the dome edge are dominated by the direct (CB_+,VB_+) band gap exciton A, whose energy is red-shifted by the strain exerted on the specific point of the dome. The redshift amounts to $\sim$ 160 meV with respect to the A exciton of the unstrained monolayer (at 2.00 eV, as shown in Fig. 0.6). A dramatic lineshape variation is however observed with increasing in-plane strain $\varepsilon_{\text{tot}} = \varepsilon_r + \varepsilon_\theta$ as the

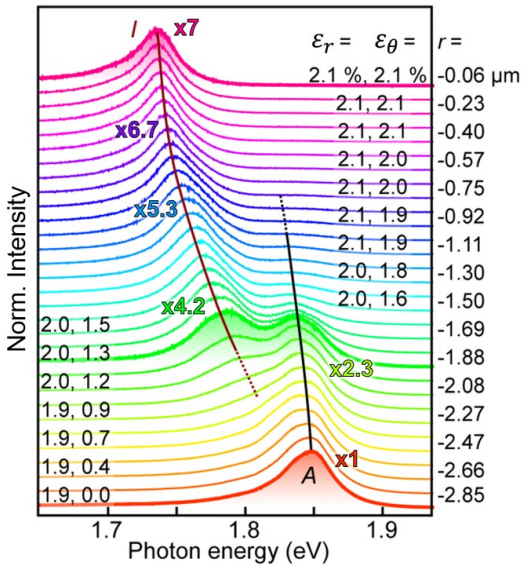

Figure 5.3: Evolution of the normalised μ-PL spectrum of the dome whose AFM profile and calculated strain tensor are shown in Fig. 5.1(b), as the laser spot is scanned from the dome's left edge (bottom) to its apex (top). The spectra were acquired at RT ($T \approx 290$ K). Some spectra are labelled with the position of the laser spot (r) and with the values of the radial (ε_r) and circumferential (ε_θ) components of the strain tensor. The solid lines follow the energy shift of the peaks associated with the A (black line) and I (wine line) exciton transition. The three shadowed spectra (in red at the bottom, in purple on top, and in green in between) were acquired in the positions highlighted by the three dots displayed in the 3D AFM image of the dome, shown in Fig. 5.1(b). Reprinted with permission from E. Blundo *et al.*, Phys. Rev. Res. **2**, 012024(R) (2020) [88]. Published under a Creative Commons Attribution 4.0 International License, Copyright 2020 The Author(s).

laser moves along the dome diameter In fact, as the excitation laser approaches the dome summit, the total strain increases and for $\varepsilon_{\text{tot}} \gtrsim 3$ % a new, less intense band —labelled I— takes over and eventually dominates the spectrum. The origin of such a peculiar behaviour can be explained in terms of a direct-to-indirect transition in the nature of the fundamental energy gap of the 2D crystal.

As discussed previously, numerous theoretical works [78, 212, 342, 345, 346, 358–361] have predicted the presence of strain in TMD MLs to lead to a direct-to-indirect bandgap transition: in WS_2 [212, 342, 345, 346, 358], in particular, the VBM should move from the K to the Γ point of the reciprocal space for a tensile biaxial strain $\varepsilon_{\text{biax}} \gtrsim 2$ % (corresponding to a total strain $\varepsilon_{\text{tot}} \gtrsim 4$ %), resulting in a change in the levels involved in the transition between the VBM and the CBM, see Fig. 5.1. Interestingly, even though this change is expected to occur for strain values that are well within reach of current strain modulation techniques [87, 243, 362–364] and this bandgap crossover should obviously result in rather dramatic variations of the optical properties of the material, to our knowledge there has not been any clear experimental evidence of this direct-to-indirect transition. This is possibly due to

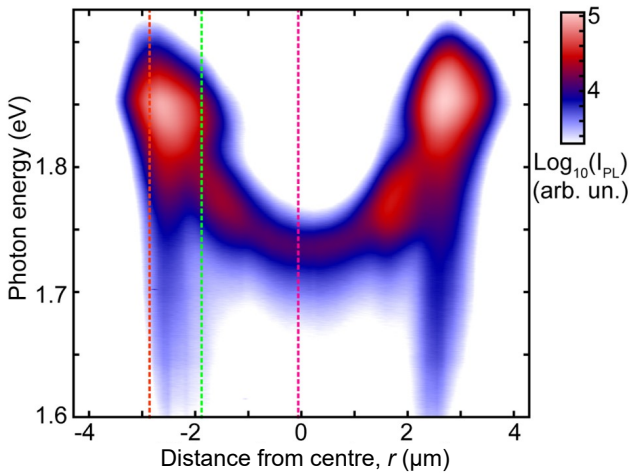

Figure 5.4: One-dimensional μ-PL scan across the dome (whose AFM profile and calculated strain tensor are shown in Figs. 5.1(b). This map is obtained by the spectra shown in Fig. 5.3. The horizontal axis indicates the laser spot position with respect to the dome centre (r), whereas the vertical axis indicates the energy of the emitted photons. The base-10 logarithm of the μ-PL intensity is shown in a false colour scale (see colourbar). The three dashed lines highlight the position of the dome apex (purple), and of its edge (red), as well as the approximate position of the direct-to-indirect band gap transition (green), and correspond to the shadowed spectra highlighted in Fig. 5.3 and to the three dots shown in Fig. 5.1(b). Reprinted with permission from E. Blundo *et al.*, Phys. Rev. Res. **2**, 012024(R) (2020) [88]. Published under a Creative Commons Attribution 4.0 International License, Copyright 2020 The Author(s).

a less-than-perfect adhesion between the material and the strain-inducing devices employed in some of the previous studies, resulting in an incomplete transfer of the applied stress to the investigated TMD ML. In the present work, however, this is not an issue, as large strains —ranging between $2-4$ %— are induced by the pressure exerted on the TMD ML by the H_2 gas trapped (and perfectly sealed) within the dome, similarly to refs. [87, 216], where, however, the direct-to-indirect transition was not noticed.

To confirm the previous attributions, we investigated the temporal decay of the μ-PL signal of WS_2 domes [88]. The domes were cooled down to 50 K to minimise the contribution of non-radiative decay channels. To do that, we developed a strategy to prevent the reduction of the dome volume at cryogenic temperatures due to the cooling of the H_2 gas trapped inside the dome. In fact, even though this phenomenon is fully reversible (each dome reappears in its original position when the temperature is increased), the shrinkage at cryogenic temperatures affects the strain magnitude and makes it difficult to spatially resolve the μ-PL signal from different zones of the dome. This turns out to be problematic for time-resolved μ-PL measurements, which must be performed at low temperature to fully appreciate differences in the temporal behaviour of the direct and indirect exciton.

We thus deposited several chemicals and polymers over the domes and studied their effect. Interestingly, we found out that the deflation process is nearly brought to a halt by the deposition of a thin methylpentane layer on the sample surface, see Fig. 5.5, thus making it possible to spatially resolve the PL signal from different zones of the dome. Indeed, the adhesion of methylpentane to the domes is enough to nearly stop their contraction with decreasing T, without altering the dome emission properties.

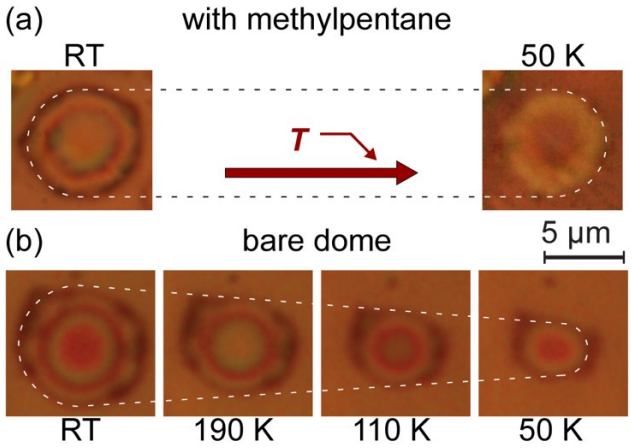

Figure 5.5: (a) Optical microscope images of the WS_2 dome on which the time-resolved μ-PL measurements were acquired. The image on the left was acquired at room temperature ($T \approx 290$ K), whereas the image on the right was taken at $T = 50$ K. Even though the same $100\times$ objective (NA = 0.75) was used for both images, the quality of the one acquired at $T = 50$ K is affected by the aberrations due to the presence of the optical cryostat window in between the objective and the sample. Nevertheless, the effects of methylpentane deposition are clearly visible, *i.e.*, the dome size becomes nearly insensitive to temperature changes. This is in sharp contrast with the situation depicted in panel (b), which displays the T dependence of the dome size in a "bare" (*i.e.*, not covered with methylpentane) sample. The dome shrinkage with decreasing T is clearly visible in the displayed optical images (acquired with a $50\times$ objective with NA = 0.5). Reprinted with permission from E. Blundo *et al.*, Phys. Rev. Res. **2**, 012024(R) (2020) [88]. Published under a Creative Commons Attribution 4.0 International License, Copyright 2020 The Author(s).

Fig. 5.6(a) shows the μ-PL spectra of a WS_2 dome recorded at the edge (where the A exciton dominates) and centre (where the I exciton can be observed along with the red-shifted A exciton recombination); see pictures in the insets. Fig. 5.6(b) shows the μ-PL decay curve relative to the different transitions displayed in (a). Most notably, the A and I excitons exhibit largely different temporal behaviours: The decay time of the A exciton is instrument-limited (< 250 ps) consistent with other reports [365, 366]. Instead, the I exciton shows a much longer temporal decay that can be fitted by a double exponential function with two decay times equal to (0.40 ± 0.06) ns and (2.9 ± 0.7) ns, which clearly points to an indirect (and thus, phonon-mediated) optical transition [366].

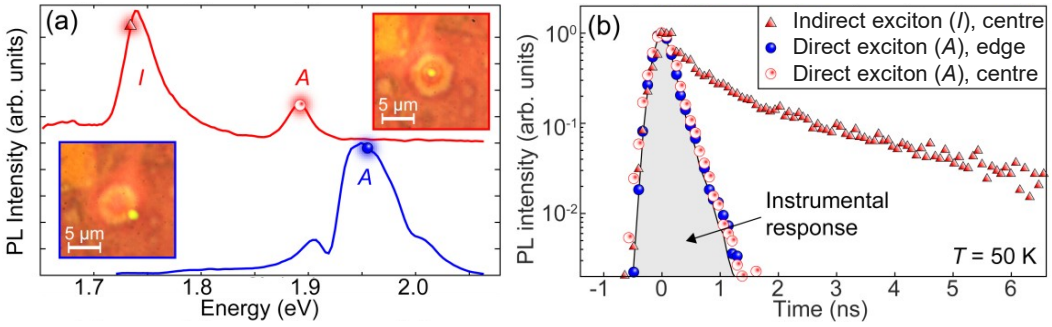

Figure 5.6: (a) $T = 50$ K μ-PL spectra recorded at the centre (red) and edge (blue) of a WS_2 dome. The insets are optical microscope images of the dome, showing the laser spot position corresponding to each spectrum. The symbols superimposed to the spectra indicate the energy at which the signal temporal decay shown in panel (b) was recorded. (b) Temporal evolution of the μ-PL signal relative to the specific photon energy and position on the dome highlighted in panel (a). The grey-shaded area refers to the exciting laser decay curve and sets the temporal resolution. Reprinted with permission from E. Blundo *et al.*, Phys. Rev. Res. **2**, 012024(R) (2020) [88]. Published under a Creative Commons Attribution 4.0 International License, Copyright 2020 The Author(s).

We now establish the strain conditions that induce the K-to-Γ crossover in the VB. This is an especially important aspect with regard to the optoelectronic properties of TMD MLs and to the enormous potential that mechanical stress holds to engineer those properties. For instance, the application of a seamless gradient of strain in these materials could be exploited as an efficient broad-band concentrator of photogenerated carriers in flexible solar cells [78]. Nevertheless, the occurrence of a strain-induced transition in the bandgap character may affect both the absorption/emission properties and the carrier dynamics characteristics of devices based on TMD MLs. Furthermore, in the present case, the strain gradient enables the spatial concentration of long-lived k-indirect excitons with potential benefit for creating exciton Bose condensates [367].

An analysis of the exciton energy shifts across the dome surface is expected to provide the strain-induced shift rates of the A and I excitons. Given the isotropic response to strain of TMDs [342], one would expect the peak energies to vary linearly with the total strain, as:

$$E_{A,I}(\varepsilon_{\text{tot}}) = E_{A,I}(0) - \Delta_{A,I}\varepsilon_{\text{tot}}. \tag{3}$$

Indeed, in Fig. 5.7 we analyse the strain dependence of the transition energies using the DFT data and including excitonic effects. The calculations were performed by our collaborators Dr. Paulo E. Faria Jr and Prof. Jaroslav Fabian (Institute for Theoretical Physics, University of Regensburg, Germany) [350]. We focus on the direct transitions, involving $CB_{\pm}$ and VB_{+} at the K-point, and the indirect transitions, involving $CB_{\pm}$ at the K-point and VB_{Γ} at the Γ-point (see Fig. 5.1 for the bands and notation). Excitonic effects are included using the effective Bethe-

Salpeter equation[368] considering parabolic bands (with the effective masses for different strain values summarised in Table 5.1) and the Rytova-Keldysh potential [369–371] for the bare monolayer (with $r_0 = 45.1$ Å [372]), following Refs. [353, 373, 374]. The optically active lowest-energy excitons (1s-like) that are probed experimentally are shown with solid lines: the A exciton stems from the CB_+ and VB_+ bands, whereas the I exciton stems from the CB_- and VB_Γ bands. The relevant energetic parameters extracted from our calculations of Fig. 5.7 are summarised in Table 5.2. Note that the shift rates are nearly the same for the DFT data and including excitonic effects. The largest difference appears in the energy separation at zero strain, $E_I(0) - E_A(0)$, and consequently in the strain value at the crossing point. The results displayed in Fig. 5.7 and Tables 5.1 and 5.2 refer to the case

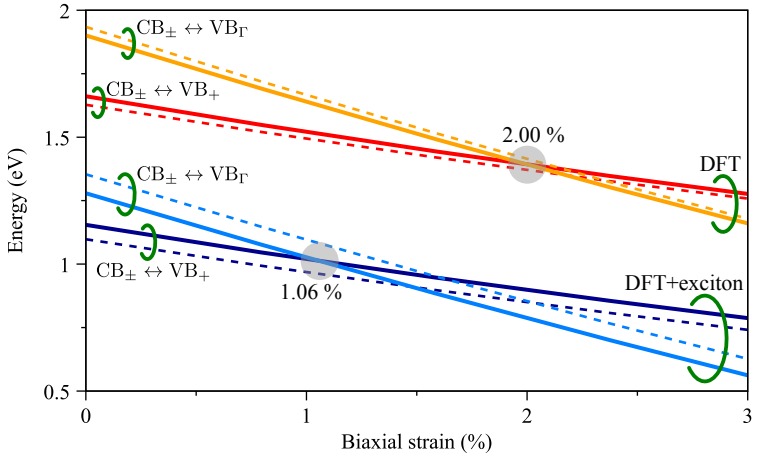

Figure 5.7: Transition energies of $CB_\pm$ (at the K point) to VB_+ (at the K point) and to VB_Γ (at the Γ point) as a function of the biaxial strain using the DFT calculations and with the inclusion of excitonic effects. The solid lines indicate the optically active excitons: the direct A exciton and the indirect I exciton. Reprinted with permission from E. Blundo *et al.*, Phys. Rev. Lett. **129**, 067402 (2022) [350]. Copyright 2022 American Physical Society.

Table 5.1: Lattice parameters, strain values and effective masses for the energy bands VB_Γ, VB_+, CB_- and CB_+.

a (Å)	ε (%)	VB_Γ	VB_+	CB_-	CB_+
3.155	0.0	-2.9129	-0.3376	0.3439	0.2580
3.180	0.8	-2.3675	-0.3330	0.3365	0.2486
3.205	1.6	-1.9903	-0.3220	0.3287	0.2388
3.230	2.4	-1.7071	-0.3124	0.3229	0.2310
3.255	3.2	-1.4928	-0.3045	0.3200	0.2252

Table 5.2: Energy separation of I (indirect) and A (direct) excitons at zero strain, $E_I(0) - E_A(0)$, shift rates Δ_A and Δ_I and the value of strain at the energy crossing for the DFT data, DFT including excitonic effects and their average value. Notice that the shift rates are calculated referring to biaxial strain.

	DFT	DFT+exciton	average
$E_I(0) - E_A(0)$ (meV)	239.6	124.8	182.2
Δ_A (meV/%)	-130.5	-124.7	-127.6
Δ_I (meV/%)	-249.8	-241.8	-245.8
Crossing (%)	2.00	1.06	1.53

of biaxial strain. To verify that the result is not significantly affected by the strain character, we performed analogous calculations also in the case of uniaxial strain. A comparison between the shift induced on the band gap by biaxial or uniaxial strain is shown in Fig. 5.8, where the results are plotted as a function of the equivalent biaxial strain for ease of comparison. Indeed, the behaviors obtained for biaxial

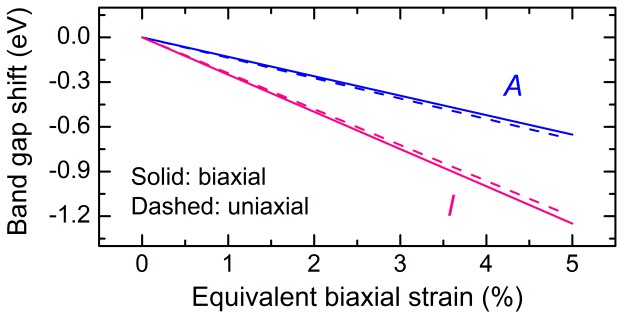

Figure 5.8: Bandgap shift induced by strain for both the direct A and indirect I transitions, in the cases of biaxial and uniaxial strain. The results are plotted as a function of the equivalent biaxial strain for ease of comparison.

and uniaxial strain almost overlap, suggesting that the electronic response to strain is substantially independent on the strain character. This result agrees with the findings of Ref. [342], where the authors calculated the bandgap of several TMDs under different kinds of strains (refer to Fig. 2 of Ref. [342]), and found that the bandgap shift rate under biaxial strain was almost exactly two times that obtained under uniaxial strain.

While a linear dependence of the energy on strain is expected, in the case of the domes a non-uniform strain distribution is present, causing the excitons to drift, thus altering the linear dependence. Fig. 5.9(a) illustrates a μ-PL experiment performed on a single dome, highlighting the relevant physical processes. Panel (b) shows the peak energy $E_{A,I}$ of the A and I exciton transitions derived from the same dome

of Figs. 5.3 and 5.4 as a function of the in-plane or total strain $\varepsilon_{\text{tot}} = \varepsilon_r + \varepsilon_\theta$ [88]. To correctly interpret the data, we have to consider that the continuous variation

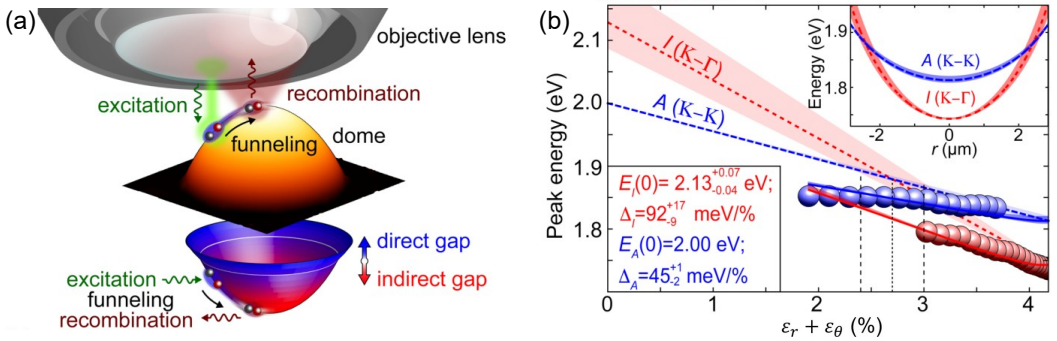

Figure 5.9: (a) Sketch of a μ-PL experiment (excitation+recombination) on a single WS_2 dome whose AFM image is shown in shaded orange), wherein an exciton drifts (funnel effect [78, 89]) over the dome due to the strain distribution, that induces a seamless bandgap reduction in going from the edge towards the centre. The blue-red paraboloid provides a correspondence between the dome AFM image and the exciton energy, highlighting the direct-to-indirect transition region. (b) Dependence of the energy of the direct (blue dots) and indirect (red dots) exciton transitions on the in-plane strain tensor, $\varepsilon_{\text{tot}} = \varepsilon_r + \varepsilon_\theta$. The continuous blue/red lines (relative to the direct/indirect exciton) are fits based on Eq. (3), while also taking funneling into account. These fits entail linear dependences of the exciton energies on ε_{tot}, which are displayed as dashed lines; the shaded areas enveloping each curve account for the uncertainty of our fitting procedure. In turn, these linear dependences yield the evolution of the direct and indirect exciton energy across the dome plotted in the inset of panel (b) (the paraboloid sketched in (a) is also based on this evolution). Reprinted with permission from E. Blundo *et al.*, Phys. Rev. Res. **2**, 012024(R) (2020) [88]. Published under a Creative Commons Attribution 4.0 International License, Copyright 2020 The Author(s).

of the strain field on the dome surface —and hence the progressive decrease of the bandgap energy from the dome edge toward its centre— leads excitons to drift towards the minimum energy available within their diffusion length before recombining, as illustrated in panel (a) [78, 89]. Such a *funnel effect*, combined with the finite exciting/collecting area of the objective, alters the correspondence between the coordinate r (and thus ε_{tot}) and the exciton energy derived from the emission spectra [89]. Refs. [89] and [78] demonstrated (experimentally and theoretically, respectively), that excitons in TMDs drift for hundreds of nm. The solid curves displayed in Fig. 5.9(b) result from a fit performed by taking into account the exciton funneling. In particular, funneling was taken into account following the model proposed in Ref. [89], *i.e.* by assuming that exciton annihilation takes place in the minimum energy available within the objective collection area (in our case, towards the dome apex) rather than at the centre of the exciting laser spot. The fit was thus performed while fixing the radius of the collection area R_c to 2.5σ ($\sigma = 0.23$ μm is the laser spot size). The actual —*i.e.*, free from the funnel effect; see Eq. (3)— "linearised" strain dependence of the A (I) exciton is shown in Fig. 5.9(b) as a blue

Table 5.3: Redshift rates of excitons in WS_2 (A, B, C and D are direct excitons located at increasingly higher energies [45]; A^- indicates trion recombination; I is the indirect exciton). Notice that the shift rate is calculated via Eq. (3), and hence with respect to the total in-plane strain ε_{tot}. Therefore, the values displayed here may differ from those reported in the corresponding works, where the shift rate is often calculated with respect to the bending/stretching strain or to the biaxial strain.

Mater.	#L	Ref.	system	measurement	Δ (meV/%)					
					A	A^-	B	C	D	I
WS_2	1L	Blundo *et al.* [[88]]	dome	PL	45^{+1}_{-2}	/	/	/	/	92^{+17}_{-9}
		Tedeschi *et al.* [[156]]	dome	PL	~ 52	/	/	/	/	/
		Y. Wang *et al.* [[364]]	stretching (uniax., mech.)	PL	15.1	/	/	/	/	24.9
		F. Wang *et al.* [[315]]	bending	PL	75.2 ± 1.8	115.1 ± 6.3	/	/	/	/
		Mennel *et al.* [[375]]	bending	PL	78.4 ± 4.9	/	/	/	/	/
		Liang *et al.* [[376]]	bending	PL	128	/	/	/	/	/
		Niehues *et al.* [[240]]	bending	PL	64	/	/	/	/	/
		Niehues *et al.* [[240]]	bending	absorption	70	/	/	/	/	/
		Li *et al.* [[246]]	bending	PL	55	/	/	/	/	/
		He *et al.* [[239]]	bending	PL	59	55	/	/	/	/
		Carrascoso *et al.* [[377]]	bending	reflectance	56.3 ± 2.8	/	/	/	/	/
		Frisenda *et al.* [[363]]	stretching (biaxial, thermal)	reflectance	47	/	/	/	/	/
	2L	Carrascoso *et al.* [[377]]	bending	reflectance	39.8 ± 3.5	/	49.3 ± 9.2	/	/	/
	3L	Carrascoso *et al.* [[377]]	bending	reflectance	50.8 ± 4.9	/	59.4 ± 9.1	/	/	/

(red) dashed line. The surrounding shaded areas —covering the regions spanned by the trends computed for $2\sigma \leq R_c \leq 3\sigma$— represent the uncertainty of our procedure. This analysis permits to set the direct-to-indirect band gap crossover point at $\varepsilon_{\text{tot}} = (2.7 \pm 0.3)$ % highlighted by vertical dashed lines in Fig. 5.9(b). Finally, the top-right inset in Fig. 5.9(b) provides the A and I exciton energy as a function of the dome radial coordinate. The displayed fits yield $\Delta_A = 45^{+1}_{-2}$ meV/%, $E_I(0) = 2.13^{+0.07}_{-0.04}$ eV and $\Delta_I = 92^{+17}_{-9}$ meV/% ($E_A(0)$ is fixed to 2.00 eV, the strain-free ML exciton energy). Our shift rate for the A exciton agrees well with those reported in previous works, as shown in Table 5.3. Our data compare also rather favourably with the theoretical ones, as shown in Table 5.4.

We finally point out that we observed similar findings also in MoS_2 and WSe_2. This gives to our results a particular relevance regarding the general electronic properties of TMD 2D crystals. In Fig. 5.10, we show the μ-PL spectra recorded in different points of a single MoS_2 (left) and WSe_2 (right) dome, showing the dramatic changes of the emission spectrum on going from the dome edge to its centre. For the Mos_2 dome, at the edges of the dome (red dot in the inset) the direct A exciton

Table 5.4: Comparison between the data reported in this work and those in different experimental (based on angle resolved photoemission spectroscopy, ARPES, experiments) and theoretical works. A (I) indicates the shift rate with strain of the A (I) exciton energy. $E_I(0) - E_A(0)$ is the indirect-direct exciton energy difference at zero strain (though this quantity in the other works corresponds to the difference of the electronic bandgap). $\varepsilon_{\text{crossover}}$ is the equivalent uniaxial strain at which the bandgap turns indirect.

		Our work	ARPES works	Theor. works
WS_2	Δ_A (meV/%)	45^{+1}_{-2}	/	59 [212], 67 [353], 66 – 75 [346]
	Δ_I/Δ_A	2.0	/	1.8 – 1.9 [346], 1.9 [353], 2.0 [212]
	$E_I(0) - E_A(0)$ (meV)	130^{+70}_{-40}	280 ± 10 [378]	77 [212], 173 [379], 242 [346], 274 [353]
	$\varepsilon_{\text{crossover}}$(%)	2.7 ± 0.3	/	≥ 2 [342, 345, 346, 353, 358, 361, 380]
MoS_2	Δ_A (meV/%)	37^{+3}_{-1}	/	47 [212], 52 – 61 [346], 66 [353]
	Δ_I/Δ_A	2.5	/	2.0 [212], 2.1 [353], 2.3 [346]
	$E_I(0) - E_A(0)$ (meV)	100^{+80}_{-50}	~ 300 [32]	13 [212], 110 [353], 127 – 184 [346], 148 [379]
	$\varepsilon_{\text{crossover}}$(%)	1.8 ± 0.7	/	≥ 0.1 [78, 212, 243, 342, 345, 346, 353, 359, 361, 380]

dominates the spectrum (red spectrum) and the B exciton can also be observed. According to our mechanical model, at the edges of MoS_2 domes the strain is strongly anisotropic with a radial component equal to ~ 2 % and an almost null circumferential component. The A peak appears to be broad and composite due to the intrinsic broad lineshape of MoS_2 and additionally to the complex strain distribution coupled to the finite resolution of our optical system and to funneling phenomena. These factors are also likely responsible for irregular behaviours close to the edges, such as the unexpected blueshift (of ~ 30 meV) observed while moving towards the dome centre (green dot). This peculiar behaviour is not fully understood and may possibly be related also to hybridisation phenomena between direct and indirect excitons (which we will discuss in more detail in the case of WS_2 in Chapter 6). Notice that deviations from the expected behavior towards higher energies were similarly observed also for uniaxially-strained MoS_2 monolayers in Ref. [243], for strains $\gtrsim 1.4$ %. The A band then redshifts while further going towards the centre, where strain features a more regular biaxial distribution with $\varepsilon_r = \varepsilon_\theta$. In between the edges and the centre (see green dot in the inset and corresponding green spectrum) a new band (I) appears, which we attribute to the indirect transition. This band starts dominating the spectrum at the dome summit (purple dot in the inset and corresponding purple spectrum). Notice that at the centre the I and A bands are redshifted by about 20 meV and 10 meV, respectively, with respect to the green dot, accordingly to the increase of biaxial strain and the theoretically predicted higher shift rate for the I transition with respect to the A transition [212, 346, 353]. The dashed orange line highlights the redshift of the I exciton. Concomitantly, a reduction in the PL signal is observed, the PL signal at the edge being ~ 10 times more intense than at the centre. Based on our μ-PL measurements on several MoS_2 domes, the bandgap crossover is found to occur for this compound for an in-plane strain of $\sim 1 - 2$ %. The results of a more quantitative analysis are displayed in Table 5.4 and therein compared with theory. The shift rate we derived is instead compared with that of other experimental works in Table 5.5.

Panel (b) shows an analogous analysis for a the WSe_2 dome —with footprint

Table 5.5: Redshift rates of excitons in MoS_2 (A, B, C and D are direct excitons located at increasingly higher energies [45]; A^- indicates trion recombination; I is the indirect exciton). Notice that the shift rate is calculated via Eq. (3), and hence with respect to the total in-plane strain ε_{tot}. Therefore, the values displayed here may differ from those reported in the corresponding works, where the shift rate is often calculated with respect to the bending/stretching strain or to the biaxial strain.

Mater.	#L	Ref.	system	measurement	Δ (meV/%) A	A^-	B	C	D	I
MoS_2	1L	Blundo *et al.* [[88]]	dome	PL	37^{+3}_{-1}	/	/	/	/	93
		Tedeschi *et al.* [[156]]	dome	PL	~ 50	/	/	/	/	/
		Lloyd *et al.* [[87]]	bulge centre	PL	50 ± 3	50 ± 3	50 ± 3	/	/	/
		Yang *et al.* [[362]]	bulging device	PL [1]	21 ± 2; 9.3	/	/	/	/	/
		Conley *et al.* [[243]]	bending	PL	60 ± 9	/	/	/	/	/
		K. He *et al.* [[235]]	bending	absorption	85 ± 7	/	91 ± 7	/	/	/
		Zhu *et al.* [[241]]	bending	PL	64	/	/	/	/	/
		Liang *et al.* [[376]]	bending	PL	53	/	/	/	/	/
		Niehues *et al.* [[240]]	bending	PL	37	/	/	/	/	/
		Niehues *et al.* [[240]-[381]]	bending	absorption [2]	56 ± 3; 56 ± 3	/	51 ± 5; 57 ± 5	/	/	/
		Li *et al.* [[246]]	bending	PL	81	/	/	/	/	/
		Li *et al.* [[246]]	bending [3]	PL	167	/	/	/	/	/
		X. He *et al.* [[239]]	bending	PL	75	/	/	/	/	/
		John *et al.* [[244]]	bending	PL	104 ± 5	/	/	/	/	/
		Carrascoso *et al.* [[377]]	bending	reflectance [4]	52.5 ± 7.9	/	41.1 ± 8.3	/	/	/
		Frisenda *et al.* [[363]]	stretching (biaxial, thermal)	reflectance	26	/	25	/	/	/
	2L	Lloyd *et al.* [[87]]	bulge centre	PL	46	/	~ 59	/	/	72
		Yang *et al.* [[362]]	bulging device	PL	13.7	/	/	/	/	44.6
		K. He *et al.* [[235]]	bending	absorption	95 ± 7	/	89 ± 7	/	/	/
		K. He *et al.* [[235]]	bending	PL	64 ± 7	/	/	/	/	103 ± 7
		Zhu *et al.* [[241]]	bending	PL	61	/	/	/	/	115
		Conley *et al.* [[243]]	bending	PL	71 ± 13	/	/	/	/	172 ± 27
		John *et al.* [[244]]	bending	PL	45 ± 4	/	/	/	/	207 ± 15
		Carrascoso *et al.* [[377]]	bending	reflectance	51.3 ± 4.0	/	55.9 ± 2.8	/	/	/
	3L	Lloyd *et al.* [[87]]	bulge centre	PL	37	/	~ 54	/	/	55
		Yang *et al.* [[362]]	bulging device	PL	15 ± 2	/	/	/	/	7 ± 1
		Carrascoso *et al.* [[377]]	bending	reflectance	50.7 ± 1.3	/	48.7 ± 1.1	/	/	/

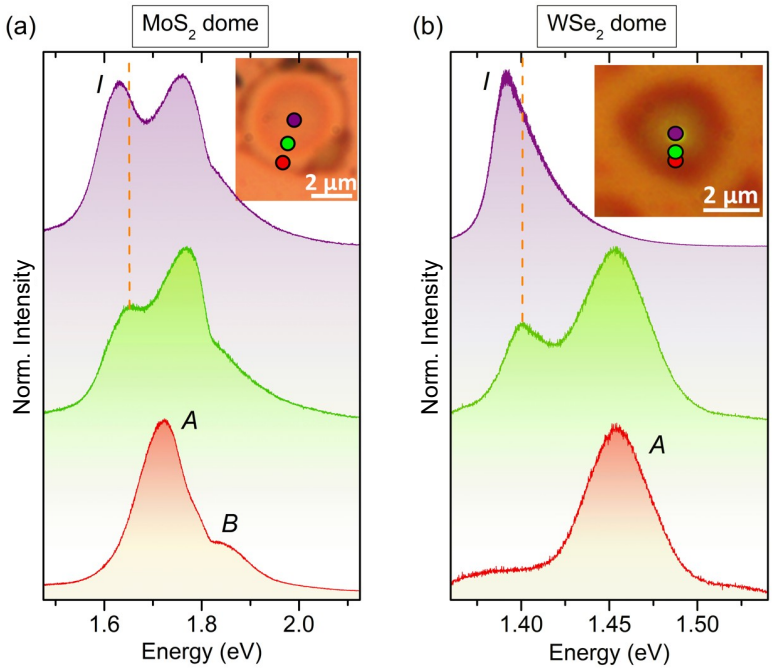

Figure 5.10: (a) μ-PL spectra acquired in the positions highlighted by the coloured dots in the MoS_2 dome (with footprint radius $R = (2.46 \pm 0.06)\mu$m) shown as inset. The spectra are peak-normalised for ease of comparison. At the edges of the dome (red dot in the inset) the direct A exciton dominates the spectrum (red spectrum) and the B exciton can also be observed. In between the edges and the centre (see green dot in the inset and corresponding green spectrum) a new band (I) appears, which we attribute to the indirect transition. This band starts dominating the spectrum at the dome summit (purple dot in the inset and corresponding purple spectrum). The dashed orange line highlights the redshift of the I exciton. (b) Same as in panel (a) for the WSe_2 dome (with footprint radius $R = (1.42 \pm 0.06)\mu$m) shown as inset. The direct A exciton dominates the spectrum at the edges (red dot in the inset and corresponding red spectrum). The indirect I band appears while moving towards the centre (green dot and corresponding green spectrum), redshifts while approaching the dome summit (as highlighted by the dashed orange line) and finally dominates the spectrum (purple dot and spectrum). Reprinted with permission from E. Blundo *et al.*, Phys. Rev. Res. **2**, 012024(R) (2020) [88]. Published under a Creative Commons Attribution 4.0 International License, Copyright 2020 The Author(s).

radius $R = (1.42 \pm 0.06)\mu$m— shown as inset. The direct A exciton dominates the spectrum at the edges (red dot in the inset and corresponding red spectrum). The indirect I band appears while moving towards the centre (green dot and corresponding green spectrum), redshifts while approaching the dome summit (as highlighted by the dashed orange line) and finally dominates the spectrum (purple dot and spectrum). On the other side, the A band does not feature any shift between the spots highlighted by the red and green dots. Indeed, given that this WSe_2 dome has a radius of 1.42μm, it's reasonable to think that when exciting the red and green spots

highlighted in the inset, the A exciton recombination takes place in the same region due to funneling, which explains why we do not see any shift.

For this compound, no significant quenching of the PL signal is observed for increasing tensile strain, the signal often increasing while going from the edges towards the dome summit. An increase in the PL emission was also observed in Ref. [242] for a WSe_2 monolayer under uniaxial strain. In our domes, however, the signal is observed not to decrease even in presence of the direct-to-indirect bandgap transition (for the dome here shown the signal at the centre is found to be almost 10 times higher than at the edges). This enhancement in the PL efficiency is likely aided by funneling effects combined with the small dimensions of the WSe_2 domes we can create: The larger domes have dimensions comparable to that of the excitation laser spot, resulting in funneling of excitons at the dome summit and thus favouring the indirect transition. For WSe_2, the bandgap crossover is found to occur for an in-plane strain of $\sim 2-3$ %.

Evidence of a direct-to-indirect transition was also later reported in a few other works in the literature, such as in the case of a MoS_2 monolayer deposited on a SiO_2 pillar [262]. Wrinkles were observed in correspondence with the pillar apex, where a maximum strain was reached. A new band was therein observed to take over the A transition, and was attributed to the k-space indirect transition involving holes at the Γ point of the VB [262]. A 2.4 % biaxial tensile strain was eventually deduced at the pillar apex from the A exciton energy shift. This is in relatively good agreement with the transition strain value $\varepsilon_{\mathrm{tot}} = (1.8 \pm 0.7)$ % found by us for MoS_2 [88].

Chapter 6

Strain effect on the valley properties of TMDs probed at high magnetic fields

TMD MLs have indeed attracted great interest since their symmetry-related electronic and optical properties provide a wealth of opportunities [382, 383]. In particular, the optical selection rules make it so that the optical transitions (A and B excitons) at the +K point of the Brillouin zone are coupled exclusively with σ^+ circularly polarised optical fields, while those at the -K point are coupled exclusively with σ^- circularly polarised optical fields [24]. On the other side, if the A exciton at the +K point involves spin-up conduction and valence spin-split subbands, due to time reversal symmetry the analogous subbands at the -K point are the spin-down ones. Notice that instead the B exciton always involves subbands with opposite spin with respect to the A exciton [24]. In turn, from the optical selections rules and time reversal symmetry, the valley optical selection rule becomes spin-dependent selection rules, in the sense that by selecting light with σ^+ (σ^-) polarisation, one is selecting the spin-up (spin-down) A exciton from the +K (-K) point of the Brillouin zone.

Hence, the valley quantum number —associated with the ±K band edges at the corners of the hexagonal Brillouin zone— can be used to encode and process binary information via exciton-mediated absorption/emission of circularly-polarised light of opposite helicity [384].

Indeed, excitons in TMD MLs can be regarded as valley-carrying bits, whose characteristics are embodied in the gyromagnetic (g-) factor determinable by magneto-optical spectroscopies [43, 46–52, 385–393]. Under magnetic field, excitons involving the ±K states (with $\sigma^\pm$ polarisation) separate in energy (E) resulting in a Zeeman splitting (ZS):

$$\mathrm{ZS}(B) = E^{\sigma^+} - E^{\sigma^-} = g_{\mathrm{exc}} \cdot \mu_{\mathrm{B}} B = 2(g_{\mathrm{c}} - g_{\mathrm{v}}) \cdot \mu_{\mathrm{B}} B, \tag{6.1}$$

where μ_{B} is the Bohr magneton, g_{exc} is the exciton g-factor and g_{c} and g_{v} are the

CB and VB g-factors.

Many reports addressed the g-factor of excitons in TMD MLs [43, 46–52, 385–393], reporting g_{exc} values of about -4, implying a relatively sensitive response to magnetic fields. Some of the above-mentioned works [46–50, 52, 388] addressed also the diamagnetic shift of the A and B excitons, and, in some cases, besides the 1s exciton states, the excited states (2s, 3s, 4s, and up to 5s) were also probed, providing experimental measurements of important fundamental parameters such as the effective exciton masses, exciton dielectric properties, exciton binding energies, and exciton radii.

Recent works addressed also the g-factors of heterostructures [274, 394–398], where high values up to 16 in absolute value were reported for exciton transitions involving electrons and holes in different layers of the heterostructure (interlayer excitons).

Research on TMDs and their heterostructures is indeed intense; surprisingly, however, the influence of strain has not been systematically studied. We thus exploited our system to investigate the role of strain on the magneto-optical response of TMD MLs, focusing on WS_2.

Since a detailed study of the g-factor in the domes requires the measurements to be performed at RT, and since all previous studied reported on low-temperature measurements, we start our discussion by investigating the g-factor of a WS_2 ML at RT.

6.1 WS_2 monolayer

To study the effect of a magnetic field on an unstrained ML, we performed μ-PL measurements in a bitter magnet under magnetic fields up to 28.5 T, in steps of 1.5 T; see details in the Additional Material, sec. A16. The ML was obtained by mechanical exfoliation and deposited atop a SiO_2/Si substrate. Some selected spectra are shown in Fig. 6.1(a), for both the σ^+ and σ^- polarisation states. The two polarisation states Zeeman-split with increasing magnetic field, as shown in Fig. 6.1(b). The ZS was determined by fitting the PL spectra corresponding to the σ^+ and σ^- states with Lorentzian functions and calculating the difference between the two. Indeed, a very clean and regular behaviour is found, which is presumably attributable to the fact that our experiments are performed at room temperature, where the ML results to be quite homogeneous. All previous measurements in the literature were instead performed at low temperatures, where the co-existence of localised states make the PL spectra more sensitive to the position. By fitting the data in panel (b) through Eq. (6.1), we estimated $g_{A,\text{ML}} = -3.913 \pm 0.004$. We also checked that similar results are obtained by other approaches. In particular, (i) we estimated the ZS as the distance between the normalised σ^+ and σ^- peaks; such energy distance was measured at ~ 80 % of the peak height; (ii) we estimated the ZS by calculating the energy centre of mass of the peaks. By fitting the ZS, we obtained in case (i) $g_{A,\text{ML}} = -3.88 \pm 0.03$, and in case (ii) $g_{A,\text{ML}} = -4.149 \pm 0.007$. These

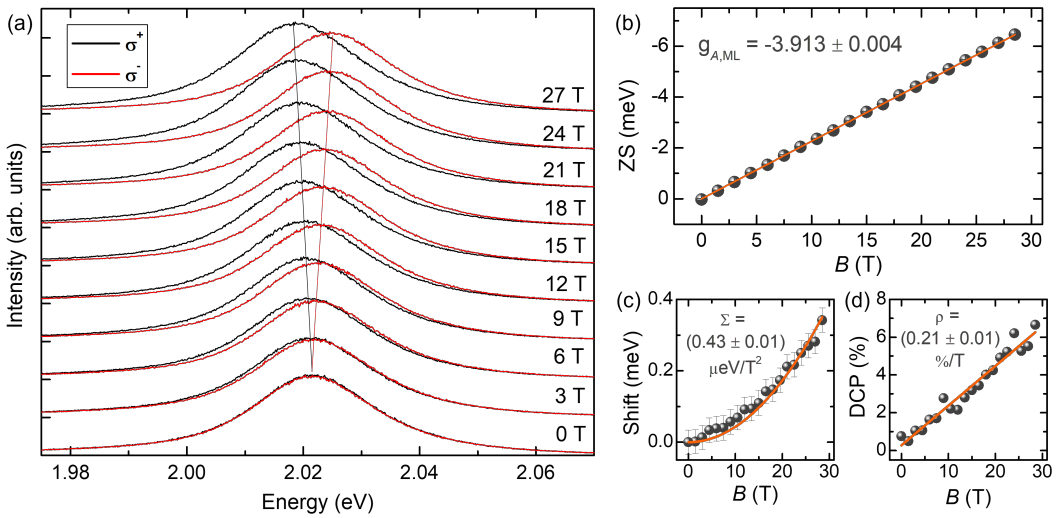

Figure 6.1: (a) Some selected spectra of the unstrained ML as a function of the magnetic field (in steps of 3 T, stacked by y-offset), for both the σ^+ and σ^- polarisation states. The spectra were taken at RT and are dominated by the A exciton. The black and red lines highlight the shift of the PL peak. (b) Zeeman splitting (ZS) *vs* B. The data were fitted via Eq. (6.1) and the obtained g-factor is displayed. (c) Shift of the PL peak energy (obtained as an average of the energies corresponding to the σ^+ and σ^- polarisation states) *vs* B. The data were fitted via Eq. (6.2) and the obtained diamagnetic shift coefficient Σ is displayed. (d) Degree of circular polarisation (DCP) *vs* B. The DCP increases linearly with B [see Eq. (6.3)], with the rate ρ displayed.

results are close to that obtained by the Lorentz-function method, which we will take as our reference. The slightly different values obtained by different approaches highlight how the standard deviation obtained by the fits underestimate the real uncertainty in the estimated g-factor.

Our estimate of the g-factor agrees well with those previously reported in the literature, as shown in Table 6.1, even though in all previous works the measurements were performed at low temperatures ~ 4.2 K. This implies that temperature does not influence much the physics of g_{exc}. This agrees with recent predictions [399] showing how g_{exc} remains nearly unchanged when the bandgap is modified, at variance with the band g-factors, that instead vary with the bandgap.

To further characterise the effect of a magnetic field on the ML, we studied the PL peak diamagnetic shift as a function of B, which is given by[46]:

$$\text{Shift}(B) = \frac{E^{\sigma^+} + E^{\sigma^-}}{2} = \frac{e^2}{8m^*}\langle r^2\rangle B^2 = \Sigma \cdot B^2, \tag{6.2}$$

where e is the electron charge, m^* is the reduced mass, and $\langle r^2\rangle$ is the expectation value of r^2 over the exciton wavefunction. The shift estimated by our data is shown in Fig. 6.1(c) and follows a quadratic behavior. By fitting the data via Eq. (6.2),

Table 6.1: Summary of the measured g-factors, diamagnetic shift coefficients (Σ, see Eq. (6.2)), and DCP rate (ρ, see Eq. (6.3)) in the literature. PL = photoluminescence, Refl. = reflectance, Tran. = transmittance, exfo. = exfoliated, CVD = chemical vapor deposition, encap. = encapsulated. The DCP refers to the PL emission, and it is thus not defined for reflectance or transmittance measurements.

g-factor	Σ (μeV/T^2)	ρ (%/T)	T (K)	Technique	Sample	Ref.
-3.5	/	/	5	PL	exfo., hBN encap.	Zinkiewicz *et al.* [387]
-4.25 ± 0.05	0.9	$0.3 - 0.7$	4.2	PL	exfo., on SiO_2	Plechinger *et al.* [388]
-3.94 ± 0.04	0.32 ± 0.02	$\times$	4	Refl.	CVD, on SiO_2	Stier *et al.* [46]
-4.3	/	/	4.2	PL	exfo., on SiO_2	Schmidt *et al.* [389]
-3.94 ± 0.10	/	/	2	PL	CVD, on SiO_2	Kuhnert *et al.* [390]
-4.35 ± 0.10	0.58 ± 0.03	$\times$	4.2	Refl.	exfo., hBN encap.	Zipfel *et al.* [49]
-3.7 ± 0.2	/	$\times$	4.2	Refl.	exfo., on SiO_2	Koperski *et al.* [43]
-4.0 ± 0.2	/	~ 1	4.3	PL	exfo., on SiO_2	
-4.0 ± 0.1	$\sim$0.41	$\times$	4	Tran.	exfo., hBN encap.	Goryca *et al.* [50]
-3.913 ± 0.004	0.43 ± 0.01	0.21 ± 0.01	$\sim$300	PL	exfo., on SiO_2	This work

we obtain a diamagnetic shift coefficient $\Sigma = (0.43 \pm 0.01)\mu\text{eV/T}^2$, in agreement with previous results (see Table 6.1). This shows that at room temperature it is still possible to get reasonable estimates of the diamagnetic shift coefficient. It should be noticed, however, that due to the very small diamagnetic shift values (less than 0.4 meV at 30 T), low temperature measurements are indeed more appropriate to get precise estimates of the coefficient due to the much smaller width of the exciton bands.

Finally, we characterised also the degree of circular polarisation (DCP) of our ML, which is found to increase linearly with B as:

$$\text{DCP}(B) = \frac{I^{\sigma^+} - I^{\sigma^-}}{I^{\sigma^+} + I^{\sigma^-}} = \rho \cdot B \tag{6.3}$$

Our experimental data are shown in Fig. 6.1(d) and a linear fit provides a DCP increase rate $\rho = (0.21 \pm 0.01)\%/\text{T}$. This value is lower than that estimated in previous works [43, 388] (see Table 6.1) consistently with the fact that our measurements were performed at RT, while in those works the data were taken at $\sim$ 4.2 K. Indeed, at low temperatures the thermal population between (Zeeman-split) higher- and lower-energy states results to be much more imbalanced with respect to RT.

6.2 Strained WS_2

While the direct-to-indirect exciton transition has been predicted in tens of theoretical works [212, 342, 345, 346, 353, 361], a compelling analysis of the I exciton in terms of bands and symmetries, and of the g-factor of A and I excitons under strain is lacking. To characterise the g-factor, one has to quantify the spin (S_z) and orbital (L_z) angular momentum of the energy bands involved in the exciton transitions. All the calculations reported in this Chapter were performed by our collaborators

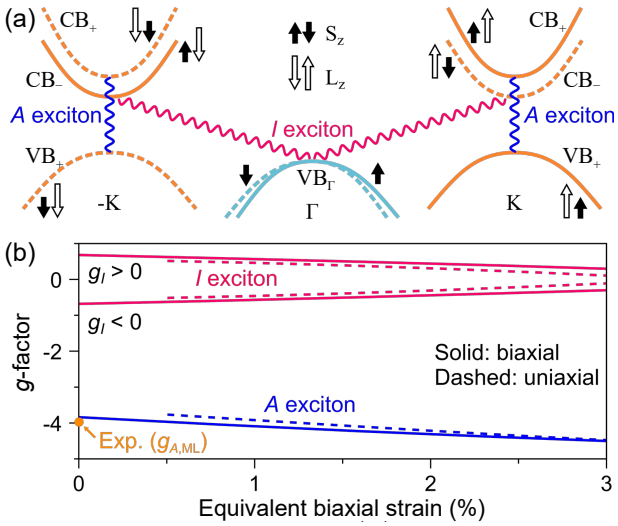

Figure 6.2: (a) Schematic of the important bands that constitute the A (CB_+,VB_+) and I (CB_-,VB_Γ) transitions. The arrows indicate the orientations of L_z and S_z. (b) First-principles calculations for the A and I exciton g-factors under biaxial (solid lines) and uniaxial (dashed lines) strain. The g-factors are plotted as a function of the equivalent biaxial strain (average of the two perpendicular strain components). The experimental g-factor at null strain is shown for comparison.

Dr. Paulo E. Faria Jr and Prof. Jaroslav Fabian (Institute for Theoretical Physics, University of Regensburg, Germany) [350]. Fig. 6.2(a) shows the schematic representation of the relevant CBs and VBs, indicating the corresponding orientation of S_z and L_z. The A exciton stems from CB_+ and VB_+ (with same spin), whereas the I exciton stems from CB_- (the lowest energy CB) and VB_Γ; see discussion of Fig. 5.7 and see Additional Material, sec. A15. The band g-factors are calculated using state-of-the-art *ab initio* techniques [399–402], which allows us to compute L_z not only at the K valleys but also at the Γ point. Particularly, we found $L_z \approx 0$ for VB_Γ over the whole range of analysed strain (see Additional Material, sec. A15). This result agrees with previous reports on unstrained $MoSe_2$ [400] and WSe_2 [401] MLs. For the A exciton, the spin-conserving selection rules that determine the g-factor sign are readily determined by the direct transitions involving CB_+ and VB_+ at the $\pm$K valleys (with $\sigma^\pm$ polarisation)[24, 403–405]. Conversely, to understand the magneto-PL emission of the I exciton, it is also necessary to account for the influence of phonons [406]. From a systematic analysis of the phonon-mediated selection rules using group theory, we found that different phonons with wavevector K (namely, the K_4 or a pair of K_5, K_6) could mediate the radiative recombination between CB_- and VB_Γ and lead to a ZS of two oppositely circularly-polarised components (see Additional Material, sec. A15). Combining the symmetry analysis of the optical transitions with first-principles calculations of the orbital angular mo-

mentum, we summarise the dependence of the effective g-factors of A and I excitons in Fig. 6.2(e), for both biaxial and uniaxial strain. Specifically, the g-factors are given by:

$$g_A = 2\left[L_z(\mathrm{CB}_+) - L_z(\mathrm{VB}_+)\right], \tag{6.4}$$

$$|g_I| = 2\left|L_z(\mathrm{CB}_-) - 2\right|, \tag{6.5}$$

L_z being calculated at different strain values. Our results reveal that strain slightly alters the g-factors of both A and I excitons. Since the radiative emission of the indirect exciton can be mediated by different phonons, we could not determine its g-factor sign and thus considered both the case of $g_I > 0$ and $g_I < 0$. For details on the selection rules, see Additional Material, sec. A15.

To probe the g-factors of strained WS_2 experimentally, we measured different domes, where the A or I transitions could be separately observed. Fig. 6.3(a) shows the RT μ-PL spectra at 0.0 T and 28.5 T recorded on an unstrained planar ML (grey-shaded) and on two different domes, showing A (light-blue-shaded) and I (pink-shaded) transitions. The planar ML was deposited on a SiO_2/Si substrate. While the substrate might induce some strain transfer, such strain is negligible with respect to the dome strains. The planar ML is thus referred to as 'unstrained'.

In all cases, a clear splitting between the σ^+ and σ^- components is observed at 28.5 T, but the strained domes feature a smaller ZS than the unstrained ML.

At 0 T, no splitting is observed for the unstrained ML, whereas a small Zeeman-like splitting can be noticed for the domes (see also the analysis performed for several other domes in the Additional Material, sec. A17. We speculate that strain-induced pseudo-gauge fields [407, 408] are at the origin of this phenomenon, which will be the object of future studies.

Fig. 6.3(b) depicts the field dependence of the ZS for the different excitons considered. As mentioned before, for the unstrained ML we have $g_{A,\mathrm{ML}} = -3.913 \pm 0.004$; see Fig. 6.1. The experimental g-factor agrees well with the theoretical calculations (-3.84) for the A exciton at zero strain, see Fig. 6.2(b) (and is also close to those estimated in previous works,[43, 46, 49, 50, 388] where the measurements were performed at $\sim$4.2 K).

Fig. 6.3(b) also shows the ZS obtained for the domes and the corresponding fits via Eq. (6.1). Interestingly, we find $g_{A,\mathrm{bubble}} = -2.47 \pm 0.10$, which amounts to a 40 % decrease with respect to the unstrained ML. Equally interesting, $g_{I,\mathrm{bubble}} = -2.49 \pm 0.12$, remarkably close to $g_{A,\mathrm{bubble}}$. We studied several other domes and estimated g_{exc} for A-type or I-type excitons subjected to slightly different strain values, finding similar g-factors, as detailed in the Additional Material, sec. A17. These results clearly contrast with the pure DFT picture given in Fig. 6.2(b). To understand the role of strain in determining the g-factor variation and bridge the gap between the null strain case and the high strain case, we studied samples characterised by lower strains. In particular, in a WS_2 dome with elongated geometry we observed a

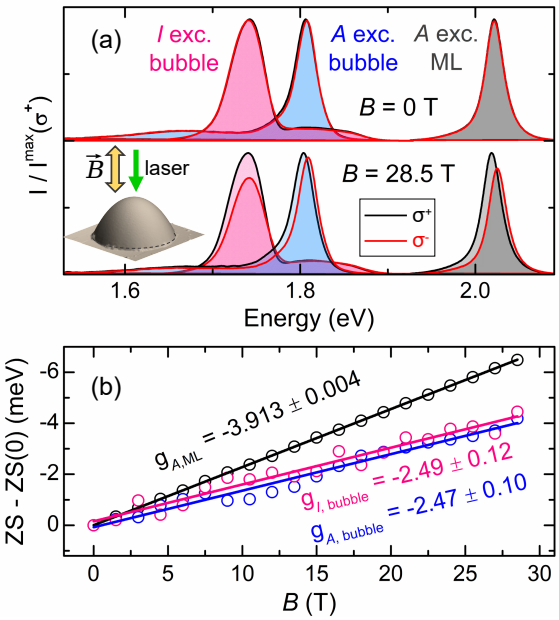

Figure 6.3: (a) $B = 0.0$ T and $B = 28.5$ T room-temperature μ-PL spectra filtered by circular polarisation $\sigma_{\pm}$. The gray-shaded spectra refer to the A exciton of the unstrained ML. The light-blue-shaded and pink-shaded spectra refer to the A and I exciton, respectively, of two WS_2 domes. Inset: Sketch of the magneto-μ-PL experiment on a single WS_2 bubble. (b) ZS *vs* B for the same samples. The error bars are not displayed for ease of visualisation (see Additional Material, sec. A17).

redshift of 90 meV ($\varepsilon_{\text{biax}} \approx 0.7$ %) and in a WS_2 ML deposited on a hBN bubble a small strain transfer was achieved, resulting in a redshift of 7 meV ($\varepsilon_{\text{biax}} \approx 0.06$ %).

6.3 Smaller strain in WS_2

6.3.1 Low-Strain Sample

To study the effect of small strains on the g-factor of WS_2 MLs, we prepared a sample as follows. We exfoliated a hBN bulk flake on a SiO_2/Si substrate and created few-layer-thick hBN domes by H-ion irradiation [169]. These domes host total strains of about 2 %, as discussed in Chapter 2 and Refs. [116, 169]. We then obtained a WS_2 thin flake by mechanical exfoliation. The flake is composed by a ML part attached to a bilayer (BL) part. The WS_2 flake was deposited in such a way that the ML portion covered a micron-size hBN dome, as demonstrated by the AFM image and by the sketch in Fig. 6.4(a). The surrounding part of the ML adheres to flat hBN. In such a manner, the ML portion on the flat area is not subjected to strain, while some strain is transferred to the ML portion deposited on the bubble. This is evident from the PL spectra shown in panel (b), acquired in the flat region (grey) and dome

region (orange) and showing how a strain-induced redshift of ∼7 meV is observable in the dome region. Based on the shift rates measured in previous works [41], the biaxial strain acting on the ML is $\sim 0.06 - 0.08$ %. Based on our comparison with the theoretical trends, we estimate $\varepsilon_{\text{biax}} \approx 0.06$ %. μ-PL measurements on

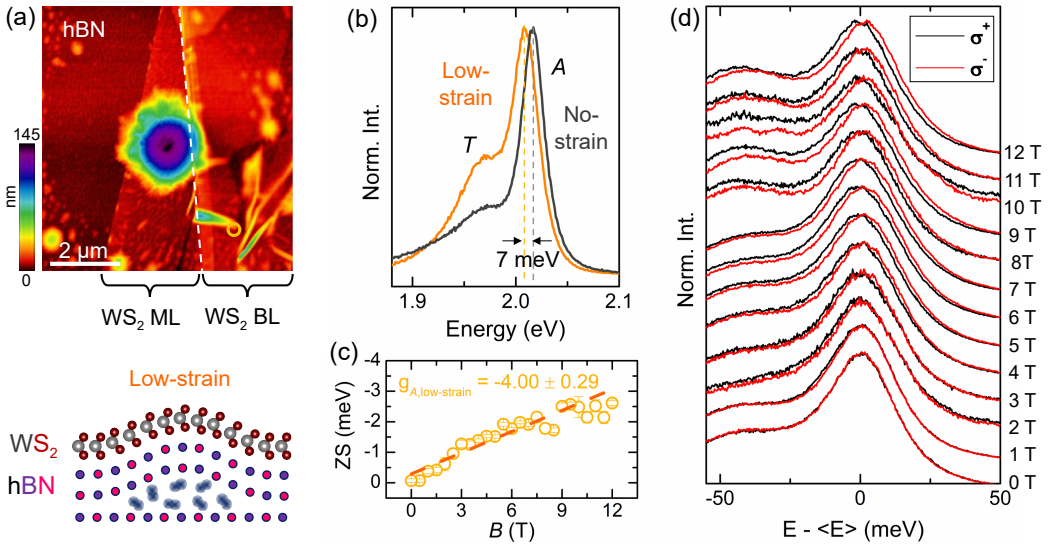

Figure 6.4: (a) Top: AFM image of the sample: An hBN sample was irradiated with H ions, resulting in the formation of H_2-filled hBN domes. A WS_2 flake was deposited atop of the hBN flake. The WS_2 flake was constituted by a ML part and by a bilayer (BL) part. The ML part covers an hBN bubble. The white dashed line highlights the border between ML and BL. Bottom: Sketch of the WS_2-covered hBN dome, where a low-strain is transferred to the WS_2 ML. (b) Normalised PL spectra acquired on the dome and on a flat area outside. The A exciton and the trion (T) are both observable. A redshift of 7 meV in the A exciton peak —induced by strain— is clearly observable on the dome. (c) Zeeman splitting (ZS) of the exciton peak *vs* B. The data were fitted via Eq. (6.1) and the obtained g-factor is displayed. (d) Some selected spectra (in steps of 1 T, stacked by y-offset) of the ML subject to a small strain as a function of the magnetic field, for both the σ^+ and σ^- polarisation states. At each field, the average energy was subtracted from the absolute energy scale for ease of comparison. The spectra were taken at RT.

this sample were taken in a superconducting magnet, from 0 T to 12 T in steps of 0.5 T, see Additional Material, sec. A16, for details. In panel (c), we show the derived ZS for the A exciton as a function of the magnetic field B, while in panel (d) we show some spectra (in steps of 1 T). From the ZS measurements, we find $g_{A,\text{low-strain}} = -4.00 \pm 0.29$, which is very close to the g-factor measured for the unstrained ML.

It should be noticed that Ref. [393] reported on g-factors between -2 and -4 measured at 4.2 K in some WSe_2 MLs subject to small uniaxial strains (redshifts <6 meV) ($g_{A,\text{ML}} = -4.02$ and -4.6 were measured in unstrained MLs), accompanied by an exciton splitting, which was attributed to a strain-induced intervalley electron-

hole exchange interaction [393]. In our case, however, neither an exciton splitting nor a g-factor variation were observed in the WS_2 ML deposited on the hBN dome, which is characterised by similar strains. We also repeated the same experiment by depositing a WSe_2 ML on hBN domes, achieving a redshift of 10 meV. Again, we found no splitting and a g-factor comparable to that of an unstrained ML; see Additional Material, sec. A18. The discrepancy between our results and those of Ref. [393] requires further investigation.

6.3.2 Medium-Strain Sample

Given the remarkable difference in the g-factor measured in highly strained domes (~ -2) and that measured in the low-strain sample (~ -4, close to the free-strain sample), we looked for samples with an intermediate strain. In particular, we noticed that by irradiating thin (few-nm-thick) WS_2 flakes with H-ions, we could form domes featuring a non-round shape, such as those in Fig. 6.5(a). By characterising the PL emission of these structures, we found that in a triangular dome the redshift of the PL band was about one half of that commonly found in round domes, see Fig. 6.5(b). Based on the shift rates measured in previous works [41], the biaxial strain acting on the ML is $\sim 0.7 - 1.0$ %. Based on our comparison with the theoretical trends, we estimate $\varepsilon_{\text{biax}} \approx 0.7$ %. We thus performed magneto-μ-PL measurements on this dome in the superconducting magnet. In this case, we performed multiple sweeps while varying the field between -12 T and +9 T in steps of 0.5 T. The choice of this range is due to the fact that we were suffering from drifts in the piezoelectric stages for fields above 6 T in absolute value. The drift was particularly relevant for fields between +9 T and +12 T. Similar problems were faced also for the other samples measured in the superconducting magnet, but in this specific case the dome had smaller size, which made it more difficult to recover the position when facing the drift. For this reason, we avoided measuring in the range from +9 T to +12 T for this dome. When using negative fields, we faced a lower drift, so that we could measure up to -12 T.

In 6.5(c), we show the derived ZS for the A exciton as a function of B including all the sweeps, which are generally in good agreement between each other. In panel (d) we show some selected spectra. From the ZS measurements, we find $g_{A,\text{low}-\text{strain}} = -3.86 \pm 0.35$, which is very close to the g-factor measured for the unstrained ML and for the low-strain sample.

6.4 Hybridisation of direct and indirect excitons and g-factor renormalisation

To interpret the experimental g-factors of ~ -2.5 in highly strained WS_2 domes (see Fig. 6.3(b)), we recall that our first-principles calculations (Fig. 6.2(e)) clearly establish that neither g_A nor g_I are strongly altered by strain at the orbital level. This

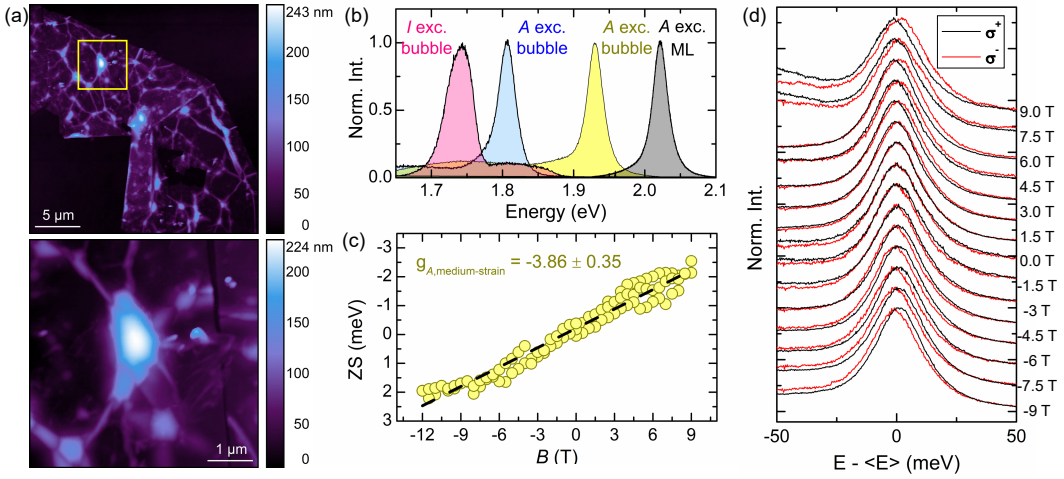

Figure 6.5: (a) Top: AFM image of the sample: A few-nm-thick WS_2 flake was irradiated with H ions, resulting in the formation of H_2-filled domes. Domes with triangular and elongated shape formed. Bottom: Zoom over the region highlighted by the yellow square in the top image, showing the presence of a dome with triangular shape. (b) Normalised PL spectra acquired on the triangular dome (yellow spectrum). The spectra acquired on the unstrained ML and on two characteristic domes (same spectra as those in Fig. 6.3) are shown for comparison. The comparison highlights how the redshift of the triangular dome —and thus the strain hosted by the dome itself— is about one half of that of round domes. (c) ZS of the PL from the triangular dome *vs* B. The data were fitted via Eq. (6.1) and the obtained g-factor is displayed. (d) Some selected spectra (in steps of 1.5 T, stacked by y-offset) of the PL peak as a function of the magnetic field, for both the σ^+ and σ^- polarisation states. At each field, the average energy was subtracted from the absolute energy scale for ease of comparison. The spectra were taken at RT.

suggests that additional mechanisms, beyond purely orbital effects, are responsible for the g-factor renormalisation. Since the two exciton species (direct and indirect excitons) become energy-resonant for increasing strain, we consider exciton hybridisation. For a generic coupling between excitons, either even or odd with respect to time-reversal symmetry, the strain and magnetic field dependence of the coupled A and I excitons can be described by the upper (U) and lower (L) branches. In particular, we can phenomenologically [409, 410] derive the following Hamiltonian, for a fixed value of strain and including the Zeeman splitting:

$$\begin{bmatrix} E_A + \frac{1}{2}g_A\mu_B B & 0 & \Delta_1 & \Delta_2 \\ 0 & E_A - \frac{1}{2}g_A\mu_B B & -\kappa\Delta_2^* & \kappa\Delta_1^* \\ \Delta_1^* & -\kappa\Delta_2 & E_I + \frac{1}{2}g_I\mu_B B & 0 \\ \Delta_2^* & \kappa\Delta_1 & 0 & E_I - \frac{1}{2}g_I\mu_B B \end{bmatrix}, \qquad (6.6)$$

in which we have used the exciton basis $\{A_1, A_2, I_1, I_2\}$ with time-reversal partners $|A_2\rangle = T\,|A_1\rangle$ and $|I_2\rangle = T\,|I_1\rangle$, *i.e.*, the basis set contains the two exciton states

(for each exciton type) that give rise to a Zeeman splitting. Assuming very general couplings, mediated by a potential V, the off-diagonal terms Δ_1 and Δ_2 are:

$$\begin{aligned}
\langle A_1 |V| I_1\rangle &= \Delta_1 \\
\langle A_2 |V| I_2\rangle &= \kappa\Delta_1^* \\
\langle A_1 |V| I_2\rangle &= \Delta_2 \\
\langle A_2 |V| I_1\rangle &= -\kappa\Delta_2^*\,,
\end{aligned} \tag{6.7}$$

with $\kappa = +(-)$ describing even (odd) operators with respect to time-reversal symmetry.

To capture the essential physics, we consider $\Delta_2 = 0$. The Hamiltonian (Eq. (6.6)) then becomes block diagonal and can be diagonalised analytically. Including the strain dependence in the parameters, we can write the energies of the Zeeman split states of the upper (U) and lower (L) branches:

$$\begin{aligned}
E_{U+}(\varepsilon) &= \frac{1}{2}\left[E_+(\varepsilon) + G_+(\varepsilon)\right] + \frac{1}{2}\sqrt{\left[E_-(\varepsilon) + G_-(\varepsilon)\right]^2 + 4\left|\Delta_1\right|^2} \\
E_{U-}(\varepsilon) &= \frac{1}{2}\left[E_+(\varepsilon) - G_+(\varepsilon)\right] + \frac{1}{2}\sqrt{\left[E_-(\varepsilon) - G_-(\varepsilon)\right]^2 + 4\left|\Delta_1\right|^2} \\
E_{L+}(\varepsilon) &= \frac{1}{2}\left[E_+(\varepsilon) + G_+(\varepsilon)\right] - \frac{1}{2}\sqrt{\left[E_-(\varepsilon) + G_-(\varepsilon)\right]^2 + 4\left|\Delta_1\right|^2} \\
E_{L-}(\varepsilon) &= \frac{1}{2}\left[E_+(\varepsilon) - G_+(\varepsilon)\right] - \frac{1}{2}\sqrt{\left[E_-(\varepsilon) - G_-(\varepsilon)\right]^2 + 4\left|\Delta_1\right|^2}\,,
\end{aligned} \tag{6.8}$$

with

$$\begin{aligned}
E_\pm(\varepsilon) &= E_A(\varepsilon) \pm E_I(\varepsilon) \\
G_\pm(\varepsilon) &= \frac{1}{2}\mu_B B\left[g_A(\varepsilon) \pm g_I(\varepsilon)\right] \\
E_{A(I)}(\varepsilon) &= E_{A(I)} + \Delta E_{A(I)}\varepsilon \\
g_{A(I)}(\varepsilon) &= g_{A(I)} + \Delta g_{A(I)}\varepsilon
\end{aligned} \tag{6.9}$$

in which $E_{A(I)}(\varepsilon)$ and $g_{A(I)}(\varepsilon)$ are the energies and g-factors as a function of strain. Indeed, both vary linearly with strain, as shown in Figs. 5.7 and 6.2. The possible energy values are given in Table 5.2 while for the g-factors we have $g_A = -3.84$, $\Delta g_A = -0.23$, $g_I = 0.68$ and $\Delta g_I = -0.12$, obtained by a linear fitting to the first-principles calculations shown in Fig. 6.2(b).

Eqs. (6.8) can be summarised as:

$$\begin{aligned}
E_{U\pm}(\varepsilon) &= \frac{E_+(\varepsilon) \pm G_+(\varepsilon)}{2} + \sqrt{\left[\frac{E_-(\varepsilon) \pm G_-(\varepsilon)}{2}\right]^2 + \Delta^2} \\
E_{L\pm}(\varepsilon) &= \frac{E_+(\varepsilon) \pm G_+(\varepsilon)}{2} - \sqrt{\left[\frac{E_-(\varepsilon) \pm G_-(\varepsilon)}{2}\right]^2 + \Delta^2}\,,
\end{aligned} \tag{6.10}$$

where, the subindex $\pm$ refers to the $\sigma^{\pm}$ component, and Δ is the coupling parameter encoding the exciton hybridisation.

Fig. 6.6(a) shows the effect of exciton hybridisation on the energy levels E_{U} and E_{L} (at zero magnetic field). At zero strain, the A exciton is below the I exciton. With increasing strain, the two excitons hybridise, marked by a distinct anticrossing in the energy levels. Eventually, for sufficiently large strain, the two exciton species are decoupled again and the I exciton is below the A exciton. Interestingly, this anticrossing has never been observed experimentally in a 2D system, differently from, *e.g.*, bulk semiconductor alloys [411]. Indeed, strain-induced exciton transitions (direct-to-indirect for MLs, indirect-to-direct for bilayers) were predicted [212, 342, 353, 361] and observed [88, 242, 262, 364] in several TMDs. Clear-cut evidences were however reported only at room temperature and in microscopic structures with variable strain and in particular in the domes (see Chapter 5 or our work [88]) or in MLs deposited on micro-pillars [262]. In these circumstances, exciton funnelling makes it difficult to establish experimentally a relation between energy and strain [41, 88, 89], and the width of PL bands is comparable to the L/U separation in the hybridisation region. These factors possibly prevented the observation of exciton anticrossing.

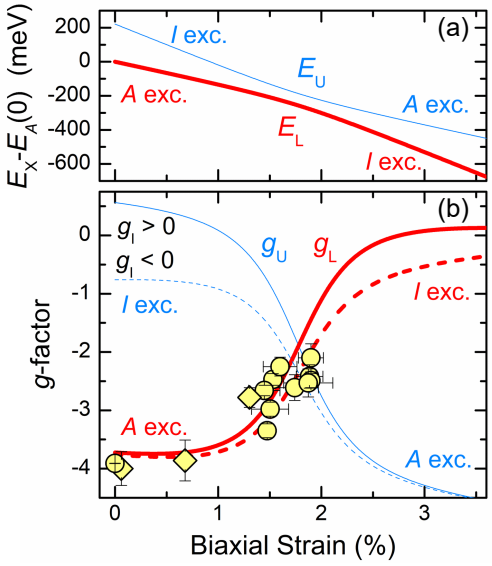

Figure 6.6: (a) Energy dependence of the U and L branches*vs* strain for $B = 0$ T. The hybridisation parameters are: $\Delta = 35$ meV, $E_I(0) - E_A(0) = 210$ meV, $\Delta E_A = -128$ meV/%, $\Delta E_I = -246$ meV/%. (b) Calculated and experimental g-factors. Circles (diamonds) refer to g-factors measured in the Bitter (superconducting) magnet. Solid (dashed) lines were obtained assuming $g_I > (<) 0$. The hybridisation parameters are: $g_A = -3.84$, $\Delta g_A = -0.23$, $g_I = 0.68$ and $\Delta g_I = -0.12$ [obtained from Fig. 6.2(e)].

Notice that the same expressions would hold if we considered $\Delta_1 = 0$ and $\Delta_2 \neq 0$

but they would be equivalent to changing the sign of $g_I(\varepsilon)$. In the presence of magnetic fields, the g-factors associated with the U (L) exciton branches are given by

$$g_{U(L)}(\varepsilon) = \frac{E_{U(L)+} - E_{U(L)-}}{\mu_B B} \,. \tag{6.11}$$

The theoretical trends obtained for the energy behaviour and g-factors of the A and I excitons for different Δ values, based on Eqs. (6.10) and (6.11), are displayed and discussed in the Additional Material, sec. A19. Therein, the theoretical results are also compared with the experimental data, in order to deduce the coupling parameter Δ that gives the best agreement with the experiment. This is obtained for $\Delta = 35$ meV, as further discussed later.

Fig. 6.6(b) compares the theoretical trends with the experimentally measured g-factors for such a coupling parameter. The strain corresponding to each experimental datum was deduced from the theoretical relationship between exciton energy and strain displayed in panel (a), where the experimental exciton recombination energy E_X is determined from the PL measurements; see further details in the Additional Material, sec. A19.

For small strains (≤ 1 %), g_{L} remains nearly unchanged. As strain increases and we enter the hybridisation region, g_L increases (toward g_I) and g_U decreases (toward g_A). The experimental g-factors nicely fall onto the calculated curves of g_L, which corresponds to the E_L branch favoured in PL. Interestingly, the majority of the measured g-factors lies in the strain range $1.5-2$ %, where the largest hybridisation is achieved. In our analysis, we still consider the two possible signs of g_I but we emphasise that in the strong hybridisation regime the g_I sign uncertainty is less pronounced.

The crucial ingredient for exciton hybridisation is the coupling parameter Δ. Although we introduced such coupling phenomenologically, we further elaborate on its possible microscopic origin. Recent studies showed that pure exciton-exciton interactions are of the order of few meV [412], whereas phonon-mediated exciton-exciton interactions may reach tens of meV [413]. In Fig. 6.6, we found the best agreement for $\Delta = 35$ meV, thus suggesting that phonons are mediating the exciton hybridisation. Interestingly, for such phonon-mediated coupling, decreasing the temperature would decrease Δ [413], resulting in a steeper slope of $g_{\mathrm{U(L)}}$ *vs* strain. Phenomenological approaches akin to ours have recently been used to explain hybridisation signatures between dark and B ($\mathrm{CB_-}$,$\mathrm{VB_-}$) excitons [409] and between A and B excitons [410] in bilayer MoS_2. These observations call for further theoretical efforts to provide a deeper microscopic understanding of exciton hybridisation mechanisms in van der Waals materials. Finally, exciton hybridisation mechanisms can also be found beyond vdW materials, *e.g.*, a qualitatively similar behaviour was found in wurtzite InP nanowires, where hybridisation between different valence bands resultied in a lower feld-dependent exciton g-factor [414, 415].

Chapter 7

hBN capping of TMD domes and observation of single photon emitters

Besides allowing for a fine tuning of the optoelectronic properties of TMD MLs, strain gradients have also been related to the appearance of single-photon emitters (SPEs) at cryogenic temperatures [120, 416–423], greatly increasing the potential of these materials for quantum technologies. Indeed, layered materials are advantageous from a production point of view —since bulk crystals provide many exfoliable MLs— and by virtue of the high extraction efficiency of the emitted photons, due to the lack of internal reflection. Even though the link between strain gradients and SPEs in TMDs is yet to be fully understood, in the last few years several different structures (*e.g.* etched holes [120], nanorods [123, 424], nanopillars [77, 425, 426], nanowires [124], nanostars [427], etc.) have been used as stressors for TMD MLs to generate ordered arrays of SPEs. Moreover, by exploiting plasmonic effects [424, 426–428] and optical cavities [429, 430] in which these 2D systems can be easily integrated, it is possible to enhance the emitter brightness by increasing their radiative recombination rate. In order to advance the field of quantum nanotechnologies, single-photon sources should be produced using manufacturing methods that are cheap, scalable, reproducible, and, preferably, compatible with current photonic integration technologies. The domes show promise in this respect, due to the possibility to create them over large-scale areas and in ordered patterns. The liquefaction of hydrogen at ~ 32 K causes however the deflation of the domes, thus hindering the observation of quantum emitters at cryogenic temperatures. In this chapter, we discuss a method based on the deposition of thin hBN flakes over the domes to keep them in shape even at low temperatures, thus enabling the generation of non-classical light.

Effects of hBN capping of TMD domes

Here, we will focus on MoS_2 and WS_2 crystals, even though the dome formation was demonstrated for several other TMD materials [156] and for hBN [169]. Such a choice is motivated by the experimental probes (Raman and PL) used to determine the dome strain, and in particular by the remarkably clear and intense Raman signal of MoS_2 and by the high PL efficiency of WS_2.

Regular arrays of WS_2 domes were obtained by hydrogenating a WS_2 bulk flake patterned with a lithographically-designed poly(methyl methacrylate) (PMMA) mask with openings of size $S = 3$ μm. Notice that at variance with what reported in Chapter 3, here we employed a different polymer. In fact, while HSQ is a negative tone e-beam resist, PMMA is a positive tone one. As a consequence, the resist dissolves when interacting with positive ions, such as the hydrogen ions. In turn, PMMA gradually self-cleans during the H-ion irradiation, thus leading to the formation of domes that are isolated and at the same time free from the neighbouring resist, without need of further processing (such as in the case of HSQ, which can be removed only via chemical treatments). This process facilitates the subsequent deposition of hBN. The deposition is performed via the standard dry transfer technique [431]: hBN flakes are first deposited over a PDMS polymer by the scotch tape method and thin flakes are identified; the selected thin flake is then deposited over the domes by gently pressing the polymer with the flake on top of them; the PDMS is then slowly peeled off and the thin hBN flake remains on the domes. At variance with the deposition of 2D crystals on flat substrates, in this case the presence of the domes make the adhesion process more difficult and air is easily trapped. To minimise these drawbacks, the peeling off process needs to be performed at a very slow rate.

Fig. 7.1(a) shows an AFM image of an ordered array of WS_2 domes capped with few-layer hBN on a specific region marked by a dashed white line. The AFM image shows an optimal adherence of the hBN flake to the domes underneath. The structural effects of the hBN capping of the TMD domes can be readily appreciated by looking at the optical microscope images of the sample at RT and at 5 K, shown in Fig. 7.1(b-c), respectively. Panel (c) clearly shows the dome deflation in the uncapped region on the right top corner of the image, while the domes covered with hBN unexpectedly retain their shape with minimal differences in size.

In order to obtain clues on this phenomenon and information on the variation of the dome strain with temperature, a bare MoS_2 dome (see AFM image in Fig. 7.2(a)) was first studied by μ-Raman measurements at different Ts. The same study was then carried out after capping the dome with hBN (see AFM image in Fig. 7.2(b)). The corresponding T-dependent μ-Raman spectra are shown in Figs. 7.2(c) (bare) and 7.2(d) (capped). In both cases, the μ-Raman spectra were recorded at the centre of the dome, where the tensile strain is maximum and features a biaxial character [116]. The μ-Raman spectra are characterised by the peaks associated to the in-plane E_{2g} and out-of-plane A_{1g} normal modes of oscillation. Two contributions are present for each mode, one due to the MoS_2 bulk underneath the dome and the other associated to the 1-layer-thick dome membrane. In the latter case, the Raman

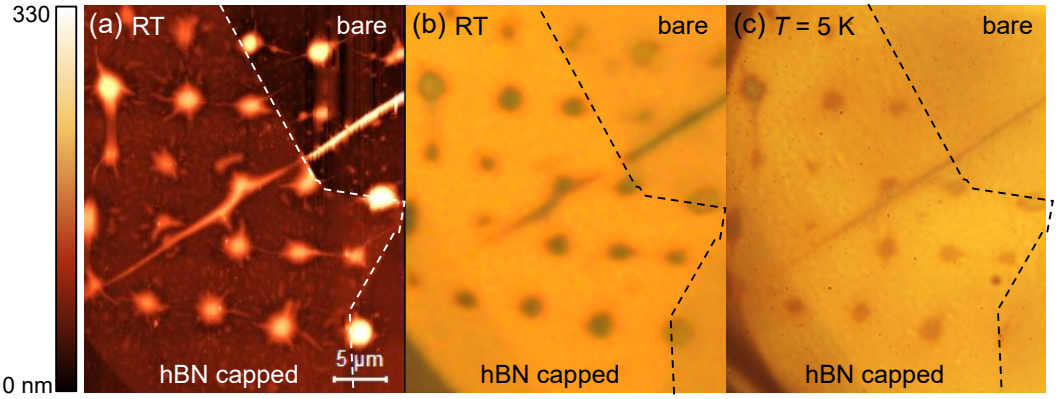

Figure 7.1: (a) AFM image of an ordered array of WS_2 domes partially capped with hBN. The dashed white line marks the border between the uncapped, or bare, area (top-right) and the remaining area capped with hBN. (b) Optical microscope image of the same area of panel (a) taken at RT. (c) Same as (b) but with the sample at 5 K. The domes in the capped area kept their shape, while those which were not capped with hBN clearly deflated. The lower quality of the image at $T = 5$ K is caused by the presence of the cryostat window.

mode is found at lower frequency with respect to the bulk one, due to the inherent tensile strain of the domes [116].

An immediately recognisable difference between the two sets of data regards the variation with T of the relative intensity of the dome and bulk peaks. Specifically, the signal from the bare MoS_2 dome exhibits a largely different intensity for different temperatures. This can be ascribed to the dome progressive deflation, which, in turn, affects the interference effect responsible for the amplification of the Raman signal occurring when the dome height matches about half the wavelength of the Raman signal. Instead, the T-dependent spectra of the same dome after being capped with hBN exhibit a remarkable stability of the dome to bulk relative intensity even at the lowest temperature considered, offering evidence of the fact that the capped dome retains its shape, regardless of the hydrogen phase. Fig. 7.2(e) displays the results of the Lorentzian fits performed on each μ-Raman spectrum, plotting the shift of the E_{2g} and A_{1g} peaks of the dome as a function of temperature. The Raman shift values were fitted with the formula:

$$\omega\left(T\right) = \omega_0 + A\left[1 + 2/\left(e^{\frac{\hbar\omega_0}{2k_B T}} - 1\right)\right], \tag{7.1}$$

where only the lower-order three-phonon processes of the anharmonic Klemens model are taken into account via the parameter A [432, 433]. The trends of the dome peaks show a strong difference between the bare and capped configurations, with the latter featuring regular temperature shifts, even in the range of temperatures for which the hydrogen gas condenses (indicated in the plots by a shaded grey area). Instead, the bare dome is characterised by a much more erratic change in the frequency position of its Raman peaks, reflecting the major structural changes it undergoes at lower

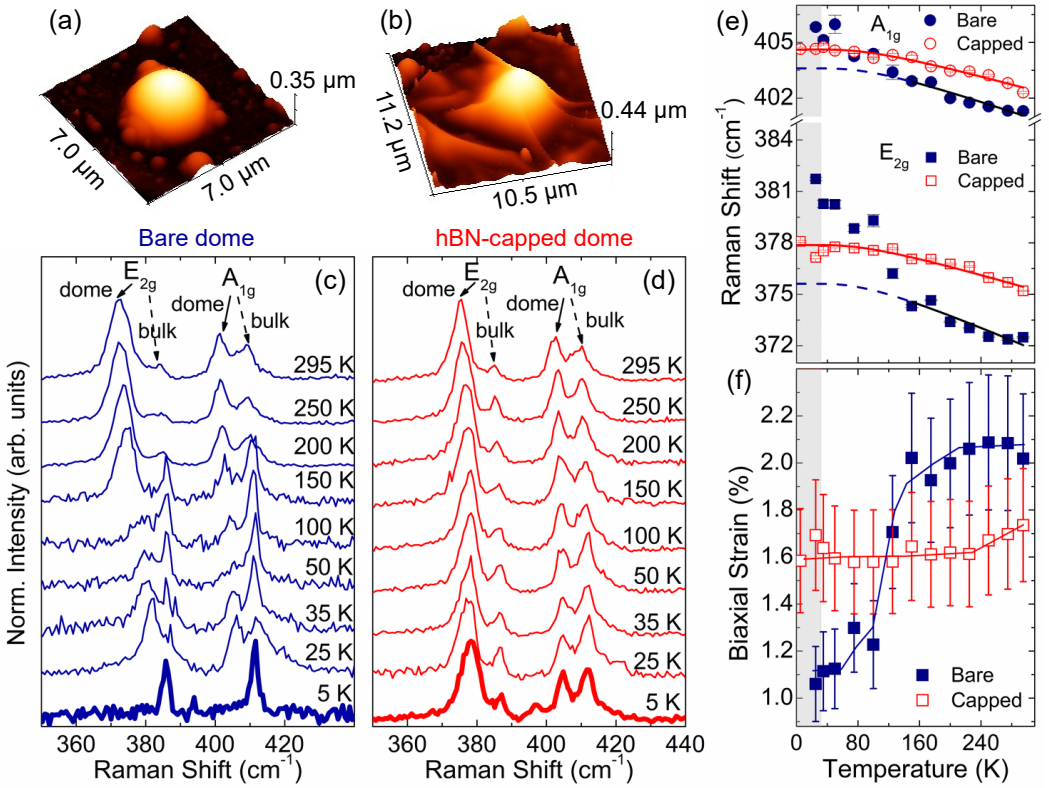

Figure 7.2: (a-b) AFM 3D image of a bare MoS_2 dome (a) and of the same dome after hBN capping (b). Both images were taken at RT. (c) Stacked normalised μ-Raman spectra at different temperatures of the bare MoS_2 dome. The peaks associated to the E_{2g} (in-plane) and A_{1g} (out-of-plane) modes of oscillation are visible for both the bulk material (indicated by a dashed arrow) and the dome membrane (indicated by a solid arrow). (d) Stacked normalised μ-Raman spectra at different temperatures of the same MoS_2 dome of panel (c) after hBN capping. A laser excitation wavelength equal to 532 nm and laser power equal to 30 μW were employed for the data in panels (c) and (d). (e) Temperature dependence of the E_{2g} (squares) and A_{1g} (circles) modes of the dome membrane before and after the hBN capping. The grey shaded area highlights the T interval for which hydrogen condenses (< 32 K). The evolution in temperature is fitted (solid lines) via Eq. (7.1). For bare domes, the fit was performed for $T = 150 - 300$ K, where a well defined trend could be observed (the dashed lines are an extrapolation at lower temperatures). (f) Values of the deduced biaxial strain *vs* T for the bare and capped MoS_2 dome obtained from Eq. (7.2). In the case of the capped dome, the strain is found to be constant even at the temperatures for which hydrogen is no longer in the gas phase (grey shaded area). The lines are guides to the eye.

temperatures. Indeed, the observed behaviour accounts for a decrease in the aspect ratio (and equivalently in the strain) of the dome below about 150 K. The complex dynamics of the system when reducing T is ruled by the interplay between the elasto-mechanical properties of the 2D membrane and the presence of a pressurised gas within the domes. A precise theoretical modelling of the thermodynamics of

the system is lacking, but some previous theoretical works provided an insight into the complex thermodynamics of van der Waals domes and predicted a decrease of the aspect ratio when lowering T [434]. Our studies represent the first experimental investigation of the mechanical behaviour of 2D domes *vs* T and further theoretical efforts would be necessary to account for the observed trends.

Given the peculiar behaviour found at low Ts, only the peaks in the temperature range $150-300$ K were fitted by Eq. (7.1) with the resulting fit being indicated by a navy solid line. The line obtained from the fit is extended, for lower temperatures, by a navy dashed line, which highlights the stark contrast between the expected evolution in temperature and the actual measured frequencies. The Raman mode frequency of the reference unstrained ML, $\omega^{\mathrm{ML}}(T)$, can be obtained from the measured bulk mode by just adding (subtracting) a small (1.5 cm^{-1}), rigid shift to the $\mathrm{E_{2g}}$ ($\mathrm{A_{1g}}$) peak [116]. Therefore, from the frequency position of the Raman peaks associated to the bulk and to the dome modes (the full set of data is shown in the Additional Material, sec. A21), the information on the biaxial strain ε at different temperatures can be extracted quantitatively by applying the following formula:

$$\varepsilon(T) = \frac{1}{2} \cdot \left(\frac{\omega^{\mathrm{ML}}_{\mathrm{E_{2g}}}(T) - \omega^{\mathrm{dome}}_{\mathrm{E_{2g}}}(T)}{\omega^{\mathrm{ML}}_{\mathrm{E_{2g}}}(T)} \right) \frac{1}{\gamma_{\mathrm{E_{2g}}}} \tag{7.2}$$

where $\omega^{\mathrm{ML}}_{\mathrm{E_{2g}}}(T)$ is the Raman shift of the in-plane mode of a strain-free MoS_2 ML at a given temperature T, $\gamma_{\mathrm{E_{2g}}}$ is the Grüneisen parameter equal to 0.84 ± 0.11 [116] (assumed constant at all temperatures [435]) and the total biaxial strain is divided by 2 to obtain the strain exerted on just one direction (*i.e.* the radial or the circumferential one that are equivalent at the dome summit). The values of strain obtained with such a procedure are shown in Fig. 7.2(f). The evolution of the strain characterising the bare dome (denoted by navy full squares) with decreasing T indicates that the dome membrane becomes progressively less stretched by the diminishing pressure of the hydrogen gas inside. When the gas eventually condenses, for temperatures falling in the grey-shaded area, the dome collapses onto the bulk crystal, so that the corresponding μ-Raman signal disappears at T=5 K (see the bottom-most spectrum in Fig. 7.2(c). In the case of the capped MoS_2 dome, instead, the values of strain show virtually no evolution for all temperatures, as displayed by the red empty squares. The same strain evolution in temperature was observed for several other bare and capped MoS_2 domes, see Additional Material, sec. A21. This provides further confirmation that the MoS_2 domes can be rigidly and systematically kept in shape by the hBN layer deposited atop. Even though the exact mechanism by which the hBN thin flake causes such a phenomenon is still not fully understood, we envisage that the hBN high rigidity may play an important role. Additionally, it is noteworthy that at RT the capping procedure reduces the membrane strain from $\varepsilon = 2$ % to about 1.7 % (see Fig. 7.2(f)). This indicates a likely elastic energy transfer from the dome membrane to the hBN layer, which possibly provides the energy necessary to maintain the dome structure regardless of the inner hydrogen phase state.

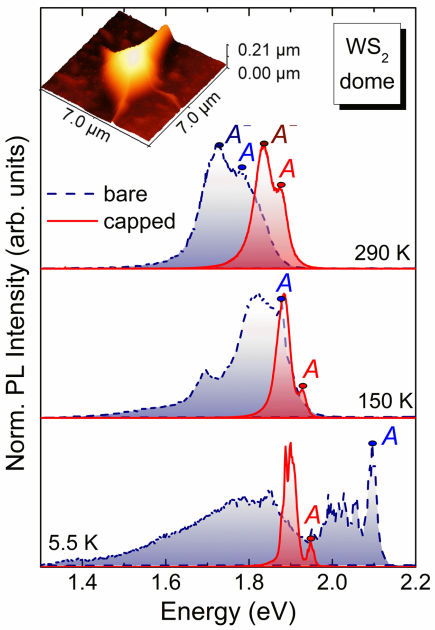

Figure 7.3: Stacked normalised μ-PL spectra taken at different temperatures on a WS_2 dome, before (navy dashed line) and after (red solid line) the capping with few-layer-thick hBN. A laser power equal to 44 μW was employed. The free neutral exciton is indicated as A, while recombination from charged excitons is indicated with A^-. At $T = 290$ K, the A (and A^-) band of the capped dome is about 90 meV higher in energy than that of the bare dome, indicating a sizeable tensile strain reduction following the capping. At lower temperatures, in the bare dome, several bands contribute to the emission spectra likely originating from morphological defects associated to the progressively deflating membrane. On the contrary, the hBN-capped dome maintains a well-defined lineshape at all Ts (the A^- band label is omitted for clarity purposes). The inset shows an AFM 3D map of the dome capped with hBN, taken at RT.

The effects of hBN capping were also investigated by performing μ-PL measurements both prior to and after the capping procedure on the ordered array of WS_2 domes displayed in Fig. 7.1. As discussed in Chapter 5, for our system the redshift of the exciton emission is intimately related to the evolution of the strain tensor along the dome surface [88, 156]. In particular, the biaxial strain values that can be attained on top of the bare WS_2 domes are close to those necessary to observe the direct-to-indirect exciton transition [88]. Fig. 7.3 illustrates the effects of hBN capping on the emission properties of a WS_2 dome belonging to the array shown in Fig. 7.1. The spectra were recorded at the dome centre both before (navy dashed lines) and after (red solid lines) the hBN capping. At 290 K, the first clear difference between the bare and capped configurations is a reduction in strain following the capping procedure, as demonstrated by the blueshift of the neutral exciton peak A in the capped dome. The lower-energy bands, labelled A^-, can be attributed in both cases to negatively charged exciton species [436, 437]), *i.e.*, trions. The ob-

servation of such a prominent trion peak, unlike the PL spectra typically found in random domes or in domes created within HSQ patterns, is presumably due to the different patterning procedure used in this case. In fact, the use of a positive tone e-beam resist (PMMA) implies that the areas where the openings are created are directly exposed with the e-beam prior to H-ion irradiation. This might induce an accumulation of negative charges, that contribute to the observation of the trion.

The strain reduction is in accordance with the μ-Raman results of the MoS_2 domes (see Figure 7.2 and related discussion). However, for this patterned WS_2 dome, the $\simeq 90$ meV blueshift of the exciton energy at 290 K indicates a remarkable biaxial strain reduction by about 1 % after the hBN capping [88]. When cooling the sample from RT to 5 K, the changes in the bare dome morphology can be seen in the evolution of the dome emission spectrum, characterised by a broad lineshape with several contributing bands and by an exciton peak showing an anomalously large "thermal" blueshift of 250 meV. This value clearly contrasts the regular blueshift observed for the exciton of the capped dome (85 meV) when T decreases. Indeed, at 5.5 K the bare dome is completely deflated, and the peak visible at ~ 2.1 eV comes from the WS_2 ML laying on the WS_2 bulk, being decoupled from this latter by the likely presence of condensed hydrogen. Lower-energy recombination bands are attributable to defect-related states. As a matter of fact, the progressive decrease of tensile strain when the H_2 pressure inside the dome decreases induces a blueshift of the exciton energy that adds to the usual band gap increase with decreasing T. For decreasing T, the regular blueshift of the A peak of the capped dome leads thus to a peculiar trend in which the capped dome exciton, compared to the bare one, is at higher energies for high temperatures and lower energies for low temperatures. A more detailed temperature study for this capped WS_2 dome can be found in the Additional Material, sec. A22. In Fig. 7.4, we compare the evolution in temperature of the A exciton energy of the capped dome with that of an unstrained WS_2 ML. Indeed, as shown in panel (b), the two trends almost overlap, demonstrating that the A exciton shift in the capped dome is induced solely by temperature, while no strain change is occurring.

The hBN capping procedure —along with the high spatial control over the dome formation site— prompts the opportunity for the creation of light sources in TMD materials. Indeed, one of the most striking features of the capping procedure is the appearance, in the μ-PL spectra of domes brought to low temperature, of intense, relatively narrow (full-width at half-maximum $= 1 - 5$ meV) and spectrally isolated lines, whose quantum nature will be shown next.

Observation of single photon emitters in hBN-capped WS_2 domes

Previous studies already reported the appearance of SPEs in WSe_2 MLs at low temperature. In many cases, their origin was ascribed to strain gradients, which are provided either by the wrinkling caused by the deposition procedure [422, 438] or by nanostructured stressors, such as nanopillars, nanorods, etc. [77, 123, 425]. Even though the exact origin of these SPEs has not been fully clarified, yet, it is

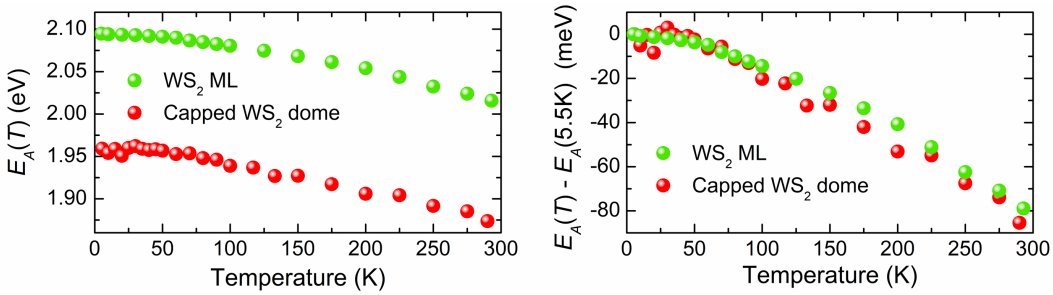

Figure 7.4: (a) Energy of the A exciton, E_A, *vs* temperature in the case of a hBN-capped dome, extracted from the spectra shown in the Additional Material, sec. A22. The peak energy was deterined by via Voigt fits. The result is compared with the evolution of E_A of an unstrained WS_2 ML deposited on SiO_2. (b) Same data of panel (a) but rescaled by substracting, for each set of data, the A exciton energy at 5.5 K. The two trends are almost identical, confirming the preserving effect of hBN on the dome geometry and strained configuration.

strongly suggested that they could stem from the interplay between dark states, strain gradients, and defect-related levels [439–441]. In particular, darkish materials such as WSe_2 and WS_2 are characterised by opposite spins in the bottom CB and in the top VB, resulting in a dark ground state (see Fig. 0.5). As described in Ref. [439], strain lowers the conduction bands and may bring the lowest energy CB to become resonant with defect states, leading to a hybridisation between the two. While dark strain-localised exciton states remain dark, hybridisation with a point defect breaks the valley selectivity and leads to efficient photoemission.

In our system the strain gradient is naturally provided by the dome morphology with an ensuing strain increase from the edge to the top of the dome, where the strain is maximum [116, 156]. Based on a theoretical ground, such a strain increase from the edge towards the summit should lead to the formation of localised states towards the dome apex, due to strain-induced quantum confinement [442]. However, in our system, by approaching the top of the dome, the exciton recombination character changes from direct to indirect, thus leading to a less intense emission [88]. As a matter of fact, we observe that the emitters appear almost exclusively at the edge of slightly asymmetric domes, as depicted in the optical images in the insets of Fig. 7.5(a) and 7.5(f). The images show the point of the domes excited by the laser spot from which the corresponding spectra displayed in the main panel originate. Our result is the first experimental investigation of micron-sized WS2 domes, whose exciton character changes from direct to indirect from the edge towards the centre. Some previous studies focused instead on TMD nanodomes which were studied at room temperature by near-field PL measurements. In that case the presence of localised, deeply bound exciton states only in the dome periphery was reported [443]. Those nanodomes were created by deposition of a TMD ML on a hBN substrate, and the observation of SPEs at the dome periphery was explained in terms of atomic-scale wrinkling taking place at the edge of the nanodomes, thus

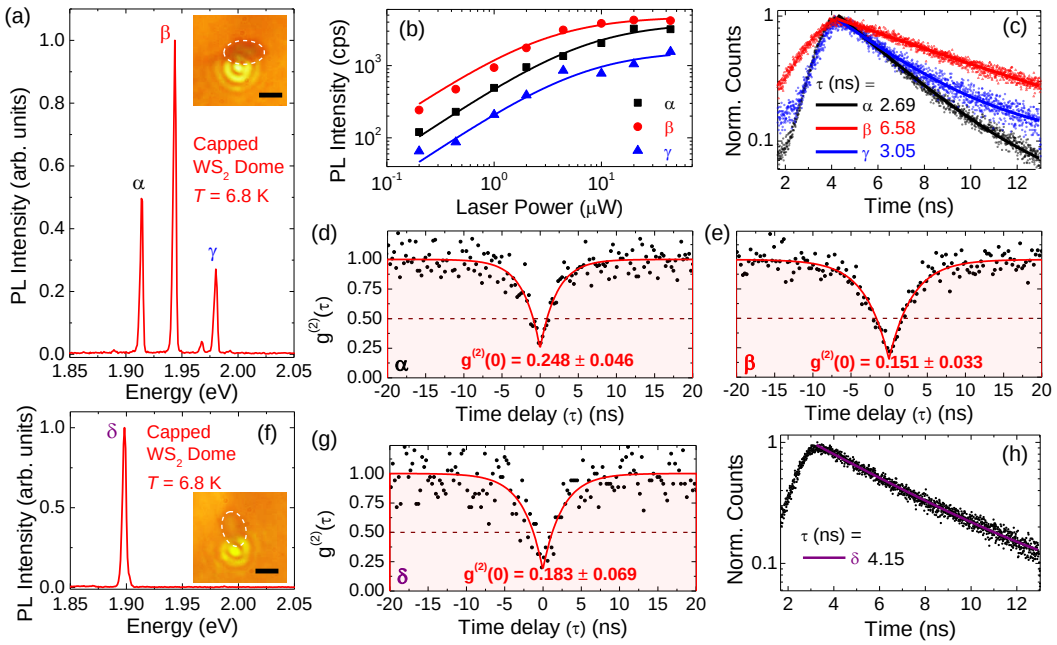

Figure 7.5: (a) Narrow lines (labelled α, β and γ) in the μ-PL spectrum of a capped dome at 6.8 K. The excitation wavelength is 532 nm and the laser power is 200 nW. The right inset is an optical image, taken at 6.8 K, showing the area excited by the laser. The white dashed line highlights the dome asymmetric profile. Scalebar: 2 μm. (b) PL intensity (I) *vs* laser power (P) of all the three lines shown in panel (a), fitted via Eq. (7.3), and showing a saturation behaviour. (c) Time-decay curves of the three emitters of panel (a) fitted by an exponential decay function. The decay times extracted from the fits are equal to (2.690 ± 0.029) ns, (6.58 ± 0.20) ns and (3.045 ± 0.042) ns for the emitters α (black), β (red) and γ (blue), respectively. (d-e) Second-order autocorrelation function $g^{(2)}(\tau)$ measured for the emitters α (d) and β (e) whose values at zero-time delay are equal to 0.248 ± 0.046 and 0.151 ± 0.033. (f) μ-PL spectrum of a different WS_2 dome capped with hBN at a temperature of 6.8 K. Laser power: 20 μW. The spectrally isolated emitter is labelled as δ. The inset on the right shows an optical image of the dome and its area excited by the laser at 6.8 K. The white dashed line highlights the dome asymmetric profile. Scalebar: 2 μm. (g) Second-order autocorrelation function $g^{(2)}(\tau)$ measured for emitter δ, whose $g^{(2)}(0)$ value is equal to 0.183 ± 0.069. (h) Time-decay curve of emitter δ fitted with an exponential decay function. The extracted decay time is of (4.148 ± 0.055) ns.

causing strain maxima to be at the edges and not at the centre, as theoretically found in Ref. [444]. Furthermore, in that theoretical work, the simulated system differs remarkably from ours, since that work focuses on the study of a MoS_2 ML deposited over a MoS_2 ML, so that a bilayer configuration is achieved around the nanodome.

Indeed, the theoretical framework described in that work [444] and used to explain the near-field experiments of Ref. [443] cannot be applied to our domes, which are created by a bottom-up approach (hydrogen-ion irradiation) resulting in well-

clamped edges (with no wrinkling) and in a strain increase from the edges towards the centre. We rather believe that the more pronounced direct character of the exciton at the edge of the domes could act as the driving force leading to the appearance of the emitters therein.

The spectrum of Fig. 7.5(a) features three distinct lines (labelled with the letters α, β and γ), whose intensity for increasing laser power is shown in Fig. 7.5(b). For each of the three lines, the emission intensity displays the saturating behavior usually associated to discrete defect states [120] and described by the equation:

$$I = I_{\text{sat}} \left(\frac{P}{P + P_N} \right), \tag{7.3}$$

where I_{sat} is the saturation intensity and P_N is the laser power at which the intensity is half of I_{sat}.

Time-resolved μ-PL measurements (see Additional Material, sec. A4), performed by exciting the sample with a supercontinuum laser spectrally filtered at 532 nm, were taken for all these emitters in order to extract their decay time. Fig. 7.5(c) shows the PL decay curves of the emitters α, β and γ, fitted by an exponential function, yielding time decay time values of (2.690 ± 0.029) ns, (6.58 ± 0.20) ns and (3.045 ± 0.042) ns, respectively. All the obtained decay times are in accordance with those measured for localised states in WSe_2 MLs [77, 120, 416, 417, 424, 425, 427, 428, 445]. To determine whether the studied lines originate from quantum emitters, the second-order autocorrelation function $g^{(2)}(\tau)$ was measured for line α (Fig. 7.5(d)) and β (Fig. 7.5(e)). The samples were excited with a continuous-wave laser at 532 nm and the emission was filtered by a monochromator in order to select a specific emitter (details on the Hanbury-Brown and Twiss setup we employed are provided in the Additional Material, sec. A4). The autocorrelation function was not measured for line γ due to its lower intensity and to the presence of nearby smaller-intensity emissions that would have hindered the source purity. All the measured emitters display the characteristic antibunching dip at zero time delay, with values of $g^{(2)}(0)$ equal to 0.248 ± 0.046 and 0.151 ± 0.033 for the α and β emitters, respectively. The spectrum of another capped WS_2 dome is shown in Fig. 7.5(f), and it is characterised by the presence of a single, isolated emitter (labelled as δ) that is observed by exciting the dome close to its edge. Fig. 7.5(g) shows the second-order autocorrelation function of this line, whose behavior as a SPE is confirmed by a value of $g^{(2)}(0)$ equal to 0.183 ± 0.069. The corresponding time-resolved μ-PL measurement is displayed in Fig. 7.5(h), and it shows a mono-exponential decay curve, whose fitting returns a decay time of (4.148 ± 0.055) ns. We point out that while most of the research interest on TMD-based SPEs has been focused on WSe_2, WS_2 has been the object of much fewer studies [421, 425, 446]; our work presents, to our knowledge, the first non-electrical generation of WS_2 SPEs, with the highest purity to date and the first measurement of the emitter decay time.

SPEs in TMD MLs can be also relevant for valley- and spin-tronics applications. To this regard, the exciton g-factor is the important parameter determining the

response of the carrier states to magnetic fields. Therefore, the emitters discussed above, as well as several others, were studied in the presence of a magnetic field (B) parallel to the luminescence wavevector (Faraday configuration) up to 12 T (in a superconducting magnet), at a temperature of 10 K (see Additional Material, sec. A16). After being excited by a 515 nm laser, the light emitted by the sample is analysed in terms of σ^+ and σ^- polarisations, as in Chapter 6. Fig. 7.6(a) shows the magneto-μ-PL spectra of line α displayed in Fig. 7.5(a). In order to compensate for slight changes in the emission energy of the line caused by slight drifts of the sample during the field sweep, the spectra are shifted on the x-axis with respect to the mean value in energy of the two polarisations. A less intense line is also present about 4 meV above line α. Due to the sample drift, this secondary line does not shift regularly with respect to the main line α. The intensity factors next to each spectrum show the increasing degree of circular polarisation of the emission with increasing B, reaching a value of 69 % at 8 T, which is consistent with that obtained for similar emitters in WSe_2 [447]. By fitting the spectra of the two circular polarisations with a Lorentzian function we can extract the Zeeman splitting energy of the exciton $\Delta E\,(B) = E\,(\sigma^+) - E\,(\sigma^-)$, and from the relation

$$\Delta E = g\mu_{\mathrm{B}}B \tag{7.4}$$

(where μ_{B} is the Bohr magneton) we can obtain the value of the exciton g-factor, see Fig. 7.6(b). Emitters α and β (for this latter, refer to the Additional Material, sec. A23, Fig. A23.1, panel (l)) have values of g equal to -8.034 ± 0.054 and -8.176 ± 0.025, respectively. The values of g related to several other narrow lines (all the linear fits performed on the Zeeman splitting of these emitters can be found in the Additional Material, sec. A23) were collected in the red histogram of Fig. 7.6(c), giving a mean value of $g = -8.20 \pm 0.51$. The additional high-energy peak visible in the spectra of Fig. 7.6(a) was not included in this histogram since it is the only outlier of the distribution, with a g equal to -5.39 ± 0.13. This anomalous value of g requires further studies, since it could be linked to an excitonic species different from that of the other emitters.

Due to the lack of preceding results on the exciton g-factor of WS_2 SPEs, we compare our results with those of free excitons in strain-free WS_2 MLs reported in the literature [43, 46, 49, 50, 350, 387–390]; see the green histogram of Fig. 7.6(c). A comparison between the two histograms shows that the absolute value of g for our SPEs is about twice that of the free exciton of unstrained WS_2 MLs. We also notice that a similar finding was observed for analogous emitters in strained WSe_2 MLs [120, 416–418, 420, 438, 448, 449]. No correlation is observed between the energy of the emitters and the value of their g-factor, as it can be seen from the inset of Fig. 7.6(c).

In the case of WSe_2 emitters, it was proposed that this large g value is a consequence of the emitter radiative transition involving an electron in a defect state and a hole in the valence band. While the hybridised orbitals $d_{x^2-y^2} \pm id_{xy}$ ($l_z = \pm 2h$) constituting the valence band are responsible for the intrinsic valley exciton g-factor

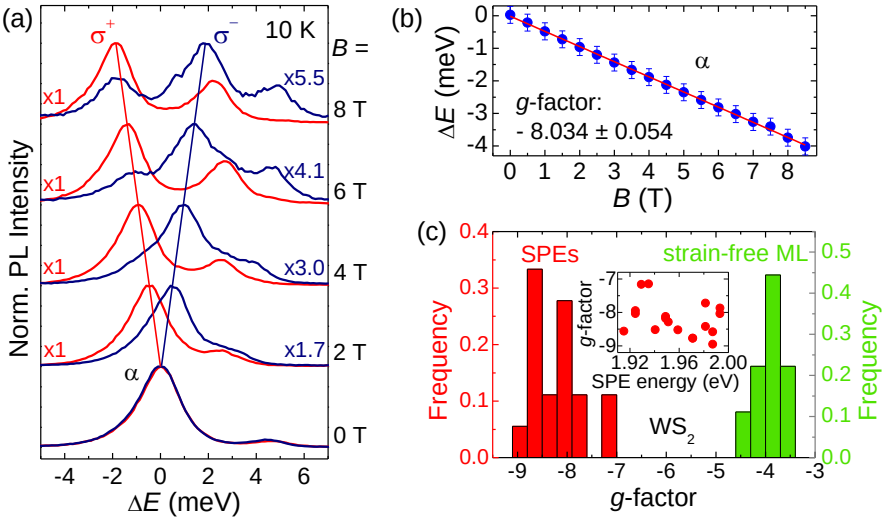

Figure 7.6: (a) Helicity-resolved normalised μ-magneto-PL spectra of the SPE labelled as α in Fig. 7.5(a). In order to compensate for slight changes in the emission energy caused by a slight drift of the sample during the field sweep, the spectra are shifted on the x-axis with respect to the mean value in energy of the two polarisations. The splitting of a less intense line is also visible at higher energy. (b) Zeeman splitting ΔE of the line of panel (a) as a function of the magnetic field. The linear fit, following Eq. (7.4), gives a value of the exciton g-factor equal to -8.034 ± 0.054. (c) In red, we show the histogram of the values of the g-factor obtained by performing fits analogous to that of panel (b) on 18 narrow lines (see Additional Material, sec. A23). The histogram is characterised by a mean value of $g = -8.20 \pm 0.51$. In green, we show the histogram of the g-factor of the free exciton of unstrained WS_2 MLs. The histogram was built from the values available in the literature in Refs. [43, 46, 49, 50, 350, 387–390] giving a mean value of $g = -4.00 \pm 0.28$. The inset displays the correspondence between the energy of the SPE and their g-factor, showing no apparent correlation.

of -4 (the conduction band d_{z^2} orbitals do no contribute having $l_z = 0$), the defect state adds to the orbital component of g increasing its absolute value [448]. Alternatively, the large g-factor reported in the histogram of Fig. 7.6(c) would be compatible with the value found for dark excitonic species (both neutral and charged) in WS_2 [387] and WSe_2 MLs [450]. In our case, the presence of strain and ensuing microscopic disorder could favour dark states as the origin of the observed emission lines and new experiments are planned to address this point.

Chapter 8

Strain as an extra degree of freedom in 2D heterostructures: the case of TMD/InSe heterostructures

vdW HSs offer a vast playground for the realisation of novel electronic and optoelectronic devices, due to the multitude of degrees of freedom they display, including layer number, layer order and twist angle. Indeed, the weak vdW adhesion [116] that keeps together different 2D crystals is responsible for this unprecedented tunability, overcoming lattice mismatch issues and rotational constraints [18]. This high tunability has been exploited to engender novel phenomena —such as superconductivity in twisted multilayer graphene [273]— and to realise efficient electronic devices [280–285]. Indeed, in HSs made of two different semiconducting materials, different scenarios can be found: in type I HSs, the bandgap of one material is completely contained within the bandgap of the other material, see Fig. 8.1(a); in type II HSs, a staggered configuration is found, in which the minimum of the VB belongs to one material, while the maximum of the CB belongs to the other material, see Fig. 8.1(b). In type I HSs, carrier tunnelling [451] from the largest bandgap material to the smallest bandgap one can occur. This typically happens in VB if the VBMs of the two materials are located at the same point of the Brillouin zone and are not too far in energy (the same for CB). In type II HSs, carrier tunnelling can also occur [451] under the same conditions said above. In this case, however, the tunnelling may occur from one material to the other in VB, and in the opposite direction in the CB. Fig. 8.1(b) illustrates the case in which holes in material A tunnel towards the VBM of material B. This can lead to the formation of electron-hole pairs, where electrons and holes are located in the two different materials [451]. In 2D materials, this has been shown to give rise to the observation of the so-called *interlayer excitons* (IXs). Efficient IXs have been observed in several TMD-based HSs, such as in

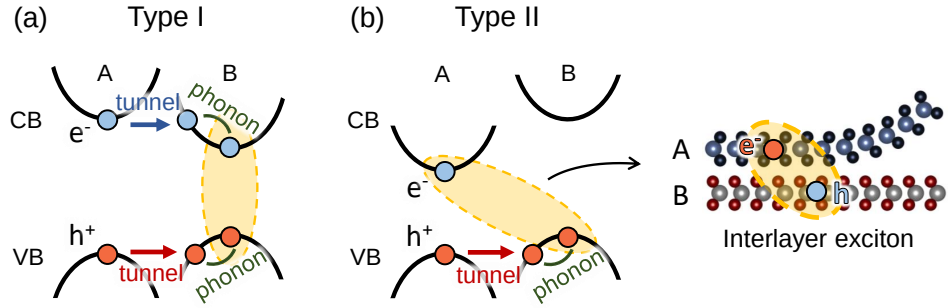

Figure 8.1: (a) Sketch of a type I HS: the bandgap of material B is fully contained within the bandgap of material A. Tunnelling of electrons and holes from material A to material B can occur. (b) Sketch of a type II HS: a staggered configuration is found, in which the minimum of the VB belongs to one material, while the maximum of the CB belongs to the other material. In the present sketch, the VBs are close enough in energy to allow hole tunnelling from material A to material B, leading to the formation of the so-called interlayer exciton.

$WSe_2/MoSe_2$ HSs [452].

The observation of the IX is however strongly dependent on the twist angle between the two materials. Only if the twist angle is close to 0° or 60°, the K points of the two materials are aligned and the transition is direct in k-space. Otherwise, a k-space mismatch is introduced and the optical efficiency of the IX drops.

Fig. 8.2 shows the optical image, sketch and some optical characterisations of a $MoSe_2/WSe_2$ HS that we fabricated and investigated, and where the IX was observed. In particular, Fig. 8.2(a) shows the HS optical microscope image and corresponding sketch. The investigated HS was fabricated by first depositing a $MoSe_2$ flake containing a ML on a Si/SiO_2 substrate and then depositing a WSe_2 ML on top. The HS was then capped with a thin hBN layer to prevent oxidation. The relative twist angle between the two MLs is $\theta \approx 0°$ corresponding to a R-type HS (while when $\theta \approx 60°$ the HS is referred to as H-type).

The possibility to play with the twist angle has indeed opened the door to a vibrant research field. In fact, when stacking different layers together at an arbitrary twist angle, periodic patterns with hexagonal symmetry form, as illustrated in Fig. 8.3. These patterns —referred to as moiré patterns— act as a periodic potential landscape for charged carriers, that are trapped at the potential minima. Clear signatures of the formation of moiré-trapped IXs (for small twist angles of $0° \pm 5°$ or $60° \pm 5°$) were reported [274, 453–457], leading to peculiar properties, such as remarkably long decay times of the order of hundreds of ns, showing promise for the achievement of Bose condensates. Trapped moiré excitons are also attracting great attention since they feature potentiality towards the formation of arrays of localised single-photon emitters serving as a platform in quantum optics [274, 275, 398, 454, 456, 458, 459].

Fig. 8.2(b) shows the T=6 K μ-PL spectrum (blue line) of the investigated

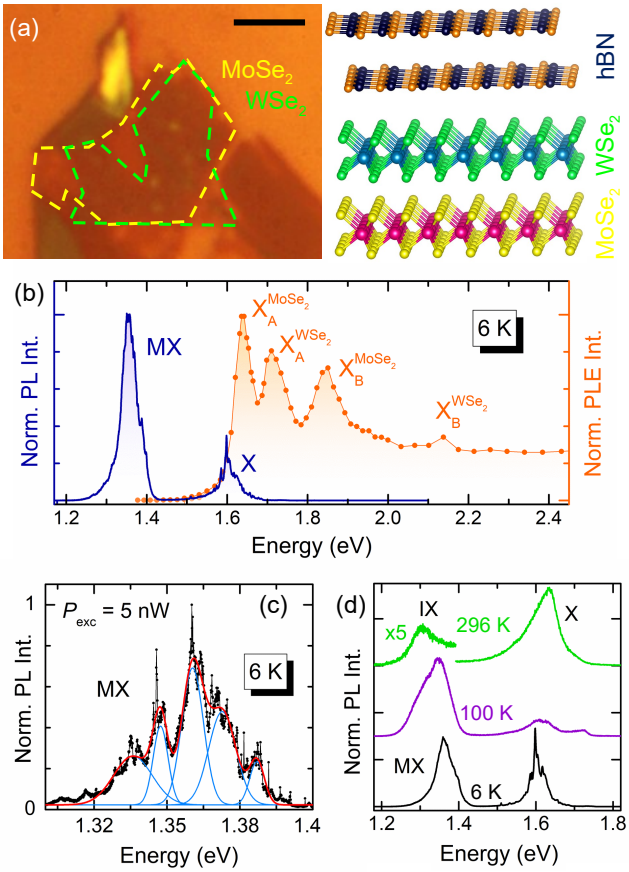

Figure 8.2: (a) Optical micrograph of the investigated $WSe_2/MoSe_2$ HS. (b) Low-T μ-PL and μ-PLE spectra of the HS, left and right axis, respectively. In the μ-PL spectrum, X indicates intralayer exciton recombination from localised states of the $MoSe_2$ and WSe_2 layers (lower- and higher-energy side, respectively). MX is the moiré exciton band. In the μ-PLE spectrum, four exciton resonances are observed. These resonances can be attributed to the A and B excitons (see Fig. 0.5) of the $MoSe_2$ and WSe_2 MLs. (c) μ-PL spectrum of the MX band acquired upon low-power excitation (5 nW). The spectrum can be reproduced by five gaussian functions (azure: single components; red line: total fit) that are spaced by (12.9 ± 1.1) meV. The narrow lines that appear in the spectrum likely correspond to single MXs recombining in a moiré minimum. (d) μ-PL spectra recorded at different temperatures and $P_{exc} = 20$ μW/cm^2). The moiré/interlayer (MX/IX) exciton band is visible up to room temperature. X indicates the exciton band related to the single layer $MoSe_2$ and WSe_2 constituents of the HS.

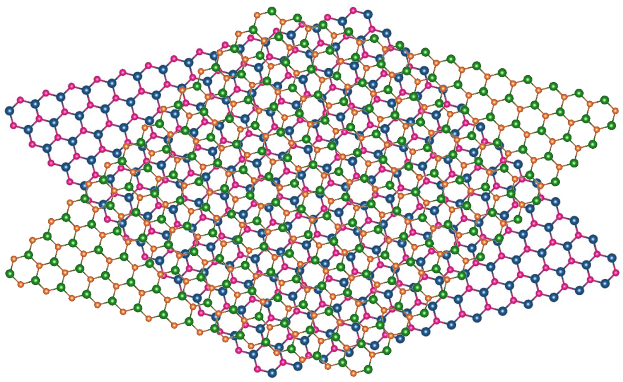

Figure 8.3: Sketch of a moiré pattern, obtained by stacking two TMD MLs with a twist angle of 30°.

$MoSe_2/WSe_2$ HS. Two bands are observed. The one peaked at 1.6 eV, labelled as X, is due to a group of localised (intralayer) exciton states originating from the $MoSe_2$ ML with a small contribution from similar transitions in the WSe_2 ML on the higher energy side of the band. The band centred at 1.35 eV, labelled as MX, is due to the moiré interlayer exciton (MX) recombination (with the electron and hole being confined in the $MoSe_2$ and WSe_2 layer, respectively). The orange line in Fig. 8.2(b) is the μ-PL excitation (μ-PLE, see Additional Material, sec. A4) spectrum obtained by monitoring the MX signal while scanning the excitation laser wavelength. The MX signal shows a resonant contribution from the $MoSe_2$ and WSe_2 ML A and B exciton states, thus confirming the interlayer nature of the MX band.

Fig. 8.2(c) displays the MX spectrum recorded at $T = 6$ K with P_{exc} as small as 5 nW (corresponding to 0.64 W/cm^2). The spectrum can be deconvolved into several gaussian components. These latter are equally spaced by (12.9 ± 1.1) meV, reflecting the quantised states of the moiré potential [274, 275, 456, 460, 461]. The gaussian lineshape maps onto the ensemble of MXs confined in moiré minima randomly distributed by the inevitable imperfections present in the HS plane. The very narrow lines superimposed to the multi-gaussian lineshape of the MX band likely correspond to single MXs confined in just one moiré minimum [457, 458]. The peak energy of the MX band (1.35 eV) indicates that the investigated HS is R-type ($\theta \approx 0°$) [274, 455, 456, 462, 463]. In fact, for H-type HSs ($\theta \approx 60°$) the MX recombination is centred at an higher energy (of about 40 meV) [274, 394, 396, 459, 464, 465] due to the shallower moiré potential for H-type with respect to R-type HSs [457]. The excellent alignment endows the MX/IX exciton with an intense signal that persists up to room temperature, as shown in Fig. 8.2(d) where the free A exciton from the WSe_2 ML eventually dominates. Note that the recombination from the HS is indicated as MX at $T = 6$ K and IX at $T = 296$ K pointing to a qualitative T-induced transition in the character of the exciton.

Indeed, while vdW HSs have attracted a great interest and are widely studied,

the achievement of high-performance optoelectronic devices is however still a challenge, due to the necessity to find materials with specific band alignments, k-space matching CBM or VBM, and efficient charge transfer. Fine tuning mechanisms to design ideal HSs are in fact sill lacking. Strain has been used to shift the PL signal of TMD-based HSs [466] and to modify the geometry of the moiré potential in twisted bilayer HSs [467]. In all cases, the whole HS was stretched. Here, we propose a novel paradigm, by selectively straining only one of the constituent materials of vdW HSs. Specifically, strain is applied to MS_2 (M=Mo,W) monolayers to induce a reshuffling of the VBM, which shifts from K to Γ. This allows us to efficiently couple the MS_2 layer with the vdW crystal InSe.

The choice of InSe is grounded on the excellent properties it exhibits. Indeed, while MoS_2 and WS_2 monolayers show intense light emission [41], their mobility μ (up to $\sim$ 200 $cm^2V^{-1}s^{-1}$) [468, 469] is far from being as exceptional as that of graphene, where μ exceeds 10^4 $cm^2V^{-1}s^{-1}$ [6]. InSe has instead shown promise in this respect, with μ values in excess of 10^3 $cm^2V^{-1}s^{-1}$ [470, 471] and a quasi-direct and tunable optical bandgap E_{gap}. This latter characteristic, combined with the high μ values of InSe, could be particularly appealing for fast photodetectors operating from the UV to near-IR range. Indeed, E_{gap} varies from about 1.2 eV to 2.0 eV on going from bulk to 2L InSe crystals (for 1L, the lowest-energy exciton transition is optically inactive for photons absorbed/emitted perpendicular to the layer) [471, 472].

Research on InSe has rapidly developed with the realisation of HSs, such as graphene/InSe [473], and n-InSe/p-GaSe [474] for the realisation of junctions with excellent transport characteristics. The use of InSe for optoelectronic devices, though, is made difficult by its relatively low radiative efficiency. As a matter of fact, while the CBM of InSe is located at Γ, the VB has a mexican hat shape with the VBM slightly off the Γ point (see Fig. 8.4(a)). From 7L on, the VBM gets closer to Γ and InSe becomes basically a direct gap semiconductor [475]. In addition, the electric dipole orientation of InSe is perpendicular to the exfoliation planes, which leads to a poor coupling to light perpendicular to the InSe plane [475, 476].

In a recent work [477], InSe was coupled to multilayer ($\geq$ 2L) TMDs, having their VBM at the Γ point (see Fig. 0.3). Type-II HSs were thus obtained and k-space direct (at Γ) interlayer excitons between electrons in the InSe CBM and holes in the TMD VBM were reported. While those HSs presented the advantage of lacking the need of lattice matching or rotational requirements, their light emission was affected by poor optical efficiency and large sample-to-sample fluctuations [477]. This is probably ascribable to the intrinsic low radiative efficiency of InSe and to the indirect nature of the bandgap in TMD multilayers.

Indeed, even with our approach the TMD bandgap is made indirect through strain. At variance with multilayer TMD, however, the indirect exciton in strained TMD MLs is characterised by a remarkable oscillator strength due to hybridisation phenomena with the nearly energy-resonant direct exciton [350]. In fact, as discussed in Chapter 5, the indirect exciton is typically only a factor of 10 less intense than the

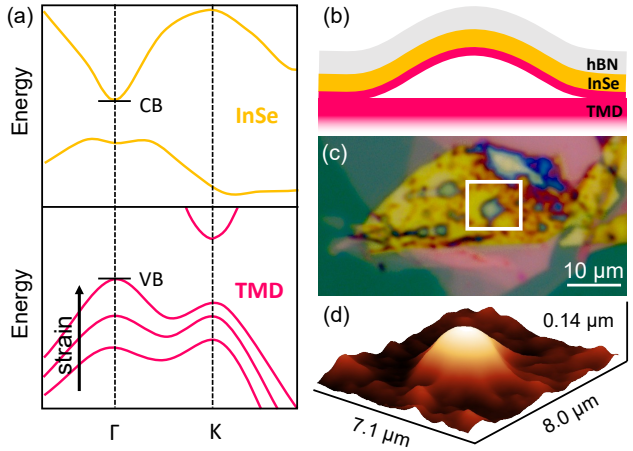

Figure 8.4: (a) Sketch of the band structure of few-layer-thick InSe and of 1-layer-thick TMDs. The effect of strain on the VB of TMDs is highlighted. (b) Sketch of the system studied in this work, consisting in a heterostructured dome: a few-layer-thick InSe flake is deposited atop of a strained TMD-ML in the shape of a dome; hBN is used to cap the system. (d) Optical image of a flake with heterostructured domes. (e) AFM image of the dome within the white rectangle in panel (d).

direct one [88]; see Figs. 5.3 and 5.4). This might imply that a larger hole population is achieved at Γ in the strained ML case with respect to TMD multilayers. In turn, this might enable a larger charge transfer between the TMD and InSe. On the other side, several other factors may influence the charge transfer and play a role. Among them, the relative position of the VB at Γ of the TMD with respect to the VB at Γ of InSe indeed plays a role. A different alignment in the case of the strained TMD ML and of TMD multilayers could affect the charge transfer towards the InSe flake.

To create HSs where only the MS_2 crystal is subjected to high strain, while the InSe layer is not, we exploited WS_2 and MoS_2 micro-domes.

InSe and hBN flakes were mechanically exfoliated onto PDMS, and flakes with the desired thickness (∼6-10 L for InSe, $<$ 20 nm for hBN) were identified based on their optical contrast. The InSe flakes were then deposited over some selected TMD domes; right after, hBN was deposited atop of the HS to prevent InSe from oxidising. A sketch of the final HS-dome is shown in Fig. 8.4(b), while the optical image of a real sample is shown in panel (c). Fig. 8.4(d) shows the 3D AFM image of the HS-dome highlighted by the white rectangle in panel (b).

The optical properties of the HS-domes were investigated both at RT and 5 K, both in the case of MoS_2 and WS_2. In all cases, an efficient emission at $\sim 1.2 - 1.4$ eV was detected. While this emission corresponds to the emission energy of InSe, its efficiency is much higher than that typically found in InSe. To have a direct comparison with the same InSe flake, in Fig. 8.5 we compare the PL signal recorded on the HS-dome (IN) and right outside (OUT), *i.e.*, where InSe is deposited on the bulk TMD flake (see sketch in panel (b)).

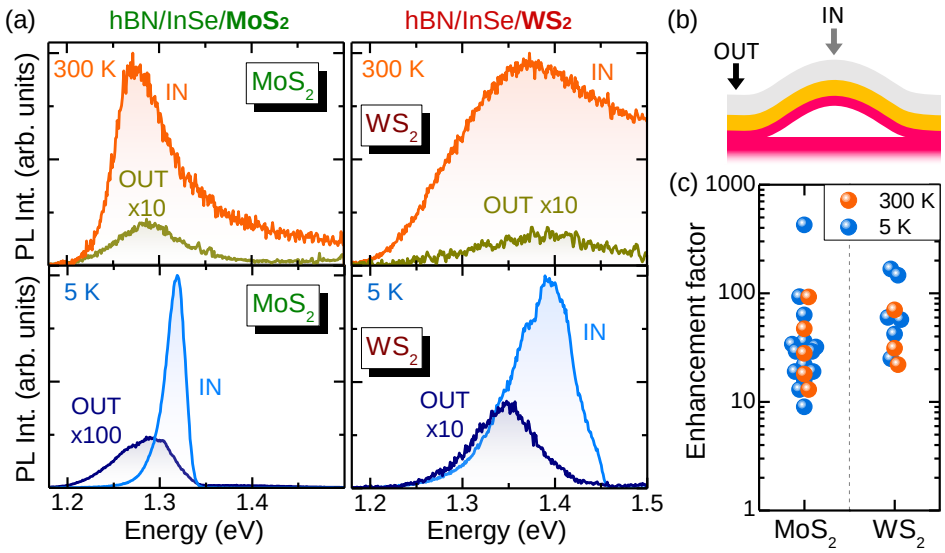

Figure 8.5: (a)PL spectra at 300 K and at 5 K of two HS-domes (one with MoS_2 as TMD, left, and one with WS_2, right) and of the region right outside the dome, as indicated in the sketch in panel (b). (b) Sketch of the system, highlighting the meaning of IN and OUT. (c) Summary of the ratios between the PL intensity in the HS-domes and outside, measured in several MoS_2 and WS_2 -based structures at 5 K or at 300 K.

A summary of the enhancement factors —defined as the ratios between the peak intensities measured IN and OUT (I_{IN}/I_{OUT}, where I is the peak intensity)— measured for many HS-domes is shown in Fig. 8.5(c). Indeed, values between 10 and 400 are found, indicating that the coupling of InSe with a strained MS_2 flake leads to a huge enhancement of the InSe PL signal.

To verify that the enhancement is due to the effect of strain, and not to the coupling with the ML or to a Fabry-Perót effect related to the presence of a dome underneath, we prepared the following check samples: (i) planar hBN/InSe/MS_2 HSs deposited atop of a bulk hBN flake, the MS_2 flake being a ML (see Figs. 8.6(a-b) for MoS_2, and Figs. 8.6(c-d) for WS_2); (ii) HS-domes where the dome is made of hBN [169] instead of MS_2 (see Figs. 8.6(e-f)). For case (i), a decrease of the PL signal is observed (of a factor of $1-5$), as shown in Figs. 8.6(b) and 8.6(d), contrary to the PL enhancement observed in the strained case. For case (ii), a moderate PL enhancement is found (of a factor of $1-2$), as shown in Fig. 8.6(f). The check experiments thus confirm that strain solely is responsible for the giant PL enhancement of InSe. A charge transfer from the strained MS_2 layer toward InSe is thus expected to occur. We thus performed μ-PLE measurements (see Additional Material, sec. A4) both on hBN/InSe/MoS_2 HS-domes and on hBN/InSe/WS_2 HS-domes. The PL spectra of the selected HS-domes and the corresponding PLE spectra are shown in Fig. 8.7. For hBN/InSe/MoS_2 HS-domes, two resonances can be seen, at 1.84 eV and 2.01 eV. The former is redshifted by about 0.1 eV with respect to the

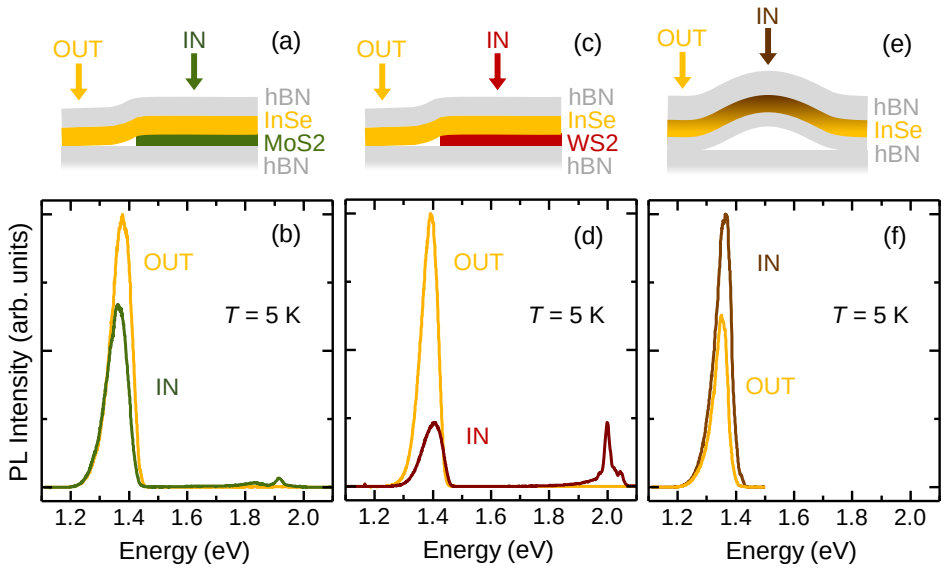

Figure 8.6: PL spectra of several check samples. (a-b) Sketch (a) and PL spectra (b) of a planar hBN/InSe/MS_2 HS (with MS_2 being a MoS_2 ML) where the MS_2 ML is thus not strained (IN), and comparison with the PL spectra in the regions where the TMD is not present (OUT). (c-d) Same as panels (a-b) but in the case of a WS_2 ML. (e-f) Sketch and PL spectrum (IN) of a hBN/InSe/hBN HS-dome (*i.e.* where the TMD dome is replaced by a hBN bubble) and comparison with the PL spectrum right outside the dome (OUT).

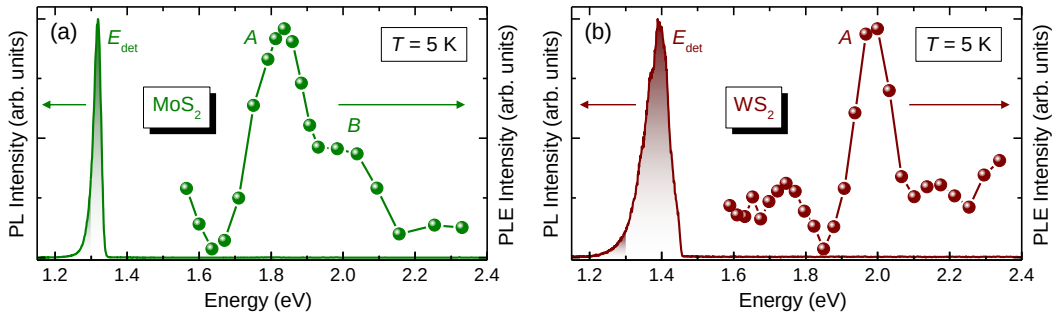

Figure 8.7: PLE spectra of a HS-dome based on MoS_2 (a) and of one based on WS_2 (b). The corresponding PL band whose intensity was detected during the PLE measurements is displayed. Exciton resonances attributable to the A and B excitons of the TMD are highlighted.

direct A exciton in unstrained MoS_2 monolayers. This redshift would be consistent with a biaxial strain $\varepsilon_{\text{biax}} \approx 1.1$ %. The second exciton resonance at 2.01 eV is ~ 0.17 eV above the lowest energy one. Such a distance is compatible with the A-B exciton distance, and we thus ascribe the 2.01 eV to the B exciton [45]. In the case of hBN/InSe/WS_2 HS-domes, instead, one clear resonance is observed at 1.98 eV, *i.e*, about 0.1 eV lower in energy with respect to the direct A exciton in

unstrained WS_2 monolayers. Such redshift is analogous to that found in the case of MoS_2, consistent with a biaxial strain $\varepsilon_{\text{biax}} \approx 1.1$ %. As a check, analogous PLE measurements were performed also in hBN/InSe/MS_2 planar HSs (those of Fig. 8.6(a-b)) and no resonances were found in that case. To verify the attribution of the main resonance in PLE to the A exciton, we performed μ-Raman measurements in hBN/InSe/MoS_2 HS-domes *vs* T to obtain information on the strain of the MoS_2 ML, similarly to the studies presented in Chapter 7 for hBN/MoS_2 domes. Fig. 8.8(a) displays the Raman spectra acquired on a HS-dome in the phonon regions of the E^1_{2g} and A_{1g} modes. To derive the strain behaviour, we performed an analogous analysis to that reported in Chapter 7. The strain values so derived are shown in panel (b). A smooth strain reduction is observed when decreasing T, and at ~ 5 K,

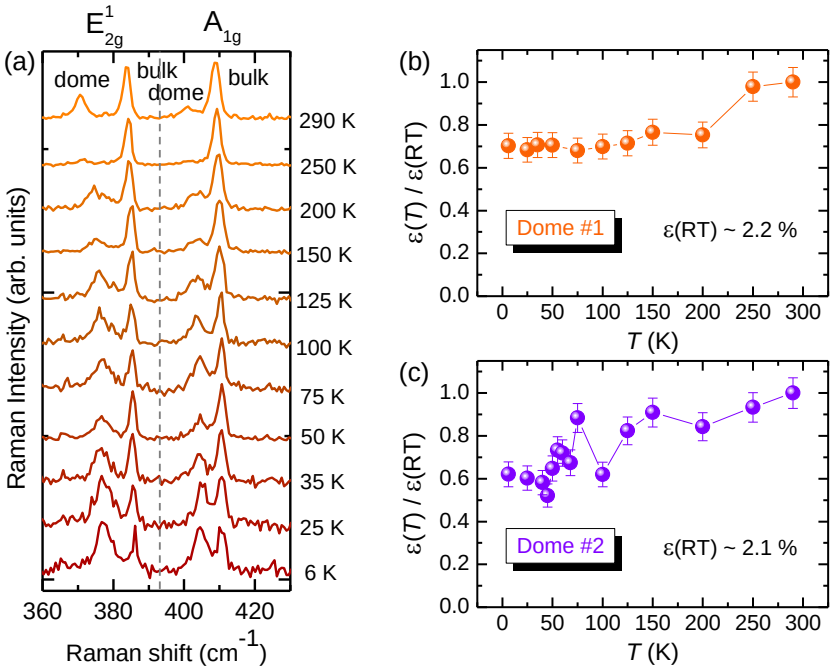

Figure 8.8: (a) Raman spectra of a hBN/InSe/MoS_2 HS-dome in the phonon regions of the E^1_{2g} and A_{1g} modes, as a function of T. (b) Strain behaviour as derived from the data in panel (a), from an analysis of the E^1_{2g} mode. The strain is normalised by the strain at RT. (c) Results of an analogous study for a different hBN/InSe/MoS_2 HS-dome.

the strain is found to be about 70 % of the RT value. To ensure the general validity of this result, we repeated analogous studies on another HS-dome, whose derived strain behaviour is shown in Fig. 8.8(c). In this case, at ~ 5 K the strain is found to be about 60 % of the RT value. From these studies, we estimate a strain at ~ 5 K of about $1.2 - 1.6$ %, in good agreement with the biaxial strain deduced from the A exciton shift based on PLE measurements ($\varepsilon_{\text{biax}} \approx 1.1$ %).

The PLE measurements clearly point to a charge transfer between the MS_2 monolayer and the InSe flake, which is activated by strain. To further elucidate on

the effect of strain on such HSs, we performed DFT calculations. The latter were performed by our colleagues Dr. Michele Re Fiorentin (Center for Sustainable Future Technologies, Istituto Italiano di Tecnologia, Turin, Italy.) and Prof. Maurizia Palummo (Physics Department, Tor Vergata University of Rome, Italy). Indeed, previous theoretical works investigated the case of InSe/MoS_2 HSs, where both InSe and MoS_2 were MLs. In such a HS, it's under debate whether a type I or type II alignment is obtained. The case of thicker InSe layers was not considered, to our knowledge. In Fig. 8.9, we show DFT calculations for the case of 6L-thick InSe,

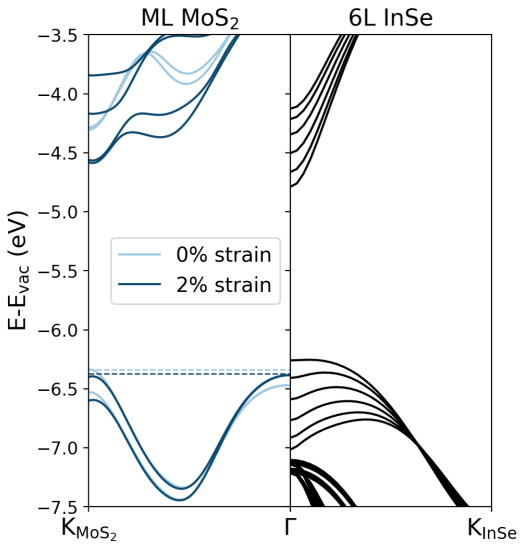

Figure 8.9: Band structure of a MoS_2 ML and of a 6L-thick InSe flake, calculated at the DFT-HSE06 level (*i.e.*, by using the Heyd-Scuseria-Ernzerhof hybrid functional). For MoS_2, the cases of null strain and 2 % biaxial strain are displayed.

revealing that a type I alignment is obtained even at null strain. In that case, however, the VBM and CBM of MoS_2 lie at the K point, while those of InSe at the Γ point. A 2 % biaxial strain indeed shifts the VBM of MoS_2 from the K to the Γ point, thus possibly activating a charge transfer from the MoS_2 layer to the InSe, whose valence bands are nearly resonant with that of MoS_2. Such calculations are promising to explain the experimental data. Further theoretical investigations are however required to achieve a complete understanding. Further efforts are in fact needed to understand possible charge transfer mechanisms in the CB and the role possibly played by defect states, and to include excitonic effects.

Conclusions

Straining 2D materials indeed holds great potential to modify their properties and to induce therein fascinating effects. The methods themselves employed to deform mechanically 2D crystals represent a very interesting experimental playground, where researchers have developed increasingly inventive approaches exploiting diverse growth techniques (either on deformed/patterned or dissimilar substrates), devices able to bend, bulge, stretch or indent atomically thin membranes, or endogenous phenomena (such as gas trapping) [41]. These approaches are characterised by different strain configurations, that provide a precious tool to understand the mechanical and electronic properties of the investigated materials, as well as a means to deliberately modify those properties. Indeed, the bandgap energy, the vibrational properties and the linear and non linear optical characteristics can be modulated, down to the micro- and nanometre scale [41]. Furthermore, great prospects have been envisioned regarding the quantum optical applications of strained 2D crystals as host of single photon sources that can be made site-controlled, scalable and integrable in photonic devices [478].

Within this contest, methods to induce strain in a controllable manner have been sought after, with the aim of enabling a fine strain-tuning of 2D materials.

In this Thesis, one such methods is developed (and presented in Chapter 1), consisting in the formation of micro- or nano-domes in TMDs and hBN [156, 169]. The method itself is original and innovative, since it is based on the interaction of these vdW crystals with hydrogen: Trapping of molecular hydrogen is achieved by exploiting the permeability of TMDs and hBN to protons and their impermeability to H_2 molecules. The caging of hydrogen induces a blistering of the upper layer(s) of the crystal, resulting in the creation of domes and thus in the achievement of localised strains.

The domes are widely studied from a variety of different points of view. The correlation between strain and its effects on the vibrational properties of TMDs and hBN is addressed in Chapter 2, by combining numerical calculations with μ-Raman and nano-IR measurements [116, 169].

Control over the size, position and even over the strain magnitude of the domes is then achieved by exploiting e-beam lithography-based approaches [156, 171], as discussed in Chapter 3. This enables the engineered creation of ordered arrays of light emitters or even of SHG hotspots.

Chapter 4 fullfills the knowledge of the morphological and mechanical properties of the system, by investigating them with a multidisciplinary approach. Indeed, an analytical model to describe the system in terms of its morphological, elastic, and adhesive properties is developed [116]. On the other hand, AFM-based studies including morphological characterisations as well as nano-indentation experiments are performed [75, 76, 116, 319]. The combination of theory and experiments leads to unprecedented knowledge over the elasto-mechanical and adhesive properties of 2D crystals, showing how the domes represent unique platforms to obtain precious fundamental knowledge on vdW materials.

Indeed, the precise knowledge of the strain distribution in the investigated system opens the doors to the study of the effect of strain on various properties. In the case of TMDs, given the huge interest they raised as promising materials for optoelectronics, the effect of strain on their bandstructure and optical response is of high relevance. Chapter 5 addresses this point, focusing on WS_2 domes (though MoS_2 and WSe_2 domes are also investigated), via steady-state and time-resolved PL studies. Strain is found to have a peculiar and important effect on these materials, by inducing a reshuffling of the VB maxima and thus inducing a direct-to-indirect bandgap transition, and in turn a direct-to-indirect exciton transition [88]. Our studies fully unveil this phenomenon, also showing how concomitant phenomena such as exciton funnelling take place in the domes, due to the peculiar non-uniform strain distribution that characterises the domes [88].

Even more interesting and unexpected phenomena are unveiled in Chapter 6, where PL studies are performed by subjecting the system to high magnetic fields. The studies per se are scientifically and technologically challenging, since the combination of such high strains with such high fields had never been achieved before in 2D systems. Such pioneering magneto-μ-PL studies show that strain affects the g-factor of WS_2 MLs when subjected to total strains of ≈ 4 % (or equivalent biaxial strains $\varepsilon_{\text{biax}} \approx 2$ %), inducing a reduction of the g-factor absolute value [350]. The experimental results, combined with an in-depth theoretical investigation based on state-of-the-art DFT calculations and phenomenological modelling, are explained in terms of hybridisation phenomena between nearly resonant direct and indirect excitons [350].

The final chapters of this Thesis are more visionary, since they look for original strategies to exploit the domes for quantum applications or to engender novel fundamental phenomena.

Chapter 7 exploits in fact the mechanical effect of hBN capping of the domes, that allows us to preserve their shape in temperature (despite the hydrogen liquefaction at low temperatures), to achieve single-photon emission from highly strained WS_2 MLs. Our approach can be potentially exploited to create ordered arrays of quantum emitters, by exploiting e-beam lithography, and to integrate the emitters in photonic or plasmonic cavities, which will be the object of future studies.

Finally, given the huge interest raised by vdW HSs in the past decade, Chapter 8 investigates the possibility to create strained HSs by exploiting the domes. The

approach is totally original since strain is selectively applied only to the material the dome is made of, while the material deposited atop is subjected to a null or minimal strain. HSs of this kind, where only one of the two materials is strained, have never been studied so far, to our knowledge. Our studies are focused in particular on HS-domes created by depositing InSe flakes over WS_2 and MoS_2 domes. Strain is found to trigger a relevant effect in the system, by activating a charge transfer from the TMD to the InSe crystal, leading to a huge PL enhancement of the InSe emission.

Overall, this Thesis pinpoints how strain can play a relevant role towards the utilisation of layered materials, and especially TMDs, in optoelectronics, valleytronics and spintronics.

Based on the widespread fundamental and practical applications of strain here presented, mechanically structuring certainly turns out to be a most promising method to exploit and boost the enormous potential of 2D materials, either as a built-in source enhancing the properties of the material or as an external perturbation that can be suitably engineered or variably tuned. Far from being exhausted, this research field still continues to progress and to provide novel exciting opportunities.

Additional Material

A1 μ-PL statistical characterisation of $MoSe_2$ and WS_2 domes

Fig. A1.1(a) shows the RT PL spectrum of a representative $MoSe_2$ dome. In Fig. A1.1(b), the same can be seen for a WS_2 dome of similar size. In both cases, the spectra display a main peak associated to the radiative recombination of the A exciton. In Fig. A1.1(c), a statistical study of the PL emission energy from 21 $MoSe_2$ and 21 WS_2 domes is presented. Given that the lineshape is not always perfectly symmetric (see, *e.g.*, panels (a) and (b)), the emission energy of each dome was estimated as the centroid of the spectrum, as:

$$E_{\text{centroid}} = \frac{\int_{E_1}^{E_2} E\ I(E)\, dE}{\int_{E_1}^{E_2} I(E)\, dE} \tag{A1.1}$$

in which E and I are the energy and the intensity associated to the data points belonging to the spectrum, respectively, whereas E_1 and E_2 are the energies corresponding to the endpoints of the chosen interval.

The peak energy distribution found for $MoSe_2$ is relatively narrow. A gaussian fit to the histogram provides a FWHM of 34 meV (with the emission being centred at 1.405 eV). The peak energy distribution of WS_2 is instead broader, with a FWHM of 55 meV (with the emission being centred at 1.796 eV, in excellent agreement with the PL spectrum of an ensemble of WS_2 domes displayed in Fig. 1.3(b)). Furthermore, in this case the gaussian fit does not perfectly reproduce the data due to the presence of a low-energy shoulder at about 1.75 eV. The presence of this shoulder is consistent with the macro-PL spectrum of an ensemble of WS_2 domes shown in the inset of Fig. 1.3(b).

This peculiar behaviour of WS_2 and the difference with the behaviour observed for $MoSe_2$ can be explained in terms of the effect of strain on the bandstructure of the two materials. In fact, as discussed in detail in Chapter 5, strain induces a direct-to-indirect exciton transition in WS_2 domes, resulting in the appearance of a low-energy component in the PL spectra [88]. Based on theory, the same transition is expected to occur also in $MoSe_2$, but at larger strain values [353], which are not achieved in our system. Therefore, $MoSe_2$ retains its direct character in the domes. This makes it so that the energy distribution of $MoSe_2$ is narrower, while that of WS_2 gets broader and presents a low-energy shoulder, due to the contribution of the indirect exciton

band to the PL spectra. A spatial characterisation of the PL spectrum across the surface of WS_2 domes is presented in detail in Chapter 5. Indeed, the coexistence of direct and indirect exciton species in WS_2 domes also causes the PL spectrum to be generally broader than in $MoSe_2$. We therefore performed a statistical analysis of the FWHM of the PL spectra of the same $MoSe_2$ and WS_2 domes of panel (c), and we show the result in Fig. A1.1(d). Indeed, a broader distribution is found for WS_2 with respect to $MoSe_2$. While the width of the distribution of $MoSe_2$ can be mainly ascribed to the fact that the PL spectrum is the result of the convolution of the light emitted from regions subjected to different strain values, the additional broadening of WS_2 can indeed be ascribed to the direct-to-indirect exciton transition.

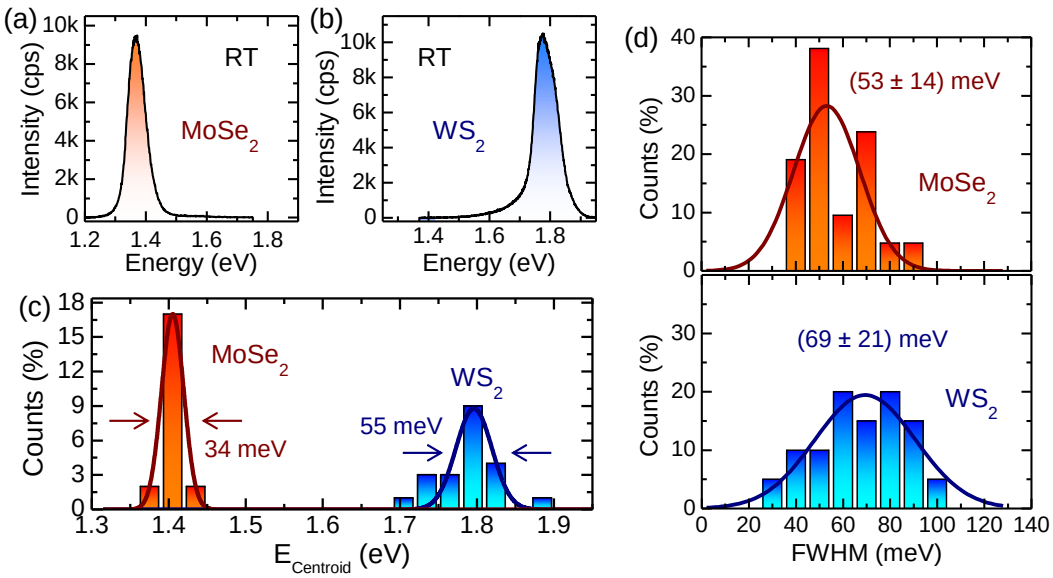

Figure A1.1: (a) PL spectrum of a micrometric (radius $R = 860$ nm) $MoSe_2$ dome. (b) Same as panel (a) for a micrometric ($R = 830$ nm) WS_2 dome. (c) Histograms of the spectral centroids of 21 domes on a WS_2 flake (blue) and 21 domes on a $MoSe_2$ flake (red). The arrows point to the FWHM of the two peak energy distributions, estimated through a gaussian fit of the histograms. (d) Histograms of the FWHM of the PL bands measured for the same $MoSe_2$ and WS_2 domes of panel (c). The continuous lines represent gaussian fits to the histograms, providing the average FWHM for $MoSe_2$ and WS_2 domes. Panels (a-c) were readapted with permission from S. Cianci *et al.*, Opt. Mater. **125**, 112087 (2022) [478]. Copyright 2022 Elsevier B.V.

A2 Poisson's ratio of 2D materials

The Poisson's ratios of 2D materials used in this work are listed in table A2.1. Their values were estimated via DFT calculations in Refs. [21, 331, 332]. In the case of black phosphorus (BP), while a positive value of ν has been reported for bulk BP in some works [21, 331, 332, 479], a negative value has been calculated for single layers of BP [480].

Table A2.1: Poisson's ratio ν for the most common 2D materials. Unless otherwise specified, these values were deduced from The Materials Project[21, 331, 332]

Material	Poisson's ratio (ν)
Graphene	0.176
hBN	0.223
MoS_2	0.250
$MoSe_2$	0.233
$MoTe_2$	0.245
WS_2	0.219
WSe_2	0.196
WTe_2	0.176
1T-VS_2	0.18
β-InSe	0.291
γ-InSe	0.264
β-GaSe	0.241
Bi_2Se_3	0.266
Bi_2Te_3	0.244
BP	0.23 (bulk), -0.93 (ML)

A3 Numerical strain modelling

Here, we will provide details about the finite element method numerical approach.

The force and momentum equilibrium conditions in the domes lead to a set of coupled nonlinear equations and which cannot be solved analytically. In the absence of external loads, this set of equations takes the form:

$$\begin{aligned} u''(r) + \frac{1}{r}u'(r) - \frac{u}{r^2} &= \frac{\nu - 1}{2r}h'(r)^2 - h'(r)h''(r). \\ D\left(h'''(r) + \frac{1}{r}h''(r) - \frac{1}{r^2}h'(r)\right) - h'(r)N_r &= \frac{r}{2}\Delta p, \end{aligned} \tag{A3.1}$$

where u is the radial displacement, D is the bending modulus, N_r is the radial stress, and Δp is the pressure applied by the substance inside the dome. We can seek a numerical solution by discretising these equations by the finite difference method, as discussed in Ref. [217].

To do that, we employed a model implemented in COMSOL Multiphysics 5.1. A line element is used to simulate the membrane with the starting thickness of a single or several layers of the considered crystal. One end of the line element is subjected to a fixed constraint (*i.e.*, null displacement) while the rest of the line is free to move in the longitudinal direction. The presence of a fluid within the dome is modelled as a pressure load acting on the flat membrane surface, thus causing the dome inflation. The membrane is deformed until the footprint radius R and the maximum height h_0 reach the target value, which is achieved by varying the internal pressure. The effects of the bending stiffness are neglected since $h_0/t \gg 1.5$ [74] (where t is the membrane thickness). An extra fine mesh is used for all simulations and a 0.001 convergence setting is used to ensure the numerical accuracy of the solutions. A constant Newtonian solver is used for the numerical solver procedure. Due to the anisotropic stiffness of the layered compounds, an anisotropic stiffness matrix was implemented in the linear elastic material node. The matrices used in this work are listed below.

The numerical simulations allow us to calculate the dome height profile and the strain tensor components and to determine the internal pressure for a given equilibrium condition (*i.e.*, for a given radius and maximum height). As discussed in Ref. [156], the height profiles compare well with the experimental ones. Indeed, the strain tensor in polar coordinates is a diagonal matrix (*i.e.*, there are no shear-strain components to worry about), where the two in-plane components are the radial and circumferential one (see sketch in Fig. 1.9). As expected for a system with negligible bending stiffness, no differences were observed in the strain components for layer thicknesses from 1 to 20 layers (very small discrepancies of the order of 10^{-4} were observed).

Stiffness matrices

FEM calculations require the stiffness matrices as an input. The stiffness matrices C are the matrices that relate the stress tensor to the strain tensor. We will herein

use Einstein notation with 6-vectors of the form v^α,

$$v^\alpha, \qquad \alpha = 1, ..., 6, \tag{A3.2}$$

where we identify (in Voigt notation):

$$1 \longleftrightarrow xx, \qquad 2 \longleftrightarrow yy, \qquad 3 \longleftrightarrow zz, \qquad 4 \longleftrightarrow yz, \qquad 5 \longleftrightarrow xz, \qquad 6 \longleftrightarrow xy. \tag{A3.3}$$

In this notation, we define the strain 6-vector ϵ as:

$$\epsilon^\alpha = (\varepsilon^1, \varepsilon^2, \varepsilon^3, 2\varepsilon^4, 2\varepsilon^5, 2\varepsilon^6), \tag{A3.4}$$

where ε^α is the Green-Lagrange strain vector. We also consider the 3D stress 6-vector defined as:

$$S^\alpha = \frac{N^\alpha}{t}, \tag{A3.5}$$

where t is the thickness of a single layer of the material and N^α is the 2D stress, given by:

$$N_{ij} = \frac{\partial \Phi_\varepsilon}{\partial \varepsilon_{ij}} = \frac{E_{2D}}{1+\nu}\left(\varepsilon_{ij} + \frac{\nu}{1-\nu}\sum_k \varepsilon_{kk}\delta_{ij}\right), \tag{A3.6}$$

where $E_{2\mathrm{D}}$ is the 2D Young's modulus. The stiffness matrix is then defined by the expression:

$$S^\alpha = C^\alpha_\beta \epsilon^\beta, \tag{A3.7}$$

where summation is understood over repeated indices. Notice that C is symmetric and that, due to the transverse isotropy, several matrix elements are null, so that the general form for the matrix C is:

$$C = \begin{pmatrix} C_1^1 & C_2^1 & C_3^1 & 0 & 0 & 0 \\ C_2^1 & C_2^2 & C_3^1 & 0 & 0 & 0 \\ C_3^1 & C_3^1 & C_3^3 & 0 & 0 & 0 \\ 0 & 0 & 0 & C_4^4 & 0 & 0 \\ 0 & 0 & 0 & 0 & C_4^4 & 0 \\ 0 & 0 & 0 & 0 & 0 & C_6^6 \end{pmatrix}; \tag{A3.8}$$

By combining (4.30) and (A3.5), we get that:

$$\begin{aligned} S^1 &= \frac{Y}{1-\nu^2}[\varepsilon^1 + \nu\varepsilon^2] = \frac{Y}{1-\nu^2}[\epsilon^1 + \nu\epsilon^2], \\ S^2 &= \frac{Y}{1-\nu^2}[\varepsilon^2 + \nu\varepsilon^1] = \frac{Y}{1-\nu^2}[\epsilon^2 + \nu\epsilon^1], \\ S^6 &= \frac{Y}{1-\nu^2}[(1-\nu)\varepsilon^6] = \frac{Y}{1-\nu^2}\left[\frac{(1-\nu)}{2}\epsilon^6\right], \end{aligned} \tag{A3.9}$$

where Y is the 3D Young's modulus.

Our matrix will be therefore of the form:

$$C = \begin{pmatrix} \Sigma & \nu\Sigma & C_3^1 & 0 & 0 & 0 \\ \nu\Sigma & \Sigma & C_3^1 & 0 & 0 & 0 \\ C_3^1 & C_3^1 & C_3^3 & 0 & 0 & 0 \\ 0 & 0 & 0 & C_4^4 & 0 & 0 \\ 0 & 0 & 0 & 0 & C_4^4 & 0 \\ 0 & 0 & 0 & 0 & 0 & \frac{1-\nu}{2}\Sigma \end{pmatrix}, \tag{A3.10}$$

where:

$$\Sigma = \frac{Y}{1-\nu^2}. \tag{A3.11}$$

For the Young's moduli, we take the values experimentally measured in Refs. [15, 56, 74, 75, 305, 311, 313, 316, 317, 333–337], as listed in Chapter 4, Table 4.3. For the Poisson's ratio ν and for the matrix elements C_3^1, C_3^3, and C_4^4, we take the parameters calculated by DFT in The Materials Project [21, 331, 332] or given in Ref. [156] (see Additional Material, sec. A2 for the values of the Poisson's ratio). The matrix elements were rescaled by keeping into account the experimental Young's moduli. With this procedure, we home-built the following matrices (where all the values are in GPa):

- Graphite:

$$C = \begin{pmatrix} 1029.1 & 181.1 & -1.1 & 0 & 0 & 0 \\ 181.1 & 1029.1 & -1.1 & 0 & 0 & 0 \\ -1.1 & -1.1 & 9.1 & 0 & 0 & 0 \\ 0 & 0 & 0 & 2.3 & 0 & 0 \\ 0 & 0 & 0 & 0 & 2.3 & 0 \\ 0 & 0 & 0 & 0 & 0 & 424.0 \end{pmatrix}; \tag{A3.12}$$

- hBN:

$$C = \begin{pmatrix} 860.2 & 191.9 & 1.2 & 0 & 0 & 0 \\ 191.9 & 860.2 & 1.2 & 0 & 0 & 0 \\ 1.2 & 1.2 & 5.9 & 0 & 0 & 0 \\ 0 & 0 & 0 & 2.4 & 0 & 0 \\ 0 & 0 & 0 & 0 & 2.4 & 0 \\ 0 & 0 & 0 & 0 & 0 & 334.2 \end{pmatrix}; \tag{A3.13}$$

- MoS_2:

$$C = \begin{pmatrix} 287.1 & 71.8 & 1.6 & 0 & 0 & 0 \\ 71.8 & 287.1 & 1.6 & 0 & 0 & 0 \\ 1.6 & 1.6 & 4.9 & 0 & 0 & 0 \\ 0 & 0 & 0 & 1.6 & 0 & 0 \\ 0 & 0 & 0 & 0 & 1.6 & 0 \\ 0 & 0 & 0 & 0 & 0 & 107.7 \end{pmatrix}; \tag{A3.14}$$

- $MoSe_2$:

$$C = \begin{pmatrix} 212.2 & 49.4 & 1.3 & 0 & 0 & 0 \\ 49.4 & 212.2 & 1.3 & 0 & 0 & 0 \\ 1.3 & 1.3 & 3.8 & 0 & 0 & 0 \\ 0 & 0 & 0 & 1.3 & 0 & 0 \\ 0 & 0 & 0 & 0 & 1.3 & 0 \\ 0 & 0 & 0 & 0 & 0 & 81.4 \end{pmatrix}; \tag{A3.15}$$

- $MoTe_2$:

$$C = \begin{pmatrix} 108.5 & 26.6 & 1.1 & 0 & 0 & 0 \\ 26.6 & 108.5 & 1.1 & 0 & 0 & 0 \\ 1.1 & 1.1 & 2.2 & 0 & 0 & 0 \\ 0 & 0 & 0 & 4.4 & 0 & 0 \\ 0 & 0 & 0 & 0 & 4.4 & 0 \\ 0 & 0 & 0 & 0 & 0 & 41.0 \end{pmatrix}; \tag{A3.16}$$

- WS_2

$$C = \begin{pmatrix} 272.6 & 59.7 & 1.6 & 0 & 0 & 0 \\ 59.7 & 272.6 & 1.6 & 0 & 0 & 0 \\ 1.6 & 1.6 & 4.9 & 0 & 0 & 0 \\ 0 & 0 & 0 & 1.6 & 0 & 0 \\ 0 & 0 & 0 & 0 & 1.6 & 0 \\ 0 & 0 & 0 & 0 & 0 & 106.4 \end{pmatrix}. \tag{A3.17}$$

- WSe_2:

$$C = \begin{pmatrix} 171.8 & 33.6 & 1.1 & 0 & 0 & 0 \\ 33.6 & 171.8 & 1.1 & 0 & 0 & 0 \\ 1.1 & 1.1 & 2.2 & 0 & 0 & 0 \\ 0 & 0 & 0 & 1.1 & 0 & 0 \\ 0 & 0 & 0 & 0 & 1.1 & 0 \\ 0 & 0 & 0 & 0 & 0 & 69.0 \end{pmatrix}. \tag{A3.18}$$

- WTe_2:

$$D = \begin{pmatrix} 82.6 & 14.5 & 0.9 & 0 & 0 & 0 \\ 14.5 & 82.6 & 0.9 & 0 & 0 & 0 \\ 0.9 & 0.9 & 1.9 & 0 & 0 & 0 \\ 0 & 0 & 0 & 0.9 & 0 & 0 \\ 0 & 0 & 0 & 0 & 0.9 & 0 \\ 0 & 0 & 0 & 0 & 0 & 34.0 \end{pmatrix}. \tag{A3.19}$$

A4 Experimental setup

Our measurements were taken at the Optical Spectroscopy of Nanostructured Materials laboratory, at the Physics Department of Sapienza, University of Rome. Different kind of measurements were performed, including macro-photoluminescence (PL) experiments and imaging, micro-photoluminescence (μ-PL) and micro-Raman (μ-Raman) mapping. We will here provide a description of the experimental apparatus used to perform the measurements. A sketch of the experimental setup can be seen in Fig. A4.1(a).

Primary source Our primary source was a frequency-doubled solid-state laser DPSS series by Lasos, emitting at (532.2 ± 0.2) nm. The laser exploits neodymium-doped yttrium vanadate (Nd:YVO4) —with an output frequency corresponding to a wavelength of ~ 1064 nm— as active medium. Green light is generated via second harmonic generation by a lithium triborate (LBO) type-I non-linear crystal. The output power can amount to 300 mW with a warming-up time of a few minutes. The laser guarantees with a wavelength stability after 8 hours within 5 picometres, and a power stability less than $\pm$ 2 %. The generated beam is characterised by a beam waist diameter equal to (0.70 ± 0.07) mm, a beam divergence inferior to 1.3 mrad and an ellipticity of 1.00 ± 0.15 (that is, the spot is a virtually perfect circular spot). Laser light is sent onto the sample surface by mirrors, and focused by microscope objectives, as will be detailed next. The power incident on the sample is measured through a Si photodiode positioned in front of a mirror, where it measures the light reflected by the mirror itself. The presence of mirrors and lenses can be seen in Fig. A4.1(b), where the optical table is shown; the μ-PL / μ-Raman setup can be seen in the background.

Objectives Our focusing system was equipped with several microscope objectives. In particular, the following objectives were used for our measurements:

- a 10× Leitz objective with numerical aperture (NA) equal to 0.2 used to take large-scale images of the sample and for collective PL experiments (the dimension of the spot is around 5 μm, as detailed next);
- two Olympus *Long working-distance Metallographic Plan Fluorite semi apochromat* (LMPLFLN) objectives with magnification 20× (NA = 0.4) and 50× (NA = 0.5). The main characteristic of these objectives is their long working-distance —equal to 12 mm and 10.6 mm, respectively— which make them suitable for measurements at low temperature, where the windows of the cryostat are positioned in between the objective and the sample. These objectives are characterised by a very high transmittance ($\sim$ 90 %) and high correction of chromatic aberrations in the visible range;
- a *Long working Distance Enhanced Contrast Plan Neofluar* (LD EC Epiplan-Neofluar) Zeiss objective with magnification 100× and NA = 0.75. This ob-

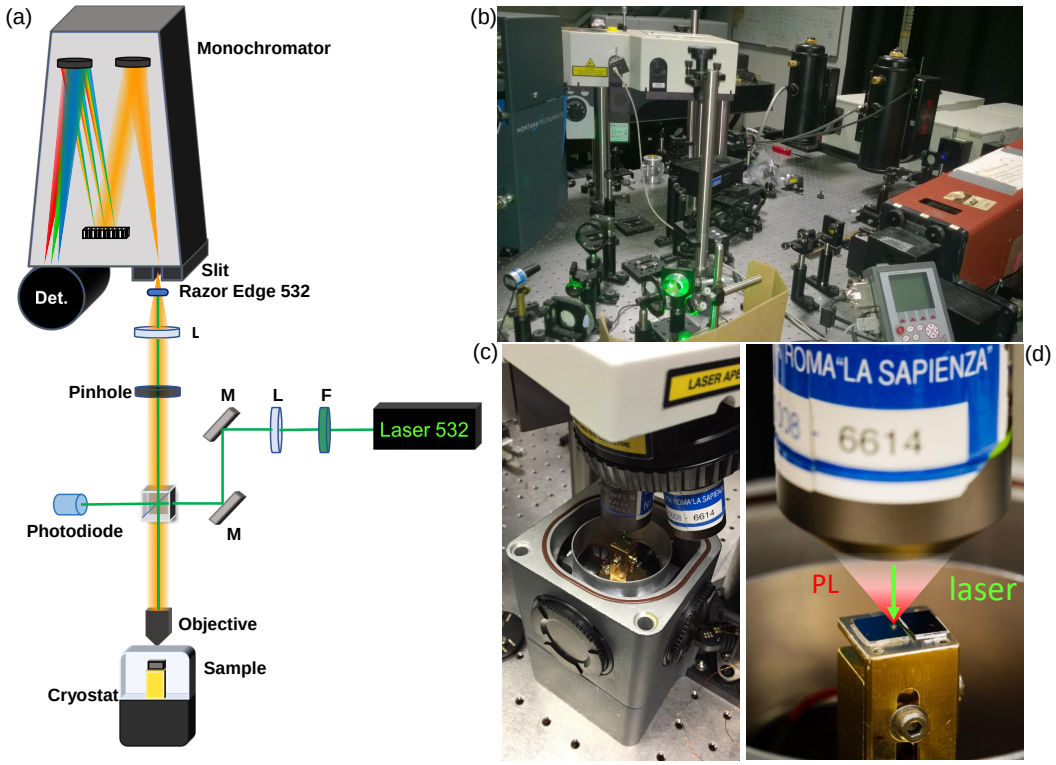

Figure A4.1: (a) Sketch of the experimental setup used for μ-Raman and μ-PL measurements, from its primary source (the laser), to the detector. M indicates mirrors, L lenses, F filters. The laser beam (green in this sketch) is used to excite the sample. The laser light reflected by the sample is filtered out with a razor edge filter, whereas the signal emitted by the sample (orange beam) is sent through a pinhole (confocal configuration) and enters the monochromator. A schematic representation of the Czerny-Turner scheme, which allows the monochromatisation of light is depicted in the monochromator. Det. indicates the detector, which can be either a silicon CCD or an InGaAs array, depending on the spectral range of interest. (b) Real image of our optical table. In the foreground, mirrors and filters can be seen; via these objects, the laser signal is sent to the μ-Raman/PL setup in the background. On the right (light gray), two monochromators can be seen. (c) Zoom of the μ-Raman/PL setup: The 50× objective is focused onto the sample, which is mounted on the holder. (d) Zoom of the objective focused onto the sample and sketch of the excitation/collection process: The laser is focused onto the sample via the objective; the illuminated area is thus excited and emits a PL (or Raman) signal, which is collected by the same objective, in a back-scattering geometry.

jective works at a working distance of 4 mm in spite of its high magnification and NA, so that it can be used also in presence of an interposed window, for low temperature measurements;

- an Olympus *Metallographic Plan Apochromat* (MPLN) objective with magnification 100×. It is characterised by a high NA = 0.9, but it works at a

short working distance (0.21 mm), which makes it suitable only for room temperature measurements (namely, when there are not windows in between the objective and the sample). Its transmittance in the visible range is equal to 90 % and it is characterised by a high correction of chromatic aberrations in the visible range. Due to its characteristics, this objective is highly appropriate for μ-PL/Raman measurements and mapping, due to the high NA and therefore to the small dimension of the spot, as it will be right now detailed.

The objectives allow us to focus the laser onto our sample, with a spot whose dimension is determined by the diffraction limit. It is known, in fact, that the diffraction limit is proportional to $1/\tan(\theta)$, where θ is the maximal half-angle of the light cone that can enter/exit the considered lens, and is therefore related to the NA via the formula NA = n·sin(θ), where n is the refractive index of the medium in which the system is immersed. Since the spot of the laser can be modelled as a gaussian, and since the dimension of the spot of the laser focused onto the sample is defined by the diffraction limit of the objective through which the laser is focused, it follows that the gaussian-spot will have a σ depending on the NA of the objective. In particular, it holds that —in air (where n = 1.0)— $\sigma \sim \frac{1}{\tan(\mathrm{asin}(\mathrm{NA}))}$. Consequently, the higher the NA, the lower the dimension of the spot. For this reason, the objectives with low NA were mostly used for collective measurements —due to the relatively large excited area— whereas those with high NA were used for μ-PL and μ-Raman measurements and mapping. The σ of our green laser had been estimated for the 20× and 50× objectives by means of the knife-edge technique [481], resulting in $\sigma_{20\times} = (0.75 \pm 0.02)$ μm for the 20× objective with NA = 0.4, and $\sigma_{50\times} = (0.39 \pm 0.02)$ μm for the 50× objective with NA = 0.5. In the case of the 100× Olympus objective with NA = 0.9 —that is, the one we used for all our μ-PL and μ-Raman mappings, where the knowledge of the size of the spot is extremely important— we experimentally determined the laser spot size as follows: Under the same experimental conditions employed in μ-PL/Raman experiments, the laser was scanned across a reference sample, lithographically patterned with features of known width (1 μm) and known spacing (2 μm). The intensity of the reflected light, collected through the same path used in the μ-PL/Raman experiments, was fitted with the ideal reflectance profile, convolved with a Gaussian peak. The standard deviation of this peak, obtained as a fitting parameter, provides our estimate of $\sigma_{100\times} = (0.23 \pm 0.01)$ μm. For the other objectives, a rough numerical estimation can be obtained via an interpolation of the known σ of the 20×, 50× and 100× objectives as a function of $\frac{1}{\tan(\mathrm{asin}(\mathrm{NA}))}$, getting $\sigma_{10\times} \sim 2.4$ μm and $\sigma_{\mathrm{Zeiss}100\times} \sim 0.28$ μm. A precise estimation would require a direct measurement. However, due to the limited use of these objectives in our experiments, this has not been considered necessary.

Signal detection The PL signal was collected by the same objective employed to focus the laser beam, in a backscattering geometry, where the laser and the emitted signal wavevectors are anti-parallel. The signal emitted from the sample and collected with the objective passed through collimating lenses and a pinhole,

was then reflected by mirrors and reached to a last lens, which sent the emitted luminescence and reflected light onto the entrance slit of the monochromator, in the form of a focused beam matching the optical characteristics of the dispersing system; see sketch in Fig. A4.1(a). More specifically, the F-number of the focusing lens should match that of the monochromator in order to fill up exactly the monochromator grating: This condition avoids loss of signal and unwanted additional stray light in the monochromator. The reflected laser light was filtered out by filters positioned at the entrance of the monochromator. In the case of the 532 nm laser, it was filtered out by a very sharp high-pass Razor edge filter at 535 nm (Semrock 532 nm MaxLine laser clean-up filter), while when using the supercontinuum laser longpass filters were employed. The analysis of the emitted signal was performed with two different monochromators both operating in the common Czerny-Turner scheme:

- an Acton SpectraPro 750 monochromator with focal length 75.0 cm, equipped with three possible diffraction gratings: a 300 grooves/mm grating and a 600 grooves/mm grating blazed at 1.0 μm, and a 1200 grooves/mm grating blazed at 0.5 μm;

- an IsoPlane 160 (from Princeton Instruments) having focal length 20.3 cm, equipped with a 150 grooves/mm grating blazed at 800 nm, a 300 grooves/mm grating blazed at 1.0 μm, and a 150 grooves/mm grating blazed at 2.0 μm (the latter was not used in the present thesis).

The gratings were mounted on a rotating turret driven by a stepping-motor, that allowed remote-controlled wavelength scan and grating switch. To detect the signal, two different detectors were used, depending on the wavelength range:

- a back-illuminated Si CCD Camera (model 100BRX) by Princeton Instruments, liquid-N_2 cooled to -120 ℃ to reduce thermal noise. The CCD is made of 1340 pixels $\times$ 100 pixels, where each pixel dimension is 20 μm $\times$ 20 μm. The CCD works in the VIS-NIR frequency range 400-1100 nm with dispersion $\Delta\lambda = 2.2 \cdot 10^{-3}$ nm in the case of the 1200 grooves/mm grating. The CCD was used for most of our measurements: All our Raman measurements and all our PL experiments concerning the compounds WS_2, MoS_2, WSe_2 and $MoSe_2$.

- An InGaAs linear array, liquid-N_2 cooled to -100 ℃ . The array consists of 512 pixels with size 50 μm $\times$ 500 μm and can detect in the wavelength range 800-1400 nm, with dispersion $\Delta\lambda = 5.5 \cdot 10^{-3}$ nm in the case of the 1200 grooves/mm grating. The array was only used for PL measurements of $MoTe_2$ domes and to check the PL of some thick InSe flakes.

Sample and piezoelectric motors When taking measurements, the sample was either placed or glued (by silver paint, for those measurements in which thermal contact was needed) to a copper sample holder, like in Fig. A4.1(c-d). The sample holder was mounted on top of two piezoelectric motors (Attocube), which enabled

independent movements along x and y axis in the sample plane with minimal spatial resolution equal to 50 nm. The movements could be controlled via computer, and all our μ-PL/Raman mappings were taken by exploiting a program capable of making the holder move at a constant rate along the x direction, using a compact open loop piezoelectric xy-scanner. The scanning step was of the desired size (typically set between 80 nm and 200 nm) and the size was set by increasing the voltage of a given amount, corresponding to the desired step.

Due to the non-perfect linearity of the scanner in response to voltage variations, the laser was scanned across a reference sample, lithographically patterned with features of known width equal to 1 μm and known spacing equal to 2 μm. The intensity of the reflected light was collected, resulting in a maximum intensity at the centre of the features, and a minimum one in the spacings. The measurement was acquired by increasing the voltage of a constant amount (the same used for μ-PL/Raman mappings) from 0 to the maximum voltage. The distance between the maxima in the collected spectra was therefore equal to the centre-to-centre distance of the patterned features and a comparison between this distance and the nominal distance of the scanner allowed us to obtain a (real distance)/(nominal distance) *vs* voltage curve. This curve was characterised by a non-linear behaviour for small voltages, becoming then linear after a certain voltage. All our maps were therefore either acquired in the linear interval or duly recalibrated via the (real distance)/(nominal distance) *vs* voltage curve.

System response All optical measurements were intensity-normalised by the set-up spectral response in order to have correct estimates of the intensity ratios at different wavelengths. This response was acquired for each grating and objective used for our μ-PL experiments, by using a calibrated black-body source at 3050 K. The source was turned on and its spectrum was acquired in the whole wavelength range of interest for our measurements. A comparison between the acquired spectrum and the black-body spectrum allowed to get the response of the system.

μ-Raman measurements

For Raman measurements, the excitation laser was provided by a single frequency Nd:YVO_4 lasers (DPSS series by Lasos) emitting at 532 nm, or by a diode laser emitting at 405 nm. The measurements shown in this work concerning TMD and hBN domes were taken with the 532 nm laser. An x–y motorised stage by Attocube was used for precise positioning of the sample. The Raman signal was spectrally dispersed by a 750 mm focal length ACTON SP750 monochromator equipped with a 1200 groove/mm grating and detected by a back-illuminated N_2-cooled Si CCD camera (100BRX by Princeton Instruments). The laser light was filtered out by a very sharp long-pass Razor edge filter (Semrock) at 535 nm. The micro-Raman (μ-Raman) spectral resolution was 0.7 cm^{-1}. A 100$\times$ objective with NA=0.9 was

employed to excite and collect the light, in a backscattering configuration.

In establishing the correspondence between strain and radial distance r, a convolution of the strain distribution within the laser spot was duly taken into account.

μ-PL measurements

PL measurements were taken by using a single frequency Nd:YVO_4 lasers (DPSS series by Lasos) emitting at 532 nm. An x–y motorised stage by Attocube was used for precise positioning of the sample. For RT measurements, the laser was focused via the 100× objective with NA =0.9; while for studies at low temperature or as a function of temperature, the 100× objective with NA=0.75 (spot of ∼1 μm) was used, being a long-working distance objective. The signal was collected through the same objective, in a backscattering configuration. The signal was dispersed by using a 0.2 m long monochromator with a 150 grooves/mm and with a a 300 grooves/mm grating, and detected by a N2-cooled Si-charge-coupled device camera.

PL imaging experiments

To get a spatially-resolved image of the light emitted by our samples, we used the setup depicted in Fig. A4.2. In particular, the excitation laser was focused on the chosen flake by a lens of 20 cm focal length, which was positioned laterally with respect to the luminescence-collecting objective. In this manner, the samples were excited over an area in excess of 100×100 μm^2. The PL emission from the sample was then collected via an objective (typically, the 50× objective with NA = 0.5 was used for these experiments), the laser light being filtered out by a longpass filter at 550 nm (with transmission of ∼ 98 % above 550). The optical images were acquired with a power density between 40 and 600 W/cm^2, setting the frame rate of the camera at 1 frame/s and setting the red gain at 100 % (the PL signal of WS_2 domes being at about 690 nm. This setup was used to take the luminescence image shown in Fig. 5.2(b).

It should be noticed that the luminescence pattern obtained in that Figure is not uniform but, for every dome, it gets dimmer on the bottom left side. This is due to the peculiar geometry of the imaging setup. More specifically, as shown in Fig. A4.2, the laser that excites the sample is focused on the sample itself throughout a lens which is placed laterally. Therefore, as sketched in Fig. A4.3, the laser reaches the sample surface at an angle of about $20° - 30°$. For this reason, given the spherical shape of the domes, the side towards the laser beam direction is excited at about 45° (the angle at the dome edge is of about $-20°$, so that the laser beam is at an angle of about $40° - 50°$), while the side which is opposite to the excitation direction is excited in an oblique way with a very small angle (the angle at the dome edge is of about $+20°$, so that the laser beam is at an angle of about $0° - 10°$).

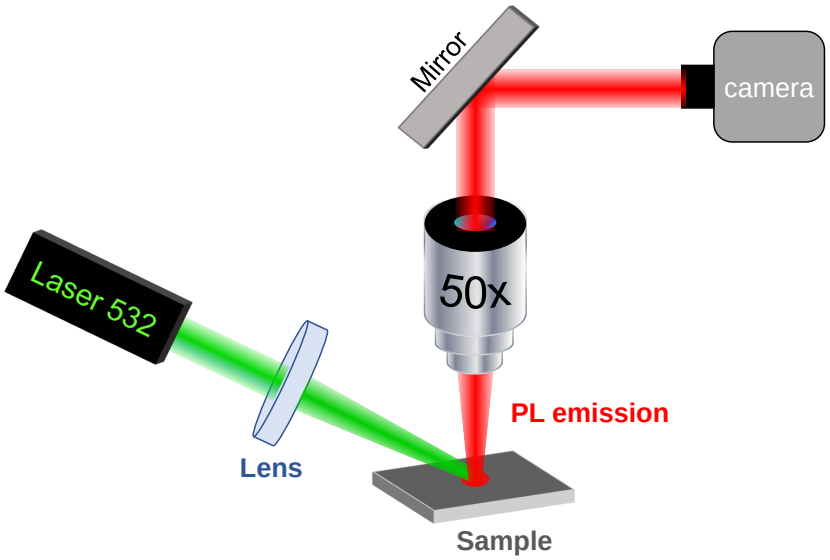

Figure A4.2: (a) Sketch of the experimental setup used to get a spatial image of the light emitted by the sample. The excitation laser is focused on the chosen flake by a lens of 20 cm focal length which is positioned laterally with respect to the luminescence-collecting objective: The sample is excited over an area in excess of 100×100 μm^2. The PL emission from the sample is then collected via an objective (typically, the $50\times$ objective with NA $=$ 0.5) and focused onto a camera.

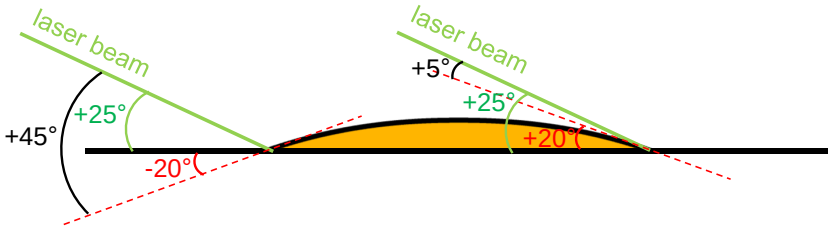

Figure A4.3: Sketch of the imaging experiment on a dome. The aspect ratio of the dome corresponds to the real ones (around 0.16). The laser beam is sent to the sample laterally and forms an angle of $20° - 30°$ with the sample surface (in this sketch, an angle of 25° was chosen). At the edges, the dome surface is tilted with respect to the bulk flake surface of about $\pm20°$. Therefore, on one edge the laser beam reaches the dome surface at an angle of 45°, while on the other side it forms an angle of just 5°.

Time-resolved PL experiments

A supercontinuum pulsed laser, with 50 ps pulse width and a tunable repetition rate (with maximum repetition rate of 77.8 MHz) was used as a source for time-resolved μ-PL measurements, from which the signal decay times were evaluated. The repetition rate was chosen depending on the decay time of the signal. The

laser emission was filtered by an acoustic-optic tunable filter tuned at (532 ± 8) nm. Longpass filters were used to filter our the laser signal. The specific signal of interest was then either filtered by a combination of shortpass and longpass filters (in the case of broad PL bands) or by a monchromator (in the case of narrow lines), and was then focused on a Si avalanche photodiode (APD) with 50 ps temporal resolution. The instrumental response of our setup was always checked by using the laser as a reference.

Second-order autocorrelation measurements

The assessment of the emitter single-photon purity was performed with a Hanbury Brown-Twiss setup, which measured the second-order autocorrelation function ($g^{(2)}(\tau)$) of the emitted light. The measurements were performed under continuous-wave excitation via a 532 nm laser. The PL signal coming from the sample was spectrally filtered with a 20 cm focal length Isoplane 160 monochromator, equipped with a 600 grooves/mm grating. The filtered signal was then divided by a 50/50 beam splitter and collected by two Si avalanche photodiodes with 250 ps temporal resolution. The coincidence counts were calculated by the PicoHarp 300 time-correlated single-photon counting module with a maximum resolution of 4 ps.

PL excitation (PLE) measurements

PLE measurements were taken by using the picosecond supercontinuum laser (by NKT Photonics). The emission wavelength was selected through a tunable filter based on Acousto-Optic Tunable Filter technology, resulting in monochromatic beam with 8 nm full width at half maximum. The measurements were taken in the same configuration used for PL measurements. The signal to be detected was selected by longpass filters before entering the monochromator. The intensity was monitored on the summit of the studied PL peak.

A5 Nano-IR characterisations

The infrared spectra of hBN domes in Chapter 2 were collected with a scanning near-field optical microscopy (SNOM) microscope (NeaSNOM from NeaSpec). A difference-frequency generation laser, yielding a linearly polarised, broadband IR radiation, is focused on a gold-coated AFM probe tip through a parabolic mirror, which is also used to collect the backscattered radiation. The AFM is operated in tapping mode at ~ 220 kHz. The scattered signal is demodulated at several higher harmonics n, and, by selecting those with $n \geq 2$, one has a signal dominated by the near-field interaction of the tip with the sample over the far-field scattered background. The SNOM setup is based on an asymmetric Michelson interferometer (the tip and sample are in one of the arms of a Michelson interferometer), which provides both amplitude and phase of the backscattered radiation [218]. The scattered signal is collected by a N_2-cooled MCT (Mercury-Cadmium-Telluride) detector. The measurements were taken by averaging ten interferograms with a spectral resolution of 8 cm^{-1} [219]. The demodulated phase and amplitude signals are normalised to the reference quantities measured on Au patches in the vicinity of the flakes of interest as:

$$\eta_n(\omega) = s_n^{\text{norm}} e^{i\phi_n^{\text{norm}}} = \frac{s_n^{\text{flake}}}{s_n^{\text{ref}}} e^{i\left(\phi_n^{\text{flake}} - \phi_n^{\text{ref}}\right)}, \tag{A5.1}$$

where s is the near-field amplitude, ϕ the phase, and the suffix n indicates the n^{th} harmonic demodulation. As shown in the literature for materials such as hBN, where one measures strong phonon modes, the scattered amplitude provides the best way to identify the vibrational modes of the flake [221, 222]. It should be noticed that for the SNOM technique, the polarisation plays a relevant role in many cases, such as the intersubband transitions in two-dimensional heterostructures, where the transition can only be excited by light polarised in the vertical direction [225]. For hBN phonons, however, the SNOM technique allows one to measure both the in-plane and out-of plane transverse optical modes [221, 223].

A6 IR-SNOM mapping measurements of hBN domes

Comparison between different harmonics

nanoFTIR spectra are measured with a near-field microscope (sSNOM, NeaSNOM from NeaSPEC). The broadband illumination is focused via a parabolic mirror on the sample and the AFM tip. As the focus is diffraction-limited, there is an unavoidable background that arises from the light scattered by the sample regions that are not under the tip apex and by the tip shaft. In order to suppress the contribution of the background to the total signal, it is possible to demodulate the signal at high harmonics of the tip oscillation frequency, thus obtaining the near-field signal scattered from the volume under the tip only [482]. In Fig. A6.1, we show line scans taken on the dome of Fig. 2.8, ad specifically along the grey short-dashed line in Fig. 2.8(a). Fig. A6.1 compares the signal amplitude $S(\omega, r)$ at different harmonic demodulations. The scattered signal recorded at the fundamental harmonic shows the signature of the phonon peak of the unstrained hBN coming from outside the dome or from beneath the dome together with the red-shifted phonon mode of the strained material. Moving to the amplitude demodulated at the second harmonic, we can detect only the signal scattered by the thin strained hBN that comprises the dome, and an almost identical line scan is obtained at the 3$^{\text{rd}}$ harmonic demodulation.

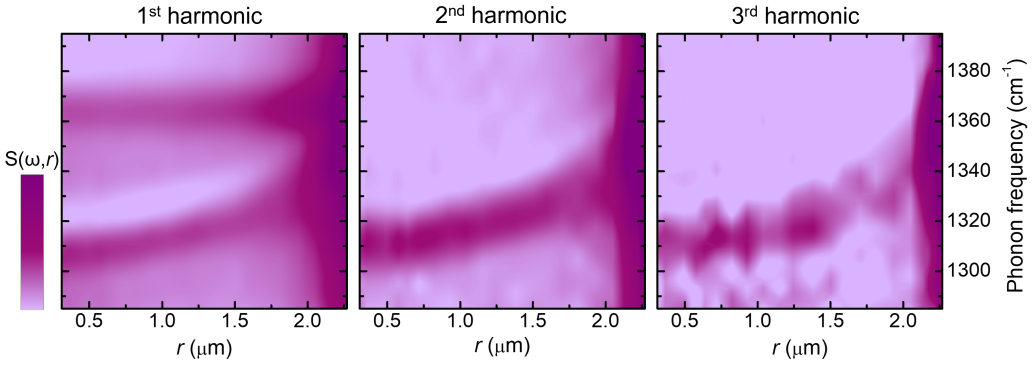

Figure A6.1: Comparison among the first three harmonics of the scattered signal obtained by nanoFTIR line scans taken along the grey short-dashed line in Fig. 2.8(a).

Mapping measurements of other bubbles

To complement the results presented in Fig. 2.8, we performed similar nanoFTIR measurements on other two domes. In Fig. A6.2(a), we show the AFM image of the second dome we studied. This dome has $R = 0.94$ μm and $h_0 = 99$ nm, resulting in $h_{\text{m}}/R = 0.105$. The height profile of this dome measured along a diameter (cyan dashed line in panel (a)) is shown in panel (b). The nanoFTIR measurements were

taken along the same diameter. FEM calculations reproduce quite well the height profile. Indeed, this dome features a lower aspect ratio with respect to that of Fig. 2.8. This results in a lower strain, whose maximum value reaches 1.5 %, as shown in panel (c). Analogously to the case of the previous dome, we show the first three harmonics of the scattered amplitude associated to the IR phonon, see panel (d). The measurements were performed along the cyan dashed line superimposed to the AFM image in panel (a). Similarly to the previous dome, the 1$^{\text{st}}$ harmonic shows the signature of both the strained dome phonon peak and that of the unstrained hBN outside or beneath the dome. In the second harmonic there is still a weak trace of the unstrained hBN, which is instead negligible in the line scan of the third harmonic. By exploiting the one-to-one correspondence between $\varepsilon_{\text{tot}} = \varepsilon_r + \varepsilon_\theta$ and r determined in panel (c), we performed a fit to the data in panel (e), providing an extrapolation frequency at null strain $\omega^0_{1\text{u}} = (1369.0 \pm 5.2)$ cm^{-1} and a shift rate $\Delta_{1\text{u}} = (36.2 \pm 3.6)$ cm^{-1}/%, resulting in a Grüneisen parameter (see Eq. (2.11)) $\gamma_{1\text{u}} = 2.64 \pm 0.27$.

Analogous measurements were performed for a third dome, whose AFM mage is shown in Fig. A6.3(a). In this case, the linescan was acquired along a radius to limit the map acquisition time. The corresponding colour plot is given in panel (b). A similar analysis to that discussed for the previous two domes was performed also for this dome. As summarised in panel (c), from the frequency dependence on r —and in turn on $\varepsilon_{\text{tot}} = \varepsilon_r + \varepsilon_\theta$— we determined a strain-free frequency $\omega^0_{1\text{u}} = (1369.9 \pm 2.3)$ cm^{-1} and the shift rate $\Delta_{1\text{u}} = (29.4 \pm 1.8)$ cm^{-1}/%, resulting in a Grüneisen parameter (see Eq. (2.11)) $\gamma_{1\text{u}} = 2.15 \pm 0.12$.

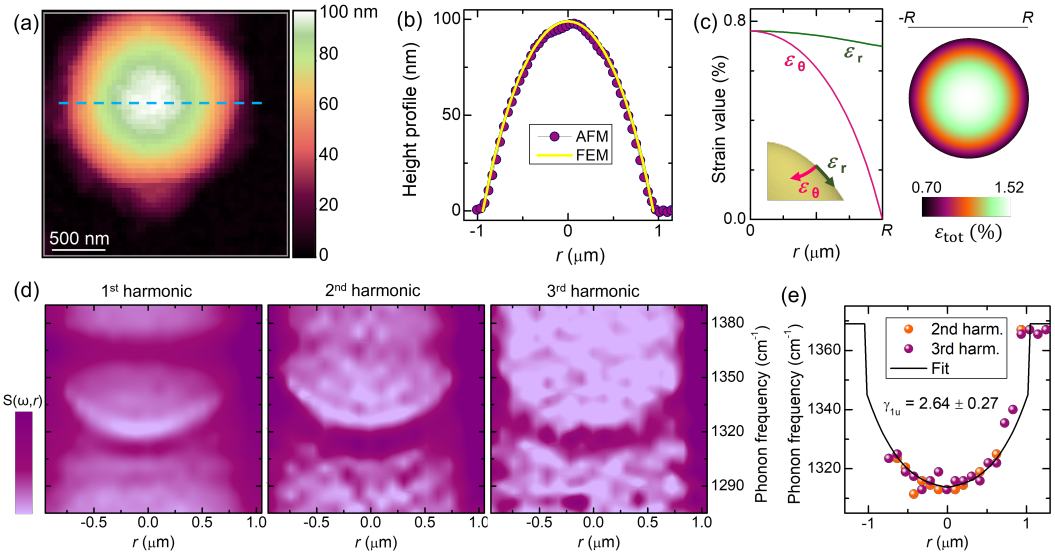

Figure A6.2: IR-active mode *vs* strain for a second dome. (a) 2D AFM image of a circular hBN dome, with $R = 0.94$ μm and $h_0 = 99$ nm ($h_m/R = 0.105$) and created in a deuterated sample (beam energy equal to 6 eV). (b) Comparison between the AFM profile acquired along a diameter of the dome (highlighted in panel (a) by a cyan dashed line) and the profile obtained by FEM calculations. (c) Left: Radial dependence —obtained by FEM calculations— of the in-plane circumferential (ε_θ) and radial (ε_r) strain components, a sketch of which is depicted as inset. Right: Spatial distribution of the total in-plane strain $\varepsilon_{tot} = \varepsilon_r + \varepsilon_\theta$. (d) Colour map of the intensity of the first three harmonics of the signal associated to the IR active mode (E_{1u}) while scanning the SNOM tip along the cyan dashed line shown in panel (a). (e) IR phonon frequency dependence of the 2nd and 3rd harmonic on the radial distance r. The black solid line is a fit to the data assuming a linear dependence of the phonon frequency on ε_{tot}, provided by Eqs. (2.3) and (2.4). Figure reproduced with permission from E. Blundo *et al.*, Nano Lett. **22**, 1525 (2022) [169]. Copyright 2022, The Authors.

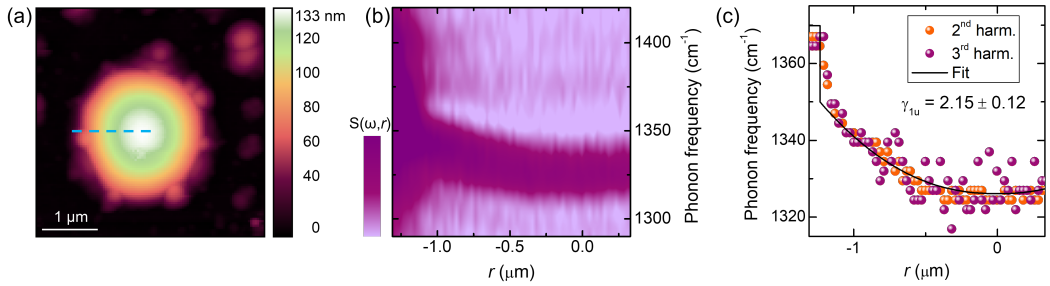

Figure A6.3: IR-active mode *vs* strain for a third dome. (a) 2D AFM image of a circular hBN dome, with $R = 1.23$ μm and $h_0 = 126$ nm ($h_\mathrm{m}/R = 0.102$) and created in an hydrogenated sample (beam energy equal to 34 eV). (b) Amplitude line scan of the 2$^\mathrm{nd}$ harmonic signal associated to the IR active mode ($E_{1\mathrm{u}}$) along the cyan dashed line shown in panel (a). (c) IR phonon frequency dependence of the second and third harmonic line scans as a function of the radial distance r. The black solid line is a fit to the data assuming a linear dependence as extracted from the phonon frequency on ε_tot, provided by Eqs. (2.3) and (2.4). Figure reproduced with permission from E. Blundo *et al.*, Nano Lett. **22**, 1525 (2022) [169]. Copyright 2022, The Authors.

A7 Raman mapping measurements of hBN domes

Here, we show additional Raman mapping measurements taken along the diameter of other hydrogen- (or deuterium-) filled hBN bubbles. In panel (a) of Figs. A7.1 and A7.2, we show the false colour plots of the intensity associated to the Raman spectra measured along the diameter of two different hBN bubbles. The most intense peak of the plots is assigned to the E_{2g} mode of the unstrained hBN bulk under the bubble. The weak peak that shifts as a function of the position of the excitation spot is the E_{2g} mode of the hBN layers comprised in the bubble. In panels (b), we show the corresponding Raman spectra, stacked by y-offset. Finally, in panels (c), we show the dependence of the Raman mode frequency as a function of the distance from the centre r. We also show the fit to the experimental data to extract the Grüneisen parameter of the Raman mode.

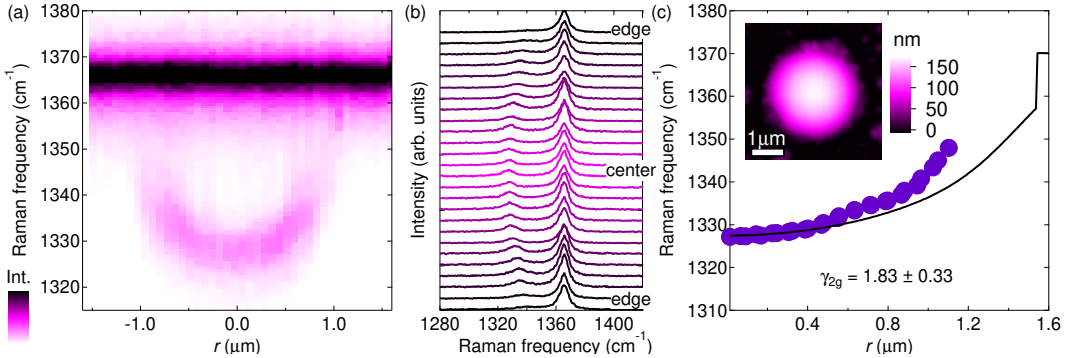

Figure A7.1: Summary of the Raman measurements performed on a hBN dome with $R = 1.59$ μm and $h_0 = 181$ nm ($h_m/R = 0.114$) and created in a deuterated sample (beam energy equal to 6 eV). (a) False colour image of the intensity of Raman spectrum as a function of position along a diameter of a bubble. (b) Corresponding Raman spectra. (c) E_{2g} Raman mode frequencies as a function of the distance from the centre of the dome r. The solid line is a linear fit. The Grüneisen parameter is $\gamma_{2g} = 1.83 \pm 0.33$, which corresponds to a shift rate of $\Delta_{2g} = (25.1 \pm 4.5)$ cm^{-1}/%. Figure reproduced with permission from E. Blundo *et al.*, Nano Lett. **22**, 1525 (2022) [169]. Copyright 2022, The Authors.

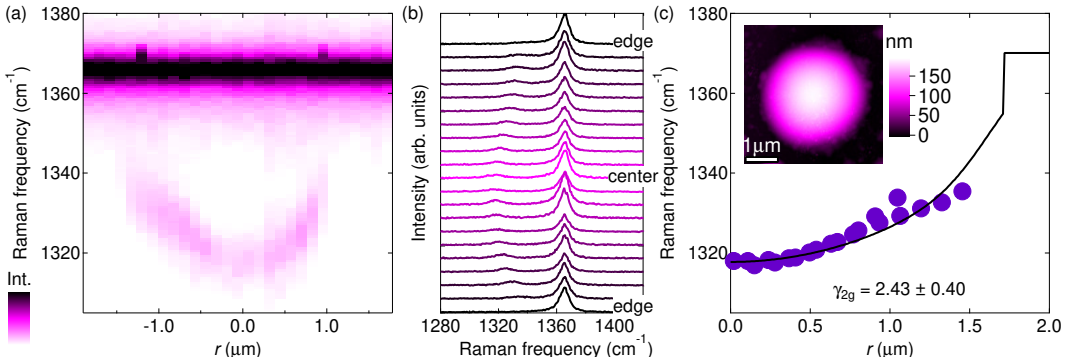

Figure A7.2: Summary of the Raman measurements performed on a hBN dome with $R = 1.71$ μm and $h_0 = 179$ nm ($h_\mathrm{m}/R = 0.105$) and created in a deuterated sample (beam energy equal to 6 eV). (a) False colour image of the intensity of Raman spectrum as a function of position along a diameter of a bubble. (b) Corresponding Raman spectra. (c) E_{2g} Raman mode frequencies as a function of the distance from the centre of the dome r. The solid line is a linear fit. The Grüneisen parameter found experimentally for this dome is $\gamma_{2g} = 2.43 \pm 0.40$, which corresponds to a shift rate of $\Delta_{2g} = (33.2 \pm 5.2)$ cm^{-1}/%. Figure reproduced with permission from E. Blundo *et al.*, Nano Lett. **22**, 1525 (2022) [169]. Copyright 2022, The Authors.

A8 Statistical analysis of the shift rates and Grüneisen parameters of hBN domes

To have a larger statistical analysis of the shift rates and Grüneisen parameters, we measured the Raman shifts at the centre of about ten bubbles. We chose to perform Raman measurements rather than nano-FTIR measurements since the latter are more demanding. The resulting histogram is shown in Fig. A8.1. A Gaussian fit to the data provides an average shift with respect to the frequency of the unstrained membrane (assumed to be $\omega_{2g}^0 = 1370$ cm^{-1}) equal to 53 ± 11 cm^{-1}. To estimate the Grüneisen parameter, we need to estimate the average strain at the dome center. Indeed, the latter is related to the aspect ratio via the following equation [116]:

$$\varepsilon^{\text{center}} = 0.715 \cdot \left(\frac{h_0}{R}\right)^2, \tag{A8.1}$$

We thus considered the aspect ratios measured for a hundredth of domes (see Fig. 1.10(f)), and estimated a average value equal to 0.115 ± 0.011, see Fig. A8.1. In turn, from Eq. 4.64, we estimate $\varepsilon^{\text{center}} = (1.90 \pm 0.35)$ %. We can finally estimate the average Grüneisen parameter as:

$$\gamma_{2g} = \frac{\omega_{2g}^{\text{center}} - \omega_{2g}^0}{\omega_{2g}^0 \cdot \varepsilon^{\text{center}}}, \tag{A8.2}$$

getting $\gamma_{2g} = 2.04 \pm 0.48$. This value agrees well with that estimated via Raman mapping measurements (see Table 2.1).

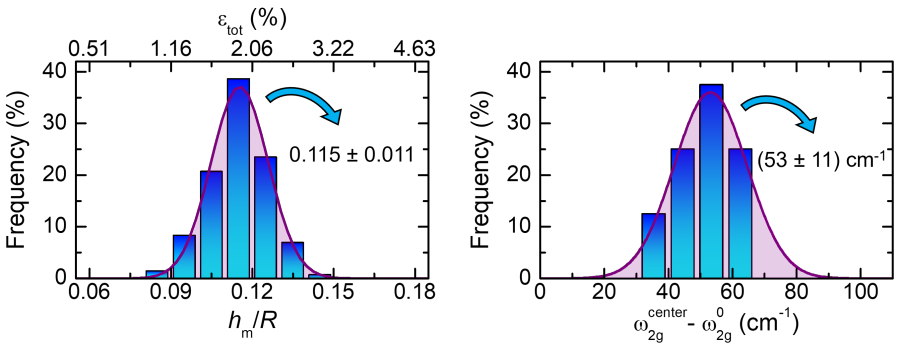

Figure A8.1: Histograms of the aspect ratios h_0/R (left) and Raman shifts measured at the summit of the domes $\omega_{2g}^{\text{center}} - \omega_{2g}^0$ (right). The Raman shift was calculated with respect to the unstrained value, which is assumed to be $\omega_{2g}^0 = 1370$ cm^{-1}. A Gaussian fit to the data (purple) provides the average values for both the two quantities. Figure reproduced with permission from E. Blundo *et al.*, Nano Lett. **22**, 1525 (2022) [169]. Copyright 2022, The Authors.

A9 Polarisation-resolved Raman measurements in hBN domes

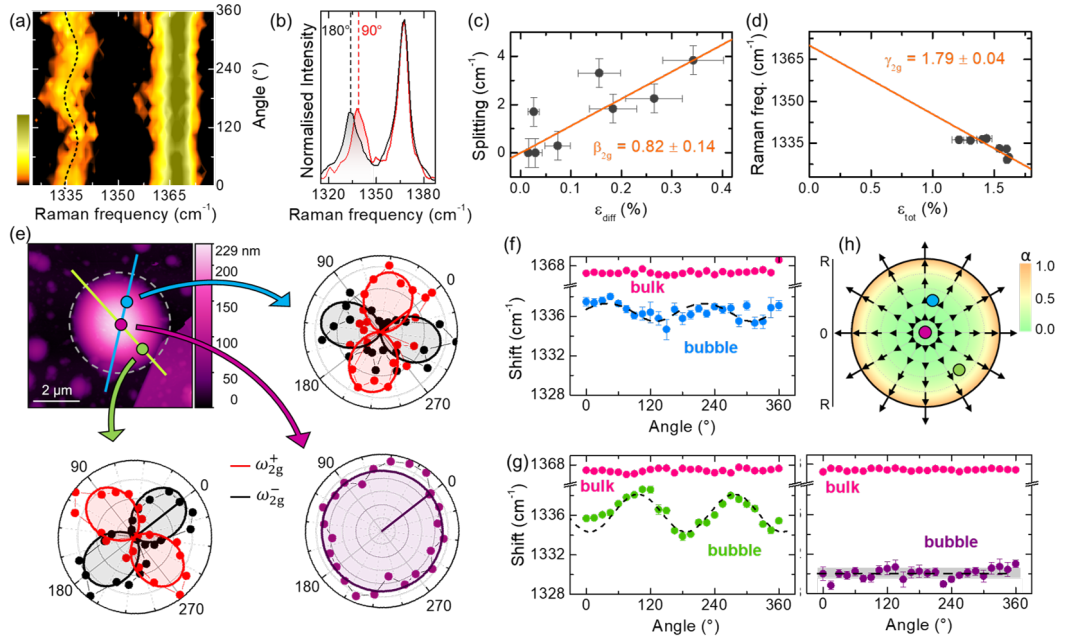

Figure A9.1: (a) Colour map of the intensity of the E_{2g} Raman mode as a function of the angle of the polarisation analyser. The bulk mode at ∼1367 cm^{-1} shows no modulation. The dome mode at ∼1335 cm^{-1} shows a clear frequency oscillation, as highlighted by the black dashed line. (b) Two illustrative spectra corresponding to perpendicular angles equal to 90° and 180°. A splitting is clearly visible. (c-d) Summary of the splittings *vs* $\varepsilon_{\rm diff}$ (c) and average frequencies *vs* $\varepsilon_{\rm tot}$ (d) measured by performing a similar analysis on several points over the bubble. The corresponding strain values were estimated via FEM calculations. The solid lines are linear fits. (e) AFM image of the studied hBN bubble. The measurements of panels (a-b) were acquired in the position highlighted by the green dot. Fitting procedures of the spectra allow us to derive the polar plot of the intensities of the low (black) and high (red) frequency Raman modes as a function of the analyser angle. Analogous polar plots were derived from the measurements acquired on the purple and cyan dots. The solid lines in the polar plots are fits to the data. (f) Average frequency behavior obtained from the measurements acquired on the cyan dot. The dashed line follows the sinusoidal behavior of the frequency, which is caused by the strain anisotropy. (g) Average frequency behavior analogous to that of panel (f) but referring to the green and purple dots. (h) Spatial distribution of the strain anisotropy $\alpha = (\varepsilon_r - \varepsilon_\theta)/(\varepsilon_r + \varepsilon_\theta)$, determined based on FEM calculations. The arrows point to the direction of the strain field. Their length is calculated as $\log_{10}(100\alpha)$. The cyan, purple and green dots are in one-to-one correspondence with those superimposed to the AFM image of panel (e). Figure reproduced with permission from E. Blundo *et al.*, Nano Lett. **22**, 1525 (2022) [169]. Copyright 2022, The Authors.

Analogous measurements to those shown in Fig. 2.10 were taken on a second bubble. The dome has $R = 2.04$ µm and $h_0 = 216$ nm ($h_{\rm m}/R = 0.106$) and was created in a deuterated sample (beam energy equal to 25 eV). Fig. A9.1(a) shows an inten-

sity map formed by polarisation-dependent μ-Raman spectra recorded on a given point of the bubble. While the E_{2g} bulk mode at ~ 1367 cm^{-1} remains constant in intensity and frequency, the strain-softened E_{2g} mode of the dome at ~ 1335 cm^{-1} exhibits a sinusoidal behavior of its center-of-mass frequency, pointing to a mode splitting. The splitting is clearly visible from the spectra of Fig. A9.1(b), recorded with opposite polarisations ($\phi = 180°$ and $90°$, corresponding to a minimum and a maximum of the sinusoidal behavior, respectively). Similar measurements were taken on several other points of the dome, in order to determine the splitting and average Raman frequency. From the knowledge of the radial distance r, it was possible to establish the radial and circumferential strain components corresponding to each set of data via FEM calculations. In panels (c) and (d), we display the measured splittings *vs* $\varepsilon_{\text{diff}}$ and the average frequencies *vs* ε_{tot}, respectively. From a linear fit, we could determine the shear deformation potential and Grüneisen parameter. From a detailed analysis of the polarisation-resolved measurements, it is possible to determine also the angular dependence of the high-frequency and low-frequency modes. This is exemplified in panel (e) for three different points of the bubble. The latter are highlighted by the coloured dots superimposed to the AFM image of the bubble. It should be noticed that the data displayed in panels (a) and (b) were acquired on the green spot superimposed to the AFM image in panel (e). Indeed, the angular behavior follows the same rotation of the strain direction. To make it more apparent, the polar plots were rotated counter-clockwise by 38°. In such a manner, it is possible to notice how the red lobes (corresponding to the high-frequency mode) are always aligned parallel to the strain axes, indicated in cyan and green on the AFM image. At the dome centre (purple dot), instead, no splitting could be observed and the dome mode remains constant in intensity when varying the angle of the polarisation analyser. Indeed, the existence of a splitting and in turn the presence of two oppositely-polarised modes is a consequence of the presence of an anisotropic strain. The extent of the anisotropy manifests itself in the amplitude of the oscillating behavior of the centre of mass frequency. This is exemplified in panel (f) for the cyan point, where a splitting of 1.8 cm^{-1} was measured. Indeed, as shown in panel (g), an analysis of the centre of mass frequency reveals a noticeably larger splitting for the green point —equal to 3.8 cm^{-1}— and the absence of splitting for the purple point. This is attributable to the fact the cyan point corresponds to an r value in between those of the purple point —where the anisotropy is null— and of the green point —where the anisotropy is larger— as highlighted by the anisotropy plot in panel (h).

A10 Aspect ratio in random and engineered domes

Fig. A10.1 shows the histograms of the aspect ratio measured in random and engineered MoS_2 domes, obtained from the data displayed in Fig. 3.5(e). Gaussian fits to the histograms allow us to obtain the average aspect ratio for each set of data. These values compare well with the values calculated as an average of the data of Fig. 3.5(e) mentioned in the main text.

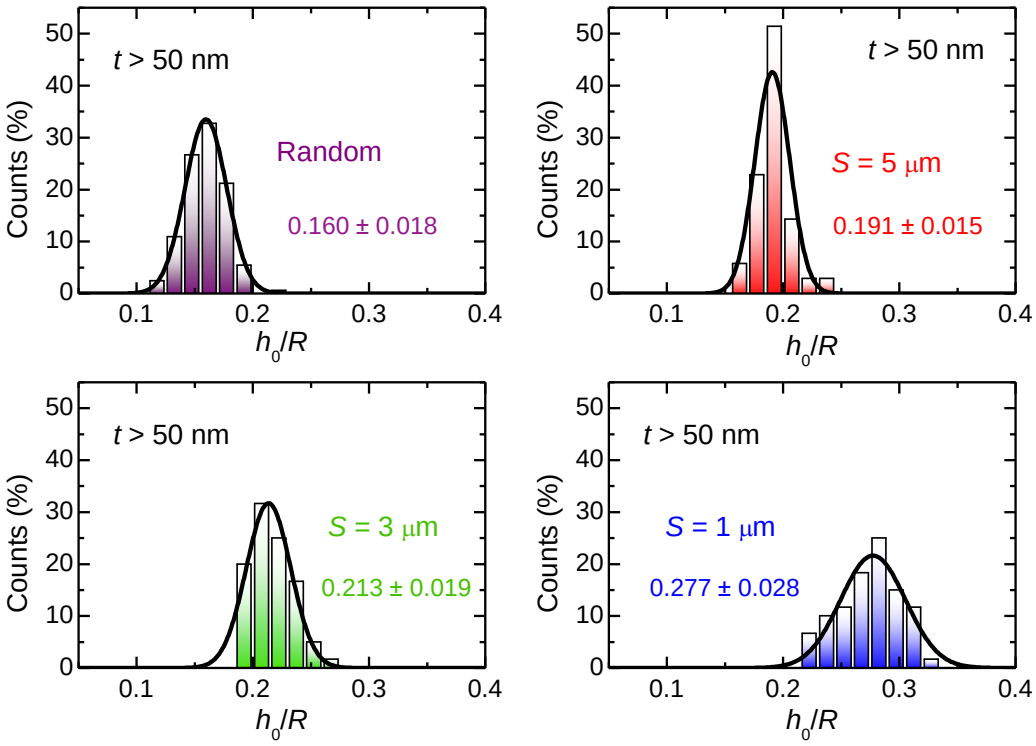

Figure A10.1: Histograms of the aspect ratio measured in random and engineered MoS_2 domes. These histograms were obtained from the data displayed in Fig. 3.5(e). In particular, the engineered domes were created in HSQ resists with thickness $t > 50$ nm and in holes with sizes of 5 μm, 3 μm, and 1 μm. The black continuous lines are gaussian fits to the histograms, providing the average values displayed in the plots.

Indeed, this statistical analysis highlights a significant increase in the aspect ratio in engineered domes, if the resist is sufficiently thick. As mentioned in the main text, this effect is attributable to the mechanical constraint applied by the mask on the domes: If the mask is too thin, its contribution to the total energy of the system is negligible, so that the highly pressurised gas within the domes is able to raise the resist; if the mask it thick enough, its contribution is instead significant and the aspect ratio of the domes is increased.

As a further proof of the role played by the resist, we used an AFM tip to indent a patterned dome with high aspect ratio, in order to cause a deflating process and

reduce a bit its size. In this manner, the dome would not be anymore in contact with the resist and its aspect ratio should relax to its natural universal value.

More specifically, we applied an extra mechanical stress to a patterned dome through an AFM tip. This experiment was done on several patterned domes, but in most cases no deflating processes could be induced due to the remarkable robustness of the system. After several attempts, we were able to induce a deflating process in a patterned dome ($S = 3$ μm) with $h_0/R = 0.206$. By pushing down the tip, a deflating process was induced and the original dome was separated in four smaller domes, all with an aspect ratio of about 0.16. Finally, by scanning the tip over the domes we were able to induce a coalescence phenomenon, resulting in the formation of a single dome. This dome has smaller dimensions than the original one due to the initial deflation and therefore is no more in contact with the resist. Interestingly, this dome features an aspect ratio $h_0/R = 0.169$, close the universal ratio.

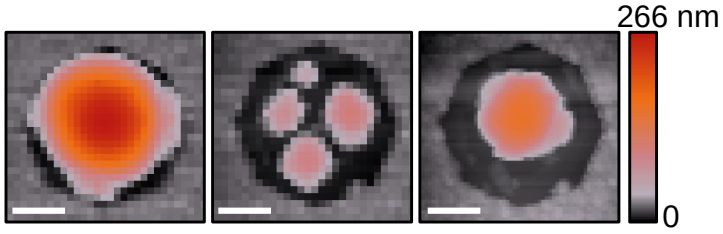

Figure A10.2: Left: AFM image of a patterned dome ($S = 3$ μm) with $h_0/R = 0.206$. Centre: AFM image acquired after indentation of the dome with the AFM tip. The dome was caused to deflate giving rise to four smaller domes with aspect ratio of about 0.16. Right: The four domes were induced to coalesce by the AFM tip, resulting in a single dome with $h_0/R = 0.169$. The whole process took ≈ 10 min. The white scale bar is 1 μm.

A11 Review of previous analytical models for the dome mechanics

Plate analysis by Yue *et al.* [326]

Whenever the height of the dome is comparable to its thickness, the bending stiffness of the membrane is expected to play a role in defining its properties. In that case, the von Karman nonlinear plate theory may be used in the analysis of the domes to take into account the effect of bending stiffness. In this framework, an analytical solution can be found as discussed by Yue *et al.* [326]. In particular, it is assumed the height profile to be:

$$h(r) = h_0 \left(1 - \frac{r^2}{R^2}\right)^2, \tag{A11.1}$$

and a radial displacement:

$$u(r) = r(R - r)(c_1 + c_2 r), \tag{A11.2}$$

where c_1 and c_2 are parameters to be determined. From the Green-Lagrange equations for the radial (Eq. (4.38)) and circumferential (Eq. (4.39)) strain components, one finds that:

$$\varepsilon_r(r) = c_1(R - 2r) + c_2 r(2R - 3r) + \frac{8h^2 r^2 (R^2 - r^2)^2}{R^8}, \tag{A11.3}$$

$$\varepsilon_\theta(r) = (R - r)(c_1 + c_2 r). \tag{A11.4}$$

By imposing equilibrium conditions, it is possible to show that:

$$c_1 = \frac{179 - 89\nu}{126} \frac{h_0^2}{R^3}, \tag{A11.5}$$

$$c_2 = \frac{13\nu - 79}{42} \frac{h_0^2}{R^4}. \tag{A11.6}$$

Finally, equilibrium conditions lead to the following equation for the pressure difference:

$$\Delta p = 64\eta(\nu) E_{2D} \frac{h_0^3}{R^4} + 64D \frac{h_0}{R^4}, \qquad \eta(\nu) = \frac{7505 + 4250\nu - 2791\nu^2}{211680(1 - \nu^2)}. \tag{A11.7}$$

Membrane analysis by Yue *et al.* [326]

If the thickness of the membrane is much smaller than the height of the dome, the bending stiffness of the membrane is expected to be negligible and the membrane

theory can be used, as discussed by Yue *et al.* [326]. In this framework, the height profile is assumed to be

$$h(r) = h_0 \left(1 - \frac{r^2}{R^2}\right), \tag{A11.8}$$

which is approximately a spherical cap for relatively small h_0 compared to R. In addition, a radial displacement is assumed

$$u(r) = u_0 \cdot \frac{r}{R} \cdot \left(1 - \frac{r}{R}\right), \tag{A11.9}$$

where u_0 is a parameter to be determined. From the Green-Lagrange equations for the radial (Eq. (4.38)) and circumferential (Eq. (4.39)) strain components, we have that:

$$\varepsilon_r(r) = \frac{u_0}{R}\left(1 - \frac{2r}{R}\right) + \frac{2h_0^2 r^2}{R^4}, \tag{A11.10}$$

$$\varepsilon_\theta(r) = \frac{u_0}{R}\left(1 - \frac{r}{R}\right). \tag{A11.11}$$

By imposing equilibrium conditions, it is possible to show that:

$$h_0 = \left[\phi(\nu)\frac{\Delta p R^4}{E_{2D}}\right]^{1/3}, \qquad \phi(\nu) = \frac{75(1-\nu^2)}{8(23 + 18\nu - 3\nu^2)}, \tag{A11.12}$$

$$u_0 = \left[\psi(\nu)\frac{\Delta p^2 R^5}{E_{2D}^2}\right]^{1/3}, \qquad \psi(\nu) = \frac{45(3-\nu)^3(1-\nu^2)^2}{8(23 + 18\nu - 3\nu^2)^2}. \tag{A11.13}$$

Since from Eqs. (A11.10) and (A11.11), $\varepsilon_r(0) = \varepsilon_\theta(0) = u_0/R$ and we expect that $\varepsilon_r(0) = \varepsilon_\theta(0) \propto (h/R)^2$, we have that:

$$\varepsilon_r(0) = \varepsilon_\theta(0) = C(\nu)\left(\frac{h_0}{R}\right)^2, \qquad C(\nu) = \frac{u_0 R}{h_0^2} = \left[\frac{\psi(\nu)}{\phi(\nu)^2}\right]^{1/3}. \tag{A11.14}$$

Furthermore, equilibrium conditions lead to the following equation for the pressure difference:

$$\Delta p = \frac{E_{2D}}{\phi(\nu)}\frac{h_0^3}{R^4}. \tag{A11.15}$$

Hencky and Fichter's model [164]

The main idea of this model is to consider polynomial expansions for the height profile and stress components. More specifically, we can first define the dimensionless quantities

$$\rho = \frac{r}{R}$$

$$H(\rho) = \frac{h(\rho)}{R}$$

$$\varsigma = \frac{\Delta p R}{E_{2D}}.$$

After Hecky's approach we have that:

$$N_r(\rho) = \frac{E_{2D}}{4}\varsigma^{2/3}\sum_0^\infty b_{2n}(\nu)\rho^{2n}, \tag{A11.16}$$

$$N_\theta(\rho) = \frac{E_{2D}}{4}\varsigma^{2/3}\sum_0^\infty (2n+1)b_{2n}(\nu)\rho^{2n}, \tag{A11.17}$$

$$H(\rho) = \varsigma^{1/3}\sum_0^\infty a_{2n}(\nu)(1-\rho^{2n+2}), \tag{A11.18}$$

where $b_{2n}(\nu)$ and $a_{2n}(\nu)$ are the coefficients of the expansion. This model allows to find a simple analytical solution for $r = 0$. In that case:

$$N_r(0) = \frac{E_{2D}}{4}\varsigma^{2/3}b_0(\nu), \tag{A11.19}$$

$$N_\theta(\rho) = \frac{E_{2D}}{4}\varsigma^{2/3}\sum_0^\infty b_0(\nu), \tag{A11.20}$$

$$H(\rho) = \varsigma^{1/3}a_0(\nu). \tag{A11.21}$$

From Eqs. (4.50) and (4.51), we can calculate the strain components:

$$\varepsilon_r(0) = \varepsilon_\theta(0) = \frac{1}{4}\varsigma^{2/3}\cdot(1-\nu)\cdot b_0(\nu). \tag{A11.22}$$

Since numerical studies suggested that, for negligible bending stiffness, one has [217]:

$$\frac{\Delta p R^4}{E_{2D}h_0^3} = A(\nu) = \frac{1}{\phi(\nu)}, \tag{A11.23}$$

where $\phi(\nu)$ had been defined in Eq. (A11.12), we can express the strain at the dome centre via Eq. (1.1) with

$$f(\nu) = \frac{1}{4}A(\nu)^{2/3}\cdot(1-\nu)\cdot b_0(\nu). \tag{A11.24}$$

Hencky estimated $b_0(\nu)$ for some values of ν. However, an error was found in Hencky's estimate, which was corrected by Fichter [164]. The resulting function $f(\nu)$ differs remarkably from the constant $C(\nu)$ found in the membrane analysis (see Eq. (A11.14)), as we will discuss in more detail in the following.

Scaling analysis by Khestanova *et al.* [112]

Khestanova *et al.* [112] formulated an alternative model in terms of functionals of the height profile and in-plane displacement. In particular, they assumed the height profile to be given by:

$$h(r) = h_0 \cdot \tilde{h}\left(\frac{r}{R}\right), \tag{A11.25}$$

where $\tilde{h}$ is a function satisfying the boundary conditions $\tilde{h}(1) = 0$ and $\tilde{h}(0) = 1$. The authors of that work suggest that —for negligible bending stiffness— this function is well approximated by $\tilde{h}(x) = 1 - x^2 + 0.25(x^2 - x^4)$. The radial in-plane displacement is then taken to be:

$$u_r(r) = \frac{h_0^2}{R} \cdot \tilde{u_r}(R), \tag{A11.26}$$

The total energy of the dome is then expressed in terms of some functionals of the height profile (c_1, c_2, c_3, c_V) as:

$$\begin{aligned} U_{\text{tot}} = c_1\left[\tilde{h}\right] \cdot E_{2D}\frac{h_0^4}{R^2} + c_2\left[\tilde{h}\right] \cdot E_{2D} \cdot \varepsilon_{ext} h_0^2 + \\ + \pi\gamma R^2 + c_3\left[\tilde{h}\right]\kappa\frac{h_0^2}{R^2} + c_V\left[\tilde{h}\right]\Delta p \cdot h_0 R^2, \end{aligned} \tag{A11.27}$$

where ε_{ext} is a generic external isotropic strain applied to the membrane, which is generally null in the absence of external forces. For negligible bending stiffness, the term proportional to the c_3 functional is null and minimisation of the total energy (for $\varepsilon_{ext} = 0$) leads to:

$$\Delta p = \frac{4c_1 E_{2D}}{c_V}\frac{h_0^3}{R^4}. \tag{A11.28}$$

The authors of that work gave the following approximate values for the scaling functionals:

$$c_1 \approx 0.7 \qquad c_2 \approx 0.6 \qquad c_V \approx 1.7. \tag{A11.29}$$

Blister analysis by Dai *et al.* [115]

Dai *et al.* developed a model to describe 2D material blisters both in the shape of domes and of tents. For the height profile and in-plane displacement, they assumed a generic formulation capable of describing both domes and tents:

$$h(r) = h_0\left[1 - \left(\frac{r}{R}\right)^q\right], \qquad u(r) = f(\nu)\frac{h_0^2}{R}\left[\frac{r}{R} - \left(\frac{r}{R}\right)^{2q-1}\right] + u_s\frac{r}{R}, \tag{A11.30}$$

where the last term in the in-plane displacement takes into account possible slippage phenomena at the edge of the blister. For their analysis, the authors set $q = 2/3$ for tents and $q = 2$ for domes, so that the height profile assumed for the domes is the

same of the membrane analysis (Eq. (A11.8)). By developing their analysis in the absence of slippage phenomena ($u_s = 0$), one finds a strain behavior qualitatively analogous to that determined in this work, but that differs quantitatively due to the different height profile function. More details will be given when discussing our model.

For gas filled domes in the absence of slippage phenomena, their model predicts the pressure difference to be:

$$\Delta p = \frac{1}{V}\frac{\pi(7-\nu)}{6(1-\nu)}E_{2D}\frac{h_0^4}{R^2} = \frac{(7-\nu)}{3(1-\nu)}E_{2D}\frac{h_0^3}{R^4} \tag{A11.31}$$

(V being the volume of the bubble).

A12 Analysis of the dome profiles from previous works in the literature

Contrary to previous analytical models, where the membrane analysis height profile was assumed *a priori*, here we consider a more general formulation, given by Eq. (4.57). In the membrane theory, the constant q is assumed to be equal to 2. Here instead, we determine its value experimentally. As shown in Fig. A12.1, the membrane profile (red line) features deviations from the experimental profile measured by AFM for a 2D-material bubble. On the contrary, by increasing the constant q to 2.2 an almost perfect agreement with the experimental data is achieved.

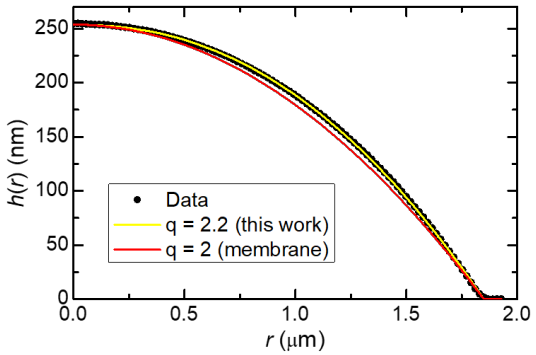

Figure A12.1: Points: AFM data reproducing the height profile of a 2D-material bubble. Red line: Membrane analysis profile ($q = 2.0$). Yellow line: Height profile for $q = 2.2$.

Besides studying the experimental profiles of domes created by us (see Figs. 4.6 and 4.7), to gain a more complete picture of the mechanical properties of the domes, we also studied several AFM profiles extracted from the literature [112, 156, 166, 170, 171, 216, 327] and also included 2D-material blisters realised by Lloyd *et al.* by depositing 2D materials on holey substrates and creating a pressure difference [87]. We also considered the scanning tunnelling microscopy (STM) profiles measured by Larciprete *et al.* [328] (at room temperature), and by Kim *et al.* [329] (at few K) in tiny graphene domes. All the data and fits related to RT profiles are shown in Fig. A12.2 and are ordered for decreasing dome size. Additionally, in Fig. A12.3, we display the data and fit concerning the low temperature STM measurements [329].

In all cases, q values larger than 2.0 are obtained, in agreement with the results obtained for our domes in Figs. 4.6 and 4.7.

Interestingly, values larger than 2.0 are measured also in some very tiny domes, where however our model is expected no to apply anymore for several reasons, including a non-negligible bending stiffness, a non-negligible contribution from the substance inside the dome, and a non-negligible role played by the vdW forces. Indeed, further studies would be needed to confirm this observation and better characterise the nanodomes.

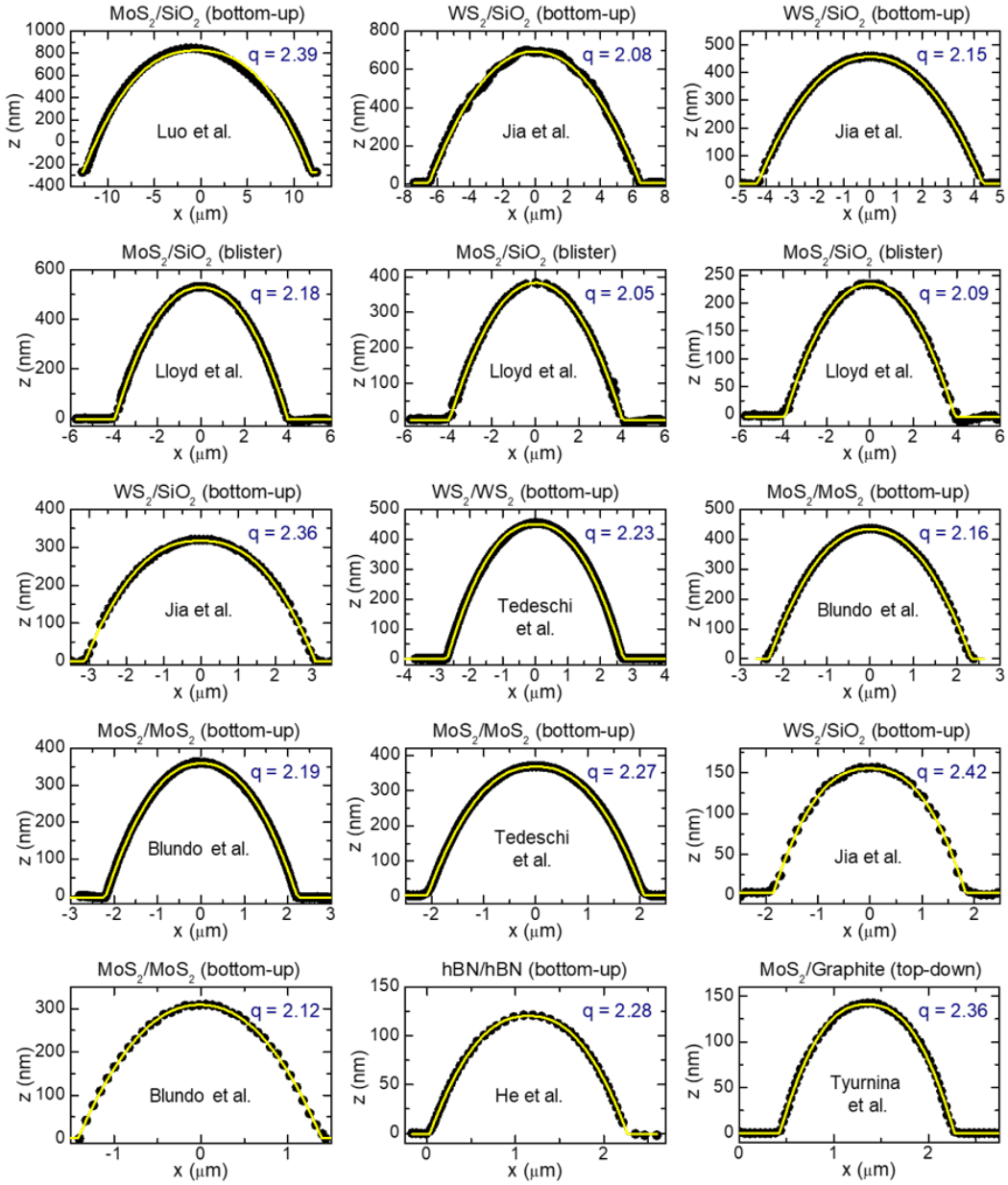
MoS2/SiO2 (bottom-up)
q = 2.39
Luo et al.
WS2/SiO2 (bottom-up)
q = 2.08
Jia et al.
WS2/SiO2 (bottom-up)
q = 2.15
Jia et al.
MoS2/SiO2 (blister)
q = 2.18
Lloyd et al.
MoS2/SiO2 (blister)
q = 2.05
Lloyd et al.
MoS2/SiO2 (blister)
q = 2.09
Lloyd et al.
WS2/SiO2 (bottom-up)
q = 2.36
Jia et al.
WS2/WS2 (bottom-up)
q = 2.23
Tedeschi et al.
MoS2/MoS2 (bottom-up)
q = 2.16
Blundo et al.
MoS2/MoS2 (bottom-up)
q = 2.19
Blundo et al.
MoS2/MoS2 (bottom-up)
q = 2.27
Tedeschi et al.
WS2/SiO2 (bottom-up)
q = 2.42
Jia et al.
MoS2/MoS2 (bottom-up)
q = 2.12
Blundo et al.
hBN/hBN (bottom-up)
q = 2.28
He et al.
MoS2/Graphite (top-down)
q = 2.36
Tyurnina et al.
z (nm)
x (μm)

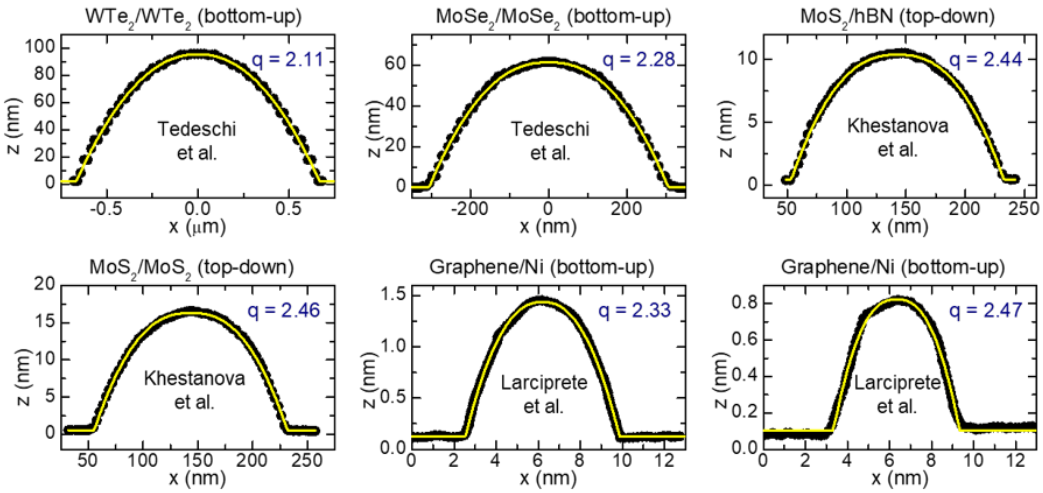

Figure A12.2: Black points: AFM profiles of 2D-material domes measured in previous works by Tedeschi *et al.* [156], Blundo *et al.* [171], Khestanova *et al.* [112], He *et al.* [170], Tyurnina *et al.* [166], Jia *et al.* [216], and Luo *et al.* [327]. The domes were fabricated either by top-down or bottom-up approaches. Also the data concerning 2D-material blisters realised by Lloyd *et al.* [87] were included. The last two panels concern STM profiles measured by Larciprete *et al.* [328]. The profiles are ordered for decreasing dome size. The 2D-material/substrate for each dome is indicated on top of each panel, together with the fabrication approach. Yellow lines: fits to the data using Eq. (4.58). The q value resulting from the fit is given in each panel.

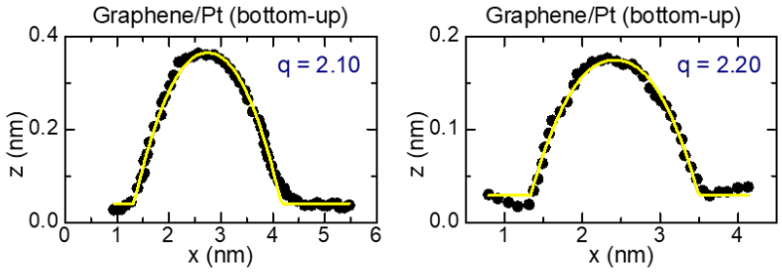

Figure A12.3: Same as in the previous figure. The data shown here concern STM profiles measured by Kim *et al.* [329] at low temperature (2.8 K).

A13 FEM analysis of the dome profile and comparison with the experiments

In order to address thoroughly the issue of the dome profile, we performed studies of the value of q in Eq. (4.57) as a function of the ratio h_0/R, based on numerical simulations. To study the q value in the domes, we considered negligible bending rigidity and calculated the height profile of MoS_2 domes with a fixed R value and by changing h_0. We then fitted the profiles by Eq. (4.57). In such a way, we estimated the values of q for h_0/R varying in the largest possible range explorable via numerical calculations.

In Fig. A13.1, we display the normalised profiles calculated for MoS_2 domes with a given R value and different h_0, in such a way that h_0/R assumes the values 0.001 (black curve), 0.01 (red curve), 0.1 (green curve) and 0.3 (blue curve). While the

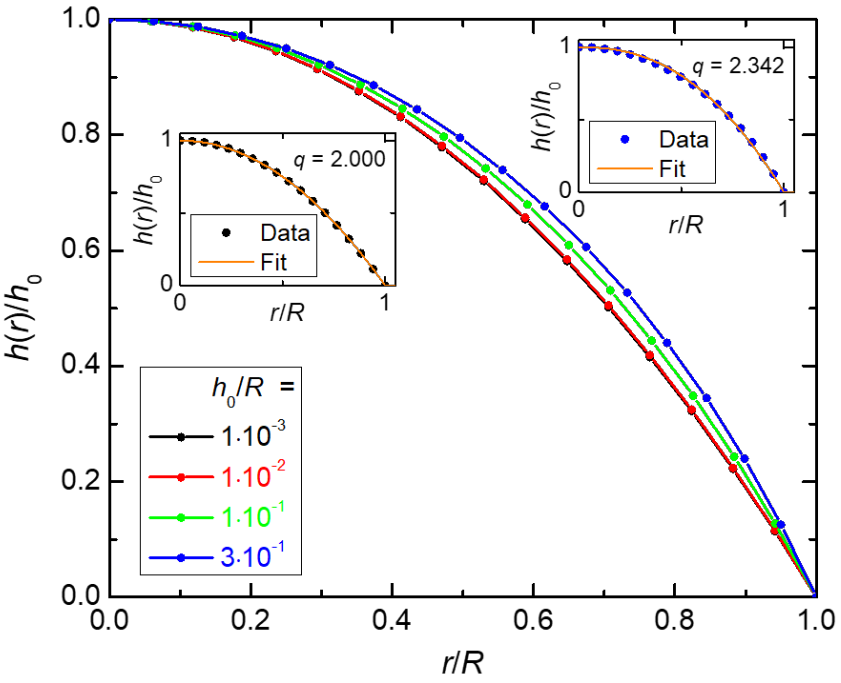

Figure A13.1: Main plot: Normalised height profiles calculated numerically for MoS_2 domes with radius $R = 85$ nm, and variable maximum height h_0, in such a way that $h_0/R = 0.001$ (black curve), 0.01 (red curve), 0.1 (green curve) and 0.3 (blue curve). Insets: fits (in orange) via (4.57) of the numerical data corresponding to $h_0/R = 0.001$ (black data) and $h_0/R = 0.3$ (blue data). The q values given by the fits are displayed.

profiles corresponding to $h_0/R = 0.001$ and 0.01 almost overlap, a clear difference can be observed for $h_0/R = 0.1$ and $h_0/R = 0.3$. In any event, the fits via (4.57) capture well the numerical profiles, as shown as insets for the limiting cases $h_0/R = 0.001$ and $h_0/R = 0.3$. Indeed, the fit gives a q value equal to 2.000 for $h_0/R = 0.001$. However, for $h_0/R = 0.3$, we find an increased q value equal to 2.342.

By performing such an analysis for many other h_0/R in between 0.001 and 0.3, we find the trend displayed in Fig. 4.10. We repeated analogous calculations for the other 2D materials ($MoSe_2$, $MoTe_2$, WS_2, WSe_2, WTe_2, hBN, and graphite), and in Fig. 4.10 we highlighted with a grey shaded area the q-value range embedding all the studied 2D materials. Indeed, q is equal to 2 for very small aspect ratios, say $h_0/R < 0.01$, and then shows an increasing trend. However, it should be noticed that such small aspect ratios $h_0/R < 0.01$ do not correspond to the real physical situation, since the aspect ratios found experimentally are typically > 0.1. As discussed in Chapter 4, the range of h_0/R values measured experimentally corresponds to a range of q values centred around $q = 2.2$, in excellent agreement with our statistical analysis of the experimental profiles. It should be noticed that the same behavior is found independently of R and that the q value shows only a weak dependence on the membrane thickness, as shown in Fig. A13.2.

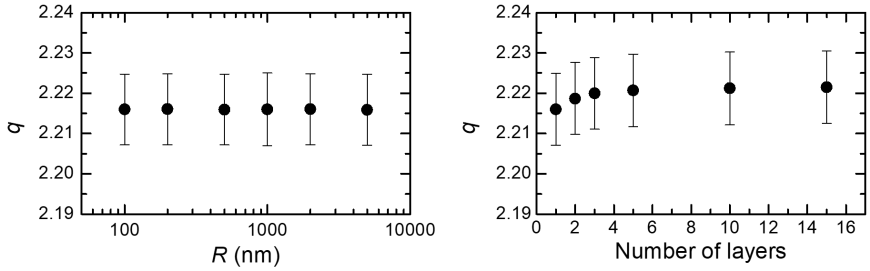

Figure A13.2: Numerical calculations of the constant q in (4.57) for MoS_2 domes with h_0/R=0.164, as a function of the R value (left, for a 1L-thick membrane) and of the thickness of the MoS_2 membrane (right).

To do a more compelling analysis of the experimental *vs* theoretical data for each material, we considered the analysis of the experimental profiles shown in Figs. 4.8 and 4.9. From there, we could determine the experimental average q values. We then performed a statistical analysis of the aspect ratio h_0/R for each combination of 2D materials, see Fig. 4.15. From that analysis, we determined the universal h_0/R values and, in turn, we could estimate the q values numerically. In Fig. A13.3, we plot the experimental values *vs* those obtained numerically. The plot shows how the agreement between the experimental data and numerical ones is generally good, with only some points lying slightly below the expected trend, which might be due to the fact that the real samples show some deviations from ideality (such as the fact the largest domes are sometimes surrounded by small satellite bubbles). Such deviations from ideality are chiefly also at the origin of the spread in the distributions obtained from the experimental data.

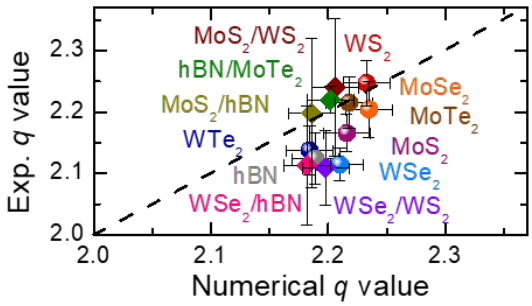

Figure A13.3: q values obtained via the fits of the data in Fig. 4.8 and via the averages of the data in Fig. 4.9, *vs* the theoretical q values. The latter were obtained starting from the universal aspect ratios measured experimentally for each set of data. The black dashed line highlights the ideal trend.

A14 Experimental adhesion energy *vs* DFT calculations

As discussed in the main text, the adhesion energy obtained with the approach proposed in this work shows a clear material-dependent trend. On the contrary, DFT calculations in most of the previous works predicted an almost identical adhesion energy for all the compounds [286, 322]. A comparison between our results and the DFT-predicted values is shown in Fig. A14.1.

The information obtained with our method is particularly relevant, since in the absence of experimental measurements of the adhesion energy, the values calculated by DFT represented the only estimates of such an important parameter.

Our results on the one hand highlight the limits of most DFT schemes used in previous works, due to the difficulty in modeling the vdW interaction; on the other hand, our results provide an unprecedented benchmark for the development and optimisation of new schemes to take into account the vdW forces. It should be noticed, however, that the discrepancies between our experimental result and DFT calculations are possibly also due to several factors playing a role in the real system, such as oxidation, defects, and other factors. In this respect, a direct comparison between the experimental result and the output of DFT calculations may not always be straightforward.

Here, we first discuss our experimental result and then provide a look into DFT calculations for layered materials, which might be useful for readers interested in DFT.

Comparison between the experimental adhesion energy and DFT results

In Fig. A14.1, we show a comparison between the adhesion energy measured via the domes with our method, and the DFT values obtained for single crystals with several methods by Rydberg *et al.* [483], Björkman *et al.* [286], and Mounet *et al.* [322]. Generally, DFT calculations predict an almost identical adhesion energy for all the compounds [286, 322]. On the contrary, our results show a clear-cut dependence on the material, where γ can vary by about one order of magnitude.

The almost constant value found by DFT calculations is chiefly attributable to the difficulty in finding appropriate functionals to describe by DFT systems where one must account for both strong local atom bonds and weak nonlocal vdW forces [483–488]. A good qualitative trend was seemingly found by LDA, which gives lower adhesion energies for graphite and hBN with respect to TMDs. This trend provides much larger estimates of γ with respect to the experimental values for TMD materials such as $MoTe_2$, WSe_2 and WTe_2, which could however be due to the high sensitivity of these materials to oxidation that is not considered in the DFT calculations, as discussed later. Promising results seem to have been achieved also with the nonlocal density functional proposed by Rydberg *et al.* [483] (vdw-DF0, orange pentagons), which predicted adhesion energies in good agreement with our

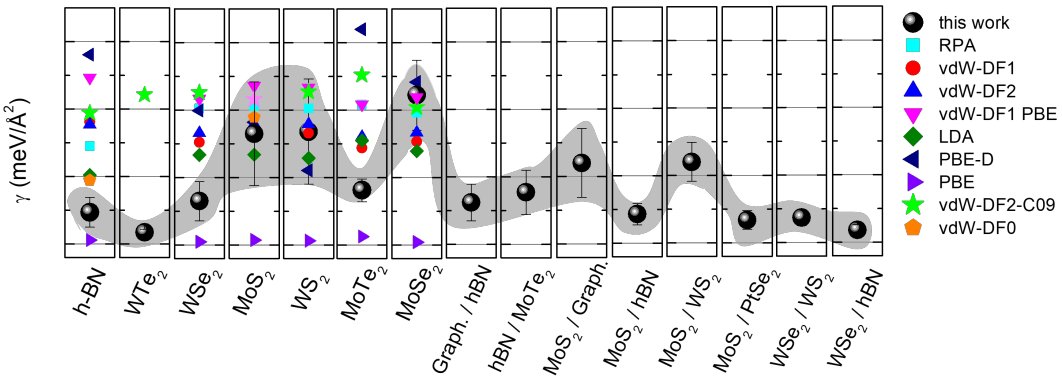

Figure A14.1: Adhesion energies of several vdW homo- and hetero-structures calculated with the approach proposed in this work (black spheres). The grey shaded area is meant to highlight the observed trend. The results obtained via DFT calculations for homostructures in Refs. [483] (vdW-DF0, orange pentagons), [322] (DF2-C09, green stars) and [286] (all the others) are displayed for comparison.

results for MoS_2 and hBN. It is also relevant that successive versions of nonlocal functionals [488] were used in Refs. [286, 322], leading however to different results. This highlights how DFT calculations are highly sensitive to the employed scheme when dealing with vdW interactions.

Besides the intrinsic difficulties of DFT in dealing with vdW forces, the ideal system simulated by DFT might differ from the real crystal, being characterised by the intrinsic presence of defects [489] or oxidation [339]. In fact, as discussed in the main text, the different γ values found experimentally for different crystals can be attributed to the different interplay between covalent and vdW bonds for the different crystal structures, as well as to the different chemical environment for different atomic species, and to other effects. For instance, a slightly ionic bonding character was reported for hBN [338], which might play a role in ruling the interaction of these materials with others; additionally, WTe_2, $MoTe_2$ and WSe_2 are known to quickly oxidise and degrade [339], and oxidation might lead to an adhesion energy decrease [340], as we observed for these materials with respect to the other TMDs (MoS_2, WS_2, and $MoSe_2$).

A look into DFT calculations for vdW materials

Generally, two different approaches have been used to account for the vdW interaction in layered materials: (1) The method of dispersion correction as an add-on to the standard Kohn–Sham density functional theory [484]; (2) The use of nonlocal vdW functionals [485–488]. A historical perspective of the development of these nonlocal functionals can be found in Ref. [488]. For our purposes, it is worth mentioning that Rydberg *et al.* [483, 485] first developed the nonlocal functional

referred to as vdw-df0. Further studies led to the development of later versions. These later versions were then employed in most of the papers dealing with vdW layered materials.

In this note, we focus on graphite, hBN, and MoS_2 and perform DFT calculations by using both the two approaches mentioned above to estimate the binding energy. First, we checked that analogous results (discrepancies within 3 %) are obtained by estimating the binding energy (energy to bring all the layers of a crystal apart) or the adhesion/exfoliation energy (energy to detach a single layer from a bulk), as already discussed in Ref. [286]. The calculations were performed by using the Quantum ESPRESSO distribution [490]. The cutoff energy and k-mesh were optimised by convergence tests. First, we study the effect of using different pseudopotentials. In Ref. [322], the binding energy was estimated by performing the calculations with the fully relativistic optimised norm-conserving Vanderbilt (oncv) pseudopotentials. Here, we test also the use of the projector augmented wave method (paw) and of ultrasoft pseudopotentials (uspp). As shown in Fig. A14.2, different pseudopotentials result in slight variations (discrepancies within 15 %) in the binding energy of a given material. This suggests that the use of different pseudopotentials cannot be the source of major differences between different approaches.

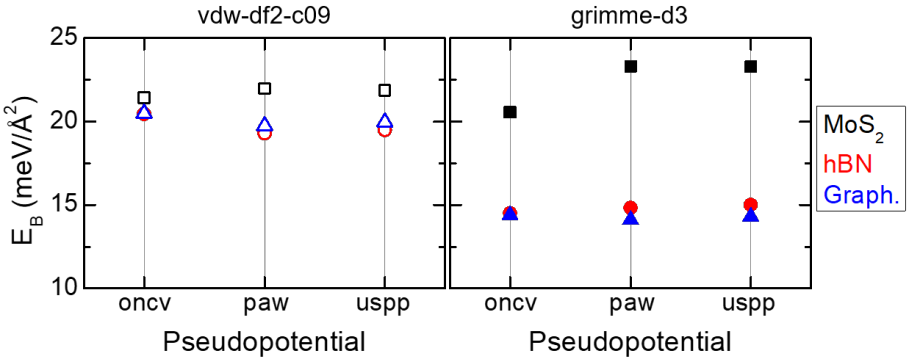

Figure A14.2: DFT-calculated values of the binding energy of MoS_2 (black), hBN (red) and graphite (blue) calculated by using different pseudopotentials. On the left, the calculations were performed by using a nonlocal functional, as in Ref. [322]; on the right, we used the method of dispersion correction by Grimme *et al.* [484].

Interestingly, while the use of a nonlocal functional (vdw-df2-c09, as in Ref. [322]) gives an almost material-independent energy, the use of the method of dispersion correction (grimme-d3) [484] gives lower energies for graphite and hBN with respect to MoS_2, in qualitative agreement with the adhesion energies estimated in this work (see Fig. A14.1). This suggests that the latter approach may capture qualitatively the physics of vdW layered materials, though resulting in quantitative discrepancies. To obtain a better understanding of the use of nonlocal functionals, we performed DFT calculations by using the most updated versions of nonlocal functionals (vdw-df1, -df2, -df-c09, -df2-c09) and compared our results with those obtained with the

method of dispersion correction (grimme-d3) and with the first nonlocal functional (vdw-df0) by Rydberg *et al.* [483]. Indeed, the material-independent trend discussed above is obtained also by using other nonlocal functionals [486, 487], as shown in Fig. A14.3. This flat trend agrees with the results of Ref. [286] and [322], but it is in contrast with the results obtained by Rydberg *et al.* [483] (df0). Indeed, the vdw-df0 functional is the only functional that gives different binding energies for MoS_2 and for hBN. Mostly, the predicted values are in quite good quantitative agreement with the adhesion energies estimated in this work (dashed lines).

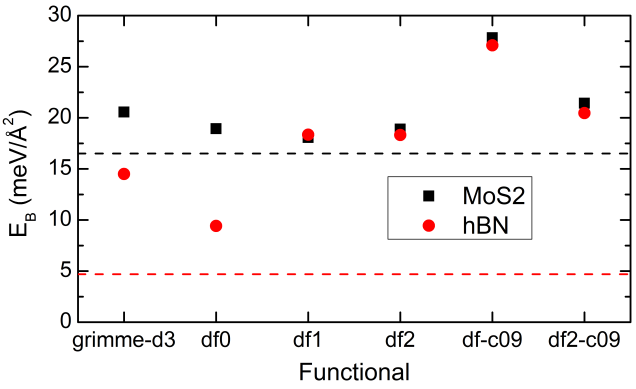

Figure A14.3: DFT-calculated values of the binding energy of MoS_2 (black) and hBN (red) calculated with oncv pseudopotentials, by using different nonlocal functionals. In particular, df0 refers to the values obtained in Ref. [483] with the vdw-df0 nonlocal functional, while the other results were obtained in this work with successive versions of the functional [488]. The dashed lines account for the values determined with the approach proposed in this work and given in Table 4.4.

These results suggest that the vdw-df0 functional could be reconsidered for vdW layered materials and that future studies in this field could lead to even better results.

A15 Identifying the indirect exciton *g*-factor

The valence band at the Γ-point is two-fold degenerate and therefore can host two types of g-factors for the optical transition involving CB_- at the K-point:

$$\begin{aligned} g_I &= 2\left[g_z(\mathrm{CB}_-) - g_z(\mathrm{VB}_{\Gamma,\uparrow})\right] \\ &= 2\left[L_z(\mathrm{CB}_-) + S_z(\mathrm{CB}_-) - L_z(\mathrm{VB}_{\Gamma,\uparrow}) - S_z(\mathrm{VB}_{\Gamma,\uparrow})\right] \\ g'_I &= 2\left[g_z(\mathrm{CB}_-) - g_z(\mathrm{VB}_{\Gamma,\downarrow})\right] \\ &= 2\left[L_z(\mathrm{CB}_-) + S_z(\mathrm{CB}_-) - L_z(\mathrm{VB}_{\Gamma,\downarrow}) - S_z(\mathrm{VB}_{\Gamma,\downarrow})\right] \end{aligned} \tag{A15.1}$$

in which the two valence bands at Γ are distinguished by their spin. Our calculations reveal that the angular momentum of VB_Γ is negligible (on the order of 10^{-2}) for the strain values analysed. This is consistent with similar calculations of unstrained $MoSe_2$[400] and WSe_2[401] at zero strain. Furthermore, the spin expectation value is nicely polarised along the out-of-plane direction, allowing us to write $S_z(\mathrm{CB}_-) = -1$ and $S_z(\mathrm{VB}_{\Gamma,\uparrow(\downarrow)}) = 1(-1)$. Therefore, the two possible g-factors for the I excitons are

$$\begin{aligned} g_I &= 2\left[L_z(\mathrm{CB}_-) - 2\right] \\ g'_I &= 2L_z(\mathrm{CB}_-) \end{aligned} \tag{A15.2}$$

and are clearly dominated by the angular momentum of CB_-.

In Fig. A15.1(a) we show the calculated values of the orbital angular momenta, L_z, as a function of the strain for the relevant bands (VB_+ and $\mathrm{CB}_\pm$ for the K valley and VB_Γ at the Γ-point). In Fig. A15.1(b) we present the absolute value of the possible g-factors of the I exciton. We found $|g_I| < |g'_I|$. We have also explored the possibility of indirect excitons coming from CB_+ and found that the absolute values of the g-factors greater than g'_I, which is an unlike candidate since the experimentally obtained g-factors are $\sim$ -2.

In order to unambiguously identify which of these two g-factors are being probed experimentally, we investigate the symmetry of the optical selection rules assisted by phonons. Let us first look at the symmetry of the energy bands involved. At the Γ-point —with D_{3h} (or $\overline{6}$m2) point group— the valence band belongs to the irreducible representation (irrep) Γ_7 (in the double group notation). Mapping this Γ_7 irrep to the K-point —with C_{3h} (or $\overline{6}$) point group— via the compatiblity relations we obtain $K_7 \oplus K_8$. From these irreps we can easily associate K_7 to spin up and K_8 to spin down. In fact, the conduction bands at the K-point CB_+ and CB_- also belong to K_7 and K_8 irreps, respectively. The valence band at the K-point, VB_+, belongs to the K_{10} irrep. The character tables, compatibility relations and direct product tables are given in Ref. [491]. To clarify, we denote the irreps at Γ-point by Γ_i and at the K-point by K_i. In summary, we have the following irreps for the relevant

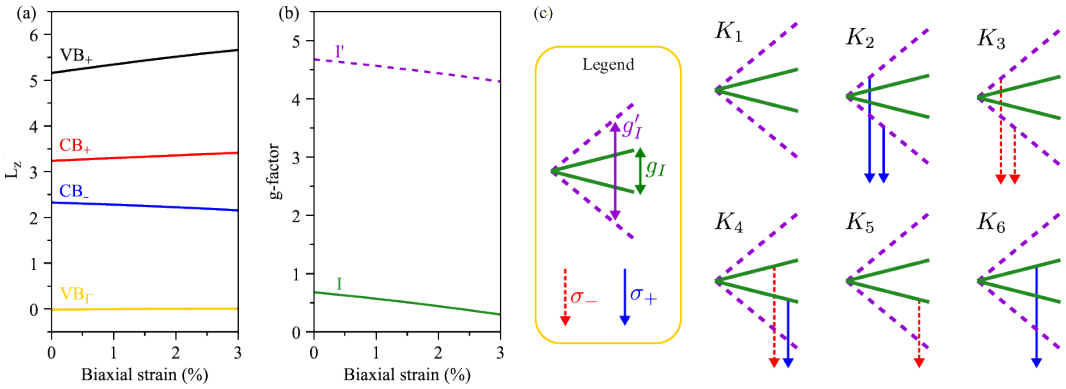

Figure A15.1: (a) Orbital angular momentum, L_z, for the relevant energy bands as a function of the strain. (b) Indirect exciton g-factors (absolute value) as function of strain. (c) Selection rules with phonons.

energy bands

$$\begin{aligned} \mathrm{CB}_{+,\mathrm{K}} &\sim K_7 \\ \mathrm{CB}_{-,\mathrm{K}} &\sim K_8 \\ \mathrm{VB}_{+,\mathrm{K}} &\sim K_{10} \\ \mathrm{VB}_{\Gamma,\uparrow} &\sim K_7(\text{from } \Gamma_7) \\ \mathrm{VB}_{\Gamma,\downarrow} &\sim K_8(\text{from } \Gamma_7)\,, \end{aligned} \tag{A15.3}$$

and the irreps at -K are the complex conjugate of the irreps at K, i.e., $K_7^* = K_8$, $K_8^* = K_7$, $K_{10}^* = K_9$.

To set up the stage for the phonon-assisted optical transitions, let us first look at the direct transitions from VB_+, given by the dipole matrix element [492]

$$\langle i\,|H_\mathrm{d}|\,f\rangle \sim \Gamma_i^* \otimes \Gamma_\mathrm{d} \otimes \Gamma_f\,, \tag{A15.4}$$

with $\Gamma_{i(f)}$ representing the irrep of the initial (final) state and Γ_d the irrep of the dipole transitions transforming as vector operators: K_2 for σ_-, K_3 for σ_+ and K_4 for z polarisations. If the direct product $\Gamma_i^* \otimes \Gamma_\mathrm{d} \otimes \Gamma_f$ returns the value of K_1, the identity irrep, then the transition is allowed.

Particularly, at the K-point

$$\begin{aligned} &\mathrm{VB}_{+,\mathrm{K}} \to \mathrm{CB}_{-,\mathrm{K}} \sim K_{10}^* \otimes K_8 = K_9 \otimes K_8 = K_4 \Rightarrow K_4 \otimes (\Gamma_d = K_4) = K_1 \to z \\ &\mathrm{VB}_{+,\mathrm{K}} \to \mathrm{CB}_{+,\mathrm{K}} \sim K_{10}^* \otimes K_7 = K_9 \otimes K_7 = K_2 \Rightarrow K_2 \otimes (\Gamma_d = K_3) = K_1 \to \sigma_+\,, \end{aligned} \tag{A15.5}$$

and at the -K point

$$\begin{aligned} &\mathrm{VB}_{+,\text{-K}} \to \mathrm{CB}_{-,\text{-K}} \sim K_9^* \otimes K_7 = K_{10} \otimes K_7 = K_4 \otimes (\Gamma_d = K_4) = K_1 \to z \\ &\mathrm{VB}_{+,\text{-K}} \to \mathrm{CB}_{+,\text{-K}} \sim K_9^* \otimes K_8 = K_{10} \otimes K_8 = K_3 \otimes (\Gamma_d = K_2) = K_1 \to \sigma_-\,, \end{aligned} \tag{A15.6}$$

The transitions with in-plane circular polarisation ($\mathrm{VB}_{+,\pm\mathrm{K}} \rightarrow \mathrm{CB}_{+,\pm\mathrm{K}}$) give rise to the A exciton with valley-dependent selection rules [24, 403], whereas transitions with out-of-plane dipole matrix element ($\mathrm{VB}_{+,\pm\mathrm{K}} \rightarrow \mathrm{CB}_{-,\pm\mathrm{K}}$) give rise to the so called dark excitons [404, 405].

Let us now look at the indirect optical transitions mediated by phonons involving the valence band at Γ point. The matrix elements in this case are given by [406]:

$$\sum_{l} \langle i\,|H_{\text{e-ph}}|\,l\rangle\,(E_f - E_l)^{-1}\,\langle l\,|H_{\mathrm{d}}|\,f\rangle \rightarrow \Gamma_i^* \otimes \Gamma_{\text{ph}} \otimes \Gamma_{\mathrm{d}} \otimes \Gamma_f\,, \tag{A15.7}$$

in which $H_{\text{e-ph}}$ takes into account the electron-phonon coupling and transforms as the irrep Γ_{ph}. We investigate all the allowed phonons with momentum K in monolayer TMDs, which span all the irreps of the single group [493, 494]. We show the step-by-step calculation of the direct products $[(\Gamma_i^* \otimes \Gamma_f) \otimes \Gamma_{\text{ph}}] \otimes \Gamma_{\mathrm{d}}$ in the Tables A15.2, A15.3 and A15.4.

To summarize our findings, we depict in Fig. A15.1(c) the selection rules for the indirect excitons involving phonons given in Table A15.4. Our symmetry analysis reveal that, for the transitions that give rise to the largest g-factor, g_I', both branches contribute with the same polarisation and thus no net Zeeman splitting would be observed. Only the transitions that give rise to the smallest g-factor, g_I, would provide a Zeeman splitting signature. This transition can be triggered by a phonon with symmetry K_4 or a pair of phonons with symmetries K_5 and K_6. Although the sign of g_I depends on the particular symmetry of the phonon mediating the optical transition, our symmetry analysis firmly indicates that the indirect exciton g-factor is ruled by g_I and not g_I'. Furthermore, this symmetry analysis remains valid for the biaxial strain case since the structural symmetry of the TMD remains unchanged.

Table A15.2: Direct product of irreps for $\Gamma_i^* \otimes \Gamma_f$.

	$\mathrm{CB}_{-,\mathrm{K}} \sim K_8$	$\mathrm{CB}_{-,\text{-K}} \sim K_7$
$\mathrm{VB}_{\Gamma,\uparrow} \sim K_7$	$K_7^* \otimes K_8 = K_6$	$K_7^* \otimes K_7 = K_1$
$\mathrm{VB}_{\Gamma,\downarrow} \sim K_8$	$K_8^* \otimes K_8 = K_1$	$K_8^* \otimes K_7 = K_5$

Table A15.3: Direct product of irreps for $(\Gamma_i^* \otimes \Gamma_f) \otimes \Gamma_{\text{ph}}$.

	K_1	K_2	K_3	K_4	K_5	K_6
$\mathrm{VB}_{\Gamma,\uparrow} \leftrightarrow \mathrm{CB}_{-,\mathrm{K}}$	K_6	K_4	K_5	K_3	K_1	K_2
$\mathrm{VB}_{\Gamma,\downarrow} \leftrightarrow \mathrm{CB}_{-,\text{-K}}$	K_5	K_6	K_4	K_2	K_3	K_1
$\mathrm{VB}_{\Gamma,\downarrow} \leftrightarrow \mathrm{CB}_{-,\mathrm{K}}$	K_1	K_2	K_3	K_4	K_5	K_6
$\mathrm{VB}_{\Gamma,\uparrow} \leftrightarrow \mathrm{CB}_{-,\text{-K}}$	K_1	K_2	K_3	K_4	K_5	K_6

Table A15.4: Direct product of irreps $[(\Gamma_i^* \otimes \Gamma_f) \otimes \Gamma_{\mathrm{ph}}] \otimes \Gamma_{\mathrm{d}}$ highlighting the nonzero contributions with their respective dipole polarisation.

	K_1	K_2	K_3	K_4	K_5	K_6
$\mathrm{VB}_{\Gamma,\uparrow} \leftrightarrow \mathrm{CB}_{-,\mathrm{K}}$		z		σ_-		σ_+
$\mathrm{VB}_{\Gamma,\downarrow} \leftrightarrow \mathrm{CB}_{-,\text{-K}}$			z	σ_+	σ_-	
$\mathrm{VB}_{\Gamma,\downarrow} \leftrightarrow \mathrm{CB}_{-,\mathrm{K}}$		σ_+	σ_-	z		
$\mathrm{VB}_{\Gamma,\uparrow} \leftrightarrow \mathrm{CB}_{-,\text{-K}}$		σ_+	σ_-	z		

A16 magneto-PL experiments

Magneto-micro-PL (magneto-μ-PL) measurements were performed either in a Bitter magnet [414] reaching up to 28.5 T or in a superconducting magnet reaching up to 12 T. The experiments with the bitter magnet were performed at the High Field Magnet Laboratory (HFML), in Nijmegen, The Netherlands, under projects approved and funded by the European Magnetic Field Laboratory (EMFL). The experiments with the superconducting magnet were performed at the Faculty of Physics of the University of Warsaw, under ISABEL projects approved by the EMFL and funded within the Horizon2020 Research and Innovation Programme.

In the Bitter magnet, the μ-PL was excited by a linearly polarised laser with $\lambda = 532$ nm or 633 nm focused by an aspheric lens with NA = 0.68, resulting in a spot size on the sample of about 1 μm. In the superconducting magnet, a 515-nm-laser and a 100$\times$ microscope objective with NA = 0.82 were used. The same lens/objective was used to collect the luminescence. Light with left or right circular polarisation was analysed using a rotating quarter-wave plate and a linear polariser, or a fixed quarter-wave plate and a Wollaston prism. x-y-z piezoelectric stages were used to collect the signal from the desired point of the domes. A monochromator with 0.3 m focal length and a 300 grooves/mm grating (Bitter magnet) or with a 0.75 m focal length and a 600 grooves/mm grating (superconducting magnet) was used to disperse the PL signal. A liquid-nitrogen-cooled Si-CCD was employed to collect the signal.

The field was directed perpendicular to the sample surface (*i.e.*, parallel to the emitted photon wavevector, Faraday configuration).

A17 g-factors of direct and indirect excitons in strained WS_2 monolayers

To derive the g-factors of WS_2 under high strain, we measured 11 different domes by magneto-μ-PL. As shown in the top-left panel of Fig. A17.1, we chose domes whose emission was varying over a range of about 100 meV (from 1.74 to 1.84 eV). Given the high strains hosted by these domes, they were all measured in the Bitter magnet up to 28.5 T, apart from dome #1. The latter was measured in the superconducting magnet up to 12 T, in order to verify that we were getting consistent results with the two different setups. In Fig. A17.1, for each of the considered domes we show some selected spectra for increasing magnetic field, stacked by y-offset. A more quantitative analysis of the Zeeman splitting (ZS) is provided in Fig. A17.2. The ZS splitting values were mostly obtained by fitting the data with peak functions. In a couple of cases (domes #6 and #9), where the fits were subject to a large uncertainty, we derived the ZS from the spectral centroids. From a linear fit to the ZS data, we obtained the g-factors displayed in each plot. The same values can be found in Fig. 6.6, along with a few other points at lower strains, as discussed in the following.

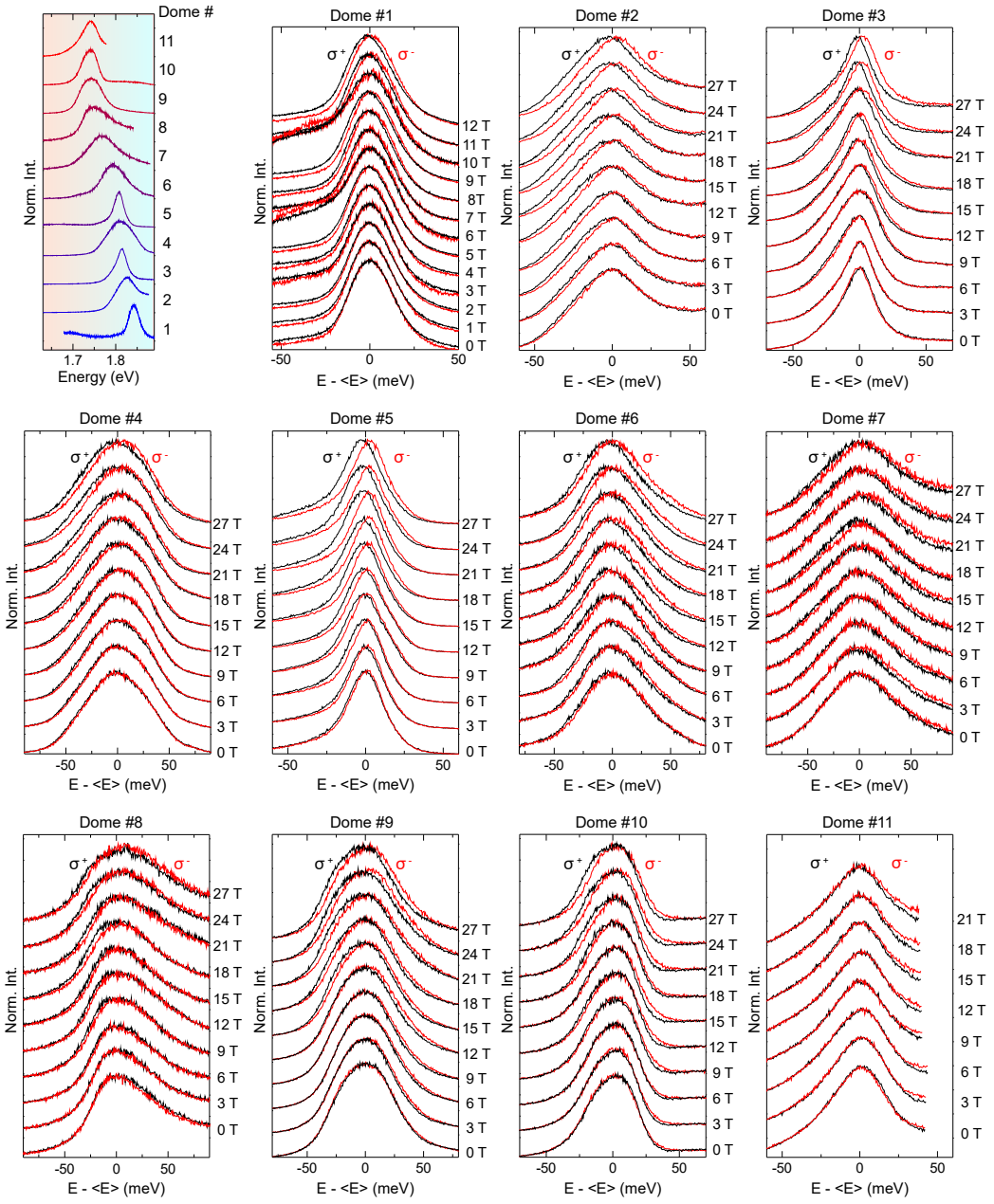

Figure A17.1: PL spectra of the 11 WS_2 domes studied by magneto-μ-PL. For each dome, some selected spectra for increasing magnetic field, stacked by y-offset, are displayed. At each field, the average energy was subtracted from the absolute energy scale for ease of comparison. Dome #1 was measured in the superconducting magnet up to 12 T in steps of 0.5 T; the other domes were measured in the Bitter magnet up to 28.5 T in steps of 1.5 T. For dome #11, the data above 24 T showed a shift in position and were not considered, and the displayed spectra were cut due to the queue of a signal from a small nearby dome.

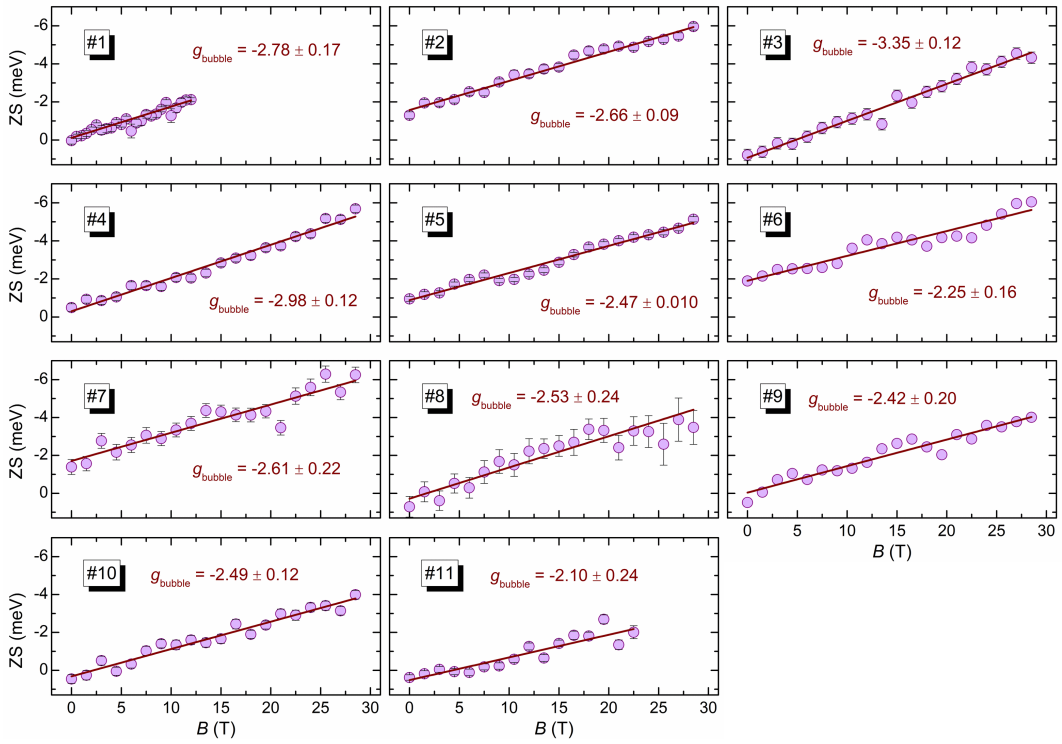

Figure A17.2: ZS of the measured WS_2 domes *vs* magnetic field. The corresponding g-factors were derived by a linear fit. Domes #5 and #10 are the same shown in Fig. 6.3.

A18 WSe_2 ML analysis of the g-factor at low and null strain

To study the effect of small strains on the g-factor of WSe_2 MLs, we prepared a sample similar to that prepared for WS_2. In particular, we obtained a WSe_2 ML by mechanical exfoliation and deposited atop a hBN bulk flake with few-layer-thick hBN. bubbles[169] The WSe_2 flake was deposited in such a way to cover a micron-size hBN dome, as shown in Fig. A18.1(a). The surrounding part of the ML is instead deposited on flat hBN. In such a manner, the ML portion on the flat area is not subject to strain, while some strain is transferred to the ML portion deposited on the bubble. This is evident from the PL spectra shown in panel (b), acquired in the flat region (grey) and dome region (orange) and showing how a strain-induced redshift of ∼10 meV is observable in the dome region. Based on the shift rates measured in previous works[41], the biaxial strain acting on the ML is ∼0.07-0.10 % (*i.e.*, total strain ∼0.15-0.20 %). This value is close to that reported in Ref. [393], where a decrease of the g-factor in the strained sample was reported. To estimate the

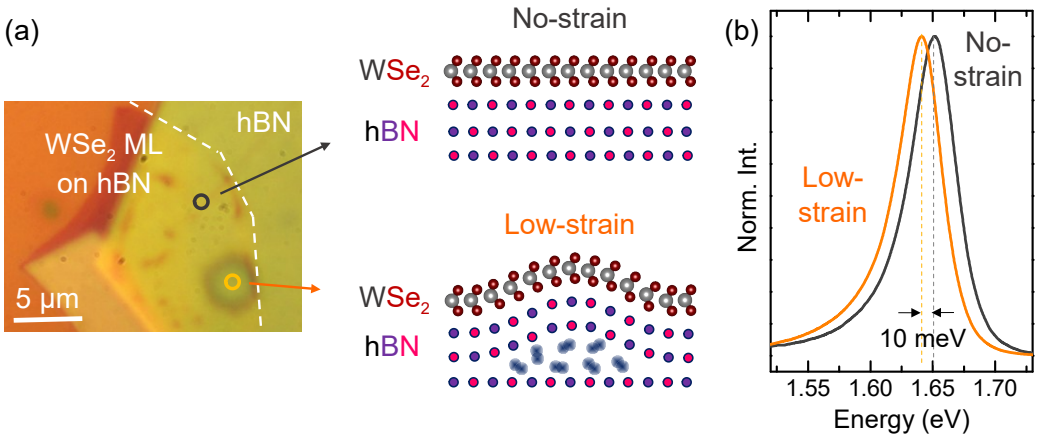

Figure A18.1: (a) Left: Optical image of the sample: An hBN sample was hydrogen-irradiated, resulting in the formation of H_2-filled hBN bubbles. A WSe_2 ML was deposited atop of the hBN flake, covering an hBN dome and the surrounding flat area. Right: Sketch of the flat area, where no strain is present, and of the WSe_2-covered hBN dome, where a low-strain is transferred to the WSe_2 ML. (b) Normalised PL spectra acquired on the dome and on a flat area outside (see orange and grey dots superimposed to the optical image). A red-shift of 10 meV induced by strain is clearly observable on the bubble.

g-factor in the unstrained ML and in the ML subject to small strain, we performed μ-PL measurements in the superconducting magnet, while increasing the field from 0 T to 12 T, in steps of 0.5 T. In Fig. A18.2(a), we show some spectra (in steps of 1 T), for both the σ^+ and σ^- polarisation states. At each field, the average energy was subtracted from the absolute energy scale for ease of comparison. Indeed, while the field B increases, the two polarisation states Zeeman-split, and the extent of such splitting looks very similar for the unstrained and low-strain sample. From a

fitting analysis of the spectra, we derived the ZS and DCP shown in panel (b). The two sets of data almost overlap, showing how no difference is observed in our case in the presence of small strains, in contrast with Ref. [393]. To conclude, it should

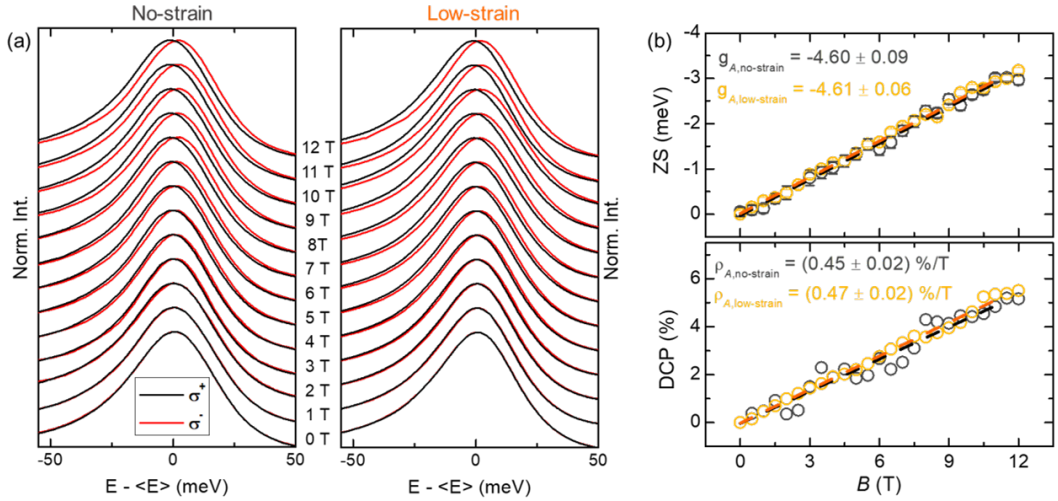

Figure A18.2: (a) Some selected spectra (in steps of 1 T, stacked by y-offset) of the unstrained ML and of the ML subject to a small strain as a function of the magnetic field, for both the σ^+ and σ^- polarisation states. At each field, the average energy was subtracted from the absolute energy scale for ease of comparison. The spectra were taken at RT and are dominated by the A exciton. (b) Top: Zeeman splitting (ZS) *vs* B. The data were fitted via Eq. (6.1) and the obtained g-factor is displayed. Bottom: Degree of circular dichroism (DCP) *vs* B. The DCP increases linearly with B [see Eq. (6.3)], with the rate ρ displayed.

be noticed that similarly to the case of WS_2, our estimate of the g-factor agrees well with those previously reported in the literature, as shown in Table A18.5, even though in all previous works the measurements were performed at low temperatures $\sim$4 K.

Table A18.5: Summary of the measured g-factors, diamagnetic shift coefficients (Σ, see Eq. (6.2)), and DCP rate (ρ, see Eq. (6.3)) measured in unstrained WSe_2 MLs in the literature. PL = photoluminescence, Refl. = reflectance, Tran. = transmittance, exfo. = exfoliated, CVD = chemical vapor deposition, encap. = encapsulated. The DCP refers to the PL emission, and it is thus not defined for reflectance or transmittance measurements.

g-factor	Σ (μeV/T^2)	ρ (%/T)	T (K)	Technique	Sample	Ref.
-4.0 ± 0.5	/	/	4.2	PL	exfo.	Mitioglu *et al.* [391]
-3.7 ± 0.2	/	$\sim$0	4	PL	exfo., on SiO_2	Wang *et al.* [392]
-4.52 ± 0.37	/	$\times$	4.2	Refl.	exfo., on SiO_2	Srivastava *et al.* [51]
-4.37 ± 0.15	/	/	4.2	PL	exfo., on SiO_2	
-4.05 ± 0.10	0.32 ± 0.02	$\times$	4	Tran.	exfo., hBN-capped	Stier *et al.* [48]
-4.2	0.31 ± 0.02	$\times$	4	Tran.	exfo., hBN-encap.	Stier *et al.* [47]
-4.02 ± 0.5	/	/	4.2	PL	exfo., on SiO_2	Mitioglu *et al.* [393]
-4.60 ± 0.05	/	/	4.2	PL	exfo., on SiO_2	
-4.30 ± 0.02	0.5	/	2	PL/refl.	exfo., hBN-encap.	Chen *et al.* [52]
-3.8 ± 0.2	/	$\times$	4.2	Refl.	exfo., on SiO_2	Koperski *et al.* [43]
-4.3 ± 0.2	/	/	4.3	PL	exfo., on SiO_2	
-4.60 ± 0.09	/	0.45 ± 0.02	$\sim$300	PL	exfo., on hBN	This work

A19 Hybridisation mechanism

Our results are summarised in Fig. A19.1. Since the gauge factors are quite similar with and without excitonic effects, the crossing point is ruled by the energy difference of A and I excitons at zero strain. However, regardless of the position of the crossing point, the g-factor physics is the same in all cases. Around the crossing region, the g-factors are a mixture of the isolated A and I exciton g-factors. The coupling Δ_1 essentially controls the extent of mixing of the g-factors and how fast the mixing is, around the crossing point. This implies that the larger (smaller) the value of Δ_1, the smoother (steeper) the mixing slope. Furthermore, the same qualitative trends are observed independently of the sign of g_I.

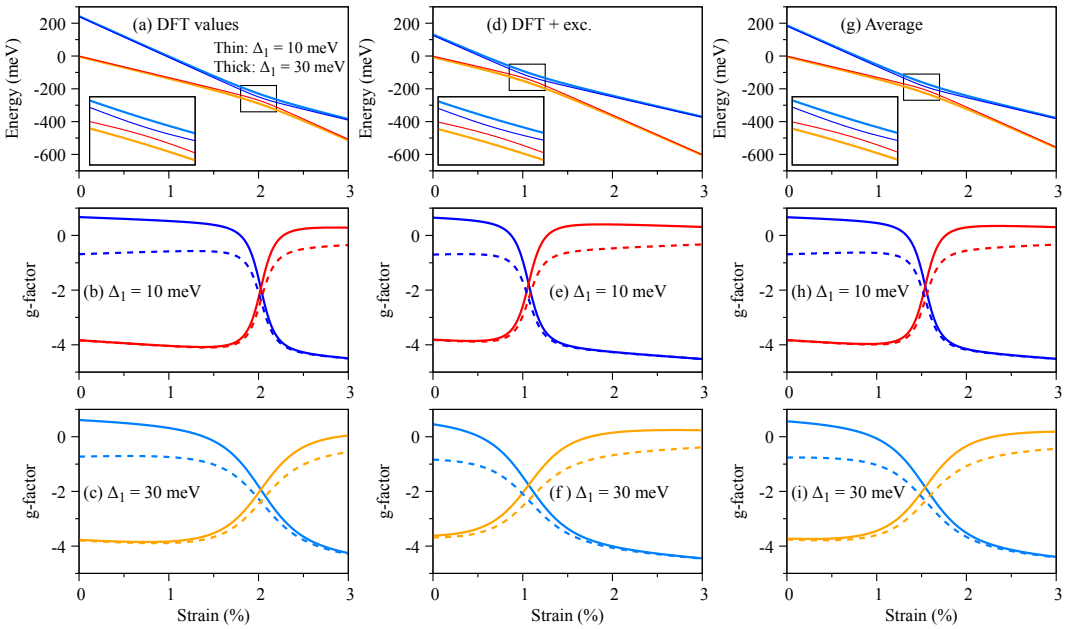

Figure A19.1: Energies, at $B = 0$ T from Eq. (6.8) and the calculated g-factors from Eq. (6.11) for (a-c) DFT, (d-f) DFT+exciton and (g-i) average parameters (given in Table (5.2)) for two coupling strengths of $\Delta_1 = 10$ meV and $\Delta_1 = 30$ meV. The A exciton energy is set at zero for the zero strain case.

A20 Comparison between our model and the experimental data

When comparing the theoretical results with the experimental data, one should consider that DFT calculations are subject to a relatively high variability when determining the values of the shift rates and of $E_I(0) - E_A(0)$. However, several theoretical studies discussed how the shift rate of the I exciton is about two times that of the A exciton: $\Delta E_I/\Delta E_A \approx 2$. This information is thus quite robust and holds independently on the estimated values of ΔE_A and ΔE_I. Since the crossing point between direct and indirect excitons is determined mainly by $\Delta E_I/\Delta E_A$ and by the energy separation at zero strain $E_I(0) - E_A(0)$, the only critical parameter is the latter, as shown in Fig. A19.1. Given the uncertainty in this parameter, we varied it in between 200 meV and 250 meV and compared the so-obtained results with the experimental data. The comparison is shown in Fig. A20.2. The coupling strength Δ_1 was also optimised by a comparison with the data, and we found that Δ_1 between 30 and 40 meV was providing the best agreement with our experiments. We thus set $\Delta_1 = 35$ meV in Fig. A20.2. As highlighted in the figure by black dashed lines, the crossing strain ε_c varies between 1.61 % and 2.03 % depending on the value of $E_I(0) - E_A(0)$. To compare the experimental data with the theoretical trends we employed the same procedure we used for Fig. 6.6. In particular: i) For each experimental datum, we estimated the quantity $E_X - E_A(0)$ where E_X is the peak position at 0 magnetic field of the PL band; (ii) We compared this quantity with the lowest energy curve (E_L) estimated theoretically, and from this comparison we derived the corresponding strain; (iii) We used the derived strain value for the comparison between the experimental g-factors and the theoretical ones. We employed the above procedure instead of deriving the strain from mechanical models[116] since in our magneto-optical experiments it was not possible to check the precise shape and dimensions of the investigated domes and to know the exact position where the measurements were taken. The knowledge of the dome shape, dimension, and exact position are indeed essential requirements to estimate the strain via numerical or analytical models[116], while they are not needed for the approach used in this work, where strain is deduced solely by the shift observed in the exciton peak by PL measurements and related to strain through theoretical calculations. This approach also permits us to overcome another problem which is common to strained 2D materials: exciton funnelling. Whenever a 2D material is subjected to a strain gradient on the nano/micro scale, excitons preferentially drift toward regions with minimum energy.[41, 88, 89] Such drift can be even equal to hundreds of nm [89]. Therefore, the PL signal often comes from areas which do not exactly coincide with the areas excited by the laser spot. Therefore, funnelling phenomena often make it difficult to establish the strain value corresponding to the region where the carrier recombination occurs. Funnelling does not instead affect our estimates, since we estimate the strain just from the recombination energy, and thus "after funnelling has occurred". It should also be noticed that the width of the PL peak is related to the strain distribution within the recombination region. Therefore, the width of the PL band was used to estimate the error on the associated

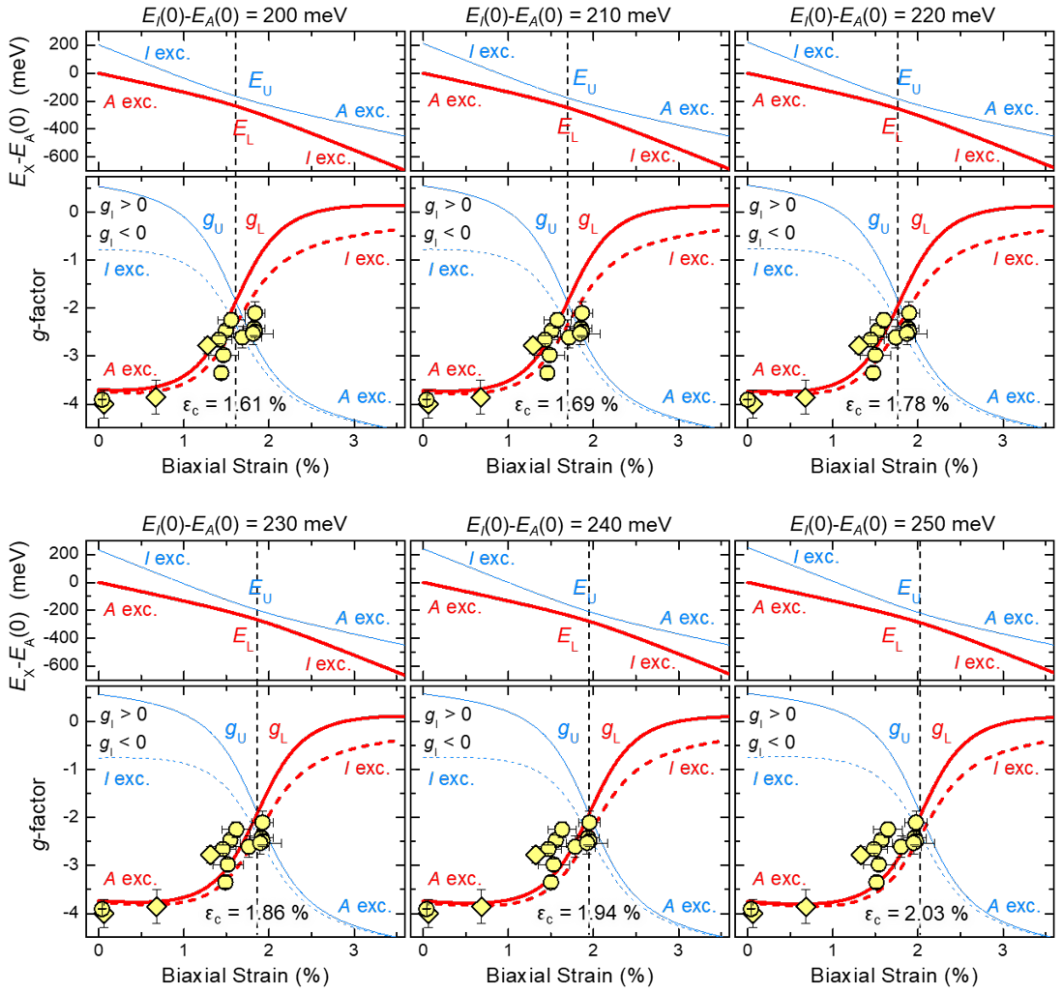

Figure A20.2: Top panels: Energy behavior *vs* biaxial strain, (at $B = 0$ T) calculated via Eq. (6.8) in the DFT+exciton picture (where the shift rates are $\Delta E_A = -128$ meV/%, $\Delta E_I = -246$ meV/%). Bottom panels: corresponding g-factors calculated via Eq. (6.11) for (a-c) DFT. A coupling strength $\Delta_1 = 35$ meV was assumed. In the different plots, we varied the difference between the direct and indirect exciton at zero strain $E_I(0) - E_A(0)$ between 200 and 250 meV. As a consequence, the strain at which the excitons cross (ε_c) varies between 1.61 % and 2.03 %, as highlighted in the plots by the black dashed line. The theoretical g-factors are compared with the experimental data.

strain value.

The best agreement between experimental data and theory is obtained for $E_I(0) - E_A(0)$ between 210 and 230 meV, depending on the sign of g_I. For $g_I > 0$ ($g_I < 0$), the data are best reproduced for $E_I(0) - E_A(0) = 230$ meV ($E_I(0) - E_A(0) = 210$ meV). Since the sign of g_I is unknown, in Fig. 6.6 we displayed the result obtained

for $E_I(0) - E_A(0) = 220$ meV, as the best compromise.

A21 μ-Raman studies of hBN-capped MoS_2 domes

Fig. A21.1 shows the temperature-dependent μ-Raman studies of a MoS_2 dome before and after capping with few-layer hBN. The Raman spectra in panels (c-d) were fitted with Lorentzian functions to derive the frequency behaviour (displayed in panels (e-f)) of the dome and bulk peaks in the phonon regions of the in-plane E_{2g} and out-of-plane A_{1g} modes. Indeed, the almost parallel trends of the peaks associated to the bulk crystal and the capped dome of panel (f) contrasts with the erratic behaviour of the bare dome peak of panel (e), proving the effect of hBN even for temperatures below the gas-to-liquid transition of H_2 at $\sim$ 32 K (grey shaded area).

Analogous studies were performed for several other hBN-capped MoS_2 domes. From the Raman shifts of the E_{2g} peak, we estimated the corresponding strain. In particular, the biaxial strain of the dome is estimated via Eq. (7.2). The results of our analysis are displayed in Fig. A21.2.

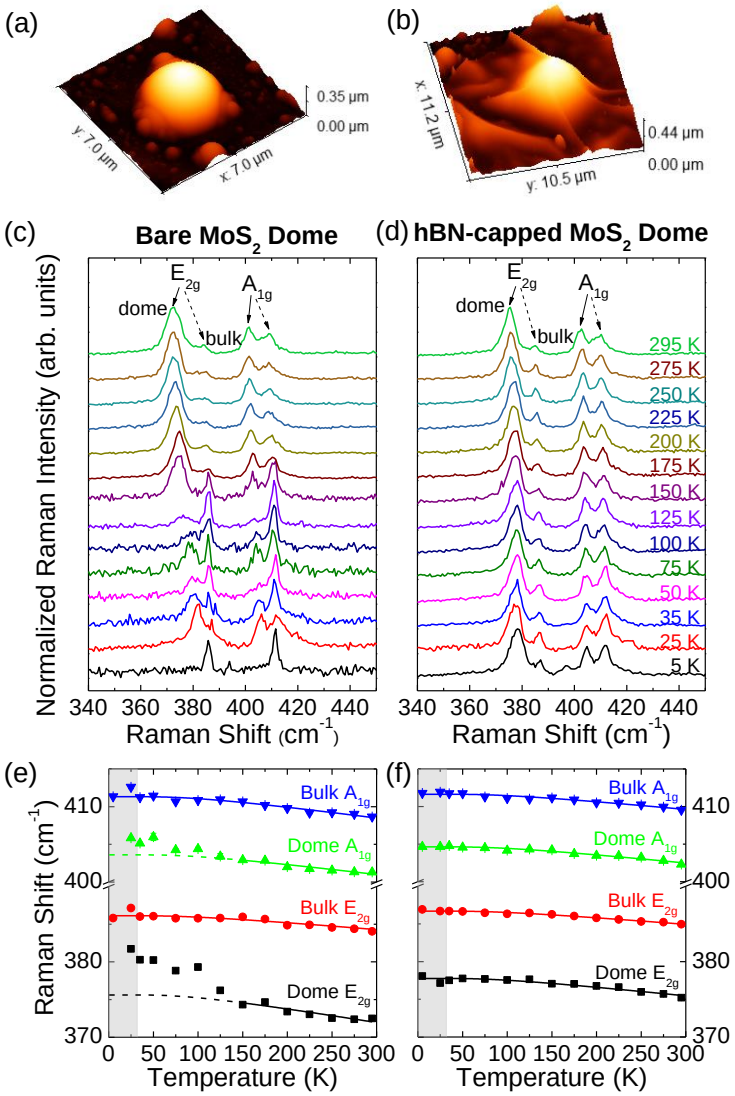

Figure A21.1: Temperature-dependent μ-Raman studies of a MoS_2 dome before and after capping with few-layer hBN. (a-b) AFM 3D maps of the dome before (a) and after (b) the capping procedure. (c-d) Stacked μ-Raman spectra, for all the temperatures considered, of the MoS_2 dome before and after hBN capping (laser excitation wavelength equal to 532 nm and laser power equal to 30 μW). The peaks refer to the E_{2g} (in-plane) and A_{1g} (out-of-plane) modes of oscillation associated to the bulk crystal (dashed arrow) and to the dome membrane (full arrow). (e-f) Evolution with temperature of the peaks of panels (c-d) extracted by performing Lorentzian fits of the μ-Raman spectra. The trends are fitted with Eq. 7.1. The grey shaded area highlights the temperature range in which hydrogen is in its liquid form (below $\sim$ 32 K).

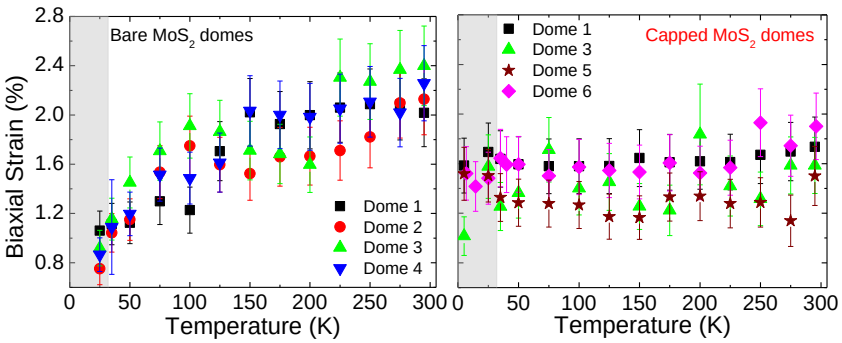

Figure A21.2: Biaxial strain *vs* temperature calculated from the Raman shifts of the E_{2g} peak for several MoS_2 domes. The biaxial strain values are calculated using Eq. (7.2). The left panel shows the evolution in temperature of the strain of the bare domes, while the right panel that of the strain after the capping with few-layer hBN. At RT the capping procedure leads to a reduction in strain, which is then kept constant at all temperatures. The range of temperatures below the gas-to-liquid transition of H_2 is indicated by the grey shaded area.

A22 μ-PL studies of hBN-capped WS_2 domes

Fig. A22.1 shows the full *vs* T μ-PL study of the same hBN-capped WS_2 dome of Fig. 7.3. The neutral A exciton and the negative trion (A^-) are highlighted.

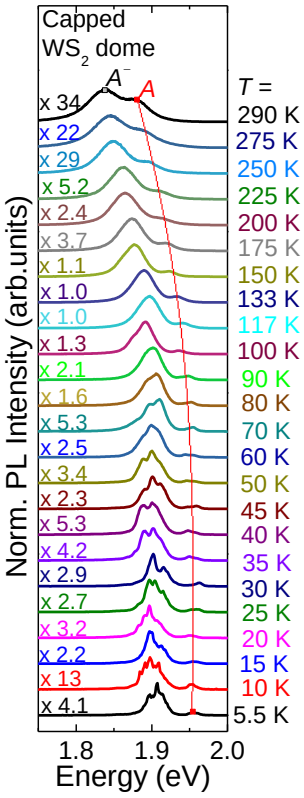

Figure A22.1: μ-PL spectra of a WS_2 dome capped with few-layer hBN as a function of temperature. Excitation wavelength equal to 532 nm and laser power equal to 4.4 μW. The exciton peak A is highlighted at 290 K and 5.5 K by a red square, with its evolution at intermediate temperatures followed by a red line as a guide for the eye. The predominant energy band at lower energy (A^-) is due to charged exciton recombination [436, 437]. The intensity factors of each spectrum are quoted.

A23 g-factor of SPEs in hBN-capped WS_2 domes

Fig. 7.6 shows the Zeeman splitting as a function of the magnetic field for narrow lines in the PL spectra of hBN-capped WS_2 domes at 10 K. From linear fits, the corresponding g-factor values were derived.

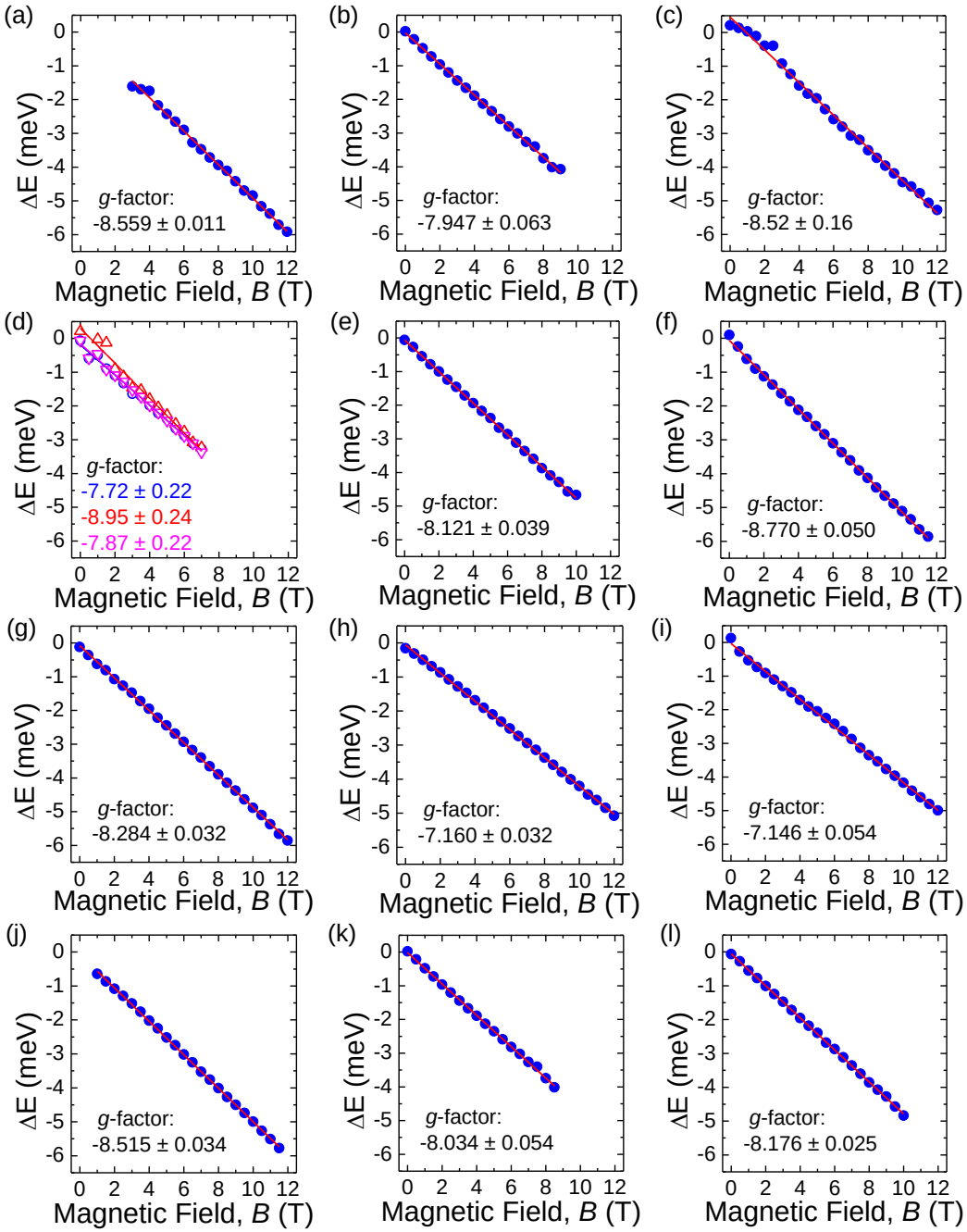

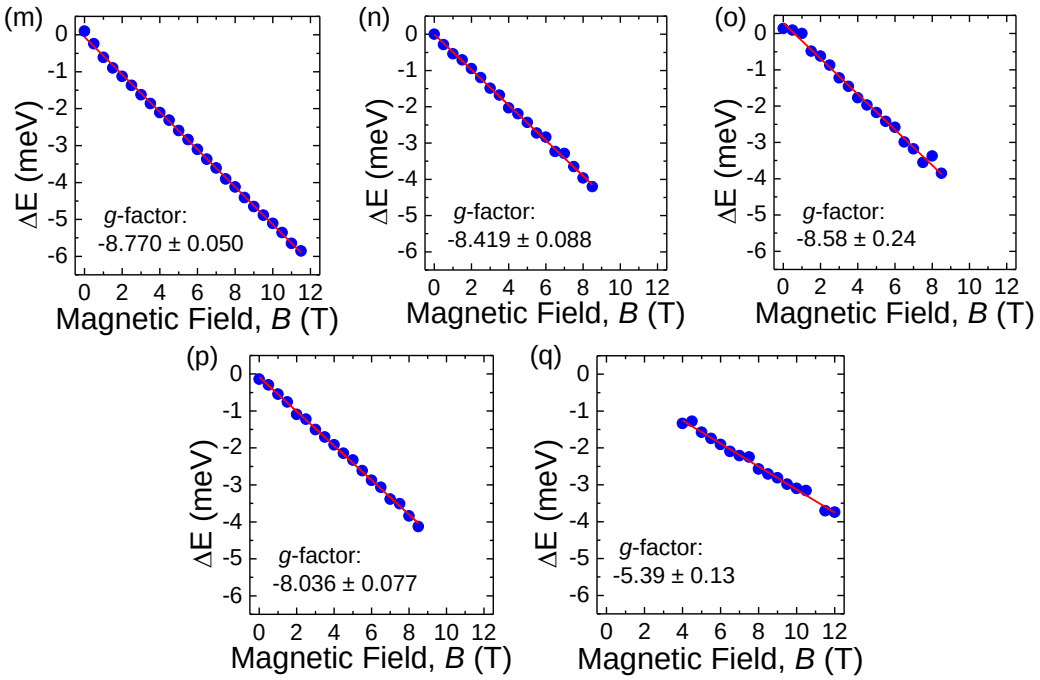

Figure A23.1: g-factors of the emitters appearing in the PL spectra of hBN-capped WS_2 domes at 10 K. The difference in energy ΔE between the σ^+ and σ^- polarisation (Zeeman splitting) of the emitters is plotted as a function of the applied out-of-plane magnetic field B. Panel (d) shows three emitters in the same plot since their emission energies are in a narrow spectral window and were extracted performing a multi-peak Lorentzian fit. A more complete discussion on the distribution of the values of g, extracted from these fits, can be found in the main text. All the points in the plots have an uncertainty of 0.26 meV. Excitation wavelength, 515 nm. Laser powers between 1 μW and 15 μW.

Thankings

Heartfelt thanks go to my supervisor Antonio Polimeni, who's been a special person to me and a great supervisor. He was a precious guide to me and at the same time allowed me to develop my own ideas and my own independence. I am sincerely grateful to him and happy for what we shared.

I am very grateful to Giorgio Pettinari and Marco Felici for what we shared and all that I could learn working together, I'm happy I could interact with them during my PhD.

I thank Marta De Luca for our joint research and discussions. I am happy I could interact with her during the last period of my PhD, and, indeed, she is to me a very positive example of what a young woman and researcher should be. I wish her all the best with her "new research life".

I thank Prof. Mario Capizzi for his kind advices and suggestions.

I thank Antonio Miriametro for always being gentle and available, I really find his knowledge and capabilities impressive.

I thank Cinzia Di Giorgio and Prof. Fabrizio Bobba for their exceptional work and our very constructive interaction. I am really happy of our collaboration, which has led to intriguing research.

I thank Salvatore Cianci for what we shared, I hope I could represent a positive example to him and wish him the best for the continuation of his PhD.

I thank Marzia Cuccu and Federico Tuzi for what we shared, and I hope I could be a good mentor to them as well.

I thank Alessandro Latini and Lorenza Romagnoli for our joint collaboration on perovskites, I was happy to work together and to explore the "chemistry world" with them.

I thank Davide Tedeschi for introducing me to the laboratory life, and Alessandro Surrente and Atanu Patra for the research we carried out together as teammates.

I thank Peter Christianen for his support during our stay at the High Field Magnet Laboratory to carry out our research proposals. It was a great experience to me, where I could learn a lot about the fascinating world of science in high magnetic fields. I also thank Mikhail Prosnikov for his precious support during my first stay there, and Koen van den Hoven for his support during my second stay.

I thank Maciej Molas for hosting us at the University of Warsaw to carry out our research proposals under magnetic fields. I am happy that this allowed us to establish a fruitful collaboration among our groups. Indeed, I am thankful to him and to his group members, especially Katarzyna Olkowska-Pucko, and also Tomasz Kazimierczuk and Adam Babiński for their precious support during our stay.

I want then to thank Tanju Yildrim for his valuable theoretical work and for our useful discussions, I really enjoyed our fruitful collaboration.

I thank Prof. Amalia Patanè, James Felton and Dr. Zakhar Kudrynskyi for our collaboration, for our joint research and useful discussions. I also thank Prof. Amalia Patanè for her availability and suggestions.

I thank Paulo E. Faria Jr. for our exciting joint research and useful discussions. I also thank his group members, Prof. Jaroslav Fabian, Klaus Zollner, Tomasz Woźniak and Andrey Chaves, for our research.

I thank Prof. Yuerui Lu and Boqing Liu for our joint research, and for our useful discussions.

I thank Prof. Maria Grazia Betti for being always available to me as my tutor within the PhD board, and for supporting me. I also appreciated our collaboration, for which I thank also Prof. Carlo Mariani, Giulia Avvisati, Mahmoud Abdelnabi, Ernesto Placidi, Marco Sbroscia and all the students involved in the research.

I thank Prof. Leonetta Baldassarre and Dr. Davide Spirito for out joint research and useful discussions.

I thank also Simona Sennato for her preliminary work in this field of research and for discussions; Drs. Emmanuele Cappelluti, Diego Di Girolamo, and Daniele Meggiolaro for our joint works; Profs. Takashi Taniguchi and Kenji Watanabe for providing us with their hBN crystals; Prof. Maurizia Palummo and Dr. Michele Re Fiorentin, and Profs. Javier M. Sanchez, Pablo Alonso-González and their group for our recent collaborations.

I'm very happy I had the opportunity to interact with all of these people, which was a source of great personal enrichment to me.

Publications

— 2023 —

28. Boqing Liu, Tanju Yildirim, Tieyu Lü, Elena Blundo, Li Wang, Lixue Jiang, Hongshuai Zou, Lijun Zhang, Huijun Zhao, Zongyou Yin, Fang-Bao Tian, Antonio Polimeni, and Yuerui Lu

    Variant Plateau's Law in Atomically Thin Transition Metal Dichalcogenide Dome Networks

    Nature Communications (2023), accepted, in press. [IF 2021: 17.694]

27. Arkadeb Pal, Khyati Anand, TW Yen, Atanu Patra, A Das, SM Huang, Elena Blundo, Antonio Polimeni, HD Yang, Sandip Chatterjee

    Magnetic properties and coupled spin-phonon behavior in quasi-one-dimensional screw-chain compound $BaMn_2V_2O_8$

    Physical Review Materials **7**, 014402 (2023). [IF 2021: 3.980]

26. Katarzyna Olkowska-Pucko, Elena Blundo, Natalia Zawadzka, Salvatore Cianci, Diana Vaclavkova, Piotr Kapuściński, Dipankar Jana, Giorgio Pettinari, Marco Felici, Karol Nogajewski, Miroslav Bartos, Kenji Watanabe, Takashi Taniguchi, Clement Faugeras, Marek Potemski, Adam Babiński, Antonio Polimeni, and Maciej R. Molas

    Excitons and trions in WSSe monolayers

    2D Materials **10**, 015018 (2023). [IF 2021: 7.687]

— 2022 —

25. Lorenza Romagnoli, Andrea D'Annibale, Elena Blundo, Antonio Polimeni, Alberto Cassetta, Giuseppe Chita, Riccardo Panetta, and Alessandro Latini

    Synthesis, structure and characterization of 4,4'-(anthracene-9,10-diylbis(ethyne-2,1-diyl))bis(1-methyl-1-pyridinium) bismuth iodide $(C_{30}H_{22}N_2)_3Bi_4I_{18}$*, an air, water and thermally stable 0D hybrid perovskite with high photoluminescence*

efficiency,
Crystal Growth & Design (2022), DOI: 10.1021/acs.cgd.2c01005.
[IF 2021: 4.076]

24. Maria Grazia Betti, Elena Blundo, Marta De Luca, Marco Felici, Riccardo Frisenda, Yoshikazu Ito, Samuel Jeong, Dario Marchiani, Carlo Mariani, Antonio Polimeni, Marco Sbroscia, Francesco Trequattrini, Rinaldo Trotta,
Homogeneous Spatial Distribution of Deuterium Chemisorbed on Free-Standing Graphene, Nanomaterials **12**, 2613 (2022). [IF 2021: 5.719]

23. James Felton, Elena Blundo, Zakhar Kudrynskyi, Sanliang Ling, Jonathan Bradford, Giorgio Pettinari, Timothy Cooper, Matthew Wadge, Zakhar Kovalyuk, Antonio Polimeni, Peter Beton, David Grant, Gavin Walker, Amalia Patanè
The Reaction of SnS_2 with H_2 as a Method to Produce SnS_2/SnS Heterostructures for Hydrogen Technologies and Beyond
Small **18**, 2202661 (2022). [IF 2021: 15.153]

22. Elena Blundo, Paulo E. Faria Junior, Alessandro Surrente, Giorgio Pettinari, Mikhail A. Prosnikov, Katarzyna Olkowska-Pucko, Klaus Zollner, Tomasz Woźniak, Andrey Chaves, Tomasz Kazimierczuk, Marco Felici, Adam Babiński, Maciej R. Molas, Peter C. M. Christianen, Jaroslav Fabian, and Antonio Polimeni.
Strain-induced exciton hybridization in WS_2 monolayers unveiled by Zeeman splitting measurements
Physical Review Letters, **129**, 067402 (2022). [IF 2021: 9.185]

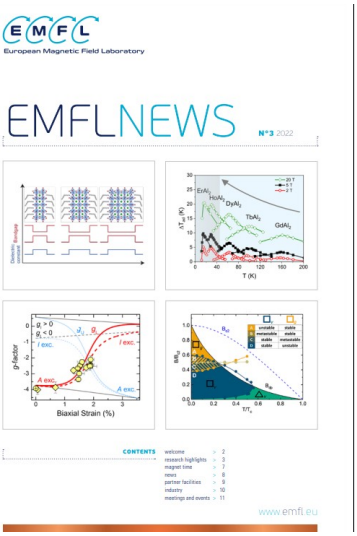

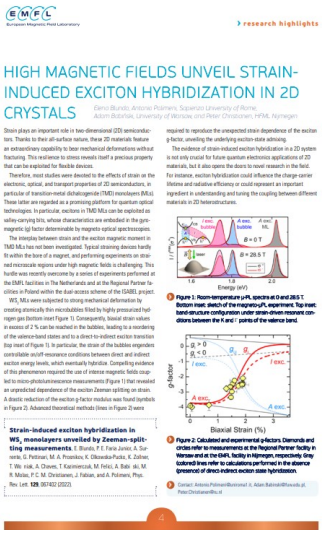

Media/press releases:
— https://emfl.eu/emfl website/wp-content/uploads/2022/11/emfl_newsletter_n3_22_web.pdf

21. Cinzia Di Giorgio†, Elena Blundo†, Giorgio Pettinari, Marco Felici, Fabrizio Bobba, and Antonio Polimeni

    Mechanical, elastic and adhesive properties of two-dimensional materials: From straining techniques to state-of-the-art local probe measurements

    † co-first authors

    Advanced Materials Interfaces **9**, 2102220 (2022). [IF 2021: 6.389]

20. Maria Grazia Betti, Ernesto Placidi, Chiara Izzo, Elena Blundo, Antonio Polimeni, Marco Sbroscia, José Avila, Pavel Dudin, Kailong Hu, Yoshikazu Ito, Deborah Prezzi, Miki Bonacci, Elisa Molinari, and Carlo Mariani*

    Gap opening in double side highly hydrogenated free standing graphene

    Nano Letters **22**, 2971 (2022). [IF 2021: 12.262]

19. Salvatore Cianci, Elena Blundo, Marco Felici, Antonio Polimeni, and Giorgio Pettinari

    Tailoring the optical properties of 2D transition metal dichalcogenides by strain

    Optical materials **125**, 112087 (2022). [IF 2021: 3.754]

18. Elena Blundo, Alessandro Surrente, Davide Spirito, Giorgio Pettinari, Tanju Yildirim, Carlos Alvarado Chavarin, Leonetta Baldassarre, Marco Felici, and Antonio Polimeni

    Vibrational properties in highly strained hexagonal boron nitride bubbles

    Nano Letters **22**, 1525 (2022). [IF 2021: 12.262]

17. Arkadeb Pal, T. W. Kuo, Chia-Hsiu Hsu, D. C. Kakarla, Ajay Tiwari, M. C. Chou, Atanu Patra, P. Yanda, Elena Blundo, Antonio Polimeni, A. Sundaresan, F. C. Chuang, and H. D. Yang

    Interplay of lattice, spin and dipolar properties in $CoTeMoO_6$: Emergence of Griffiths-like phase, metamagnetic transition and magnetodielectric effect

    Physical Review B **105**, 024420 (2022). [IF 2021: 3.908]

16. Diego Di Girolamo, Elena Blundo, Giulia Folpini, Corinna Ponti, Guixiang Li, Mahmoud Aldamasy, Zafar Iqbal, Jorge Pascual, Giuseppe Nasti, Meng Li, Roberto Avolio, Olga Russina, Alessandro Latini, Fahad Alharthi, Marco Felici, Annamaria Petrozza, Antonio Polimeni, and Antonio Abate

    Energy distribution in tin halide perovskite

    Solar RRL **6**, 2100825 (2022). [IF 2021: 9.173]

15. Francesco Filippone, Saeed Younis, Giuseppe Mattioli, Marco Felici, Elena Blundo, Antonio Polimeni, Giorgio Pettinari, Damiano Giubertoni, Eduard Sterzer, Kerstin Volz, Dan Fekete, Alok Rudra, Eli Kapon, and Aldo Amore Bonapasta

    Selective effects of the host matrix in hydrogenated InGaAsN alloys: a new defect engineering paradigm.

    Advanced Functional Materials **32**, 2108862 (2022). [IF 2021: 19.924]

— 2021 —

14. Cinzia Di Giorgio, Elena Blundo, Giorgio Pettinari, Marco Felici, Antonio Polimeni, and Fabrizio Bobba

    Exceptional elasticity of micro-scale constrained MoS_2 domes

    ACS Applied Materials and Interfaces **13**, 48228 (2021). [IF 2021: 10.383]

13. Elena Blundo*, Cinzia Di Giorgio, and Giorgio Pettinari

    * corresponding author

    Bubble formation in van der Waals crystals: A platform for fundamental studies

    Il Nuovo Cimento C **44**, 1 (2021), Invited Paper. [IF 2021: 0.252]

12. Elena Blundo*, Tanju Yildirim, Giorgio Pettinari, and Antonio Polimeni*

    * co-corresponding authors

    Experimental Adhesion energy in van der Waals crystals and heterostructures from atomically-thin domes

    Physical Review Letters **127**, 046101 (2021). [IF 2021: 9.185]

11. Elena Blundo, Antonio Polimeni, Daniele Meggiolaro, Andrea D'Annibale, Lorenza Romagnoli, Marco Felici, and Alessandro Latini

    Brightly Luminescent and Moisture Tolerant Phenyl-Viologen Lead Iodide Perovskites for Light Emission Applications

    The Journal of Physical Chemistry Letters **12**, 5456 (2021). [IF 2021: 6.888]

10. Elena Blundo, Emmanuele Cappelluti, Marco Felici, Giorgio Pettinari and Antonio Polimeni

    Strain-tuning of the electronic, optical, and vibrational properties of two-dimensional crystals

    Applied Physics Reviews **8**, 021318 (2021). Invited paper. [IF 2021: 19.527]

9. Mahmoud M. S. Abdelnabi, Chiara Izzo, Elena Blundo*, Maria Grazia Betti, Marco Sbroscia, Giulia Di Bella, Gianluca Cavoto, Antonio Polimeni, Isabel Garcia-Cortes, Isabel Rucandio, Alejandro Moroño, Kailong Hu, Yoshikazu Ito, and Carlo Mariani*

    * co-corresponding authors

    Deuterium Adsorption on Free-Standing Graphene

    Nanomaterials **11**, 130 (2021). [IF 2021: 5.719]

8. Mahmoud M. S. Abdelnabi, Elena Blundo, Maria Grazia Betti, Gianluca Cavoto, Ernesto Placidi, Antonio Polimeni, Alessandro Ruocco, Kailong Hu, Yoshikazu Ito, and Carlo Mariani

    Towards Free-Standing Graphane: Atomic Hydrogen and Deuterium Bonding to Nano-Porous Graphene

    Nanotechnology **32**, 035707 (2021). [IF 2021: 3.953]

— 2020 —

7. Cinzia Di Giorgio, Elena Blundo, Giorgio Pettinari, Marco Felici, Yuerui Lu, Anna Maria Cucolo, Antonio Polimeni, and Fabrizio Bobba

    Nano-scale measurements of elastic properties and hydrostatic pressure in H_2-bulged MoS_2 membranes

    Advanced Materials Interfaces **7**, 2001024 (2020). [IF 2020: 6.147]

6. Elena Blundo

   Proton-induced straining of two-dimensional crystals

   Il Nuovo Cimento C **43**, 112 (2020), Invited paper. [IF 2020: 0.288]

5. Davide Tedeschi, H. Aruni Fonseka, Elena Blundo, Andrés Granados del Aguila, Yanan Guo, Hark H Tan, Peter CM Christianen, Chennupati Jagadish, Antonio Polimeni, and Marta De Luca

   Hole and Electron Effective Masses in Single InP Nanowires with a Wurtzite-Zincblende Homojunction

   ACS Nano **14**, 11613 (2020). [IF 2020: 15.881]

4. Elena Blundo*, Cinzia Di Giorgio, Giorgio Pettinari, Tanju Yildirim, Marco Felici, Yuerui Lu, Fabrizio Bobba, and Antonio Polimeni*

   * co-corresponding authors

   Engineered creation of periodic giant, non-uniform strains in MoS_2 monolayers

   Advanced Materials Interfaces **7**, 2000621 (2020). [IF 2020: 6.147]

3. James Felton, Elena Blundo, Sanliang Ling, Joseph Glover, Zakhar R. Kudrynskyi, Oleg Makarovsky, Zakhar D. Kovalyuk, Elena Besley, Gavin Walker, Antonio Polimeni, and Amalia Patanè

   The Interaction of Hydrogen with the van der Waals Crystal γ-InSe

   Molecules **25**, 2526 (2020). [IF 2020: 4.411]

2. Elena Blundo, Marco Felici, Tanju Yildirim, Giorgio Pettinari, Davide Tedeschi, Antonio Miriametro, Boqing Liu, Wendi Ma, Yuerui Lu, and Antonio Polimeni

   Evidence of the direct-to-indirect band gap transition in strained two-dimensional WS_2, MoS_2, and WSe_2

   Physical Review Research **2**, 012024 (2020). Rapid Communication.
   [IF 2020: /]

— 2019 —

1. Davide Tedeschi†, Elena Blundo†, Marco Felici, Giorgio Pettinari, Boqing Liu, Tanju Yildirim, Elisa Petroni, Chris Zhang, Yi Zhu, Simona Sennato, Yuerui Lu, and Antonio Polimeni

   † co-first authors

   Controlled micro/nano-dome formation in proton-irradiated bulk transition-metal dichalcogenides

   Advanced Materials **31**, 1903795 (2019). [IF 2019: 27.398]

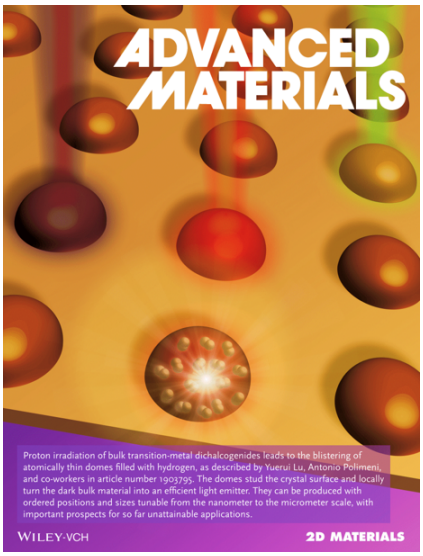

Media/press releases:

– https://www.agi.it/scienza/bolle_idrogeno_semiconduttori-6297600/news/2019-10-05/
– https://fidest.wordpress.com/2019/10/08/bolle-di-idrogeno-un-nuovo-meccanismo-per-generare-luce-dai-cristalli/
– https://www.radio24.ilsole24ore.com/programmi/smart-city/puntata/nano-cupole-inventato-nuovo-modo-creare-materiali-bidimensionali-210415-ACpxr56
– https://www.uniroma1.it/it/notizia/bolle-di-idrogeno-un-nuovo-meccanismo-generare-luce-dai-cristalli

Submitted works

- Lorenza Romagnoli, Andrea D'Annibale, Elena Blundo, Atanu Patra, Antonio Polimeni, Daniele Meggiolaro, Iryna Adrusenko, Danilo Marchetti, Mauro Gemmi, and Alessandro Latini

  4,4'-(anthracene-9,10-diylbis(ethyne-2,1-diyl))bis(1-methyl-1-pyridinium) lead iodide $C_{30}H_{22}N_2Pb_2I_6$: a highly luminescent, chemically and thermally stable 1D hybrid perovskite

  Under review.

- Salvatore Cianci, Elena Blundo, Federico Tuzi, Giorgio Pettinari, Katarzyna Olkowska-Pucko, Eirini Parmenopoulou, Djero B. L. Peeters, Antonio Miriametro, Takashi Taniguchi, Kenji Watanabe, Adam Babinski, Maciej R. Molas, Marco Felici, and Antonio Polimeni

  Spatially controlled single photon emitters in hBN-capped WS_2 domes

  Under review.

- Boqing Liu, Tanju Yildirim, Elena Blundo, Domenico de Ceglia, Zongyou Yin, Daniel Macdonald, Hieu T. Nguyen, Giorgio Pettinari, Marco Felici, Antonio Polimeni, and Yuerui Lu

  Extraordinary Second Harmonic Generation modulated by Divergent Strain Field in Pressurized Monolayer Domes

  Under review.

Works in preparation

- Elena Blundo, Federico Tuzi, et al.

  Localisation-to-delocalisation transition of moiré excitons in a $WSe_2/MoSe_2$ heterostructure

- Elena Blundo, Marzia Cuccu, Federico Tuzi, et al.

  Layer selective strain engineering in van der Waals heterostructures: Giant photoluminescence enhancement in InSe/strained-MS_2 (M=Mo,W) heterostructures

Oral presentations

Invited Talks at national/international conferences

— 2022 —

1. Elena Blundo, Paulo E. Faria Junior, Alessandro Surrente, Giorgio Pettinari, Mikhail A. Prosnikov, Katarzyna Olkowska-Pucko, Klaus Zollner, Tomasz Woźniak, Andrey Chaves, Tomasz Kazimierczuk, Marco Felici, Adam Babiński, Maciej R. Molas, Peter C. M. Christianen, Jaroslav Fabian, and Antonio Polimeni.

   Gyromagnetic factor of k-space direct and indirect excitons in strained WS2 monolayers.

   European Magnetic Field Laboratory User Meeting, 15 June 2022, Grenoble, France.

Oral presentations at national/international conferences

The candidate presented her work at the following conferences and workshops.

— 2022 —

9. Elena Blundo, Cinzia Di Giorgio, Giorgio Pettinari, Tanju Yildirim, Alessandro Surrente, Paulo Eduardo Faria Junior, Mikhail Prosnikov, Katarzyna Olkowska Pucko, Maciej R Molas, Marco Felici, Adam Babinski,, Peter Christianen, Fabrizio Bobba, Jaroslav Fabian, and Antonio Polimeni

   Strain fields at the micro-scale in two-dimensional materials.

   MRS 2022 Fall Meeting & Exhibit, 27 November - 2 December 2022, Boston, Massachusetts, USA.

8. Elena Blundo, Marzia Cuccu, Giorgio Pettinari, Salvatore Cianci, Atanu Patra, Marco Felici, Antonio Polimeni

   Strain-tuning of the optoelectronic and spin properties of 2D crystals.

   Graphene 2022, 5-8 July 2022, Aachen, Germany.

— 2020 —

7. Elena Blundo, Marzia Cuccu, Giorgio Pettinari, Salvatore Cianci, Atanu Patra, Marco Felici, Antonio Polimeni

   Tuning the optoelectronic properties of van der Waals heterostructures.

   107° Congresso Nazionale SIF, 13-17 September 2021, Online conference.

6. Elena Blundo, Giorgio Pettinari, Tanju Yildirim, Paulo E. Faria Junior, Marco Felici, Jaroslav Fabian, Antonio Polimeni

   Bubbling-induced straining of Two-Dimensional Crystals.

   Workshop 2Day, 17-18 June 2021, La Sapienza, Rome.

5. Elena Blundo, Marzia Cuccu, Giorgio Pettinari, Cinzia Di Giorgio, Tanju Yildirim, Paulo E. Faria Junior, Marco Felici, Fabrizio Bobba, Antonio Polimeni

   Strain Tuning of the Optoelectronic Properties of Two-Dimensional Crystals.

   MRS 2021 Virtual Spring Meeting & Exhibit, 17-23 April 2021, Online conference.

— 2020 —

4. Elena Blundo, Cinzia Di Giorgio, Marco Felici, Giorgio Pettinari, Tanju Yildirim, Yuerui Lu, Fabrizio Bobba, Antonio Polimeni

   Bubble formation in van der Waals crystals: A platform for fundamental studies.

   106° Congresso Nazionale SIF, 14-18 September 2020, Online conference.

— 2019 —

3. Elena Blundo, Davide Tedeschi, Marco Felici, Giorgio Pettinari, Boqing Liu, Tanju Yildirim, Chris Zhang, Yuerui Lu, Antonio Polimeni

   Proton-induced straining of two-dimensional crystals

   105° Congresso Nazionale SIF, 23-27 September 2019, L'Aquila, Italy.

2. Elena Blundo, Davide Tedeschi, Marco Felici, Giorgio Pettinari, Boqing Liu, Tanju Yildirim, Chris Zhang, Yi Zhu, Yuerui Lu, Antonio Polimeni

   Controllable micro/nano-dome creation in proton-irradiated bulk transition-metal dichalcogenides

   Nanoinnovation 2019, 12-14 June 2019, Rome, Italy.

— 2018 —

1. Elena Blundo, Davide Tedeschi, Marco Felici, Giorgio Pettinari, Simona Sennato, Elisa Petroni, Tanju Yildirim, Chris Zhang, Ankur Sharma, Boqing Liu, Yuerui Lu, Antonio Polimeni

   Hydrogen-driven generation of atomically thin, light emitting domes in transition metal dichalcogenides

   Materials 2018, 22-26 October 2018, Bologna, Italy.

Awards and grants

Awards

- **Nano Letters Seed Grant 2022** (Europe, Australia and New Zealand region) for later-stage graduate students.
- **'Graphene 2022' conference Travel Grant** for PhD students.
- **Nanomaterials 2022 Travel Award** for PhD and post docs sponsored by the open access journal Nanomaterials published by MDPI.
- **Materials 2022 Travel Award** for PhD and post docs sponsored by the open access journal Materials published by MDPI.
- **Prize "Michele Cantone" 2021** for *young graduated students* by the Italian Physical Society.
- Communication selected among the *Best Communications* at the 106° national conference 2020 by the Italian Physical Society.
- First prize for the **Best oral communication** at the 105° national conference 2021 (Physics of Matter section) by the Italian Physical Society.

Grants as principal investigator

- Nano Letters Seed Grant 2022 – Europe, Australia and New Zealand region (`https://axial.acs.org/2022/03/15/nano-letters-seed-grants/` and `https://pubs.acs.org/doi/full/10.1021/acs.nanolett.2c03880`)
  Project: "*Engineering quantum emitters at telecom wavelengths from strained 2D crystals*"
  Funding = 2500 $.
- Avvio alla Ricerca Tipo II 2022, Sapienza University of Rome
  Project: "*electrical Devices based on InnOvative van Der waals hEterostructures - DIODE*".
  Funding = 4000 €.

- European Magnetic Field Laboratory (EMFL), ISABEL project
  Project: "*Spin and valley physics of quantum emitters in strained 2D materials*" (ref. number NSC07-221)
  Experiment performed at the University of Warsaw, Poland, in July 2022.

- Avvio alla Ricerca Tipo I 2021, Sapienza University of Rome
  Project "*Tuneable lIGht Emission fRom flexible, atomIcally-thin SandwicHes - a TIGERISH project*".
  Funding = 1600 €

- European Magnetic Field Laboratory (EMFL), ISABEL project
  Project: "*Strain tuning of the spin/valley physics of k-space direct and indirect excitons in transition-metal dichalcogenides*" (ref. number NSC01-121)
  Experiments performed at the University of Warsaw, Poland, in September 2021, and at the High Field Magnet Laboratory (HFML), Nijmegen, The Netherlands, in November 2022.

- Avvio alla Ricerca Tipo I 2020, Sapienza University of Rome
  Project: "*AssembLing and mEchanically-straininG nOvel promisinG heterostructures mAde of two-diMensional matErials - LEGO GAME*"
  Funding = 1600 €

References

[1] R. P. Feynman, *There's Plenty of Room at the Bottom*, Eng. Sci. **23**, 22 (1960).

[2] R. E. Peierls, *Quelques proprietes typiques des corpses solides*, Ann. I. H. Poincare **5**, 177 (1935).

[3] L. D. Landau, *Zur Theorie der phasenumwandlungen II*, Phys. Z. Sowjetunion **11**, 26 (1937).

[4] L. D. Landau and E. M. Lifshitz, *Statistical Physics, Part I*, Pergamon, Oxford (1980).

[5] N. D. Mermin, *Crystalline order in two dimensions*, Phys. Rev. **176**, 250 (1968).

[6] A. K. Geim and K. S. Novoselov, *The rise of graphene*, Nat. Mater. **6**, 183 (2017).

[7] R. F. Frindt, *Superconductivity in ultrathin $NbSe_2$ layers*, Phys. Rev. Lett. **28**, 299 (1972).

[8] R. F. Frindt, *Single crystals of MoS_2 several molecular layers thick*, J. Appl. Phys. **37**, 1928 (1966).

[9] K. S. Novoselov, A. K. Geim, S. V. Morozov, D. Jiang, Y. Zhang, S. V. Dubonos, I. V. Grigorieva, and A. A. Firsov, *Electric field effect in atomically thin carbon films*, Science **306**, 666 (2004).

[10] E. A. Abbott, *Flatland: A Romance of Many Dimensions*, Seeley & co (1884).

[11] P. Ajayan, P. Kim, and K. Banerjee, *Two-dimensional van der Waals materials*, Physics Today **69**, 38 (2016).

[12] S. Z. Butler, S. M. Hollen, L. Cao, Y. Cui, J. A. Gupta, H. R. Gutierrez, T. F. Heinz, S. S. Hong, J. Huang, A. F. Ismach, E. Johnston-Halperin, M. Kuno, V. V. Plashnitsa, R. D. Robinson, R. S. Ruoff, S. Salahuddin, J. Shan, L. Shi, M. G. Spencer, M. Terrones, W. Windl, and J. E. Goldberger, *Progress, challenges, and opportunities in two-dimensional materials beyond graphene*, ACS Nano **7**, 2898 (2013).

[13] C. Lee, X. Wei, J. W. Kysar, and J. Hone, *Measurement of the elastic properties and intrinsic strength of monolayer graphene*, Science **321**, 385 (2008).

[14] M. K. Blees, A. W. Barnard, P. A. Rose, S. P. Roberts, K. L. McGill, P. Y. Huang, A. R. Ruyack, J. W. Kevek, B. Kobrin, D. A. Muller, and P. L. McEuen, *Graphene kirigami*, Nature **524**, 204 (2015).

[15] S. Bertolazzi, J. Brivio, and A. Kis, *Stretching and breaking of ultrathin MoS_2*, ACS Nano **5**, 9703 (2011).

[16] X. Li, L. Tao, Z. Chen, H. Fang, X. Li, X. Wang, J.-B. Xu, and H. Zhu, *Graphene and related two-dimensional materials: Structure-property relationships for electronics and optoelectronics*, Appl. Phys. Rev. **4**, 021306 (2017).

[17] N. Lu, H. Guo, L. Li, J. Dai, L. Wang, W.-N. Mei, X. Wu, and X. C. Zeng, *MoS_2 / MX_2 heterobilayers: bandgap engineering via tensile strain or external electrical field*, Nanoscale **6**, 2879 (2014).

[18] A. K. Geim and I. V. Grigorieva, *Van der Waals heterostructures*, Appl. Phys. Rev. **499**, 419 (2013).

[19] J. A. Wilson and A. D. Yoffe, *The transition metal dichalcogenides discussion and interpretation of the observed optical, electrical and structural properties*, Advances in Physics **18**, 73 (1969).

[20] *The Materials Project*, https://materialsproject.org/ (2018).

[21] A. Jain, S. P. Ong, G. Hautier, W. Chen, W. D. Richards, S. Dacek, S. Cholia, D. Gunter, D. Skinner, G. Ceder, and K. A. Persson, *Commentary: The Materials Project: A materials genome approach to accelerating materials innovation*, APL Mater. **1**, 011002 (2013).

[22] L. Zhang and A. Zunger, *Evolution of electronic structure as a function of layer thickness in group-VIB transition metal dichalcogenides: emergence of localization prototypes*, Nano Lett. **15**, 949 (2015).

[23] Z. Y. Zhu, Y. C. Cheng, and U. Schwingenschlögl, *Giant spin-orbit-induced spin splitting in two-dimensional transition-metal dichalcogenide semiconductors*, Phys. Rev. B **84**, 153402 (2011).

[24] D. Xiao, G.-B. Liu, W. Feng, X. Xu, and W. Yao, *Coupled spin and valley physics in monolayers of MoS_2 and other group-VI dichalcogenides*, Phys. Rev. Lett. **108**, 196802 (2012).

[25] H. Min, J. E. Hill, N. A. Sinitsyn, B. R. Sahu, L. Kleinman, and A. H. MacDonald, *Intrinsic and Rashba spin-orbit interactions in graphene sheets*, Phys. Rev. B **74**, 165310 (2006).

[26] N. Kumar, S. Najmaei, Q. Cui, F. Ceballos, P. M. Ajayan, J. Lou, and H. Zhao, *Second harmonic microscopy of monolayer MoS_2*, Phys. Rev. B **87**, 161403(R) (2013).

[27] C. Janisch, Y. Wang, D. Ma, N. Mehta, A. L. Elías, N. Perea-López, M. Terrones, V. Crespi, and Z. Liu, *Extraordinary second harmonic generation in tungsten disulfide monolayers*, Sci. Rep. **4**, 5530 (2014).

[28] R. W. Boyd, *Nonlinear Optics*, Academic Press, 3rd edition (2008).

[29] R. Loudon, *The Quantum Theory of Light*, Oxford Science Publications, 3rd edition (2000).

[30] Y. Li, Y. Rao, K. F. Mak, Y. You, S. Wang, C. R. Dean, , and T. F. Heinz, *Probing Symmetry Properties of Few-Layer MoS_2 and h-BN by Optical Second-Harmonic Generation*, Nano Lett. **13**, 3329 (2013).

[31] A. Splendiani, L. Sun, Y. Zhang, T. Li, J. Kim, C.-Y. Chim, G. Galli, and F. Wang, *Emerging photoluminescence in monolayer MoS_2*, Nano Lett. **10**, 1271 (2010).

[32] H. Yuan, Z. Liu, G. Xu, B. Zhou, S. Wu, D. Dumcenco, K. Yan, Y. Zhang, S.-K. Mo, P. Dudin, V. Kandyba, M. Yablonskikh, A. Barinov, Z. Shen, S. Zhang, Y. Huang, X. Xu, Z. Hussain, H. Y. Hwang, Y. Cui, and Y. Chen, *Evolution of the valley position in bulk transition-metal chalcogenides and their monolayer limit*, Nano Lett. **16**, 4738 (2016).

[33] A. Zilli, M. De Luca, D. Tedeschi, H. A. Fonseka, A. Miriametro, H. H. Tan, C. Jagadish, M. Capizzi, and A. Polimeni, *Temperature Dependence of Interband Transitions in Wurtzite InP Nanowires*, ACS Nano **9**, 4, 4277–4287 (2015).

[34] M. De Luca, A. Zilli, H. A. Fonseka, S. Mokkapati, A. Miriametro, H. H. Tan, L. M. Smith, C. Jagadish, M. Capizzi, and A. Polimeni, *Polarized Light Absorption in Wurtzite InP Nanowire Ensembles*, Nano Letters **15**, 2, 998–1005 (2015).

[35] D. Tedeschi, H. A. Fonseka, E. Blundo, A. Granados del Águila, Y. Guo, H. H. Tan, P. C. M. Christianen, C. Jagadish, A. Polimeni, and M. De Luca, *Hole and Electron Effective Masses in Single InP Nanowires with a Wurtzite-Zincblende Homojunction*, ACS Nano **14**, 9, 11613–11622 (2020).

[36] M. De Luca and A. Polimeni, *Electronic properties of wurtzite-phase InP nanowires determined by optical and magneto-optical spectroscopy*, Applied Physics Reviews **4**, 4, 041102 (2017).

[37] Z. Jiang, Z. Liu, Y. Li, and W. Duan, *Scaling Universality between Band Gap and binding energy of Two-Dimensional Semiconductors*, Phys. Rev. Lett. **118**, 266401 (2017).

[38] G. Wang, A. Chernikov, M. M. Glazov, T. F. Heinz, X. Marie, T. Amand, and B. Urbaszek, *Colloquium: Excitons in atomically thin transition metal dichalcogenides*, Rev. Mod. Phys. **90**, 021001 (2018).

[39] J. Dean and D. G. Thomas, *Intrinsic Absorption-Edge Spectrum of Gallium Phosphide*, Phys. Rev. **150**, 690 (1966).

[40] M. Baranowski, P. Plochocka, R. Su, L. Legrand, T. Barisien, F. Bernardot, Q. Xiong, C. Testelin, and M. Chamarro, *Exciton binding energy and effective mass of $CsPbCl_3$: a magneto-optical study*, Photonics Research **8**, 50–55 (2020).

[41] E. Blundo, E. Cappelluti, M. Felici, G. Pettinari, and A. Polimeni, *Strain-tuning of the electronic, optical, and vibrational properties of two-dimensional crystals*, Appl. Phys. Rev. **8**, 021318 (2021).

[42] A. Kormányos, G. Burkard, M. Gmitra, J. Fabian, V. Zólyomi, N. D. Drummond, and V. Fal'ko, *$k \cdot p$ theory for two-dimensional transition metal dichalcogenide semiconductors*, 2D Materials **2**, 2, 022001 (2015).

[43] M. Koperski, M. R. Molas, A. Arora, K. Nogajewski, M. Bartos, J. Wyzula, D. Vaclavkova, P. Kossacki, and M. Potemski, *Orbital, spin and valley contributions to Zeeman splitting of excitonic resonances in $MoSe_2$, WSe_2 and WS_2 monolayers*, 2D Materials **6**, 1, 015001 (2018).

[44] M. R. Molas, C. Faugeras, A. O. Slobodeniuk, K. Nogajewski, M. Bartos, D. M. Basko, and M. Potemski, *Brightening of dark excitons in monolayers of semiconducting transition metal dichalcogenides*, 2D Materials **4**, 2, 021003 (2017).

[45] R. Frisenda, Y. Niu, P. Gant, A. J. Molina-Mendoza, R. Schmidt, R. Bratschitsch, J. Liu, L. Fu, D. Dumcenco, A. Kis, D. P. D. Lara, and A. Castellanos-Gomez, *Micro-reflectance and transmittance spectroscopy: a versatile and powerful tool to characterize 2D materials*, J. Phys. D: Appl. Phys. **50**, 074002 (2017).

[46] A. V. Stier, K. M. McCreary, B. T. Jonker, J. Kono, and S. A. Crooker, *Exciton diamagnetic shifts and valley Zeeman effects in monolayer WS_2 and MoS_2 to 65 Tesla*, Nature Commun. **7**, 10643 (2016).

[47] A. V. Stier, N. P. Wilson, K. A. Velizhanin, J. Kono, X. Xu, and S. A. Crooker, *Magnetooptics of Exciton Rydberg States in a Monolayer Semiconductor*, Phys. Rev. Lett. **120**, 057405 (2018).

[48] A. V. Stier, N. P. Wilson, G. Clark, X. Xu, and S. A. Crooker, *Probing the influence of dielectric environment on excitons in monolayer WSe_2: Insight from high magnetic fields*, Nano Lett. **16**, 7054 (2016).

[49] J. Zipfel, J. Holler, A. A. Mitioglu, M. V. Ballottin, P. Nagler, A. V. Stier, T. Taniguchi, K. Watanabe, S. A. Crooker, P. C. Christianen *et al.*, *Spatial extent of the excited exciton states in WS_2 monolayers from diamagnetic shifts*, Physical Review B **98**, 7, 075438 (2018).

[50] M. Goryca, J. Li, A. V. Stier, T. Taniguchi, K. Watanabe, E. Courtade, S. Shree, C. Robert, B. Urbaszek, X. Marie *et al.*, *Revealing exciton masses and dielectric properties of monolayer semiconductors with high magnetic fields*, Nature Commun. **10**, 4172 (2019).

[51] A. Srivastava, M. Sidler, A. Allain, D. Lembke, A. Kis, and A. Imamoglu, *Valley Zeeman effect in elementary optical excitations of monolayer WSe_2*, Nat. Phys. **11**, 141 (2015).

[52] S.-Y. Chen, Z. Lu, T. Goldstein, J. Tong, A. Chaves, J. Kunstmann, L. S. R. Cavalcante, T. Woźniak, G. Seifert, D. R. Reichman, T. Taniguchi, K. Watanabe, D. Smirnov, and J. Yan, *Luminescent emission of excited Rydberg excitons from monolayer WSe_2*, Nano Lett. **19**, 2464 (2019).

[53] K. Watanabe, T. Taniguchi, and H. Kanda, *Direct-bandgap properties and evidence for ultraviolet lasing of hexagonal boron nitride single crystal*, Nat. Mater. **3**, 6, 404–409 (2004).

[54] Z. Liu, Y. Gong, W. Zhou, L. Ma, J. Yu, J. C. Idrobo, J. Jung, A. H. MacDonald, R. Vajtai, J. Lou, and P. M. Ajayan, *Ultrathin high-temperature oxidation-resistant coatings of hexagonal boron nitride*, Nat. Commun. **4**, 1, 2541 (2013).

[55] L. H. Li, J. Cervenka, K. Watanabe, T. Taniguchi, and Y. Chen, *Strong oxidation resistance of atomically thin boron nitride nanosheets*, ACS Nano **8**, 2, 1457–1462 (2014).

[56] A. Falin, Q. Cai, E. J. Santos, D. Scullion, D. Qian, R. Zhang, Z. Yang, S. Huang, K. Watanabe, T. Taniguchi, M. R. Barnett, Y. Chen, R. S. Ruoff, and L. H. Li, *Mechanical properties of atomically thin boron nitride and the role of interlayer interactions*, Nat. Commun. **8**, 15815 (2017).

[57] A. Raja, L. Waldecker, J. Zipfel, Y. Cho, S. Brem, J. D. Ziegler, M. Kulig, T. Taniguchi, K. Watanabe, E. Malic, T. F. Heinz, T. C. Berkelbach, and A. Chernikov, *Dielectric disorder in two-dimensional materials*, Nat. Nanotechnol. **14**, 9, 832–837 (2019).

[58] C. R. Dean, A. F. Young, I. Meric, C. Lee, L. Wang, S. Sorgenfrei, K. Watanabe, T. Taniguchi, P. Kim, K. L. Shepard, and J. Hone, *Boron nitride substrates for high-quality graphene electronics*, Nat. Nanotechnol. **5**, 10, 722–726 (2010).

[59] F. Cadiz, E. Courtade, C. Robert, G. Wang, Y. Shen, H. Cai, T. Taniguchi, K. Watanabe, H. Carrere, D. Lagarde, M. Manca, T. Amand, P. Renucci, S. Tonday, M. X, and U. Urbaszek, *Excitonic linewidth approaching the homogeneous limit in MoS_2-based van der Waals heterostructures*, Phys. Rev. X **7**, 2, 021026 (2017).

[60] O. A. Ajayi, J. V. Ardelean, G. D. Shepard, J. Wang, A. Antony, T. Taniguchi, K. Watanabe, T. F. Heinz, S. Strauf, X. Zhu, and J. Hones, *Approaching the intrinsic photoluminescence linewidth in transition metal dichalcogenide monolayers*, 2D Mater. **4**, 3, 031011 (2017).

[61] X. Chen, Y. Wu, Z. Wu, Y. Han, S. Xu, L. Wang, W. Ye, T. Han, Y. He, Y. Cai, and N. Wang, *High-quality sandwiched black phosphorus heterostructure and its quantum oscillations*, Nat. Commun. **6**, 1, 7315 (2015).

[62] A. S. Mayorov, R. V. Gorbachev, S. V. Morozov, L. Britnell, R. Jalil, L. A. Ponomarenko, P. Blake, K. S. Novoselov, K. Watanabe, T. Taniguchi, and A. K. Geim, *Micrometer-scale ballistic transport in encapsulated graphene at room temperature*, Nano Lett. **11**, 6, 2396–2399 (2011).

[63] H. Arora, Y. Jung, T. Venanzi, K. Watanabe, T. Taniguchi, R. Hübner, H. Schneider, M. Helm, J. C. Honer, and A. Erbe, *Effective hexagonal boron nitride passivation of few-layered InSe and GaSe to enhance their electronic and optical properties*, ACS Appl. Mater. Interfaces **11**, 43480 (2019).

[64] J. Wierzbowski, J. Klein, F. Sigger, C. Straubinger, M. Kremser, T. Taniguchi, K. Watanabe, U. Wurstbauer, A. W. Holleitner, M. Kaniber, K. Müller, and J. J. Finley, *Direct exciton emission from atomically thin transition metal dichalcogenide heterostructures near the lifetime limit*, Sci. Rep. **7**, 1, 12383 (2017).

[65] A. Tartakovskii, *Excitons in 2D heterostructures*, Nat. Rev. Phys. **2**, 8–9 (2020).

[66] A. Tartakovskii, *Moiré or not*, Nat. Mater. **19**, 581–582 (2020).

[67] S. Dai, Z. Fei, Q. Ma, A. Rodin, M. Wagner, A. McLeod, M. Liu, W. Gannett, W. Regan, K. Watanabe, T. Taniguchi, M. Thiemens, G. Dominguez, A. Castro Neto, A. Zettl, F. Keilmann, P. Jarillo-Herrero, M. Fogler, and D. Basov, *Tunable phonon polaritons in atomically thin van der Waals crystals of boron nitride*, Science **343**, 6175, 1125–1129 (2014).

[68] J. D. Caldwell, A. V. Kretinin, Y. Chen, V. Giannini, M. M. Fogler, Y. Francescato, C. T. Ellis, J. G. Tischler, C. R. Woods, A. J. Giles, M. Hong, K. Watanabe, T. Tanuguchi, S. A. Maier, and K. S. Novoselov, *Sub-diffractional volume-confined polaritons in the natural hyperbolic material hexagonal boron nitride*, Nat. Commun. **5**, 1, 5221 (2014).

[69] T. T. Tran, K. Bray, M. J. Ford, M. Toth, and I. Aharonovich, *Quantum emission from hexagonal boron nitride monolayers*, Nat. Nanotechnol. **11**, 1, 37–41 (2016).

[70] T. T. Tran, C. Elbadawi, D. Totonjian, C. J. Lobo, G. Grosso, H. Moon, D. R. Englund, M. J. Ford, I. Aharonovich, and M. Toth, *Robust multicolor single photon emission from point defects in hexagonal boron nitride*, ACS Nano **10**, 8, 7331–7338 (2016).

[71] R. Bourrellier, S. Meuret, A. Tararan, O. Stéphan, M. Kociak, L. H. Tizei, and A. Zobelli, *Bright UV single photon emission at point defects in h-BN*, Nano Lett. **16**, 7, 4317–4321 (2016).

[72] T. Vogl, Y. Lu, and P. K. Lam, *Room temperature single photon source using fiber-integrated hexagonal boron nitride*, J. Phys. D: Appl. Phys. **50**, 29, 295101 (2017).

[73] C. Fournier, A. Plaud, S. Roux, A. Pierret, M. Rosticher, K. W. Watanabe, T. Taniguchi, S. Buil, X. Quélin, J. Barjon, J.-P. Hermier, and H. Delteil, *Position-controlled quantum emitters with reproducible emission wavelength in hexagonal boron nitride*, Nat. Commun. **12**, 1, 3779 (2021).

[74] G. Wang, Z. Dai, J. Xiao, S. Feng, C. Weng, L. Liu, Z. Xu, R. Huang, and Z. Zhang, *Bending of Multilayer van der Waals Materials*, Phys. Rev. Lett. **123**, 116101 (2019).

[75] C. Di Giorgio, E. Blundo, G. Pettinari, M. Felici, Y. Lu, A. M. Cucolo, A. Polimeni, and F. Bobba, *Nanoscale Measurements of Elastic Properties and Hydrostatic Pressure in H_2-Bulged MoS_2 Membranes*, Adv. Mater. Interfaces **7**, 2001024 (2020).

[76] C. Di Giorgio, E. Blundo, G. Pettinari, M. Felici, F. Bobba, and A. Polimeni, *Mechanical, Elastic, and Adhesive Properties of Two-Dimensional Materials: From Straining Techniques to State-of-the-Art Local Probe Measurements*, Adv. Mater. Interfaces **9**, 2102220 (2022).

[77] A. Branny, S. Kumar, R. Proux, and B. D. Gerardot, *Deterministic strain-induced arrays of quantum emitters in a two-dimensional semiconductor*, Nat. Commun. **8**, 15053 (2017).

[78] J. Feng, X. Qian, C.-W. Huang, and J. Li, *Strain-engineered artificial atom as a broad-spectrum solar energy funnel*, Nat. Photon. **6**, 866 (2012).

[79] P. K. Shandilya, J. E. Fröch, M. Mitchell, D. P. Lake, S. Kim, M. Toth, B. Behera, C. Healey, I. Aharonovich, and P. E. Barclay, *Hexagonal boron nitride cavity optomechanics*, Nano Lett. **19**, 2, 1343–1350 (2019).

[80] N. Mendelson, M. Doherty, M. Toth, I. Aharonovich, and T. T. Tran, *Strain-Induced Modification of the Optical Characteristics of Quantum Emitters in Hexagonal Boron Nitride*, Adv. Mat. **32**, 21, 1908316 (2020).

[81] J. Duan, R. Chen, J. Li, K. Jin, Z. Sun, and J. Chen, *Launching phonon polaritons by natural boron nitride wrinkles with modifiable dispersion by dielectric environments*, Adv. Mat. **29**, 38, 1702494 (2017).

[82] X. Fu, F. Li, J.-F. Lin, Y. Gong, X. Huang, Y. Huang, B. Han, Q. Zhou, and T. Cui, *Pressure-dependent light emission of charged and neutral excitons in monolayer $MoSe_2$*, J. Phys. Chem. Lett **8**, 3556 (2017).

[83] S. Xie, L. Tu, Y. Han, L. Huang, K. Kang, K. U. Lao, P. Poddar, C. Park, D. A. Muller, R. A. D. Jr., and J. Park, *Coherent and atomically thin transition-metal dichalcogenide superlattices with engineered strain*, Science **359**, 1131 (2018).

[84] H. Li, M. Du, M. J. Mleczko, A. L. Koh, Y. Nishi, E. Pop, A. J. Bard, and X. Zheng, *Kinetic Study of Hydrogen Evolution Reaction over Strained MoS_2 with Sulfur Vacancies Using Scanning Electrochemical Microscopy*, J. Am. Chem. Soc. **138**, 5123 (2016).

[85] Y. K. Ryu, F. Carrascoso, R. López-Nebreda, N. Agraït, R. Frisenda, and A. Castellanos-Gomez, *Microheater Actuators as a Versatile Platform for Strain Engineering in 2D Materials*, Nano Lett. **20**, 5339 (2020).

[86] W. Wu, J. Wang, P. Ercius, N. C. Wright, D. M. Leppert-Simenauer, R. A. Burke, M. Dubey, A. M. Dogare, and M. T. Pettes, *Giant Mechano-Optoelectronic Effect in an Atomically Thin Semiconductor*, Nano Lett. **18**, 2351 (2018).

[87] D. Lloyd, X. Liu, J. W. Christopher, L. Cantley, A. Wadehra, B. L. Kim, B. B. Goldberg, A. K. Swan, and J. S. Bunch, *Band gap engineering with ultralarge biaxial strains in suspended monolayer MoS_2*, Nano Lett. **16**, 5836 (2016).

[88] E. Blundo, M. Felici, T. Yildirim, G. Pettinari, D. Tedeschi, A. Miriametro, B. Liu, W. Ma, Y. Lu, and A. Polimeni, *Evidence of the direct-to-indirect band gap transition in strained two-dimensional WS_2 and MoS_2, and WSe_2*, Phys. Rev. Res. **2**, 012024 (2020).

[89] A. Castellanos-Gomez, R. Roldán, E. Cappelluti, M. Buscema, F. Guinea, H. S. J. van der Zant, and G. A. Steele, *Local strain engineering in atomically thin MoS_2*, Nano Lett. **13**, 5361 (2013).

[90] S. Mazzucato, D. Nardin, M. Capizzi, A. Polimeni, A. Frova, L. Seravalli, and S. Franchi, *Defect passivation in strain engineered InAs/(InGa)As quantum dots*, Mater. Sci. Eng. C **25**, 8, 830 (205).

[91] B. Li, C. Ji, W. Yang, J. Wang, K. Yang, R. Xu, W. Liu, Z. Cai, J. Chen, and H. kwang Mao, *Diamond anvil cell behavior up to 4 Mbar*, Proc. Natl. Acad. Sci. U. S. A. **115**, 1713 (2018).

[92] Y. S. Choi, T. Numata, T. Nishida, R. Harris, and S. E. Thompson, *Impact of mechanical stress on gate tunneling currents of germanium and silicon* p*-type metal-oxide-semiconductor field-effect transistors and metal gate work function*, J. Appl. Phys. **103**, 6, 064510 (2008).

[93] A. R. Goñi and K. Syassen, *Optical properties of semiconductors under pressure*, *Semiconductors and Semimetals*, vol. 54, p. 247, 1st edn., Academic Press, San Diego (1998).

[94] I. E. Itskevich, S. G. Lyapin, I. A. Troyan, P. C. Klipstein, L. Eaves, P. C. Main, and M. Henini, *Energy levels in self-assembled InAs/GaAs quantum dots above the pressure-induced* Γ*-X crossover*, Phys. Rev. B **58**, 8, R4250 (1998).

[95] G. Pettinari, A. Polimeni, F. Masia, R. Trotta, M. Felici, M. Capizzi, T. Niebling, W. Stolz, and P. J. Klar, *Electron Mass in Dilute Nitrides and its Anomalous Dependence on Hydrostatic Pressure*, Phys. Rev. Lett. **98**, 146402 (2007).

[96] X. Fu, C. Su, Q. Fu, X. Zhu, R. Zhu, C. Liu, Z. Liao, J. Xu, W. Guo, J. Feng, and D. Yu, *Tailoring Exciton Dynamics by Elastic Strain-Gradient in Semiconductors*, Adv. Mater. **26**, 16, 2572 (2014).

[97] J. C. Meyer, A. K. Geim, M. I. Katsnelson, K. S. Novoselov, T. J. Booth, and S. Roth, *The structure of suspended graphene sheets*, Nature **446**, 60 (2007).

[98] E. Stolyarova, K. T. Rim, S. Ryu, J. Maultzsch, P. Kim, L. E. Brus, T. F. Heinz, M. S. Hybertsen, and G. W. Flynn, *High-resolution scanning tunneling microscopy imaging of mesoscopic graphene sheets on an insulating surface*, Proc. Natl. Acad. Sci. U. S. A. **104**, 22, 9209 (2007).

[99] M. Ishigami, J. H. Chen, W. G. Cullen, M. S. Fuhrer, and E. D. Williams, *Atomic Structure of Graphene on* SiO_2, Nano Lett. **7**, 6, 1643 (2007).

[100] T. J. Booth, P. Blake, R. R. Nair, D. Jiang, E. W. Hill, U. Bangert, A. Bleloch, M. Gass, K. S. Novoselov, M. I. Katsnelson, and A. K. Geim, *Macroscopic Graphene Membranes and Their Extraordinary Stiffness*, Nano Lett. **8**, 8, 2442 (2008).

[101] K. R. Knox, S. Wang, A. Morgante, D. Cvetko, A. Locatelli, T. O. Mentes, M. A. Nino, P. Kim, and J. R. M. Osgood, *Spectromicroscopy of single and multilayer graphene supported by a weakly interacting substrate*, Phys. Rev. B **78**, 201408(R) (2008).

[102] U. Stoberl, U. Wurstbauer, W. Wegscheider, D. Weiss, and J. Eroms, *Morphology and flexibility of graphene and few-layer graphene on various substrates*, Appl. Phys. Lett. **93**, 051906 (2008).

[103] V. Geringer, M. Liebmann, T. Echtermeyer, S. Runte, M. Schmidt, R. Rückamp, M. C. Lemme, and M. Morgenstern, *Intrinsic and extrinsic corrugation of monolayer graphene deposited on* SiO_2, Phys. Rev. Lett. **102**, 076102 (2009).

[104] A. Fasolino, J. H. Los, and M. I. Katsnelson, *Intrinsic ripples in graphene*, Nat. Mater. **6**, 858 (2007).

[105] C. H. Lui, L. Liu, K. F. Mak, G. W. Flynn, and T. F. Heinz, *Ultraflat graphene*, Nature **462**, 339 (2009).

[106] W. Zhu, T. Low, V. Perebeinos, A. A. Bol, Y. Zhu, H. Yan, J. Tersoff, and P. Avouris, *Structure and Electronic Transport in Graphene Wrinkles*, Nano Lett. **12**, 3431 (2012).

[107] K. Kim, Z. Lee, B. D. Malone, K. T. Chan, B. Alemán, W. Regan, W. Gannett, M. F. Crommie, M. L. Cohen, and A. Zettl, *Multiply folded graphene*, Phys. Rev. B **83**, 245433 (2011).

[108] H. Hattab, A. T. N'Diaye, D. Wall, C. Klein, G. Jnawali, J. Coraux, C. Busse, R. van Gastel, B. Poelsema, T. Michely, F.-J. M. zu Heringdorf, and M. Horn-von Hoegen, *Interplay of Wrinkles, Strain, and Lattice Parameter in Graphene on Iridium*, Nano Lett. **12**, 2, 678 (2012).

[109] T. M. Paronyan, E. M. Pigos, G. Chen, and A. R. Harutyunyan, *Formation of Ripples in Graphene as a Result of Interfacial Instabilities*, ACS Nano **5**, 12, 9619 (2011).

[110] Y. Zhang, T. Gao, Y. Gao, S. Xie, Q. Ji, K. Yan, H. Peng, and Z. Liu, *Defect-like Structures of Graphene on Copper Foils for Strain Relief Investigated by High-Resolution Scanning Tunneling Microscopy*, ACS Nano **5**, 5, 4014 (2011).

[111] S. J. Chae, F. Güneş, K. K. Kim, E. S. Kim, G. H. Han, S. M. Kim, H.-J. Shin, S.-M. Yoon, J.-Y. Choi, M. H. Park, C. W. Yang, D. Pribat, and Y. H. Lee, *Synthesis of Large-Area Graphene Layers on Poly-Nickel Substrate by Chemical Vapor Deposition: Wrinkle Formation*, Adv. Mater. **21**, 22, 2328–2333 (2009).

[112] E. Khestanova, F. Guinea, L. Fumagalli, A. Geim, and I. Grigorieva, *Universal shape and pressure inside bubbles appearing in van der Waals heterostructures*, Nat. Commun. **7**, 12587 (2016).

[113] T. Georgiou, L. Britnell, P. Blake, R. Gorbachev, A. Gholinia, A. K. Geim, C. Casiraghi, and K. S. Novoselov, *Graphene bubbles with controllable curvature*, Appl. Phys. Lett. **99**, 093103 (2011).

[114] D. A. Sanchez, Z. Dai, P. Wang, A. Cantu-Chavez, C. J. Brennan, R. Huang, and N. Lu, *Mechanics of spontaneously formed nanoblisters trapped by transferred 2D crystals*, Proc. Natl. Acad. Sci. U. S. A. **115**, 31, 7884–7889 (2018).

[115] Z. Dai, Y. Hou, D. A. Sanchez, G. Wang, C. J. Brennan, Z. Zhang, L. Liu, and N. Lu, *Interface-Governed Deformation of Nanobubbles and Nanotents Formed by Two- Dimensional Materials*, Phys. Rev. Lett. **121**, 266101 (2018).

[116] E. Blundo, T. Yildirim, G. Pettinari, and A. Polimeni, *Experimental Adhesion Energy in van der Waals Crystals and Heterostructures from Atomically Thin Bubbles*, Phys. Rev. Lett. **127**, 4, 046101 (2021).

[117] A. V. Kretinin, Y. Cao, J. S. Tu, G. L. Yu, R. Jalil, K. S. Novoselov, S. J. Haigh, A. Gholinia, A. Mishchenko, M. Lozada-Hidalgo, T. Georgiou, C. R. Woods, F. Withers, P. Blake, G. Eda, A. Wirsig, C. Hucho, K. Watanabe, T. Taniguchi, A. K. Geim, and R. V. Gorbachev, *Electronic Properties of Graphene Encapsulated with Different Two-Dimensional Atomic Crystals*, Nano Lett. **14**, 6, 3270–3276 (2014).

[118] G. H. Ahn, M. Amani, H. Rasool, D.-H. Lien, J. P. Mastandrea, J. W. A. III, M. Dubey, D. C. Chrzan, A. M. Minor, and A. Javey, *Strain-engineered growth of two-dimensional materials*, Nat. Commun. **8**, 608 (2017).

[119] J. Choi, H. Kim, M. Wang, J. Leem, W. King, and S. Nam, *Three-dimensional integration of graphene via swelling, shrinking, and adaptation*, Nano Lett. **15**, 4525 (2015).

[120] S. Kumar, A. Kaczmarczyk, and B. D. Gerardot, *Strain-Induced Spatial and Spectral Isolation of Quantum Emitters in Mono- and Bilayer WSe_2*, Nano Lett. **15**, 7567 (2015).

[121] Y. Luo, G. D. Shepard, J. V. Ardelean, D. A. Rhodes, B. Kim, K. Barmak, J. C. Hone, and S. Strauf, *Deterministic coupling of site-controlled quantum emitters in monolayer WSe_2 to plasmonic nanocavities*, Nat. Nanotechnol. **13**, 1137 (2018).

[122] A. Reserbat-Plantey, D. Kalita, Z. Han, L. Ferlazzo, S. Autier-Laurent, K. Komatsu, C. Li, R. Weil, A. Ralko, L. Marty, S. Guéron, N. Bendiab, H. Bouchiat, and V. Bouchiat, *Strain Superlattices and Macroscale Suspension of Graphene Induced by Corrugated Substrates*, Nano Lett. **14**, 9, 5044–5051 (2014).

[123] J. Kern, I. Niehues, P. Tonndorf, R. Schmidt, D. Wigger, R. Schneider, T. Stiehm, S. M. de Vasconcellos, D. E. Reiter, T. Kuhn, and R. Bratschitsch, *Nanoscale Positioning of Single-Photon Emitters in Atomically Thin WSe_2*, Adv. Mater. **28**, 7101 (2016).

[124] T. Cai, S. Dutta, S. Aghaeimeibodi, Z. Yang, S. Nah, J. T. Fourkas, and E. Waks, *Coupling Emission from Single Localized Defects in Two-Dimensional Semiconductor to Surface Plasmon Polaritons*, Nano Lett. **17**, 11, 6564–6568 (2017).

[125] H. Li, A. W. Contryman, X. Qian, S. M. Ardakani, Y. Gong, X. Wang, J. M. Weisse, C. H. Lee, J. Zhao, P. M. Ajayan, J. Li, H. C. Manoharan, and X. Zheng, *Optoelectronic crystal of artificial atoms in strain-textured molybdenum disulphide*, Nat. Commun. **6**, 7381 (2015).

[126] J. J. Pankove and N. M. Johnson, *Hydrogen in Semiconductors, in Semiconductors and Semimetals vol. 34*, Academic Press, Boston (1991).

[127] J. I. Pankove, D. E. Carlson, J. E. Berkeyheiser, and R. O. Wance, *Neutralization of shallow acceptor levels in silicon by atomic hydrogen*, Phys. Rev. Lett. **51**, 2224 (1983).

[128] J. Chevallier, W. C. Dautremont-Smith, C. W. Tu, and S. J. Pearton, *Neutralization of shallow acceptor levels in silicon by atomic hydrogen*, Appl. Phys. Lett. **47**, 108 (1985).

[129] N. M. Johnson, C. Herring, and D. J. Chadi, *Interstitial hydrogen and neutralization of shallow-donor impurities in single-crystal silicon*, Phys. Rev. Lett. **56**, 769 (1986).

[130] J. E. Northrup, *Theory of intrinsic and H-passivated screw dislocations in GaN*, Phys. Rev. B **66**, 045204 (2002).

[131] M. Matsubara, J. Godet, and L. Pizzagalli, *Theoretical study of hydrogen stability and aggregation in dislocation cores in silicon*, Phys. Rev. B **82**, 024107 (2010).

[132] A. Polimeni, D. Marangio, M. Capizzi, A. Frova, and F. Martelli, *Giant photoluminescence enhancement in deuterated highly strained InAs/GaAs quantum wells*, Appl. Phys. Lett. **65**, 1254 (1994).

[133] J. Neugebauer and C. G. V. de Walle, *Role of hydrogen in doping of GaN*, Appl. Phys. Lett. **68**, 1829 (1993).

[134] C. G. V. d. W. J. Neugebauer, *Hydrogen in GaN: Novel Aspects of a Common Impurity*, Phys. Rev. Lett. **75**, 4452 (1995).

[135] S. Nakamura, N. Iwasa, M. Senoh, and T. Mukai, *Hole Compensation Mechanism of p-Type GaN Films*, Jpn. J. Appl. Phys. **31**, 1258 (1992).

[136] S. Nakamura, T. Mukai, M. Senoh, and N. Iwasa, *Thermal Annealing Effects on P-Type Mg-Doped GaN Films*, Jpn. J. Appl. Phys. **31**, L139 (1992).

[137] S. Mazzucato, D. Nardin, M. Capizzi, A. Polimeni, A. Frova, L. Seravalli, and S. Franchi, *Defect passivation in strain engineered InAs/(InGa)As quantum dots*, Mater. Sci. Eng. C **25**, 830 (2005).

[138] M. Felici, G. Pettinari, F. Biccari, M. Capizzi, and A. Polimeni, *Spatially selective hydrogen irradiation of dilute nitride semiconductors: a brief review*, Semicond. Sci. Technol. **33**, 053001 (2018).

[139] F. Biccari, A. Boschetti, G. Pettinari, F. L. China, M. Gurioli, F. Intonti, A. Vinattieri, M. S. Sharma, M. Capizzi, A. Gerardino, L. Businaro, M. Hopkinson, A. Polimeni, and M. Felici, *Site-Controlled Single-Photon Emitters Fabricated by Near-Field Illumination*, Adv. Mater. **30**, 1705450 (2018).

[140] G. Pettinari, F. Filippone, A. Polimeni, G. Mattioli, A. Patanè, V. Lebedev, M. Capizzi, and A. A. Bonapasta, *Genesis of "Solitary Cations" Induced by Atomic Hydrogen*, Adv. Funct. Mater. **25**, 5353 (2015).

[141] M. Seel and R. Pandey, *Proton and hydrogen transport through two-dimensional monolayers*, 2D Materials **3**, 025004 (2016).

[142] P. Z. Sun, Q. Yang, W. J. Kuang, Y. V. Stebunov, W. Q. Xiong, J. Yu, R. R. Nair, M. I. Katsnelson, S. J. Yuan, I. V. Grigorieva, M. Lozada-Hidalgo, F. C. Wang, and A. K. Geim, *Limits on gas impermeability of graphene*, Science **579**, 229 (2020).

[143] D. Lloyd, X. Liu, N. Boddeti, L. Cantley, R. Long, M. L. Dunn, and J. S. Bunch, *Adhesion, Stiffness, and Instability in Atomically Thin MoS_2 Bubbles*, Nano Lett. **17**, 5329 (2017).

[144] J. S. Bunch, S. S. Verbridge, J. S. Alden, A. M. van der Zande, J. M. Parpia, H. G. Craighead, and P. L. McEuen, *Impermeable atomic membranes from graphene sheets*, Nano Lett. **8**, 2458 (2008).

[145] G. Wang, Z. Dai, Y. Wang, P. Tan, L. Liu, Z. Xu, Y. Wei, R. Huang, and Z. Zhang, *Measuring Interlayer Shear Stress in Bilayer Graphene*, Phys. Rev. Lett. **119**, 036101 (2017).

[146] Q. Wu, Y. Wu, Y. Hao, J. Geng, M. Charlton, S. Chen, Y. Ren, H. Ji, H. Li, D. W. Boukhvalov, R. D. Piner, C. W. Bielawski, and R. S. Ruoff, *Selective surface functionalization at regions of high local curvature in graphene*, Chem. Commun. **49**, 677 (2013).

[147] M. A. Bissett, S. Konabe, S. Okada, M. Tsuji, and H. Ago, *Enhanced Chemical Reactivity of Graphene Induced by Mechanical Strain*, ACS Nano **7**, 10335 (2013).

[148] D. W. Boukhvalov and M. I. Katsnelson, *Enhancement of Chemical Activity in Corrugated Graphene*, J. Phys. Chem. C **113**, 14176 (2009).

[149] H. McKay, D. J. Wales, S. J. Jenkins, J. A. Verges, and P. L. de Andres, *Hydrogen on graphene under stress: Molecular dissociation and gap opening*, Phys. Rev. B **81**, 075425 (2010).

[150] M. Lozada-Hidalgo, S. Hu, O. Marshall, A. Mishchenko, A. N. Grigorenko, R. A. W. Dryfe, B. Radha, I. V. Grigorieva, and A. K. Geim, *Sieving hydrogen isotopes through two-dimensional crystals*, Science **351**, 68 (2016).

[151] S. Hu, M. Lozada-Hidalgo, F. C. Wang, A. Mishchenko, F. Schedin, R. R. Nair, E. W. Hill, D. W. Boukhvalov, M. I. Katsnelson, R. A. W. Dryfe, I. V. Grigorieva, H. A. Wu, and A. K. Geim, *Proton transport through one-atom-thick crystals*, Nature **516**, 227 (2014).

[152] L. Mogg, S. Zhang, G.-P. Hao, K. Gopinadhan, D. Barry, B. L. Liu, H. M. Cheng, A. K. Geim, and M. Lozada-Hidalgo, *Perfect proton selectivity in ion transport through two-dimensional crystals*, Nat. Commun. **10**, 4243 (2019).

[153] G.-Y. Zhao, H. Deng, N. Tyree, M. Guy, A. Lisfi, Q. Peng, J.-A. Yan, C. Wang, and Y. Lan, *Recent Progress on Irradiation-Induced Defect Engineering of Two-Dimensional 2H-MoS_2 Few Layers*, Appl. Sci. **9**, 678 (2019).

[154] J. Felton, E. Blundo, S. Ling, J. Glover, Z. R. Kudrynskyi, O. Makarovsky, Z. D. Kovalyuk, E. Besley, G. Walker, A. Polimeni, and A. Patanè, *The Interaction of Hydrogen with the van der Waals Crystal γ-InSe*, Molecules **25**, 2526 (2020).

[155] N. Bauer and J. Y. Beach, *Differences in Mass Spectra of H_2 and D_2*, J. Chem. Phys. **15**, 150 (1947).

[156] D. Tedeschi, E. Blundo, M. Felici, G. Pettinari, B. Liu, T. Yildrim, E. Petroni, C. Zhang, Y. Zhu, S. Sennato, Y. Lu, and A. Polimeni, *Controlled Micro/Nanodome Formation in Proton-Irradiated Bulk Transition-Metal Dichalcogenides*, Adv. Mater. **31**, 1903795 (2019).

[157] B. Liu, T. Yildirim, T. Lü, E. Blundo, L. Wang, L. Jiang, H. Zou, L. Zhang, H. Zhao, Z. Yin, F.-B. Tian, A. Polimeni, and Y. Lu, *Variant Plateau's Law in Atomically Thin Transition Metal Dichalcogenide Dome Networks*, Nat. Commun. (2023), in press.

[158] A. S. Friedman, D. White, and H. L. Johnston, *The direct determination of the critical temperature and critical pressure of normal deuterium. Vapor pressures between the boiling and critical points*, J. Am. Chem. Soc. **73**, 1310 (1951).

[159] H. J. Hoge and R. D. Arnold, *Vapor pressures of Hydrogen, Deuterium, and Hydrogen Deuteride and dew-point pressures of their mixtures*, J. Res. Natl. Inst. Stan. **47**, 67 (1951).

[160] T. Green and D. Britz, *Kinetics of the deuterium and hydrogen evolution reactions at palladium in alkaline solution*, J. Electroanal. Chem. **412**, 59 (1996).

[161] D. Stolten and B. Emonts, *Hydrogen Science and Engineering: Materials, Processes, Systems, and Technology*, Wiley-VHC, Weinheim, Germany, 2nd Volume Set (2016).

[162] C. H. Seager, *Hydrogen in Semiconductors*, Academic Press Limited, London, UK vol. 34, Ch. 2, pp. 17 (1991).

[163] A. D. Marwick, *Hydrogen in Semiconductors*, Academic Press Limited, London, UK vol. 34, Ch. 9, pp. 220 (1991).

[164] W. B. Fichter, *Some solutions for the large deflections of uniformly loaded circular membranes*, NASA Technical Paper **3658**, 1 (1997).

[165] T. F. Aslyamov, E. S. Iakovlev, I. S. Akhatov, and P. A. Zhilyaev, *Model of graphene nanobubble: Combining classical density functional and elasticity theories*, J. Chem. Phys. **152**, 054705 (2020).

[166] A. V. Tyurnina, D. A. Bandurin, E. Khestanova, V. G. Kravets, M. Koperski, F. Guinea, A. N. Grigorenko, A. K. Geim, and I. V. Grigorieva, *Strained bubbles in van der Waals heterostructures as local emitters of photoluminescence with adjustable wavelength*, ACS Photonics **6**, 516–524 (2019).

[167] Z. Jia, J. Dong, L. Liu, A. Nie, J. Xiang, B. Wang, F. Wen, C. Mu, Z. Zhao, B. Xu, Y. Gong, Y. Tian, and Z. Liu, *Photoluminescence and Raman spectra oscillations induced by laser interference in annealing created monolayer WS_2 bubbles*, Adv. Optical Mater. (2019).

[168] T. Taniguchi and K. Watanabe, *Synthesis of high-purity boron nitride single crystals under high pressure by using Ba–BN solvent*, J. Cryst. Growth **303**, 525 (2007).

[169] E. Blundo, A. Surrente, D. Spirito, G. Pettinari, T. Yildirim, C. A. Chavarin, L. Baldassarre, M. Felici, and A. Polimeni, *Vibrational properties in highly strained hexagonal boron nitride bubbles*, Nano Lett. **22**, 4, 1525 (2022).

[170] L. He, H. Wang, L. Chen, X. Wang, H. Xie, C. Jiang, C. Li, K. Elibol, J. Meyer, K. Watanabe, T. Taniguchi, Z. Wu, W. Wang, Z. Ni, X. Miao, C. Zhang, D. Zhang, H. Wang, and X. Xie, *Isolating hydrogen in hexagonal boron nitride bubbles by a plasma treatment*, Nat. Commun. **10**, 2851 (2019).

[171] E. Blundo, C. Di Giorgio, G. Pettinari, T. Yildirim, M. Felici, Y. Lu, F. Bobba, and A. Polimeni, *Engineered creation of periodic giant, non-uniform strains in MoS_2 monolayers*, Adv. Mater. Interfaces **7**, 2000621 (2020).

[172] N. Chejanovsky, M. Rezai, F. Paolucci, Y. Kim, T. Rendler, W. Rouabeh, F. Fávaro de Oliveira, P. Herlinger, A. Denisenko, S. Yang, I. Gerhardt, A. Finkler, J. H. Smet, and J. Wrachtrup, *Structural Attributes and Photodynamics of Visible Spectrum Quantum Emitters in Hexagonal Boron Nitride*, Nano Lett. **16**, 11, 7037–7045 (2016).

[173] S. Choi, T. Trong Tran, C. Elbadawi, C. Lobo, X. Wang, S. Juodkazis, G. Seniutinas, M. Toth, and I. Aharonovich, *Engineering and Localization of Quantum Emitters in Large Hexagonal Boron Nitride Layers*, ACS Appl. Mater. Interfaces **8**, 43, 29642–29648 (2016).

[174] J. Ziegler, R. Klaiss, A. Blaikie, D. Miller, V. R. Horowitz, and B. J. Alemán, *Deterministic Quantum Emitter Formation in Hexagonal Boron Nitride via Controlled Edge Creation*, Nano Lett. **19**, 3, 2121–2127 (2019).

[175] R. Gu, L. Wang, H. Zhu, S. Han, Y. Bai, X. Zhang, B. Li, C. Qin, J. Liu, G. Guo, X. Shan, G. Xiong, J. Gao, C. He, Z. Han, X. Liu, and F. Zhao, *Engineering and Microscopic Mechanism of Quantum Emitters Induced by Heavy Ions in hBN*, ACS Photonics **8**, 10, 2912–2922 (2021).

[176] M. Fischer, J. M. Caridad, A. Sajid, S. Ghaderzadeh, M. Ghorbani-Asl, L. Gammelgaard, P. Bøggild, K. S. Thygesen, A. V. Krasheninnikov, S. Xiao, M. Wubs, and N. Stenger, *Controlled generation of luminescent centers in hexagonal boron nitride by irradiation engineering*, Sci. Adv. **7**, 7, eabe7138 (2021).

[177] N. Mendelson, D. Chugh, J. R. Reimers, T. S. Cheng, A. Gottscholl, H. Long, C. J. Mellor, A. Zettl, V. Dyakonov, P. H. Beton, S. V. Novikov, C. Jagadish, H. H. Tan, M. J. Ford, M. Toth, C. Bradac, and I. Aharonovich, *Identifying carbon as the source of visible single-photon emission from hexagonal boron nitride*, Nat. Mater. **20**, 321–328 (2021).

[178] H. Zhang, M. Lan, G. Tang, F. Chen, Z. Shu, F. Chen, and M. Li, *Discrete color centers in two-dimensional hexagonal boron nitride induced by fast neutron irradiation*, J. Mater. Chem. C **7**, 12211–12216 (2019).

[179] M. G. Betti, E. Placidi, C. Izzo, E. Blundo, A. Polimeni, M. Sbroscia, J. Avila, P. Dudin, K. Hu, Y. Ito, D. Prezzi, M. Bonacci, E. Molinari, and C. Mariani,

Gap Opening in Double-Sided Highly Hydrogenated Free-Standing Graphene, Nano Lett. **22**, 2971 (2022).

[180] J. Felton, E. Blundo, Z. Kudrynskyi, S. Ling, J. Bradford, G. Pettinari, T. Cooper, M. Wadge, Z. Kovalyuk, A. Polimeni, P. Beton, D. Grant, G. Walker, and A. Patanè, *Hydrogen-Induced Conversion of SnS_2 into SnS or Sn: A Route to Create SnS_2/SnS Heterostructures*, Small **18**, 2202661 (2022).

[181] Y. Wu, Q. Ou, Y. Yin, Y. Li, W. Ma, W. Yu, G. Liu, X. Cui, X. Bao, J. Duan, G. Álvarez Pérez, Z. Dai, B. Shabbir, N. Medhekar, X. Li, C.-M. Li, P. Alonso-González, and Q. Bao, *Chemical switching of low-loss phonon polaritons in α-MoO_3 by hydrogen intercalation*, Nat. Commun. **11**, 2646 (2020).

[182] W. Ma, P. Alonso-González, S. Li, A. Y. Nikitin, J. Yuan, J. Martín-Sánchez, J. Taboada-Gutiérrez, I. Amenabar, P. Li, S. Vélez, C. Tollan, Z. Dai, Y. Zhang, S. Sriram, K. Kalantar-Zadeh, S.-T. Lee, R. Hillenbrand, and Q. Bao, *In-plane anisotropic and ultra-low-loss polaritons in a natural van der Waals crystal*, Nature **562**, 557 (2018).

[183] Z. Zheng, N. Xu, S. L. Oscurato, M. Tamagnone, F. Sun, Y. Jiang, Y. Ke, J. Chen, W. Huang, W. L. Wilson, A. Ambrosio, S. Deng, and H. Chen, *A mid-infrared biaxial hyperbolic van der Waals crystal*, Sci. Adv. **5**, eaav8690 (2019).

[184] J. O. Sofo, A. S. Chaudhari, and G. D. Barber, *Graphane: A two-dimensional hydrocarbon*, Phys. Rev. B **75**, 153401 (2007).

[185] P. Cudazzo, C. Attaccalite, I. V. Tokatly, and A. Rubio, *Strong Charge-Transfer Excitonic Effects and the Bose-Einstein Exciton Condensate in Graphane*, Phys. Rev. Lett. **104**, 226804 (2010).

[186] F. Zhao, Y. Raitses, X. Yang, A. Tan, and C. G. Tully, *High hydrogen coverage on graphene via low temperature plasma with applied magnetic field*, Carbon **177**, 244–251 (2021).

[187] I. Di Bernardo, G. Avvisati, C. Mariani, N. Motta, C. Chen, J. Avila, M. C. Asensio, S. Lupi, Y. Ito, M. Chen, T. Fujita, and M. G. Betti, *Two-Dimensional Hallmark of Highly Interconnected Three-Dimensional Nanoporous Graphene*, ACS Omega **2**, 7, 3691–3697 (2017).

[188] I. D. Bernardo, G. Avvisati, C. Chenc, J. Avila, M. C. Asensio, K. Hu, Y. Ito, P. Hines, J. Lipton-Duffin, L. Rintoul, N. Motta, C. Mariani, and M. G. Betti, *Topology and doping effects in three-dimensional nanoporous graphene*, Carbon **131**, 258 – 265 (2018).

[189] M. M. S. Abdelnabi, E. Blundo, M. G. Betti, G. Cavoto, E. Placidi, A. Polimeni, A. Ruocco, K. Hu, Y. Ito, and C. Mariani, *Towards free-standing*

graphane: atomic hydrogen and deuterium bonding to nanoporous graphene, Nanotechnology **32**, 035707 (2021).

[190] M. G. Betti, E. Blundo, M. De Luca, M. Felici, R. Frisenda, Y. Ito, S. Jeong, D. Marchiani, C. Mariani, A. Polimeni, M. Sbroscia, F. Trequattrini, and R. Trotta, *Homogeneous Spatial Distribution of Deuterium Chemisorbed on Free-Standing Graphene*, Nanomaterials **12**, 2613 (2022).

[191] X. Sha and B. Jackson, *First-principles study of the structural and energetic properties of H atoms on a graphite (0001) surface*, Surf. Sci. **496**, 3, 318 – 330 (2002).

[192] Y. Ito, Y. Tanabe, H.-J. Qiu, K. Sugawara, S. Heguri, N. H. Tu, and et al., *High-Quality Three-Dimensional Nanoporous Graphene*, Angewandte Chemie International Edition **53**, 19, 4822–4826 (2014).

[193] Y. Tanabe, Y. Ito, K. Sugawara, D. Hojo, M. Koshino, T. Fujita, and et al., *Electric Properties of Dirac Fermions Captured into 3D Nanoporous Graphene Networks*, Adv. Mater. **28**, 46, 10304–10310 (2016).

[194] Y. Tanabe, Y. Ito, K. Sugawara, M. Koshino, S. Kimura, T. Naito, I. Johnson, T. Takahashi, and M. Chen, *Dirac Fermion Kinetics in 3D Curved Graphene*, Adv. Mater. **32**, 48, 2005838 (2020).

[195] J. M. Skelton, L. A. Burton, F. Oba, and A. Walsh, *Chemical and Lattice Stability of the Tin Sulfides*, J. Phys. Chem. C **121**, 6446 (2017).

[196] J. M. Gonzalez and I. I. Oleynik, *Layer-dependent properties of SnS_2 and $SnSe_2$ two-dimensional materials*, Phys. Rev. B **94**, 125443 (2016).

[197] T. Sriv, K. Kim, and H. Cheong, *Low-Frequency Raman Spectroscopy of Few-Layer 2H-SnS_2*, Sci. Rep. **8**, 10194 (2018).

[198] S. R. Damkale, S. S. Arbuj, G. G. Umarji, R. P. Panmand, S. K. Khore, R. S. Sonawane, S. B. Ranea, and B. B. Kale, *Two-dimensional hexagonal SnS_2 nanostructures for photocatalytic hydrogen generation and dye degradation*, Sustainable Energy Fuels **3**, 3406 (2019).

[199] B. Sainbileg, Y.-R. Lai, L.-C. Chen, and M. Hayashi, *The dual-defective SnS_2 monolayers: promising 2D photocatalysts for overall water splitting*, Phys. Chem. Chem. Phys. **21**, 26292 (2019).

[200] S. A. Patil, H. T. Bui, S. Hussain, I. Rabani, Y. Seo, J. Jung, N. K. Shrestha, H. Kim, and H. Im, *Self-standing SnS nanosheet array: a bifunctional binder-free thin film catalyst for electrochemical hydrogen generation and wastewater treatment*, Dalton Transactions **50**, 12723 (2021).

[201] O. O. Balyts'kyi, *Influence of hydrogenation on properties of layered crystals of gallium and indium monoselenides*, Mater. Sci. **46**, 473 (2011).

[202] J. S. O. Evans, T. A. Mary, T. Vogt, M. A. Subramanian, and A. W. Sleight, *Negative Thermal Expansion in ZrW_2O_8 and HfW_2O_8*, Chem. Mater. **8**, 12, 2809–2823 (1996).

[203] K. Wang and R. R. Reeber, *Mode Grüneisen parameters and negative thermal expansion of cubic ZrW_2O_8 and $ZrMo_2O_8$*, Appl. Phys. Lett. **76**, 16, 2203–2204 (2000).

[204] V. Gava, A. L. Martinotto, and C. A. Perottoni, *First-Principles Mode Gruneisen Parameters and Negative Thermal Expansion in $\alpha-\mathrm{ZrW_2O_8}$*, Phys. Rev. Lett. **109**, 195503 (2012).

[205] N. Mounet and N. Marzari, *First-principles determination of the structural, vibrational and thermodynamic properties of diamond, graphite, and derivatives*, Phys. Rev. B **71**, 205214 (2005).

[206] L. M. Malard, M. A. Pimenta, G. Dresselhaus, and M. S. Dresselhaus, *Raman spectroscopy in graphene*, Phys. Rep. **473**, 51 (2009).

[207] N. Ferralis, *Probing mechanical properties of graphene with Raman spectroscopy*, J. Mater. Sci. **45**, 5135 (2010).

[208] A. Molina-Sánchez, K. Hummer, and L. Wirtz, *Vibrational and optical properties of MoS2: From monolayer to bulk*, Surf. Sci. Rep. **70**, 4, 554 – 586 (2015).

[209] X. Zhang, X.-F. Qiao, W. Shi, J.-B. Wu, D.-S. Jiang, and P.-H. Tan, *Phonon and Raman scattering of two-dimensional transition metal dicalchogenides from monolayer, multilayer to bulk material*, Chem. Soc. Rev. **44**, 2757–2785 (2015).

[210] C. Si, Z. Sun, and F. Liu, *Strain engineering of graphene: a review*, Nanoscale **8**, 3207–3217 (2016).

[211] R. Loudon, *The Raman effect in crystals*, Advances in Physics **50**, 813–864 (2001).

[212] C.-H. Chang, X. Fan, S.-H. Lin, and J.-L. Kuo, *Orbital analysis of electronic structure and phonon dispersion in MoS_2, $MoSe_2$, WS_2, and WSe_2 monolayers under strain*, Phys. Rev. B **88**, 195420 (2013).

[213] S. Horzum, H. Sahin, S. Cahangirov, P. Cudazzo, A. Rubio, T. Serin, and F. M. Peeters, *Phonon softening and direct to indirect band gap crossover in strained single-layer $MoSe_2$*, Phys. Rev. B **87**, 125415 (2013).

[214] E. Scalise, M. Houssa, G. Pourtois, V. Afanasèv, V. Afanasév, and A. Stesmans, *First-principles study of strained 2D MoS_2*, Physica E: Low-dimensional Systems and Nanostructures **56**, 416 – 421 (2014).

[215] J.-U. Lee, S. Woo, J. Park, H. C. Park, Y.-W. Son, and H. Cheong, *Strain-shear coupling in bilayer MoS_2*, Nat. Comm. **8**, 1370 (2017).

[216] Z. Jia, J. Dong, L. Liu, A. Nie, J. Xiang, B. Wang, F. Wen, C. Mu, Z. Zhao, B. Xu, Y. Gong, Y. Tian, and Z. Liu, *Photoluminescence and Raman Spectra Oscillations Induced by Laser Interference in Annealing-Created Monolayer WS_2 Bubbles*, Adv. Opt. Mater. **7**, 1801373 (2019).

[217] P. Wang, W. Gao, Z. Cao, K. M. Liechti, and R. Huang, *Numerical analysis of circular graphene bubbles*, J. Appl. Mech. **80**, 040905 (2013).

[218] F. Huth, A. Govyadinov, S. Amarie, W. Nuansing, F. Keilmann, and R. Hillenbrand, *Nano-FTIR absorption spectroscopy of molecular fingerprints at 20 nm spatial resolution*, Nano Lett. **12**, 8, 3973–3978 (2012).

[219] S. Mastel, A. A. Govyadinov, T. V. de Oliveira, I. Amenabar, and R. Hillenbrand, *Nanoscale-resolved chemical identification of thin organic films using infrared near-field spectroscopy and standard Fourier transform infrared references*, Appl. Phys. Lett. **106**, 2, 023113 (2015).

[220] J. Duan, R. Chen, J. Li, K. Jin, Z. Sun, and J. Chen, *Launching phonon polaritons by natural boron nitride wrinkles with modifiable dispersion by dielectric environments*, Adv. Mat. **29**, 38, 1702494 (2017).

[221] Z. Shi, H. A. Bechtel, S. Berweger, Y. Sun, B. Zeng, C. Jin, H. Chang, M. C. Martin, M. B. Raschke, and F. Wang, *Amplitude- and phase-resolved nanospectral imaging of phonon polaritons in hexagonal boron nitride*, ACS Photonics **2**, 7, 790–796 (2015).

[222] P. Li, M. Lewin, A. V. Kretinin, J. D. Caldwell, K. S. Novoselov, T. Taniguchi, K. Watanabe, F. Gaussmann, and T. Taubner, *Hyperbolic phonon-polaritons in boron nitride for near-field optical imaging and focusing*, Nat. Commun. **6**, 1, 7507 (2015).

[223] S. L. Moore, C. J. Ciccarino, D. Halbertal, L. J. McGilly, N. R. Finney, K. Yao, Y. Shao, G. Ni, A. Sternbach, E. J. Telford, B. S. Kim, S. E. Rossi, K. Watanabe, T. Taniguchi, A. N. Pasupathy, C. R. Dean, J. Hone, P. J. Schuck, P. Narang, and D. N. Basov, *Nanoscale lattice dynamics in hexagonal boron nitride moiré superlattices*, Nat. Commun. **12**, 5741 (2021).

[224] J. Qian, Y. Luan, M. Kim, K.-M. Ho, Y. Shi, C.-Z. Wang, Y. Li, and Z. Fei, *Nonequilibrium phonon tuning and mapping in few-layer graphene with infrared nanoscopy*, Phys. Rev. B **103**, L201407 (2021).

[225] P. Schmidt, F. Vialla, S. Latini, M. Massicotte, K.-J. Tielrooij, S. Mastel, G. Navickaite, M. Danovich, D. A. Ruiz-Tijerina, C. Yelgel, V. Fal'ko, K. S. Thygesen, R. Hillenbrand, and F. H. L. Koppens, *Nano-imaging of intersubband transitions in van der Waals quantum wells*, Nat. Nanotech. **13**, 1035 (2018).

[226] R. Geick and C. H. Perry, *Normal Modes in Hexagonal Boron Nitride*, Phys. Rev. **146**, 2, 533–547 (1966).

[227] R. V. Gorbachev, I. Riaz, R. R. Nair, R. Jalil, L. Britnell, B. D. Belle, E. W. Hill, K. S. Novoselo, K. Watanabe, T. Taniguchi, A. K. Geim, and B. Peter, *Hunting for Monolayer Boron Nitride: Optical and Raman Signatures*, Small **7**, 4, 465–468 (2011).

[228] Q. Cai, D. Scullion, A. Falin, K. Watanabe, T. Taniguchi, Y. Chen, E. J. G. Santos, and L. H. Li, *Raman signature and phonon dispersion of atomically thin boron nitride*, Nanoscale **9**, 3059 (2017).

[229] M. Krecmarova, D. Andres-Penares, L. Fekete, P. Ashcheulov, A. Molina-Sánchez, R. Canet-Albiach, I. Gregora, V. Mortet, J. P. Martínez-Pastor, and J. F. Sánchez-Royo, *Optical Contrast and Raman Spectroscopy Techniques Applied to Few-Layer 2D Hexagonal Boron Nitride*, Nanomaterials **9**, 9, 1047 (2019).

[230] C. Androulidakis, E. N. Koukaras, M. Poss, K. Papageslis, C. Galiotis, and S. Tawfick, *Strained hexagonal boron nitride: Phonon shift and Grüneisen parameter*, Phys. Rev. B **97**, 241414(R) (2018).

[231] M. Taillefumier, V. K. Dugaev, B. Canals, C. Lacroix, and P. Bruno, *Chiral two-dimensional electron gas in a periodic magnetic field: Persistent current and quantized anomalous Hall effect*, Phys. Rev. B **78**, 155330 (2008).

[232] Y. Wang, C. Cong, C. Qiu, and T. Yu, *Raman Spectroscopy Study of Lattice Vibration and Crystallographic Orientation of Monolayer MoS_2 under Uniaxial Strain*, Small **9**, 2857 (2013).

[233] C. Rice, R. J. Young, R. Zan, U. Bangert, D. Wolverson, T. Georgiou, R. Jalil, and K. S. Novoselov, *Raman-scattering measurements and first-principles calculations of strain-induced phonon shifts in monolayer MoS_2*, Phys. Rev. B **87**, 081307(R) (2013).

[234] C. Martella, C. Mennucci, E. Cinquanta, A. Lamperti, E. Cappelluti, F. B. de Mongeot, and A. Molle, *Anisotropic MoS_2 Nanosheets Grown on Self-Organized Nanopatterned Substrates*, Adv. Mater. **29**, 1605785 (2017).

[235] K. He, C. Poole, K. F. Mak, and J. Shan, *Experimental Demonstration of Continuous Electronic Structure Tuning via Strain in Atomically Thin MoS_2*, Nano Lett. **13**, 2931 (2013).

[236] E. del Corro, L. Kavan, M. Kalbac, and O. Frank, *Strain Assessment in Graphene Through the Raman 2D′ Mode*, J. Phys. Chem. C **119**, 25651 (2015).

[237] T. M. G. Mohiuddin, A. Lombardo, R. R. Nair, A. Bonetti, G. Savini, R. Jalil, N. Bonini, D. M. Basko, C. Galiotis, N. Marzari, K. S. Novoselov, A. K. Geim, and A. C. Ferrari, *Uniaxial strain in graphene by Raman spectroscopy: G peak splitting, Grüneisen parameters, and sample orientation*, Phys. Rev. B **79**, 205433 (2009).

[238] S. Pak, J. Lee, Y.-W. Lee, A.-R. Jang, S. Ahn, K. Y. Ma, Y. Cho, J. Hong, S. Lee, H. Y. Jeong, H. Im, H. S. S. S. Shin, S. M. Morris, S. Cha, J. I. Sohn, and J. M. Kim, *Strain-Mediated Interlayer Coupling Effects on the Excitonic Behaviors in an Epitaxially Grown MoS_2/WS_2 van der Waals Heterobilayer*, Nano Lett. **17**, 5634 (2017).

[239] X. He, H. Li, Z. Zhu, Z. Dai, Y. Yang, P. Yang, Q. Zhang, P. Li, U. Schwingenschlögl, and X. Zhang, *Strain engineering in monolayer WS_2, MoS_2, and the WS_2/MoS_2 heterostructure*, Appl. Phys. Lett. **109**, 173105 (2016).

[240] I. Niehues, R. Schmidt, M. Drüppel, P. Marauhn, D. Christiansen, M. Selig, G. Berghäuser, D. Wigger, R. Schneider, L. Braasch, R. Koch, A. Castellanos-Gomez, T. Kuhn, A. Knorr, E. Malic, M. Rohlfing, S. M. de Vasconcellos, and R. Bratschitsch, *Strain Control of Exciton–Phonon Coupling in Atomically Thin Semiconductors*, Nano Lett. **18**, 1751 (2018).

[241] C. R. Zhu, G. Wang, B. L. Liu, X. Marie, X. F. Qiao, X. Zhang, X. X. Wu, H. Fan, P. H. Tan, T. Amand, and B. Urbaszek, *Strain tuning of optical emission energy and polarization in monolayer and bilayer MoS_2*, Phys. Rev. B **13**, 121301 (2013).

[242] S. B. Desai, G. Seol, J. S. Kang, H. Fang, C. Battaglia, R. Kapadia, J. W. Ager, J. Guo, and A. Javey, *Strain-induced indirect to direct Bandgap transition in multilayer WSe_2*, Nano Lett. **14**, 4592 (2014).

[243] H. J. Conley, B. Wang, J. I. Ziegler, R. F. Haglund Jr., S. T. Pantelides, and K. I. Bolotin, *Bandgap engineering of strained monolayer and bilayer MoS_2*, Nano Lett. **13**, 3626 (2013).

[244] A. P. John, A. Thenapparambil, and M. Thalakulam, *Strain-engineering the Schottky barrier and electrical transport on MoS_2* , Nanotechnology **31**, 275703 (2020).

[245] J.-U. Lee, S. Woo, J. Park, H. C. Park, Y.-W. Son, and H. Cheong, *Strain-shear coupling in bilayer MoS_2*, Nat. Commun. **8**, 1370 (2017).

[246] Z. Li, Y. Lv, L. Ren, J. Li, L. Kong, Y. Zeng, Q. Tao, R. Wu, H. Ma, B. Zhao, D. Wang, W. Dang, K. Chen, L. Liao, X. Duan, X. Duan, and Y. Liu, *Efficient*

strain modulation of 2D materials via polymer encapsulation, Nat. Commun. **11**, 1151 (2020).

[247] Y. Liu, X. Li, Y. Guo, T. Yang, K. Chen, C. Lin, J. Wei, Q. Liu, Y. Lu, L. Dong, and C. Shan, *Modulation on the electronic properties and band gap of layered $ReSe_2$ via strain engineering*, J. Alloys Compd. **827**, 154364 (2020).

[248] Y. Li, T. Wang, M. Wu, T. Cao, Y. Chen, R. Sankar, R. K. Ulaganathan, F. Chou, C. Wetzel, C.-Y. Xu, S. G. Louie, and S.-F. Shi, *Ultrasensitive tunability of the direct bandgap of 2D InSe flakes via strain engineering*, 2D Materials **5**, 2, 021002 (2018).

[249] C. Song, F. Fan, N. Xuan, S. Huang, G. Zhang, C. Wang, Z. Sun, H. Wu, and H. Yan, *Largely Tunable Band Structures of Few-Layer InSe by Uniaxial Strain*, ACS Appl. Mater. Interfaces **10**, 3994 (2018).

[250] C. Song, F. Fan, N. Xuan, S. Huang, C. Wang, G. Zhang, F. Wang, Q. Xing, Y. Lei, Z. Sun, H. Wu, and H. Yan, *Drastic enhancement of the Raman intensity in few-layer InSe by uniaxial strain*, Phys. Rev. B **99**, 195414 (2019).

[251] J. Zhou, Y. Wu, H. Wang, Z. Wu, X. Li, W. Yang, C. Ke, S. Lu, C. Zhang, and J. Kang, *Strain manipulation of the polarized optical response in two-dimensional GaSe layers*, Nanoscale **12**, 4069–4076 (2020).

[252] Z. Zhang, L. Li, J. Horng, N. Z. Wang, F. Yang, Y. Yu, Y. Zhang, G. Chen, K. Watanabe, T. Taniguchi, X. H. Chen, F. Wang, and Y. Zhang, *Strain-Modulated Bandgap and Piezo-Resistive Effect in Black Phosphorus Field-Effect Transistors*, Nano Lett. **17**, 6097 (2017).

[253] Y. Li, Z. Hu, S. Lin, S. K. Lai, W. Ji, and S. P. Lau, *Giant Anisotropic Raman Response of Encapsulated Ultrathin Black Phosphorus by Uniaxial Strain*, Adv. Funct. Mater. **27**, 1600986 (2017).

[254] G. Zhang, S. Huang, A. Chaves, C. Song, V. O. Özcelik, T. Low, and H. Yan, *Infrared fingerprints of few-layer black phosphorus*, Nat. Commun. **8**, 14701 (2017).

[255] J. Quereda, P. San-Jose, V. Parente, L. Vaquero-Garzon, A. J. Molina-Mendoza, N. Agraït, G. Rubio-Bollinger, F. Guinea, R. Roldán, and A. Castellanos-Gomez, *Strong Modulation of Optical Properties in Black Phosphorus through Strain-Engineered Rippling*, Nano Lett. **16**, 5, 2931–2937 (2016).

[256] Z. Liu, M. Amani, S. Najmaei, Q. Xu, X. Zou, W. Zhou, T. Yu, C. Qiu, A. G. Birdwell, F. J. Crowne, R. Vajtai, B. I. Yakobson, Z. Xia, M. Dubey, P. M. Ajayan, and J. Lou, *Strain and structure heterogeneity in WS_2 atomic layers grown by chemical vapour deposition*, Nat. Commun. **5**, 5246 (2014).

[257] Q. Zhang, Z. Chang, G. Xu, Z. Wang, Y. Zhang, Z.-Q. Xu, S. Chen, Q. Bao, J. Z. Liu, Y.-W. Mai, W. Duan, M. S. Fuhrer, and C. Zheng, *Strain Relaxation of Monolayer WS_2 on Plastic Substrate*, Adv. Funct. Mater. **26**, 8707 (2016).

[258] T. Jiang, R. Huang, and Y. Zhu, *Interfacial Sliding and Buckling of Monolayer Graphene on a Stretchable Substrate*, Adv. Funct. Mater. **24**, 396 (2014).

[259] F. Ding, H. Ji, Y. Chen, A. Herklotz, K. Dörr, Y. Mei, A. Rastelli, and O. G. Schmidt, *Stretchable Graphene: A Close Look at Fundamental Parameters through Biaxial Straining*, Nano Lett. **10**, 3453 (2010).

[260] B. Liu, Q. Liao, X. Zhang, J. Du, Y. Ou, J. Xiao, Z. Kang, Z. Zhang, and Y. Zhang, *Strain-Engineered van der Waals Interfaces of Mixed-Dimensional Heterostructure Arrays*, ACS Nano **13**, 9057 (2019).

[261] H. Li, C. Tsai, A. L. Koh, L. Cai, A. W. Contryman, A. H. Fragapane, J. Zhao, H. S. Han, H. C. Manoharan, F. Abild-Pedersen, J. K. Nørskov, and X. Zheng, *Activating and optimizing MoS_2 basal planes for hydrogen evolution through the formation of strained sulphur vacancies*, Nat. Mater. **15**, 48 (2016).

[262] J. Chaste, A. Missaoui, S. Huang, H. Henck, Z. B. Aziza, L. Ferlazzo, C. Naylor, A. Balan, J. Alan T. Charlie Johnson, R. Braive, and A. Ouerghi, *Intrinsic Properties of Suspended MoS_2 on SiO_2/Si Pillar Arrays for Nanomechanics and Optics*, ACS Nano **12**, 3235 (2018).

[263] Y. Y. Hui, X. Liu, W. Jie, N. Y. Chan, J. Hao, Y.-T. Hsu, L.-J. Li, W. Guo, and S. P. Lau, *Exceptional Tunability of Band Energy in a Compressively Strained Trilayer MoS_2 Sheet*, ACS Nano **7**, 7126 (2013).

[264] Q. Zhao, T. Wang, R. Frisenda, and A. Castellanos-Gomez, *Giant Piezoresistive Effect and Strong Bandgap Tunability in Ultrathin InSe upon Biaxial Strain*, Adv. Science **7**, 20, 2001645 (2020).

[265] S. Huang, G. Zhang, F. Fan, C. Song, F. Wang, Q. Xing, C. Wang, H. Wu, and H. Yan, *Strain-tunable van der Waals interactions in few-layer black phosphorus*, Nat. Commun. **10**, 2447 (2019).

[266] C. Lee, X. Wei, J. W. Kysar, and J. Hone, *Measurement of the Elastic Properties and Intrinsic Strength of Monolayer Graphene*, Science **321**, 385 (2008).

[267] H. Moon, G. Grosso, C. Chakraborty, C. Peng, T. Taniguchi, K. Watanabe, and D. Englund, *Dynamic Exciton Funneling by Local Strain Control in a Monolayer Semiconductor*, Nano Lett. **20**, 6791 (2020).

[268] Y. Sun, J. Pan, Z. Zhang, K. Zhang, J. Liang, W. Wang, Z. Yuan, Y. Hao, B. Wang, J. Wang, Y. Wu, J. Zheng, L. Jiao, S. Zhou, K. Liu, C. Cheng, W. Duan, Y. Xu, Q. Yan, and K. Liu, *Elastic Properties and Fracture Behaviors of Biaxially Deformed, Polymorphic $MoTe_2$* , Nano Lett. **19**, 761 (2019).

[269] J. Tao, W. Shen, S. Wu, L. Liu, Z. Feng, C. Wang, C. Hu, P. Yao, H. Zhang, W. Pang, X. Duan, J. Liu, C. Zhou, and D. Zhang, *Mechanical and Electrical Anisotropy of Few-Layer Black Phosphorus*, ACS Nano **11**, 11362 (2015).

[270] H. Yan, C. Vajner, M. Kuhlman, L. Guo, L. Li, P. T. Araujo, and H.-T. Wang, *Elastic behavior of Bi_2Se_3 2D nanosheets grown by van der Waals epitaxy*, Appl. Phys. Lett. **109**, 032103 (2016).

[271] L. Guo, H. Yan, Q. Moore, M. Buettner, J. Song, L. Li, P. T. Araujobe, and H.-T. Wang, *Elastic properties of van der Waals epitaxy grown bismuth telluride 2D nanosheets*, Nanoscale **7**, 11915 (2015).

[272] H. Luo, X. Li, Y. Zhao, R. Yang, L. Bao, Y. Hao, Y.-n. Gao, N. N. Shi, Y. Guo, G. Liu, L. Zhao, Q. Wang, Z. Zhang, G. Zhang, J. Sun, Y. Huang, H. Gao, and X. Zhou, *Simultaneous generation of direct- and indirect-gap photoluminescence in multilayer* MoS_2 *bubbles*, Physical Review Materials **4**, 7, 074006 (2020).

[273] Y. Cao, V. Fatemi, S. Fang, K. Watanabe, T. Taniguchi, E. Kaxiras, and P. Jarillo-Herrero, *Unconventional superconductivity in magic-angle graphene superlattices*, Nature **556**, 43 (2018).

[274] K. L. Seyler, P. Rivera, H. Yu, N. P. Wilson, E. L. Ray, D. G. Mandrus, J. Yan, W. Yao, and X. Xu, *Signatures of moiré-trapped valley excitons in $MoSe_2/WSe_2$ heterobilayers*, Nature **567**, 66 (2019).

[275] K. Tran, G. Moody, F. Wu, X. Lu, J. Choi, K. Kim, A. Rai, D. A. Sanchez, J. Quan, A. Singh, J. Embley, A. Zepeda, M. Campbell, T. Autry, T. Taniguchi, K. Watanabe, N. Lu, S. K. Banerjee, K. L. Silverman, S. Kim, E. Tutuc, L. Yang, A. H. MacDonald, and X. Li, *Evidence for moiré excitons in van der Waals heterostructures*, Nature **567**, 71 (2019).

[276] C. Jin, E. C. Regan, A. Yan, M. I. B. Utama, D. Wang, S. Zhao, Y. Qin, S. Yang, Z. Zheng, S. Shi, K. Watanabe, T. Taniguchi, S. Tongay, A. Zettl, and F. Wang, *Observation of moiré excitons in WSe_2/WS_2 heterostructure superlattices*, Nature **567**, 76 (2019).

[277] E. M. Alexeev, D. A. Ruiz-Tijerina, M. Danovich, M. J. Hamer, D. J. Terry, P. K. Nayak, S. Ahn, S. Pak, J. Lee, J. I. Sohn, M. R. Molas, M. Koperski, K. Watanabe, T. Taniguchi, K. S. Novoselov, R. V. Gorbachev, H. S. Shin, V. I. Fal'ko, and A. I. Tartakovskii, *Resonantly hybridized excitons in moiré superlattices in van der Waals heterostructures*, Nature **567**, 81 (2019).

[278] N. Zhang, A. Surrente, M. Baranowski, D. K. Maude, P. Gant, A. Castellanos-Gomez, and P. Plochocka, *Moiré Intralayer Excitons in a $MoSe_2/MoS_2$ Heterostructure*, Nano Lett. **18**, 7651 (2018).

[279] H. Chen, X. Wen, J. Zhang, T. Wu, Y. Gong, X. Zhang, J. Yuan, C. Yi, J. Lou, P. M. Ajayan, W. Zhuang, G. Zhang, and J. Zheng, *Ultrafast formation of interlayer hot excitons in atomically thin MoS_2/WS_2 heterostructure*, Nat. Comm. **7**, 12512 (2016).

[280] L. Britnell, R. V. Gorbachev, R. Jalil, B. D. Belle, F. Schedin, A. Mishchenko, T. Georgiou, M. I. Katsnelson, L. Eaves, S. V. Morozov, N. M. Peres, J. Leist, A. K. Geim, K. S. Novoselov, and L. A. Ponomarenko, *Field-effect tunneling transistor based on vertical graphene heterostructures*, Science **335**, 947–950 (2012).

[281] T. Georgiou, R. Jalil, B. D. Belle, L. Britnell, R. V. Gorbachev, S. V. Morozov, Y.-J. Kim, A. Gholinia, S. J. Haigh, O. Makarovsky, L. Eaves, L. A. Ponomarenko, A. K. Geim, K. S. Novoselov, and A. Mishchenko, *Vertical field-effect transistor based on graphene–WS_2 heterostructures for flexible and transparent electronics*, Nat. Nanotech. **8**, 100 (2013).

[282] L. Britnell, R. V. Gorbachev, R. Jalil, B. D. Belle, F. Schedin, M. I. Katsnelson, L. Eaves, S. V. Morozov, A. S. Mayorov, N. M. R. Peres, A. H. C. Neto, J. Leist, A. K. Geim, L. A. Ponomarenko, and K. S. Novoselov, *Electron Tunneling through Ultrathin Boron Nitride Crystalline Barriers*, Nano Lett. **12**, 1707–1710 (2012).

[283] A. Pospischil, M. M. Furchi, and T. Mueller, *Solar-energy conversion and light emission in an atomic monolayer p–n diode*, Nat. Nanotech. **9**, 257 (2014).

[284] B. W. Baugher, H. O. Churchill, Y. Yang, and P. Jarillo-Herrero, *Optoelectronic devices based on electrically tunable p–n diodes in a monolayer dichalcogenide*, Nat. Nanotech. **9**, 262 (2014).

[285] J. S. Ross, P. Klement, A. M. Jones, N. J. Ghimire, J. Yan, D. G. Mandrus, T. Taniguchi, K. Watanabe, K. Kitamura, W. Yao, D. H. Cobden, and X. Xu, *Electrically tunable excitonic light-emitting diodes based on monolayer WSe_2 p–n junctions*, Nat. Nanotech. **9**, 268 (2014).

[286] T. Björkman, A. Gulans, A. V. Krasheninnikov, and R. M. Nieminen, *van der Waals bonding in layered compounds from advanced density-functional first-principles calculations*, Phys. Rev. Lett. **108**, 235502 (2012).

[287] A. Castellanos-Gomez, R. van Leeuwen, M. Buscema, Herre, S. J. van der Zant, G. A. Steele, and W. J. Venstra, *Single-Layer MoS_2 Mechanical Resonators*, Adv. Mater. **25**, 6719–6723 (2013).

[288] G.-H. Lee, R. C. Cooper, S. J. An, S. Lee, A. van der Zande, N. Petrone, A. G. Hammerberg, C. Lee, B. Crawford, W. Oliver, J. W. Kysar, and J. Hone, *High-Strength Chemical-Vapor-Deposited Graphene and Grain Boundaries*, Science **340**, 6136, 1073–1076 (2013).

[289] Q.-Y. Lin, G. Jing, Y.-B. Zhou, Y.-F. Wang, J. Meng, Y.-Q. Bie, D.-P. Yu, and Z.-M. Liao, *Stretch-Induced Stiffness Enhancement of Graphene Grown by Chemical Vapor Deposition*, ACS Nano **7**, 2, 1171–1177 (2013).

[290] C. S. Ruiz-Vargas, H. L. Zhuang, P. Y. Huang, A. M. van der Zande, S. Garg, P. L. McEuen, D. A. Muller, R. G. Hennig, and J. Park, *Softened Elastic Response and Unzipping in Chemical Vapor Deposition Graphene Membranes*, Nano Lett. **11**, 6, 2259–2263 (2011).

[291] H. Rasool, C. Ophus, W. Klug, A. Zettl, and J. Gimzewski, *Measurement of the intrinsic strength of crystalline and polycrystalline graphene*, Nat. Commun. **4** (2013).

[292] M. Poot and H. S. J. van der Zant, *Nanomechanical properties of few-layer graphene membranes*, Appl. Phys. Lett. **92**, 6, 063111 (2008).

[293] C. Wong, M. Annamalai, Z. Wang, and M. Palaniapan, *Characterization of nanomechanical graphene drum structures*, J. Micromech. Microeng. **20**, 1150209 (2010).

[294] J. Lee, Z. Wang, K. He, J. Shan, and P. X.-L. Feng, *High Frequency MoS_2 Nanomechanical Resonators*, ACS Nano **7**, 6086–6091 (2013).

[295] I. W. Frank, D. M. Tanenbaum, A. M. van der Zande, and P. L. McEuen, *Mechanical properties of suspended graphene sheets*, Journal of Vacuum Science & Technology B: Microelectronics and Nanometer Structures Processing, Measurement, and Phenomena **25**, 2558 (2007).

[296] F. Traversi, F. J. Gúzman-Vázquez, L. G. Rizzi, V. Russo, C. S. Casari, C. Gómez-Navarro, and R. Sordan, *Elastic properties of graphene suspended on a polymer substrate by e-beam exposure*, New Journal of Physics **12**, 2, 023034 (2010).

[297] S. Sengupta, H. S. Solanki, V. Singh, S. Dhara, and M. M. Deshmukh, *Electromechanical resonators as probes of the charge density wave transition at the nanoscale in $NbSe_2$*, Phys. Rev. B **82**, 155432 (2010).

[298] L. D. Landau and E. M. Lifshitz, *Theory of elasticity*, vol. 7, Pergamon Press, Course on Theoretical Physics, 2nd revised edition (1970).

[299] E. Ventsel and T. Krauthammer, *Thin Plates and Shells: Theory, Analysis, and Applications*, Appl. Mech. Rev. **55(4)**, B72-B73 (2002).

[300] A. Castellanos-Gomez, M. Poot, G. A. Steele, H. S. J. van der Zant, N. Agraït, and G. Rubio-Bollinger, *Elastic Properties of Freely Suspended MoS_2 Nanosheets* , Adv. Mater. **24**, 772 (2012).

[301] A. Castellanos-Gomez, M. Poot, A. Amor-Amorós, G. A. Steele, H. S. J. van der Zant, N. Agraït, and G. Rubio-Bollinger, *Mechanical properties of freely suspended atomically thin dielectric layers of mica*, Nano Res. **5**, 8, 550–557 (2012).

[302] X. Wei, B. Fragneaud, C. A. Marianetti, and J. W. Kysar, *Nonlinear elastic behavior of graphene: Ab initio calculations to continuum description*, Phys. Rev. B **80**, 205407 (2009).

[303] F. Liu, P. Ming, and J. Li, *Ab initio calculation of ideal strength and phonon instability of graphene under tension*, Phys. Rev. B **76**, 064120 (2007).

[304] L. Zhou and G. Cao, *Nonlinear anisotropic deformation behavior of a graphene monolayer under uniaxial tension*, Phys. Chem. Chem. Phys. **18**, 1657–1664 (2016).

[305] R. C. Cooper, C. Lee, C. A. Marianetti, X. Wei, J. Hone, and J. W. Kysar, *Nonlinear elastic behavior of two-dimensional molybdenum disulfide*, Phys. Rev. B **87**, 035423 (2013).

[306] S. Xiong and G. Cao, *Molecular dynamics simulations of mechanical properties of monolayer MoS_2*, Nanotechnology **26**, 18, 185705 (2015).

[307] D. Vella and B. Davidovitch, *Indentation metrology of clamped, ultra-thin elastic sheets*, Soft Matter **13**, 2264–2278 (2017).

[308] U. Komaragiri, M. R. Begley, and J. G. Simmonds, *The Mechanical Response of Freestanding Circular Elastic Films Under Point and Pressure Loads*, J. Appl. Mech. **72**, 202 (2005).

[309] H. Chen, P. Huang, D. Guo, and G. Xie, *Anisotropic Mechanical Properties of Black Phosphorus Nanoribbons*, J. Phys. Chem. C **120**, 51, 29491–29497 (2016).

[310] C. Lee, X. Wei, Q. Li, R. Carpick, J. W. Kysar, and J. Hone, *Elastic and frictional properties of graphene*, Physica Status Solidi b **246**, 11-12, 2562–2567 (2009).

[311] N. Iguiñiz, R. Frisenda, R. Bratschitsch, and A. Castellanos-Gomez, *Revisiting the Buckling Metrology Method to Determine the Young's Modulus of 2D Materials*, Adv. Mater. **31**, 10, 1807150 (2019).

[312] Y. Li, C. Yu, Y. Gan, P. Jiang, J. Yu, Y. Ou, D.-F. Zou, C. Huang, J. Wang, T. Jia, Q. Luo, X.-F. Yu, H. Zhao, C.-F. Gao, and J. Li, *Mapping the elastic properties of two-dimensional MoS_2 via bimodal atomic force microscopy and finite element simulation*, npj Computational Materials **4**, 1, 49 (2018).

[313] J. Lee, F. Ye, Z. Wang, R. Yang, J. Hu, Z. Mao, J. Wei, and P. X.-L. Feng, *Single- and Few-Layer WTe_2 and Their Suspended Nanostructures: Raman Signatures and Nanomechanical Resonances*, Nanoscale **8**, 7854-7860 (2016).

[314] K. Liu, Q. Yan, M. Chen, W. Fan, Y. Sun, J. Suh, D. Fu, S. Lee, J. Zhou, S. Tongay, J. Ji, J. B. Neaton, and J. Wu, *Elastic Properties of Chemical-Vapor-Deposited Monolayer MoS_2, WS_2, and Their Bilayer Heterostructures*, Nano Lett. **14**, 5097–5103 (2014).

[315] F. Wang, S. Li, M. A. Bissett, I. A. Kinloch, Z. Li, and R. J. Young, *Strain Engineering in Monolayer WS_2 and WS_2 Nanocomposites*, 2D Materials **7**, 045022 (2020).

[316] Y. Yang, X. Li, M. Wen, E. Hacopian, W. Chen, Y. Gong, J. Zhang, B. Li, W. Zhou, P. M. Ajayan, Q. Chen, T. Zhu, and J. Lou, *Brittle Fracture of 2D $MoSe_2$*, Adv. Mater. **29**, 1604201 (2019).

[317] R. Zhang, V. Koutsos, and R. Cheung, *Elastic properties of suspended multilayer WSe_2*, Appl. Phys. Lett. **108**, 042104 (2016).

[318] B. H. Tan, J. Zhang, J. Jin, C. H. Ooi, Y. He, R. Zhou, K. Ostrikov, N.-T. Nguyen, and H. An, *Direct Measurement of the Contents, Thickness, and Internal Pressure of Molybdenum Disulfide Nanoblisters*, Nano Lett. **20**, 5, 3478–3484 (2020).

[319] C. Di Giorgio, E. Blundo, G. Pettinari, M. Felici, A. Polimeni, and F. Bobba, *Exceptional Elasticity of Microscale Constrained MoS_2 Domes*, ACS Appl. Mater. Interfaces **13**, 48228 (2021).

[320] L. X. Benedict, N. G. Chopra, M. L. Cohen, A. Zettl, S. G. Louie, and V. H. Crespi, *Microscopic determination of the interlayer binding energy in graphite*, Chem. Phys. Lett. **286**, 490–496 (1998).

[321] P. Zhilyaev, E. Iakovlev, and I. Akhatov, *Liquid-gas phase transition of Ar inside graphene nanobubbles on the graphite substrate*, Nanotechnology **30**, 215701 (2019).

[322] N. Mounet, M. Gibertini, P. Schwaller, D. Campi, A. Merkys, A. Marrazzo, T. Sohier, I. E. Castelli, A. Cepellotti, G. Pizzi, and N. Marzari, *Two-dimensional materials from high-throughput computational exfoliation of experimentally known compounds*, Nat. Nanotech. **13**, 246–252 (2018).

[323] S. P. Koenig, N. G. Boddeti, N. L. Dunn, and J. S. Bunch, *Ultrastrong adhesion of graphene membranes*, Nat. Nanotechnol. **6**, 543 (2011).

[324] N. G. Boddeti, S. P. Koenig, R. Long, J. Xiao, J. S. Bunch, and M. L. Dunn, *Mechanics of Adhered, Pressurized Graphene Blisters*, J. Appl. Mech. **80**, 040909 (2013).

[325] X. Liu, N. G. Boddeti, M. R. Szpunar, L. Wang, M. A. Rodriguez, R. Long, J. Xiao, M. L. Dunn, and J. S. Bunch, *Observation of Pull-In Instability in Graphene Membranes under Interfacial Forces*, Nano Lett. **13**, 2309 (2013).

[326] K. Yue, W. Gao, R. Huang, and K. M. Liechti, *Analytical methods for the mechanics of graphene bubbles*, J. Appl. Phys. **112**, 083512 (2012).

[327] H. Luo, X. Li, Y. Zhao, R. Yang, Y. Hao, Y.-N. Gao, N. N. Shi, Y. Guo, G. Liu, L. Zhao, Q. Wang, Z. Zhang, J. Sun, X. Zhou, and Y. Huang, *Simultaneous Generation of Direct- and Indirect-Gap Photoluminescence in Multilayer MoS_2 Bubbles*, Phys. Rev. Mater. **4**, 074006 (2020).

[328] R. Larciprete, S. Colonna, F. Ronci, R. Flammini, P. Lacovig, N. Apostol, A. Politano, P. Feulner, D. Menzel, and S. Lizzit, *Self-Assembly of Graphene Nanoblisters Sealed to a Bare Metal Surface*, Nano Lett. **16**, 1808–1817 (2016).

[329] H. W. Kim, W. Ko, J. Ku, I. Jeon, D. Kim, H. Kwon, Y. Oh, S. Ryu, Y. Kuk, S. W. Hwang, and H. Suh, *Nanoscale control of phonon excitations in graphene*, Nat. Comm. **6**, 7528 (2015).

[330] H. Rostami, F. Guinea, M. Polini, and R. Roldán, *Piezoelectricity and valley Chern number in inhomogeneous hexagonal 2D crystals*, npj 2D Mater. Appl **2**, 51 (2018).

[331] M. de Jong, W. Chen, T. Angsten, A. Jain, R. Notestine, A. Gamst, M. Sluiter, C. K. Ande, S. van der Zwaag, J. J. Plata, C. Toher, S. Curtarolo, G. Ceder, K. A. Persson, and M. Asta, *Charting the complete elastic properties of inorganic crystalline compounds*, Sci. Data **2**, 150009 (2015).

[332] M. M. Alyörük, Y. Aierken, D. Çakír, F. M. Peeters, and C. Sevik, *Promising Piezoelectric Performance of Single Layer Transition-Metal Dichalcogenides and Dioxides*, J. Phys. Chem. C **119**, 23231 (2015).

[333] C. Lee, X. Wei, J. W. Kysar, and J. Hone, *Measurement of the Elastic Properties and Intrinsic Strength of Monolayer Graphene*, Science **321**, 385 (2008).

[334] K. Liu, Q. Yan, M. Chen, W. Fan, Y. Sun, J. Suh, D. Fu, S. Lee, J. Zhou, S. Tongay, J. B. Neaton, and J. Wu, *Elastic Properties of Chemical-Vapor-Deposited Monolayer MoS_2, WS_2, and Their Bilayer Heterostructures*, Nano Lett. **14**, 5097 (2014).

[335] A. Castellanos-Gomez, M. Poot, G. A. Steele, H. S. J. van der Zant, N. Agraït, and G. Rubio-Bollinger, *Elastic Properties of Freely Suspended MoS_2 Nanosheets*, Adv. Mater. **24**, 772–775 (2012).

[336] Y. Sun, J. Pan, Z. Zhang, K. Zhang, J. Liang, W. Wang, Z. Yuan, Y. Hao, B. Wang, J. Wang, Y. Wu, J. Zheng, L. Jiao, S. Zhou, K. Liu, C. Cheng,

W. Duan, Y. Xu, Q. Yan, and K. Liu, *Elastic Properties and Fracture Behaviors of Biaxially Deformed, Polymorphic $MoTe_2$*, Nano Lett. **19**, 761–769 (2019).

[337] H. Jiang, L. Zheng, Z. Liu, and X. Wang, *Two-dimensional materials: From mechanical properties to flexible mechanical sensors*, InfoMat. **2**, 1077 (2020).

[338] D. Lee, B. Lee, K. H. Park, H. J. Ryu, S. Jeon, and S. H. Hong, *Scalable Exfoliation Process for Highly Soluble Boron Nitride Nanoplatelets by Hydroxide-Assisted Ball Milling*, Nano Lett. **15**, 1238–1244 (2015).

[339] F. Ye, J. Lee, J. Hu, Z. Mao, J. Wei, and P. X. Feng, *Environmental Instability and Degradation of Single- and Few-Layer WTe_2 Nanosheets in Ambient Conditions*, Small **12**, 5802–5808 (2016).

[340] R. Rasuli and A. Iraji, *Density functional theory prediction for oxidation and exfoliation of graphite to graphene*, Appl. Surf. Science **256**, 7596–7599 (2010).

[341] W. S. Yun, S. W. Han, S. C. Hong, I. G. Kim, and J. D. Lee, *Thickness and strain effects on electronic structures of transition metal dichalcogenides: 2H-MX_2 semiconductors (M = Mo, W; X = S, Se, Te)*, Phys. Rev. B **85**, 033305 (2012).

[342] P. Johari and V. B. Shenoy, *Tuning the electronic properties of semiconducting transition metal dichalcogenides by applying mechanical strains*, ACS Nano **6**, 5449 (2012).

[343] H. Pan and Y.-W. Zhang, *Tuning the Electronic and Magnetic Properties of MoS2 Nanoribbons by Strain Engineering*, The Journal of Physical Chemistry C **116**, 21, 11752–11757 (2012).

[344] Q. Zhang, Y. Cheng, L.-Y. Gan, and U. Schwingenschlögl, *Giant valley drifts in uniaxially strained monolayer* MoS_2, Phys. Rev. B **88**, 245447 (2013).

[345] M. Ghorbani-Asl, S. Borini, A. Kuc, and T. Heine, *Strain-dependent modulation of conductivity in single-layer transition-metal dichalcogenides*, Phys. Rev. B **87**, 235434 (2013).

[346] H. Shi, H. Pan, Y.-W. Zhang, and B. I. Yakobson, *Quasiparticle band structures and optical properties of strained monolayer MoS_2 and WS_2*, Phys. Rev. B **87**, 155304 (2013).

[347] D. M. Guzman and A. Strachan, *Role of strain on electronic and mechanical response of semiconducting transition-metal dichalcogenide monolayers: An ab-initio study*, Journal of Applied Physics **115**, 24, 243701 (2014).

[348] S. Bhattacharyya, T. Pandey, and A. Singh, *Effect of strain on electronic and thermoelectric properties of few layers to bulk MoS_2*, Nanotechnology **25**, 465701 (2014).

[349] M. Hosseini, M. Elahi, M. Pourfath, and D. Esseni, *Strain induced mobility modulation in single-layer MoS_2*, J. Phys. D.: Appl. Phys. **48**, 375104 (2015).

[350] E. Blundo, P. E. Faria Junior, A. Surrente, G. Pettinari, M. A. Prosnikov, K. Olkowska-Pucko, K. Zollner, T. Woźniak, A. Chaves, T. Kazimierczuk, M. Felici, A. Babiński, M. R. Molas, P. C. M. Christianen, and J. F. A. Polimeni, *Strain-Induced Exciton Hybridization in WS_2 Monolayers Unveiled by Zeeman-Splitting Measurements*, Phys. Rev. Lett. **129**, 067402 (2022).

[351] B. P. Nayak, T. Pandey, D. Voiry, J. Liu, S. T. Moran, A. Sharma, C. Tan, C.-H. Chen, L.-J. Li, M. Chhowalla, J.-F. Lin, A. K. Singh, and D. Akinwande, *Pressure-dependent optical and vibrational properties of monolayer molybdenum disulfide*, Nano Lett. **15**, 346 (2015).

[352] J.-S. Kim, R. Ahmad, T. Pandey, A. Rai, S. Feng, J. Yang, Z. Lin, M. Terrones, S. K. Banerjee, A. K. Singh, D. Akinwande, and J.-F. Lin, *Towards band structure and band offset engineering of monolayer $Mo_{1-x}W_xS_2$ via strain* , 2D Materials **5**, 015008 (2018).

[353] K. Zollner, P. E. F. Junior, and J. Fabian, *Strain-tunable orbital, spin-orbit, and optical properties of monolayer transition-metal dichalcogenides*, Phys. Rev. B **100**, 195126 (2019).

[354] B. G. Shin, G. H. Han, S. J. Yun, H. M. Oh, J. J. Bae, Y. J. Song, C. Park, and Y. H. Lee, *Indirect Bandgap Puddles in Monolayer MoS_2 by Substrate-Induced Local Strain*, Adv. Mater. **28**, 9378–9384 (2016).

[355] D. J. Trainer, Y. Zhang, F. Bobba, X. Xi, S.-W. Hla, and M. Iavarone, *The Effects of Atomic-Scale Strain Relaxation on the Electronic Properties of Monolayer MoS_2*, ACS Nano **13**, 8284–8291 (2019).

[356] C. Zhang, M.-Y. Li, J. Tersoff, Y. Han, Y. Su, L.-J. Li, D. A. Muller, and C.-K. Shih, *Strain distributions and their influence on electronic structures of WSe_2-MoS_2 laterally strained heterojunctions*, Nat. Nanotechnol. **13**, 152–158 (2018).

[357] M. Precner, T. Polaković, Q. Qiao, D. J. Trainer, A. V. Putilov, C. Di Giorgio, I. Cone, Y. Zhu, X. X. Xi, M. Iavarone, and G. Karapetrov, *Evolution of Metastable Defects and Its Effect on the Electronic Properties of MoS_2 Films*, Sci. Rep. **8**, 6724 (2018).

[358] B. Amin, T. P. Kaloni, and U. Schwingenschlögl, *Strain engineering of WS_2, WSe_2, and WTe_2*, RCS Adv. **4**, 34561 (2014).

[359] R. Das, B. Rakshit, S. Debnath, and P. Mahadevan, *Microscopic model for the strain-driven direct to indirect band-gap transition in monolayer MoS_2 and ZnO*, Phys. Rev. B **89**, 115201 (2014).

[360] R. Das, B. Rakshit, S. Debnath, and P. Mahadevan, *A model for the direct-to-indirect band-gap transition in monolayer $MoSe_2$ under strain*, Pramana J. Phys. **84**, 1033 (2015).

[361] L. Ortenzi, L. Pietronero, and E. Cappelluti, *Zero-point motion and direct-indirect band-gap crossover in layered transition-metal dichalcogenides*, Phys. Rev. B **98**, 195313 (2018).

[362] R. Yang, J. Lee, S. Ghosh, H. Tang, R. M. Sankaran, C. A. Zorman, and P. X.-L. Feng, *Tuning optical signatures of single- and few-layer MoS_2 by blown-bubble bulge straining up to fracture*, Nano Lett. **17**, 4568 (2017).

[363] R. Frisenda, M. Druppel, R. Schmidt, S. M. de Vasconcellos, D. P. de Lara, R. Bratschitsch, M. Rohlfing, and A. Castellanos-Gomez, *Biaxial strain tuning of the optical properties of single-layer transition metal dichalcogenides*, 2D Materials and Applications **1**, 10 (2017).

[364] Y. Wang, C. Cong, W. Yang, J. Shang, N. Peimyoo, Y. Chen, J. Kang, J. Wang, W. Huang, and T. Yu, *Strain-induced direct-indirect bandgap transition and phonon modulation in monolayer WS_2*, Nano Res. **8**, 2562 (2015).

[365] C. Robert, D. Lagarde, F. Cadiz, G. Wang, B. Lassagne, T. Amand, A. Balocchi, P. Renucci, S. Tongay, B. Urbaszek, and X. Marie, *Exciton radiative lifetime in transition metal dichalcogenide monolayers*, Phys. Rev. B **93**, 205423 (2016).

[366] H. Liu, T. Wang, C. Wang, D. Liu, and J. Luo, *Exciton radiative recombination dynamics and nonradiative energy transfer in two-dimensional transition-metal dichalcogenides*, J. Phys. Chem. C **123**, 10087 (2019).

[367] J. J. Esteve-Paredes, S. Pakdel, and J. J. Palacios, *Quenching of Exciton Recombination in Strained Two-Dimensional Monochalcogenides*, Phys. Rev. Lett. **123**, 077402 (2019).

[368] M. Rohlfing and S. G. Louie, *Electron-hole excitations and optical spectra from first principles*, Phys. Rev. B **62**, 4927–4944 (2000).

[369] N. S. Rytova, *The screened potential of a point charge in a thin film*, Mosc. Univ. Phys. Bull. **3**, 3, 18 (1967).

[370] L. Keldysh, *Coulomb interaction in thin semiconductor and semimetal films*, Sov. J. Exp. Theo. Phys. Lett. **29**, 658 (1979).

[371] P. Cudazzo, I. V. Tokatly, and A. Rubio, *Dielectric screening in two-dimensional insulators: Implications for excitonic and impurity states in graphane*, Phys. Rev. B **84**, 085406 (2011).

[372] T. C. Berkelbach, M. S. Hybertsen, and D. R. Reichman, *Theory of neutral and charged excitons in monolayer transition metal dichalcogenides*, Phys. Rev. B **88**, 045318 (2013).

[373] P. E. Faria Junior, M. Kurpas, M. Gmitra, and J. Fabian, *$k \cdot p$ theory for phosphorene: Effective g-factors, Landau levels, and excitons*, Phys. Rev. B **100**, 115203 (2019).

[374] K. Zollner, P. E. Faria Junior, and J. Fabian, *Proximity exchange effects in* $MoSe_2$ *and* WSe_2 *heterostructures with* CrI_3*: Twist angle, layer, and gate dependence*, Phys. Rev. B **100**, 085128 (2019).

[375] L. Mennel, M. Paur, and T. Mueller, *Second harmonic generation in strained transition metal dichalcogenide monolayers: MoS_2, $MoSe_2$, WS_2, and WSe_2*, APL Photonics **4**, 034404 (2019).

[376] J. Liang, J. Wang, Z. Zhang, Y. Su, Y. Guo, R. Qiao, P. Song, P. Gao, Y. Zhao, Q. Jiao, S. Wu, Z. Sun, D. Yu, and K. Liu, *Universal Imaging of Full Strain Tensor in 2D Crystals with Third-Harmonic Generation*, Adv. Mater. **31**, 1808160 (2019).

[377] F. Carrascoso, H. Li, R. Frisenda, and A. Castellanos-Gomez, *Strain engineering in single-, bi- and tri-layer MoS_2, $MoSe_2$, WS_2 and WSe_2*, Nano Res. (2020).

[378] L. Waldecker, A. Raja, M. Rösner, C. Steinke, A. Bostwick, R. J. Koch, C. Jozwiak, T. Taniguchi, K. Watanabe, E. Rotenberg, T. O. Wehling, and T. F. Heinz, *Rigid Band Shifts in Two-Dimensional Semiconductors through External Dielectric Screening*, Phys. Rev. Lett. **123**, 206403 (2019).

[379] Z. Jin, X. Li, J. T. Mullen, and K. W. Kim, *Intrinsic transport properties of electrons and holes in monolayer transition-metal dichalcogenides*, Phys. Rev. B **90**, 045422 (2014).

[380] L. Wang, A. Kutana, and B. I. Yakobson, *Many-body and spin-orbit effects on direct-indirect band gap transition of strained monolayer MoS_2 and WS_2*, Annalen der Physik **526**, 9-10, L7–L12 (2014).

[381] I. Niehues, A. Blob, T. Stiehm, R. Schmidt, V. Jadriško, BornaRadatović, D. Čapeta, M. Kralj, S. M. de Vasconcellos, and R. Bratschitsch, *Strain transfer across grain boundaries in MoS_2 monolayers grown by chemical vapor deposition*, 2D Materials **5**, 031003 (2018).

[382] G. Wang, A. Chernikov, M. M. Glazov, T. F. Heinz, X. Marie, T. Amand, and B. Urbaszek, *Colloquium: Excitons in atomically thin transition metal dichalcogenides*, Rev. Mod. Phys. **90**, 021001 (2018).

[383] M. Koperski, M. R. Molas, A. Arora, K. Nogajewski, A. O. Slobodeniuk, C. Faugeras, and M. Potemski, *Optical properties of atomically thin transition metal dichalcogenides: observations and puzzles*, Nanophotonics **6**, 1289 (2017).

[384] Y. Liu, Y. Gao, S. Zhang, J. He, J. Yu, and Z. Liu, *Valleytronics in transition metal dichalcogenides materials*, Nano Res. **12**, 2695 (2019).

[385] G. Aivazian, Z. Gong, A. M. Jones, R.-L. Chu, J. Yan, D. G. Mandrus, C. Zhang, D. Cobden, W. Yao, and X. Xu, *Magnetic control of valley pseudospin in monolayer WSe_2*, Nat. Phys. **11**, 148 (2015).

[386] D. MacNeill, C. Heikes, K. F. Mak, Z. Anderson, A. Kormányos, V. Zólyomi, J. Park, and D. C. Ralph, *Breaking of Valley Degeneracy by Magnetic Field in Monolayer $MoSe_2$*, Phys. Rev. Lett. **114**, 037401 (2015).

[387] M. Zinkiewicz, T. Woźniak, T. Kazimierczuk, P. Kapuscinski, K. Oreszczuk, M. Grzeszczyk, M. Bartoš, K. Nogajewski, K. Watanabe, T. Taniguchi, C. Faugeras, P. Kossacki, M. Potemski, A. Babiński, and M. R. Molas, *Excitonic Complexes in n-Doped WS_2 Monolayer*, Nano Lett. **21**, 6, 2519–2525 (2021).

[388] G. Plechinger, P. Nagler, A. Arora, A. Granados del Águila, M. V. Ballottin, T. Frank, P. Steinleitner, M. Gmitra, J. Fabian, P. C. Christianen *et al.*, *Excitonic valley effects in monolayer WS_2 under high magnetic fields*, Nano Lett. **16**, 12, 7899–7904 (2016).

[389] R. Schmidt, A. Arora, G. Plechinger, P. Nagler, A. G. del Águila, M. V. Ballottin, P. C. M. Christianen, S. M. de Vasconcellos, C. Schüller, T. Korn, and R. Bratschitsch, *Magnetic-Field-Induced Rotation of Polarized Light Emission from Monolayer WS_2*, Phys. Rev. Lett. **117**, 077402 (2016).

[390] J. Kuhnert, A. Rahimi-Iman, and W. Heimbrodt, *Magneto photoluminescence measurements of tungsten disulphide monolayers*, Journal of Physics: Condensed Matter **29**, 8, 08LT02 (2017).

[391] A. A. Mitioglu, P. Plochocka, A. G. del Aguila, P. C. M. Christianen, G. Deligeorgis, S. Anghel, L. Kulyuk, and D. K. Maude, *Optical Investigation of Monolayer and Bulk Tungsten Diselenide (WSe_2) in High Magnetic Fields*, Nano Lett. **15**, 4387 (2015).

[392] G. Wang, L. Bouet, M. M. Glazov, T. Amand, E. L. Ivchenko, E. Palleau, X. Marie, and B. Urbaszek, *Magneto-optics in transition metal diselenide monolayers*, 2D Mater. **2**, 034002 (2015).

[393] A. Mitioglu, J. Buhot, M. V. Ballottin, S. Anghel, K. Sushkevich, L. Kulyuk, and P. C. M. Christianen, *Observation of bright exciton splitting in strained WSe_2 monolayers*, Phys. Rev. B **98**, 235429 (2018).

[394] P. Nagler, M. V. Ballottin, A. A. Mitioglu, F. Mooshammer, N. Paradiso, C. Strunk, R. Huber, A. Chernikov, P. C. M. Christianen, C. Schüller, and T. Korn, *Giant magnetic splitting inducing near-unity valley polarization in van der Waals heterostructures*, Nat. Commun. **8**, 1551 (2017).

[395] A. Ciarrocchi, D. Unuchek, A. Avsar, K. Watanabe, T. Taniguchi, and A. Kis, *Polarization switching and electrical control of interlayer excitons in two-dimensional van der Waals heterostructures*, Nat. Photonics **13**, 131 (2019).

[396] T. Wang, S. Miao, Z. Li, Y. Meng, Z. Lu, Z. Lian, M. Blei, T. Taniguchi, K. Watanabe, S. Tongay, D. Smirnov, and S.-F. Shi, *Giant valley-Zeeman splitting from spin-singlet and spin-triplet interlayer excitons in $WSe_2/MoSe_2$ heterostructure*, Nano Lett. **20**, 694 (2020).

[397] A. Surrente, Łukasz Kłopotowski, N. Zhang, M. Baranowski, A. A. Mitioglu, M. V. Ballottin, P. C. Christianen, D. Dumcenco, Y.-C. Kung, D. K. Maude, A. Kis, and P. Plochocka, *Intervalley Scattering of Interlayer Excitons in a $MoS_2/MoSe_2/MoS_2$ Heterostructure in High Magnetic Field*, Nano Lett. **18**, 3994 (2018).

[398] H. Baek, M. Brotons-Gisbert, Z. X. Koong, A. Campbell, M. Rambach, K. Watanabe, T. Taniguchi, and B. D. Gerardot, *Highly energy-tunable quantum light from moiré-trapped excitons*, Sci. Adv. **6**, 37, eaba8526 (2020).

[399] T. Woźniak, P. E. Faria Junior, G. Seifert, A. Chaves, and J. Kunstmann, *Exciton g factors of van der Waals heterostructures from first-principles calculations*, Phys. Rev. B **101**, 23, 235408 (2020).

[400] T. Deilmann, P. Krüger, and M. Rohlfing, *Ab initio studies of exciton g factors: monolayer transition metal dichalcogenides in magnetic fields*, Phys. Rev. Lett. **124**, 22, 226402 (2020).

[401] J. Förste, N. V. Tepliakov, S. Y. Kruchinin, J. Lindlau, V. Funk, M. Förg, K. Watanabe, T. Taniguchi, A. S. Baimuratov, and A. Högele, *Exciton g-factors in monolayer and bilayer WSe_2 from experiment and theory*, Nature Commun. **11**, 1, 4539 (2020).

[402] F. Xuan and S. Y. Quek, *Valley Zeeman effect and Landau levels in two-dimensional transition metal dichalcogenides*, Phys. Rev. Research **2**, 033256 (2020).

[403] K. F. Mak, K. He, J. Shan, and T. F. Heinz, *Control of valley polarization in monolayer MoS_2 by optical helicity*, Nature nanotechnology **7**, 8, 494–498 (2012).

[404] M. R. Molas, A. O. Slobodeniuk, T. Kazimierczuk, K. Nogajewski, M. Bartos, P. Kapuściński, K. Oreszczuk, K. Watanabe, T. Taniguchi, C. Faugeras,

P. Kossacki, D. M. Basko, and M. Potemski, *Probing and Manipulating Valley Coherence of Dark Excitons in Monolayer* WSe_2, Phys. Rev. Lett. **123**, 096803 (2019).

[405] C. Robert, B. Han, P. Kapuscinski, A. Delhomme, C. Faugeras, T. Amand, M. Molas, M. Bartos, K. Watanabe, T. Taniguchi *et al.*, *Measurement of the spin-forbidden dark excitons in MoS_2 and $MoSe_2$ monolayers*, Nature Commun. **11**, 4037 (2020).

[406] T. Inui, Y. Tanabe, and Y. Onodera, *Group theory and its applications in physics*, Springer Science & Business Media, Berlin, Germany, vol. 78 (2012).

[407] M. Vozmediano, M. Katsnelson, and F. Guinea, *Gauge fields in graphene*, Phys. Rep. **496**, 109 (2010).

[408] H. Rostami, R. Roldán, E. Cappelluti, R. Asgari, and F. Guinea, *Theory of strain in single-layer transition metal dichalcogenides*, Phys. Rev. B **92**, 195402 (2015).

[409] T. Deilmann and K. S. Thygesen, *Interlayer excitons with large optical amplitudes in layered van der Waals materials*, Nano Lett. **18**, 5, 2984–2989 (2018).

[410] E. Lorchat, M. Selig, F. Katsch, K. Yumigeta, S. Tongay, A. Knorr, C. Schneider, and S. Höfling, *Excitons in Bilayer* MoS_2 *Displaying a Colossal Electric Field Splitting and Tunable Magnetic Response*, Phys. Rev. Lett. **126**, 037401 (2021).

[411] M. Capizzi, S. Modesti, F. Martelli, and A. Frova, *Γ-X mixing of the free and bound exciton in $GaAs_{1-x}P_x$*, Solid State Commun. **39**, 333 (1981).

[412] D. Erkensten, S. Brem, and E. Malic, *Exciton-exciton interaction in transition metal dichalcogenide monolayers and van der Waals heterostructures*, Phys. Rev. B **103**, 045426 (2021).

[413] M. Selig, G. Berghäuser, A. Raja, P. Nagler, C. Schüller, T. F. Heinz, T. Korn, A. Chernikov, E. Malic, and A. Knorr, *Excitonic linewidth and coherence lifetime in monolayer transition metal dichalcogenides*, Nature Commun. **7**, 1, 1–6 (2016).

[414] D. Tedeschi, M. De Luca, P. F. Junior, A. G. del Águila, Q. Gao, H. H. Tan, B. Scharf, P. Christianen, C. Jagadish, J. Fabian, and A. Polimeni, *Unusual spin properties of InP wurtzite nanowires revealed by Zeeman splitting spectroscopy*, Phys. Rev. B **99**, 16, 161204 (2019).

[415] P. E. Faria Jr, D. Tedeschi, M. De Luca, B. Scharf, A. Polimeni, and J. Fabian, *Common nonlinear features and spin-orbit coupling effects in the Zeeman splitting of novel wurtzite materials*, Phys. Rev. B **99**, 19, 195205 (2019).

[416] Y.-M. He, G. Clark, J. R. Schaibley, Y. He, M.-C. Chen, Y.-J. Wei, Q. Z. Xing Ding, W. Yao, X. Xu, C.-Y. Lu, and J.-W. Pan, *Single quantum emitters in monolayer semiconductors*, Nat. Nanotechnol. **10**, 497 (2015).

[417] A. Srivastava, M. Sidler, A. V. Allain, D. S. Lembke, A. Kis, and A. Imamoğlu, *Optically active quantum dots in monolayer WSe_2*, Nat. Nanotechnol. **10**, 491 (2015).

[418] Y. Koperski, K. Nogajewski, A. Arora, V. Cherkez, P. Mallet, J.-Y. Veuillen, J. Marcus, P. Kossacki, and M. Potemski, *Single photon emitters in exfoliated WSe_2 structures*, Nat. Nanotechnol. **10**, 503 (2015).

[419] P. Tonndorf, R. Schmidt, R. Schneider, J. Kern, M. Buscema, G. A. Steele, A. Castellanos-Gomez, H. S. van der Zant, S. M. de Vasconcellos, and R. Bratschitsch, *Single-photon emission from localized excitons in an atomically thin semiconductor*, Optica **2**, 347–352 (2015).

[420] C. Chakraborty, L. Kinnischtzke, K. M. Goodfellow, R. Beams, and A. N. Vamivakas, *Voltage-controlled quantum light from an atomically thin semiconductor*, Nat. Nanotechnol. **10**, 507 (2015).

[421] C. Palacios-Berraquero, M. Barbone, D. M. Kara, X. Chen, I. Goykhman, D. Yoon, A. K. Ott, J. Beitner, K. Watanabe, T. Taniguchi, A. C. Ferrari, and M. Atatüre, *Atomically thin quantum light-emitting diodes*, Nat. Commun. **7**, 1, 12978 (2016).

[422] A. Branny, G. Wang, S. Kumar, C. Robert, B. Lassagne, X. Marie, B. D. Gerardot, and B. Urbaszek, *Discrete quantum dot like emitters in monolayer $MoSe_2$: Spatial mapping, magneto-optics, and charge tuning*, Appl. Phys. Lett. **108**, 142101 (2016).

[423] C. Chakraborty, K. M. Goodfellow, and A. N. Vamivakas, *Localized emission from defects in $MoSe_2$ layers*, Opt. Mater. Express **6**, 2081–2087 (2016).

[424] O. Iff, N. Lundt, S. Betzold, L. N. Tripathi, M. Emmerling, S. Tongay, Y. J. Lee, S.-H. Kwon, S. Höfling, and C. Schneider, *Deterministic coupling of quantum emitters in WSe_2 monolayers to plasmonic nanocavities*, Opt. Express **26**, 25944 (2018).

[425] C. Palacios-Berraquero, D. M. Kara, A. R.-P. Montblanch, M. Barbone, P. Latawiec, D. Yoon, A. K. Ott, M. Loncar, A. C. Ferrari, and M. Atatüre, *Large-scale quantum-emitter arrays in atomically thin semiconductors*, Nat. Commun. **8**, 15093 (2017).

[426] T. Cai, J.-H. Kim, Z. Yang, S. Dutta, S. Aghaeimeibodi, and E. Waks, *Radiative Enhancement of Single Quantum Emitters in WSe_2 Monolayers Using Site-Controlled Metallic Nanopillars*, ACS Photonics **5**, 3466 (2018).

[427] L. Peng, H. Chan, P. Choo, T. W. Odom, S. K. R. S. Sankaranarayanan, and X. Ma, *Creation of Single-Photon Emitters in WSe_2 Monolayers Using Nanometer-Sized Gold Tips*, Nano Lett. **20**, 5866–5872 (2020).

[428] Y. Luo, G. D. Shepard, J. V. Ardelean, D. A. Rhodes, B. Kim, K. Barmak, J. C. Hone, and S. Strauf, *Deterministic coupling of site-controlled quantum emitters in monolayer WSe_2 to plasmonic nanocavities*, Nat. Nanotechnol. **13**, 12, 1137–1142 (2018).

[429] O. Iff, Q. Buchinger, M. Moczała-Dusanowska, M. Kamp, S. Betzold, M. Davanco, K. Srinivasan, S. Tongay, C. Antón-Solanas, S. Höfling, and C. Schneider, *Purcell-Enhanced Single Photon Source Based on a Deterministically Placed WSe_2 Monolayer Quantum Dot in a Circular Bragg Grating Cavity*, Nano Lett. **21**, 4715 (2021).

[430] M. Kianinia, Z.-Q. Xu, M. Toth, and I. Aharonovich, *Quantum emitters in 2D materials: Emitter engineering, photophysics, and integration in photonic nanostructures*, Appl. Phys. Rev. **9**, 011306 (2022).

[431] A. Castellanos-Gomez, M. Buscema, R. Molenaar, V. Singh, L. Janssen, H. S. J. van der Zant, and G. A. Steele, *Deterministic transfer of two-dimensional materials by all-dry viscoelastic stamping*, 2D Mater. **1**, 011002 (2014).

[432] P. Klemens, *Anharmonic decay of optical phonons*, Phys. Rev. **148,**, 845 (1966).

[433] M. Balkanski, R. Wallis, and E. Haro, *Anharmonic effects in light scattering due to optical phonons in silicon*, Phys. Rev. B **28,**, 1928 (1983).

[434] A. A. Lyublinskaya, S. S. Babkin, and I. S. Burmistrov, *Effect of anomalous elasticity on bubbles in van der Waals heterostructures*, Phys. Rev. E **101**, 033005 (2020).

[435] C. Postmus, J. Ferraro, and S. Mitra, *Pressure dependence of infrared eigenfrequencies of KCl and KBr*, Phys. Rev. **174,**, 983 (1968).

[436] G. Plechinger, P. Nagler, J. Kraus, N. Paradiso, C. Strunk, C. Schüller, and T. Korn, *Identification of excitons, trions and biexcitons in single-layer WS_2*, Phys. Status Solidi - Rapid Res. Lett. **9**, 457–461 (2015).

[437] D. Vaclavkova, J. Wyzula, K. Nogajewski, M. Bartos, A. Slobodeniuk, C. Faugeras, M. Potemski, and M. Molas, *Singlet and triplet trions in WS_2 monolayer encapsulated in hexagonal boron nitride*, Nanotechnology **29**, 325705 (2018).

[438] G. D. Shepard, O. A. Ajayi, X. Li, X.-Y. Zhu, J. Hone, and S. Strauf, *Nanobubble induced formation of quantum emitters in monolayer semiconductors*, 2D Materials **4**, 021019 (2017).

[439] L. Linhart, M. Paur, V. Smejkal, J. Burgdörfer, T. Mueller, and F. Libisch, *Localized Intervalley Defect Excitons as Single-Photon Emitters in WSe_2*, Phys. Rev. Lett. **123,**, 146401 (2019).

[440] H. Moon, E. Bersin, C. Chakraborty, A.-Y. Lu, G. Grosso, J. Kong, and D. Englund, *Strain-Correlated Localized Exciton Energy in Atomically Thin Semiconductors*, ACS Photonics **7,**, 1135 (2020).

[441] K. Parto, S. I. Azzam, K. Banerjee, and G. Moody, *Defect and strain engineering of monolayer WSe_2 enables site-controlled single-photon emission up to 150 K*, Nat. Commun. **12**, 3585 (2021).

[442] L. Chirolli, E. Prada, F. Guinea, R. Roldán, and P. San-Jose, *Strain-induced bound states in transition-metal dichalcogenide bubbles*, 2D Materials **6**, 2, 025010 (2019).

[443] T. P. Darlington, C. Carmesin, M. Florian, E. Yanev, O. Ajayi, J. Ardelean, D. A. Rhodes, A. Ghiotto, A. Krayev, K. Watanabe, T. Taniguchi, J. W. Kysar, A. N. Pasupathy, J. C. Hone, F. Jahnke, N. J. Borys, and P. J. Schuck, *Imaging strain-localized excitons in nanoscale bubbles of monolayer WSe_2 at room temperature*, Nat. Nanotechnol. **15**, 854 (2020).

[444] C. Carmesin, M. Lorke, M. Florian, D. Erben, A. Schulz, T. O. Wehling, and F. Jahnke, *Quantum-Dot-Like States in Molybdenum Disulfide Nanostructures Due to the Interplay of Local Surface Wrinkling, Strain, and Dielectric Confinement*, Nano Lett. **19**, 3182–3186 (2019).

[445] Y. Ye, X. Dou, K. Ding, Y. Chen, D. Jiang, F. Yang, and B. Sun, *Single photon emission from deep-level defects in monolayer ws e 2*, Phys. Rev. B **95,**, 245313 (2017).

[446] B. Schuler, K. A. Cochrane, C. Kastl, E. S. Barnard, E. Wong, N. J. Borys, A. M. Schwartzberg, D. F. Ogletree, F. J. G. de Abajo, and A. Weber-Bargioni, *Electrically driven photon emission from individual atomic defects in monolayer WS2*, Sci. Adv. **6**, eabb5988 (2020).

[447] Q. Wang, J. Maisch, F. Tang, D. Zhao, S. Yang, R. Joos, S. L. Portalupi, P. Michler, and J. H. Smet, *Highly polarized single photons from strain-induced quasi-1D localized excitons in WSe_2*, Nano Lett. **21**, 7175–7182 (2021).

[448] J. Dang, S. Sun, X. Xie, Y. Yu, K. Peng, C. Qian, S. Wu, F. Song, J. Yang, S. Xiao, L. Yang, Y. Wang, M. A. Rafiq, C. Wang, and X. Xu, *Identifying defect-related quantum emitters in monolayer WSe_2*, npj 2D Mater. Appl. **4**, 2 (2020).

[449] C. S. de Brito, C. R. Rabahi, M. D. Teodoro, D. F. Franco, M. Nalin, I. D. Barcelos, and Y. G. Gobato, *Strain engineering of quantum confinement in WSe_2 on nano-roughness glass substrates*, Appl. Phys. Lett. **121**, 070601 (2022).

[450] M. He, P. Rivera, D. Van Tuan, N. P. Wilson, M. Yang, T. Taniguchi, K. Watanabe, J. Yan, D. G. Mandrus, H. Yu, H. Dery, W. Yao, and X. Xu, *Valley phonons and exciton complexes in a monolayer semiconductor*, Nat. Commun. **11,**, 618 (2021).

[451] S. Ovesen, S. Brem, C. Linderälv, M. Kuisma, T. Korn, P. Erhart, M. Selig, and E. Malic, *Interlayer exciton dynamics in van der Waals heterostructures*, Commun. Phys. **2**, 23 (2019).

[452] P. Rivera, J. R. Schaibley, A. M. Jones, J. S. Ross, S. Wu, G. Aivazian, P. Klement, K. Seyler, G. Clark, N. J. Ghimire, J. Yan, D. Mandrus, W. Yao, and X. Xu, *Observation of long-lived interlayer excitons in monolayer $MoSe_2$-WSe_2 heterostructures*, Nat. Commun. **6**, 6242 (2015).

[453] C. Zhang, C.-P. Chuu, X. Ren, M.-Y. Li, L.-J. Li, C. Jin, M.-Y. Chou, and C.-K. Shih, *Interlayer couplings, moiré patterns, and 2D electronic superlattices in MoS_2/WSe_2 hetero-bilayers*, Sci. Adv. **3**, e1601459 (2017).

[454] H. Yu, G.-B. Liu, J. Tang, X. Xu, and W. Yao, *Moiré excitons: From programmable quantum emitter arrays to spin-orbit–coupled artificial lattice*, Sci. Adv. **3**, e1701696 (2017).

[455] K. Tran, G. Moody, F. Wu, X. Lu, J. Choi, K. Kim, A. Rai, D. A. Sanchez, J. Quan, A. Singh, J. Embley, A. Zepeda, M. Campbell, T. Autry, T. Taniguchi, K. Watanabe, N. Lu, S. K. Banerjee, K. L. Silverman, S. Kim, E. Tutuc, L. Yang, A. H. MacDonald, and X. Li, *Evidence for moiré excitons in van der Waals heterostructures*, Nature **567**, 7746, 71–75 (2019).

[456] J. Choi, M. Florian, A. Steinhoff, D. Erben, K. Tran, D. S. Kim, L. Sun, J. Quan, R. Claassen, S. Majumder, J. A. Hollingsworth, T. Taniguchi, K. Watanabe, K. Ueno, A. Singh, G. Moody, F. Jahnke, and X. Li, *Twist Angle-Dependent Interlayer Exciton Lifetimes in van der Waals Heterostructures*, Phys. Rev. Lett. **126**, 047401 (2021).

[457] Z. Li, X. Lu, D. F. C. Leon, Z. Lyu, H. Xie, J. Hou, Y. Lu, X. Guo, A. Kaczmarek, T. Taniguchi, K. Watanabe, L. Zhao, L. Yang, and P. B. Deotare, *Interlayer Exciton Transport in $MoSe_2/WSe_2$ Heterostructures*, ACS Nano **15**, 1539 (2021).

[458] M. Brotons-Gisbert, H. Baek, A. Campbell, K. Watanabe, T. Taniguchi, and B. D. Gerardot, *Moiré-Trapped Interlayer Trions in a Charge-Tunable $WSe_2/MoSe_2$ Heterobilayer*, Phys. Rev. X **11**, 3, 031033 (2021).

[459] E. Liu, E. Barré, J. van Baren, M. Wilson, T. Taniguchi, K. Watanabe, Y.-T. Cui, N. M. Gabor, T. F. Heinz, Y.-C. Chang, and C. H. Lui, *Signatures of moiré trions in $MoSe_2/WSe_2$ heterobilayers*, Nature **594**, 46 (2021).

[460] F. Wu, T. Lovorn, and A. H. MacDonald, *Theory of optical absorption by interlayer excitons in transition metal dichalcogenide heterobilayers*, Phys. Rev. B **97**, 035306 (2018).

[461] Q. Tan, A. Rasmita, Z. Zhang, K. S. Novoselov, and W. bo Gao, *Optical signature of cascade transitions between moiré interlayer excitons*, ArXiv e-prints p. arXiv:2202.10088v1 (2022).

[462] J. Wang, J. Ardelean, Y. Bai, A. Steinhoff, M. Florian, F. Jahnke, X. Xu, M. Kira, J. Hone, and X.-Y. Zhu, *Optical generation of high carrier densities in 2D semiconductor heterobilayers*, Sci. Adv. **5**, eaax0145 (2019).

[463] W. Li, X. Lu, S. Dubey, L. Devenica, and A. Srivastava, *Dipolar interactions between localized interlayer excitons in van der Waals heterostructures*, Nat. Mater. **19**, 624 (2020).

[464] W. Li, X. Lu, J. Wu, and A. Srivastava, *Optical control of the valley Zeeman effect through many-exciton interactions*, Nat. Nanotechnol. **16**, 148 (2021).

[465] L. Zhang, R. Gogna, G. W. Burg, J. Horng, E. Paik, Y.-H. Chou, K. Kim, E. Tutuc, and H. Deng, *Highly valley-polarized singlet and triplet interlayer excitons in van der Waals heterostructure*, Phys. Rev. B **100**, 041402(R) (2019).

[466] C. Cho, J. Wong, A. Taqieddin, S. Biswas, N. R. Aluru, S. Nam, and H. A. Atwater, *Highly Strain-Tunable Interlayer Excitons in MoS_2/WSe_2 Heterobilayers*, Nano Lett. **21**, 3956 (2021).

[467] Y. Bai, L. Zhou, J. Wang, W. Wu, L. J. McGilly, D. Halbertal, C. F. B. Lo, F. Liu, J. Ardelean, P. Rivera, N. R. Finney, X.-C. Yang, D. N. Basov, W. Yao, X. Xu, J. Hone, A. N. Pasupathy, and X.-Y. Zhu, *Excitons in strain-induced one-dimensional moiré potentials at transition metal dichalcogenide heterojunctions*, Nat. Mater. **19**, 1068 (2020).

[468] Y. Y. Y, K. Ganapathi, and S. Salahuddin, *How good can monolayer MoS_2 transistors be?*, Nano Lett. **11**, 3768 (2011).

[469] B. Radisavljevic and A. Kis, *Mobility engineering and a metalinsulator transition in monolayer MoS_2*, Nat. Mater. **12**, 815 (2013).

[470] W. Feng, W. Zheng, W. Cao, and P. Hu, *Back Gated Multilayer InSe Transistors with Enhanced Carrier Mobilities via the Suppression of Carrier Scattering from a Dielectric Interface*, Adv. Mater. **26**, 6587 (2014).

[471] D. A. Bandurin, A. V. Tyurnina, G. L. Yu, A. Mishchenko, V. Zólyomi, S. V. Morozov, R. K. Kumar, R. V. Gorbachev, Z. R. Kudrynskyi, S. Pezzini, Z. D. Kovalyuk, U. Zeitler, K. S. Novoselov, A. Patanè, L. Eaves, I. V. Grigorieva, V. I. Fal'ko, A. K. Geim, and Y. Cao, *High electron mobility, quantum Hall effect and anomalous optical response in atomically thin InSe*, Nat. Nanotechnol. **12**, 223–227 (2017).

[472] G. W. Mudd, M. R. Molas, X. Chen, V. Zólyomi, K. Nogajewski, Z. R. Kudrynskyi, Z. D. Kovalyuk, G. Yusa, O. Makarovsky, L. Eaves, M. Potemski, V. I. Falko, and A. Patanè, *The direct-to-indirect band gap crossover in two-dimensional van der Waals Indium Selenide crystals*, Sci. Rep. **6**, 39619 (2016).

[473] M. A. Bhuiyan, Z. R. Kudrynskyi, D. Mazumder, J. D. G. Greener, O. Makarovsky, C. J. Mellor, E. E. Vdovin, B. A. Piot, I. I. Lobanova, Z. D. Kovalyuk, M. Nazarova, A. Mishchenko, K. S. Novoselov, Y. Cao, L. Eaves, G. Yusa, and A. Patanè, *Photoquantum Hall Effect and Light-Induced Charge Transfer at the Interface of Graphene/InSe Heterostructures*, Adv. Funct. Mater. **29**, 1805491 (2019).

[474] F. Yan, L. Zhao, A. Patanè, P. Hu, X. Wei, W. Luo, D. Zhang, Q. Lv, Q. Feng, C. Shen, K. Chang, L. Eaves, and K. Wang, *Fast, multicolor photodetection with graphene-contacted p-GaSe/n-InSe van der Waals heterostructures*, Nanotechnology **28**, 27LT01 (2017).

[475] M. Wasala, H. I. Sirikumara, Y. R. Sapkota, S. Hofer, D. Mazumdar, T. Jayasekera, and S. Talapatra, *Recent advances in investigations of the electronic and optoelectronic properties of group III, IV, and V selenide based binary layered compounds*, J. Mater. Chem. C **5**, 11214 (2017).

[476] D. Mazumder, J. Xie, Z. R. Kudrynskyi, X. Wang, O. Makarovsky, M. A. Bhuiyan, H. Kim, T.-Y. Chang, D. L. Huffaker, Z. D. Kovalyuk, L. Zhang, and A. Patanè, *Enhanced Optical Emission from 2D InSe Bent onto Si-Pillars*, Adv. Optical Mater. **8**, 2000828 (2020).

[477] N. Ubrig, E. Ponomarev, J. Zultak, D. Domaretskiy, V. Zólyomi, D. Terry, J. Howarth, I. Gutiérrez-Lezama, A. Zhukov, Z. R. Kudrynskyi, Z. D. Kovalyuk, A. Patanè, T. Taniguchi, K. Watanabe, R. V. Gorbachev, and V. I. F. . A. F. Morpurgo, *Design of van der Waals interfaces for broad-spectrum optoelectronics*, Nat. Mater. **19**, 299 (2020).

[478] S. Cianci, E. Blundo, M. Felici, A. Polimeni, and G. Pettinari, *Tailoring the optical properties of 2D transition metal dichalcogenides by strain*, Opt. Mater. **125**, 112087 (2022).

[479] S. Appalakondaiah, G. Vaitheeswaran, A. Pradesh, S. Lebégue, N. E. Christensen, and A. Svane, *Effect of van der Waals interactions on the structural and elastic properties of black phosphorus*, Phys. Rev. B **86**, 035105 (2012).

[480] J.-W. Jiang and H. S. Park, *Negative Poisson's ratio in single-layer black phosphorus*, Nat. Commun. **5**, 4727 (2014).

[481] E. Maggio and L. Petit, *Misura di uno spot laser tramite obiettivi*, Relazione del percorso di eccellenza, Sapienza University of Rome (2014).

[482] A. A. Govyadinov, S. Mastel, F. G. F, A. Chuvilin, P. S. Carney, and R. Hillenbrand, *Recovery of permittivity and depth from near-field data as a step toward infrared nanotomography*, ACS Nano **8**, 6911 (2014).

[483] H. Rydberg, M. Dion, N. Jacobson, E. Schröder, P. Hyldgaard, S. I. Simak, D. C. Langreth, and B. I. Lundqvist, *Van der Waals Density Functional for Layered Structures*, Phys. Rev. Lett. **91**, 126402–1 (2003).

[484] S. Grimme, J. Antony, S. Ehrlich, and H. Krieg, *A consistent and accurate ab initio parametrization of density functional dispersion correction (DFT-D) for the 94 elements H-Pu*, J. Chem. Phys. **132**, 154104 (2010).

[485] H. Rydberg, B. I. Lundqvist, D. C. Langreth, and M. Dion, *Tractable nonlocal correlation density functionals for flat surfaces and slabs*, Phys. Rev. B **62**, 6997 (2000).

[486] M. Dion, H. Rydberg, E. Schröder, D. C. Langreth, and B. I. Lundqvist, *van der Waals Density Functional for General Geometries*, Phys. Rev. Lett. **92**, 246401 (2004).

[487] K. Lee, Éamonn D. Murray, L. Kong, B. I. Lundqvist, and D. C. Langreth, *Higher-accuracy van der Waals density functional*, Phys. Rev. B **82**, 081101(R) (2010).

[488] K. Berland, V. R. Cooper, K. Lee, E. Schröder, T. Thonhauser, P. Hyldgaard, and B. I. Lundqvist, *van der Waals forces in density functional theory: a review of the vdW-DF method*, Rep. Prog. Phys. **78**, 066501 (2015).

[489] J. H. Warner, E. R. Margine, M. Mukai, A. W. Robertson, F. Giustino, and A. I. Kirkland, *Dislocation-Driven Deformations in Graphene*, Science **337**, 209 (2012).

[490] P. Giannozzi *et al.*, *QUANTUM ESPRESSO: a modular and open-source software project for quantum simulations of materials*, J. Phys. Condens. Matter **21**, 395502 (2009).

[491] G. F. Koster, J. O. Dimmock, R. G. Wheeler, and H. Statz, *Properties of the thirty-two point groups*, MIT press, Cambridge, Massachusetts, US, vol. 24 (1963).

[492] M. S. Dresselhaus, G. Dresselhaus, and A. Jorio, *Group theory: application to the physics of condensed matter*, Springer Science & Business Media, Berlin, Germany (2007).

[493] J. Ribeiro-Soares, R. M. Almeida, E. B. Barros, P. T. Araujo, M. S. Dresselhaus, L. G. Cançado, and A. Jorio, *Group theory analysis of phonons in two-dimensional transition metal dichalcogenides*, Phys. Rev. B **90**, 115438 (2014).

[494] B. Peng, H. Zhang, H. Shao, Y. Xu, R. Zhang, and H. Zhu, *The electronic, optical, and thermodynamic properties of borophene from first-principles calculations*, Journal of Materials Chemistry C **4**, 16, 3592–3598 (2016).